



TECHNISCHE
UNIVERSITÄT
DARMSTADT

On the Numerics of Electrical Phenomena in Thermo-Elasto-Hydrodynamic Rolling Contacts

vom Fachbereich Maschinenbau
an der Technischen Universität Darmstadt

zur Erlangung des akademischen Grades eines
Doktor-Ingenieurs (Dr.-Ing.)
genehmigte

DISSERTATION

vorgelegt von

Marcel Neu, M.Sc.
aus Arnsberg

Erstgutachter: Prof. Dr.-Ing. Eckhard Kirchner
Zweitgutachterin: Prof. Dr.-Ing. Jeanette Hussong
Tag der Einreichung: April 25, 2022
Tag der mündlichen Prüfung: Juni 22, 2022

Darmstadt 2022
D17

On the Numerics of Electrical Phenomena in Thermo-Elasto-Hydrodynamic
Rolling Contacts

Genehmigte Dissertation von Marcel Neu, M.Sc. aus Arnsberg

Erstgutachter: Prof. Dr.-Ing. Eckhard Kirchner

Zweitgutachterin: Prof. Dr.-Ing. Jeanette Hussong

Tag der Einreichung: 25.04.2022

Tag der mündlichen Prüfung: 22.06.2022

Technische Universität Darmstadt

Darmstadt 2022 - D17

Bitte zitieren Sie dieses Dokument als:

URN: urn:nbn:de:tuda-tuprints-216475

URL: <https://tuprints.ulb.tu-darmstadt.de/id/eprint/21647>

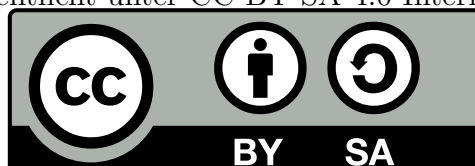
Dieses Dokument wird bereitgestellt von TUprints,

E-Publishing-Service der TU Darmstadt

<http://tuprints.ulb.tu-darmstadt.de>

tuprints@ulb.tu-darmstadt.de

Veröffentlicht unter CC BY-SA 4.0 International



Erklärung

Hiermit erkläre ich, dass ich die vorliegende Arbeit, abgesehen von den in ihr ausdrücklich genannten Hilfen, selbstständig verfasst habe.

Darmstadt, den 25. April 2022



Marcel Neu

Preface

The idea to exploit existing physical phenomena for sensorial purposes as it is done with the sensory rolling bearing, as an example for the class of sensing machine elements, seems appealing. However, such an approach comes at the cost of high model complexity. So stepping towards multi-physical simulation to tackle this intricacy on the most fundamental level appeared promising. Thus, the path for this Ph.D. thesis was clear, and the sails were set.

It quickly became apparent that this undertaking was not solely about modelling complexity. This work was the first of its kind at the institute and thus there was no experience gathered on numerical tribology yet, so much more fundamental questions first came into focus. The most far-reaching was probably the choice of the program on which the work should be based. Another one was the demand for the generality of the approach, contradicting the need to solve only a specific task concerning rolling bearings. Added to this was an extreme range of techniques for nearly every aspect connected to the goal. For example, dozens of empirical and theoretical approaches describe a lubricant's viscosity, each limited to a specific oil, a range of operational conditions, or both. The only reliable way to answer all these questions was to review an overwhelming amount of literature since no best practice was established yet.

The main challenge was to analyse the system in question while finding proper models and establishing those into the calculation framework in a sustainable way. It had to be ensured that the approach is universal enough to satisfy future research requirements without knowing which direction this might develop. Thus, auxiliary implementations were no option, and programming aspects like the implementation availability to all parts of the program had to be considered. This approach, in turn, required an in-depth understanding of the source code.

This work created a starting point for future numerical research and added a new physical domain to the complexity of Elastohydrodynamic Lubrication numerics. It extracts models and calculation procedures close to the state of research while offering a first solution to the numerical calculation of electrostatic fields and charge carrying species. Unfortunately, the possibilities and potential application areas in tribology could not yet be sorted out entirely.

Nevertheless, the point to which I was able to push this work is, regarding it actually started at square one, worth noticing. The achievement is due to the contribution of several people. First of all, my students, Justin Jung, Christoph Möller, Viviane Bauch, Fabian Bender, Patrick Fehn, Shabetha Ramachandran, Johannes Thein, Niklas Lee, Anatoly Zaiat, Harsh Mulrav and Melissa Cahill, have exceeded my expectations with their contributions.

The support of my dear colleagues at the university also advanced this work. Especially

André Harder was over-proportionately often forced to listen to me spinning in circles. He endured my monologues and almost always came up with a solution. Another group of people that participated in this thesis are Dr. Sebastian Dehe and Dr. Johannes Hartmann, who kept the bar high for me during my studies and after that, which led to this Ph.D. attempt in the first place. Furthermore, I want to thank my family and my beloved girlfriend, who supported me when I was down and had to fuel my fury when I was enraged, sometimes without even knowing what the actual problem was.

Other thanks go to Prof. Dr.-Ing. Jeanette Hussong for taking the co-review to this work. My presentations at her institute gave me another environment for input and the opportunity to improve my work. Finally, I want to thank Prof. Dr.-Ing. Eckhard Kirchner for this Ph.D. opportunity. The risk of starting something new is high, but entrusting someone with success to something new and relying on this very person's abilities is even higher. Along the way, Prof. Kirchner was always indispensable with his questions, suggestions and constructive criticism. Hopefully, I was able to deliver a satisfactory result.

Darmstadt, April 25, 2022

Marcel Neu

Contents

1. Introduction	1
1.1. Motivation	1
1.2. A Short History of Elastohydrodynamics	4
1.3. Need for Research	5
2. Fundamentals	7
2.1. Ball Bearing Systems	7
2.1.1. Kinematics	8
2.1.2. Hertzian Contact	12
2.1.3. Load Ratio	14
2.1.4. Operating Conditions and Lubrication Regimes	15
2.1.5. Bearing Materials and Lubricants	17
2.2. Multi-Physics	18
2.3. Fluid	23
2.3.1. Continuity Equation	23
2.3.2. Momentum Transport Equation	24
2.3.3. Energy Transport Equation	25
2.3.4. Equations of State and Compressibility	27
2.3.5. Viscosity	31
2.3.6. Glass Transition	33
2.4. Solid	35
2.5. Dimensionless Quantities	37
2.6. Electrostatics of Tribological Systems	39
2.6.1. Electro Quasi Static Assumption	40
2.6.2. Electrostatics	41
2.6.3. Electric Species Transport	41
2.6.4. Clausius Mossotti Equation	42
3. Research Questions	44
4. Calculation Methodology	46
4.1. Programme Architecture and Implementation	47
4.1.1. Program Selection	47
4.1.2. C++	51
4.1.3. Overarching Implementation	53
4.1.4. Fluid Solver	64
4.1.5. Solid Solver	67

4.1.6. Electrostatics Solver	68
4.2. Calculation Setup	69
4.3. Assumptions and Simplifications	80
5. Results	82
5.1. Code Verification and Simulation Validation	82
5.2. Test-Driven Development	83
5.3. Comparative Calculation with Literature Cases	97
5.4. The Capacity of Rolling Bearing Contacts	105
5.4.1. Hybrid Bearing Experiments	105
5.4.2. Temperature Corrected Hybrid Bearing Experiments	107
5.5. Further Investigations	111
5.5.1. Surface Imperfections	111
5.5.2. Charges in Rolling Bearing Contacts	115
6. Discussion	119
7. Conclusions and Outlook	124
A. FVA 3 Reference Oil Data	126
B. Compressibility	127
B.1. Murnaghan Compressibility Derivation	127
B.2. Tait Compressibility Derivation	128
C. Compression Modulus	129
C.1. Dowson Higginson	129
C.2. Tait	129
C.3. Murnaghan	129
D. Experimental Setup	130
E. Implementations and Source Codes	131
E.1. thermalEfsiFoam	131
E.2. pmdRelease	132
E.3. temperatureunstotalLagrangian	139
E.4. electrostaticthermophysicalCharge	145
E.5. ionicChargeSolver	147
Bibliography	XVIII
Acronyms	XXX
Symbols	XXXII

List of Figures

1.1.	Schematic Electric Vehicle (EV) powertrain	1
1.2.	Pulse Width Modulation (PWM) signals and superposition U_{CM} signal	2
1.3.	Capacitor analogy for rolling bearings by Schirra et al. [11] based on Bader et al. [12] and Gemeinder et al. [13]	3
2.1.	Rolling bearing geometry, based to Harris et al. [45, pp.49, 310]	8
2.2.	Contact angle α as a result of axial load and play according to Harris et al. [45, p.53]	9
2.3.	Radial load F_R and load zone φ according to Harris et al. [45]; Point contact load Q for a single rolling element according to Hamrock et al. [39]	11
2.4.	Geometry for Hertzian contact according to Harris et al. [45, p.61]	12
2.5.	Elliptical point contact	13
2.6.	Change in friction coefficient μ with specific lubrication film thickness λ ; Frictional regimes: I - solid-/boundary-friction; II - mixed friction; III - elastohydrodynamic-/hydrodynamic friction; Electrical analogy for comparison; Image adapted from Czichos [49], based on Stribek [46]	15
2.7.	Schematic domain representation and their interaction; Thermodynamics \mathcal{T} (red), fluid-mechanics \mathcal{F} (blue), structural-mechanics \mathcal{S} (green) and electrostatics \mathcal{E} (yellow)	19
2.8.	Dimensionless viscosity parameter g_v plotted over dimensionless elasticity parameter g_E ; FSI regimes according to Hamrock et al. [48, p.508]; Dashed red line indicates regions relevant to EHL; Dashed black line indicates expected conditions calculated in this work	22
2.9.	Relative density $\rho_0/\rho(p)$ plotted over pressure p for Tait equation 2.35 using parametrization from table 2.4 at $T_R = 313K$ according to Bair [72]	29
2.10.	Relative viscosity η_F/η_0 plotted over pressure p for Doolittle-Tait model with fragile/strong parametrization from table 2.6)	33
2.11.	Visualization of the free volume concept. Black - rigid molecule space; Grey - temperature dependent free space; White - free space	34
2.12.	Displacement vector \mathbf{D} indicating current position \mathbf{X} from initial position \mathbf{X}	35
4.1.	Schematic visualization of a functional structure realizing a primary function following Feldhusen et al. [108, p.45]	46
4.2.	Visualisation multi-physics programme architecture; Complete framework consisting of modules M 1-3; API connecting individual programs P 1-4	48

4.3.	Example for geometric field information; The neighbouring relations (p_i) and surface normals (\vec{n}_i) for a single cell centroid serve as the basis for calculating the balance equations	53
4.4.	Flowchart symbols according to DIN 66001 [116]	54
4.5.	Synopsis of the program architecture; Upright terms - unchanged; Italic terms - adapted; Bold terms - newly created	55
4.6.	General Grid Interface (GGI) connecting domains A and B of different resolution at a circular interface	56
4.7.	Flowchart representation of the <i>thermalEfsiFoam</i> calculation procedure .	60
4.8.	Visualisation of lubrication film thickness adaption function adaptDeltah()	61
4.9.	Flowchart representation of the pmdRelease fluid solver	64
4.10.	Flowchart representation of the <i>temperatureunstotalLagrangian</i> solid solver	67
4.11.	Flowchart representation of the ionicChargeSolver solver combining charge transport (PNP solver) and electric field calculation (Laplace solver) . .	69
4.12.	Visualisation of the maximum time-steps for the individual domains . . .	71
4.13.	Two-dimensional point/line contact representation for EHL rolling bearing numerics	73
4.14.	Schematic grid designs; Reduced presentation	76
4.15.	Visualization of severity of cell non-orthogonality due to distortion	77
4.16.	Detailed representation of the contact zone; Fluid grid shown	77
5.1.	Finite volume one-dimensional ([1,5000,1] cells) calculation region with predefined pressure and temperature values per cell to recreate viscosity and density curves for validation	84
5.2.	Finite volume pseudo one-dimensional ([5000,1,1] cells) calculation region OpenFOAM case visualization via ParaView	85
5.3.	Relative density $\rho(p)/\rho_0$ plotted over pressure p for different temperatures based on the parametrization for LVI 260 reference oil according to Bair [28], results from OpenFOAM; (a) Tait equation, exponential change in bulk modulus with temperature; (b) Tait equation, linear change in bulk modulus with temperature; (c) Murnaghan equation, exponential change in bulk modulus with temperature; (d) Murnaghan equation, linear change in bulk modulus with temperature	86
5.4.	Dynamic viscosity $\eta_F(p, T)$ plotted over pressure p for different temperatures T (legend applies to all graphs); (a) Tait-Doolittle verification results from OpenFOAM based on parametrization for ideal fragile/strong lubricant according to table 2.6	87
5.5.	Tait Doolittle model singularity and unboundedness; (a) Relative Density $\rho(p)/\rho_0$ plotted over pressure p ; (b) Dynamic viscosity η_F plotted over pressure p	88
5.6.	Dowson model implemented and parametrized according to Hartinger et al. [32]; (a) Relative Density ρ/ρ_0 plotted over pressure p ; (b) Dynamic viscosity μ_F plotted over pressure p	89

5.7. Non-orthogonal cavity geometry based on the C1 benchmark test case by Demirdzić and Peric [129]	90
5.8. (a), (b) Non-orthogonal cavity results, original images by Demirdzić and Peric [129]; (c), (d) Numerical results from OpenFOAM	91
5.9. 3D beam calculation setup	91
5.10. Maximum stress τ_{max} plotted over displacement δ ; Numerical Hertzian contact solution and analytical calculation according to Harris [45, p.198-203]	93
5.11. ParaView visualization for the linear elastic Hertzian deformation for different deformations δ according to figure 2.5	94
5.12. Infinite cylinder cooling test case	95
5.13. Dimensionless temperature Θ plotted over Fourier time Fo for increasing Biot numbers Bi - analytical solution	96
5.14. Dimensionless temperature Θ plotted over Fourier time Fo for increasing Biot numbers - numerical solution	97
5.15. Calculation scheme proposed by Turek and Hron [132, p.249] for FSI benchmark; Parabolic inflow U_x triggers periodic oscillations. Displacement amplitude and frequency of point A relative to B used for benchmark	98
5.16. Extract from the Hron Turk Simulation	98
5.17. Solution of the Hron and Turek FSI calculation performed by Tukovic [42] and isothermal compressible pmdRelease solver	99
5.18. Central film-thickness h_c plotted over force, temperature and velocity; Comparison between Dowson-Toyoda reference calculation and numerical results	101
5.19. ParaView visualization for the Hertzian deformation	104
5.20. Load Q plotted over FSI - Iteration for fluidFoam	104
5.21. Load Q plotted over FSI - Iteration for <i>fsiFoam</i>	104
5.22. Experimental setup according to Jablonka et al. [43]	106
5.23. Wheatstone bridge circuit diagram with test bearing capacity C_{Bearing} according to Puchtler et al. [102]	108
5.24. Capacity C_{Bearing} plotted over angle of rotation data gathered by Mulrav [133] for the hybrid bearing test-setup	109
5.25. Peak capacity $C_{\mathcal{E}}$ plotted over radial load F_R ; Standard deviation added for the average over several rotations	110
5.26. Measured Surface imperfections by Martin [124]	112
5.27. Integration of 5.26a and 5.26b centerline into 2D numerical Grid	112
5.28. Pressure distribution for $T= 313$ K, $u_e= 2.03$ m s ⁻¹	113
5.29. Pressure p plotted over EHL contact length for the imperfections; Blue line - centre of the EHL contact	113
5.30. Electric field for $T= 313$ K, $u_e= 2.03$ m s ⁻¹	114
5.31. Relative Permittivity ϵ_r for $T= 313$ K, $u_e= 2.03$ m s ⁻¹	114
5.32. TEHL numerical calculation	116
5.33. Temporal development of ion concentration for low ionic mobility	117
5.34. Temporal development of ion concentration for high ionic mobility	117

6.1. Incompressible stationary calculation 122
6.2. Cavitation and two phase representation for the calculation region 122
D.1. Rolling bearing test rig. CAD Visualization 130

List of Tables

2.1.	Bearing material properties for steel and ceramics	17
2.2.	Lubricant material properties in comparison based on Bartel [54]	18
2.3.	Free volume theory parametrization for equation 2.35 for ideal lubricant according to Bair [72, p.123]	29
2.4.	Tait equation 2.35 parametrization using bulk modulus equation 2.34 according to Bair [72]	30
2.5.	Temperature-density data for FVA 3 reference oil	30
2.6.	Fragile/strong parametrization for equations 2.41 and equation 2.43 according to Bair [72, p.123]	32
4.1.	Parameters for the two-dimensional numerical case by Almqvist [30] and Hajishafiee [33] compared to the present work	74
4.2.	Material parameters for the two-dimensional numerical case by Almqvist [30] and Hajishafiee [33] compared to the present work	75
4.3.	Number of cells in perimeter direction for an aspect ratio of 1 and given number of cells in height direction	78
4.4.	Boundary and interface conditions for the fluid domain	78
4.5.	Boundary and interface conditions for the solid domain	79
4.6.	Conversion of loads from experimental setup, in section 5.4.2 via the single contact onto the two-dimensional numerical case	81
5.1.	Total deformation at point A for a uniaxial deflection of a square beam; Analytical solution compared to numerical results	92
5.2.	Parameters for the mean Temperature calculation for different Biot numbers according to Taler [131, p.406]	95
5.3.	Thermal parameters for the infinite cylinder test for different Biot numbers	96
5.4.	Characteristic parameters for the Turek-Hron test	99
5.5.	Parameters for the free volume theory model based on equation 2.41 and Tait model based on equation 2.35 and 2.33	100
5.6.	Parameters for central film-thickness calculations	101
5.7.	Dimensionless parameters for the central film-thickness comparisons to Dowson-Toyoda reference calculation and numerical results	102
5.8.	Hartinger et al. [32] reference case parameter list; Compare to figure 4.13	103
5.9.	Test parameters for the Jablonka et al. experiments and the according temperature corrected values	107
5.10.	Input parameters for a full factorial experimental plan including temperature correction	108

5.11. Geometry parameter for 6205 C3 rolling bearings 109

5.12. Parameters for the free volume theory model based on equation 2.41 and
Tait model based on equation 2.35 and 2.34 for FVA 3 109

5.13. Experimental Parameters used by Harder et al. [123] 116

A.1. FVA 3 Viscosity Data taken from Bartel [54, p.120] 126

Pauca sed matura.

Carl Friedrich Gauß

Kurzfassung

Diese Arbeit stellt die methodische Entwicklung einer Simulationsumgebung vor, die für eine Berechnung der Fluid-Struktur Interaktion von Wälzlagerkontakten in Kombination mit elektrostatischen Feldern genutzt werden kann. Durch die vorgestellten Implementierungen wird eine numerische Analyse der thermisch elasto-hydrodynamischer Schmierung in elektrisch belasteten Wälzlagerkontakten möglich.

Die zur Berechnung eines solchen Systems notwendigen Differentialgleichungen, Modelle und Kopplungsmechanismen sind in den Grundlagen aus der Literatur entnommen. Basierend auf der Fluid-Struktur-Interaktions-Erweiterung des Programms foamExtend 4.0 ist eine Programmarchitektur entstanden, welche die Theorie abbildet. Alle neuen Implementierungen wurden mit dem Ansatz der testgetriebenen Entwicklung anhand etablierter numerischer und analytischer Tests verifiziert und validiert.

Da zum Zeitpunkt der Einreichung keine experimentellen Referenzdaten für elektrische Phänomene in isolierten thermisch elasto-hydrodynamischen Kontakten verfügbar sind, wird ein für die endgültige Validierung geeigneter Datensatz experimentell erfasst. Der für die Datenerfassung verwendete Versuchsaufbau und die verarbeiteten Daten selbst, sind ebenfalls Teil dieser Arbeit. Zum Vergleich mit den experimentellen Ergebnissen wird ein zweidimensionaler numerischer Fall für Referenzrechnungen vorgestellt. Erforderliche Diskretisierungs- und Lösungsverfahren werden auf der Grundlage gängiger Standards für numerische Berechnungen gewählt.

Obwohl die endgültige Validierung noch nicht erfolgt ist, wurde der Code in den performanten Parametergrenzen für die Interpretation von experimentellen Studien verwendet. Die gewonnenen Erkenntnisse über das elektrische Verhalten schadhafter Oberflächen und den Einfluss der Ionisation auf die elektrischen Schädigungsmechanismen stellen einen wissenschaftlichen Mehrwert dar.

Die aus diesen Berechnungen gewonnenen Erkenntnisse werden vor dem Hintergrund möglicher neuer Anwendungsfelder für die Toolbox diskutiert, da elektrische Phänomene nun in den Anwendungsbereich numerischer thermisch-elasto-hydrodynamischer Schmierungsberechnungen fallen. Da diese Berechnungen die Grundlage für die Schadensanalyse von Wälzlagern sind ist mit der Erweiterung die Erforschung von elektrischen Schadensmechanismen ebenfalls möglich. Die Ursachen für die Einschränkungen werden bewertet, und es werden Verbesserungen zur Überwindung der vorherrschenden Probleme genannt. Die Arbeit schließt mit einer Diskussion von Forschungsgebieten, die als vielversprechend angesehen werden. Die Bewertung dieser Bereiche basiert auf den Erkenntnissen dieser Arbeit und den Erfahrungen, die der Autor während des Prozesses gesammelt hat.

Abstract

This work presents the methodological development of a simulation toolbox intended for the Fluid-Structure Interaction calculations of rolling bearings contacts, combined with electrostatic fields. A numerical analysis of the Thermal Elastohydrodynamic Lubrication in electrically burdened rolling bearing contacts becomes possible through the presented implementations.

The differential equations, models, and coupling mechanisms necessary for such calculations are extracted from the literature in this work's fundamentals. Based on the Fluid-Structure Interaction extension of foamExtend 4.0, a program architecture is created to represent the theoretical framework. Each new implementation is verified and validated against established numerical or analytical tests following the Test-Driven Development practice.

Since no reference calculation or experimental data for electrical phenomena in isolated Thermal Elastohydrodynamic Lubrication contacts is available at the point of submission, a data set suited for the final validation is acquired experimentally. The experimental setup used for the data acquisition and the processed data itself is also part of this work. A two-dimensional numerical case for reference calculations is introduced to compare the experimental results. Necessary discretization- and solution procedures are chosen based on common standards for numerical computations.

However, a validation of the calculation procedure against the experimental data failed due to problems that arose by transferring the Fluid-Structure Interaction calculation to the Elastohydrodynamic Lubrication scale. The radial bearing loads used during the experiments are, as of now, not calculable with the proposed numerical setup. Reasons for this are discussed, and solutions are proposed.

Although the final validation has not yet been carried out, the code was used in the performant parameter limits to interpret experimental studies. The insights gained into the electrical behaviour of imperfect surfaces and the influence of ionisation on damage mechanisms is a scientific added value.

The insights gained from these calculations are discussed against the background of possible new fields of application for the toolbox since electric phenomena are now within the scope of numerical Thermal Elastohydrodynamic Lubrication calculations. Since those Thermal Elastohydrodynamic Lubrication calculations are the basis for damage analysis in rolling bearings the extension allows for the research of electric damaging mechanisms as well. Causes for the limitations are evaluated, and improvements to overcome the prevailing problems are stated. This work concludes with a discussion of research areas that are recognized as promising. The assessment of those areas is based on this work's insights and the author's gathered experience.

1. Introduction

1.1. Motivation

Electric mobility increased its market share over combustion engines in the last decade, and the trend toward electrification of transportation will hold for the time to come. Driven by green initiatives [1] and due to the need to reduce the overall output of greenhouse gas to keep the agreements made during the United Nations Climate Change Conference in Paris, research on electric powertrains has intensified. The primary architecture of an Electric Vehicle (EV) utilizes a frequency inverter fed motor, as shown in figure 1.1.

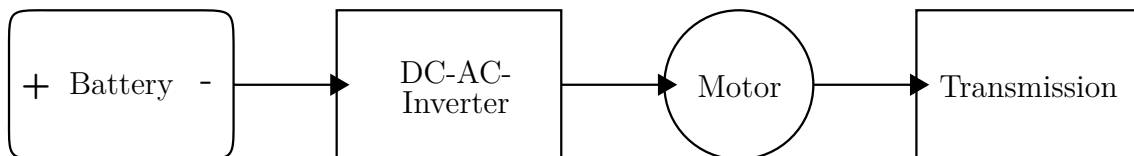


Figure 1.1.: Schematic Electric Vehicle (EV) powertrain

This design is continuously adjustable in speed, a significant advantage for automotive applications and powertrains in industrial infrastructure. Although the configuration of an EV powertrain looks more simplistic than its combustion equivalent and the benefit of continuous change in speed is apparent, there are drawbacks due to the electric signal inversion. A new type of failure became dominant in the bearings of the motor and transmission that are placed behind the inverter, as described by Furtmann et al. [2, pp.3-12] concerning Hausberg [3] and Hausberg et al. [4]. The so-called Inverter-Induced Bearing Currents (IIBC) account for 40 to 50 percent of the total damage-related failures of powertrains in EV, as Lin et al. [5, p.1661] analysed for the Asian market regarding Nandi et al. [6, p.720].

The electrical burden upon the bearing results from the powertrain concept itself. The inverter signal, generated through Pulse Width Modulation (PWM), consists of rectangular pulses with varying lengths. The superposition of these pulses creates an Alternating Current (AC) signal from the Direct Current (DC) battery supply. As a side effect, PWM leads to common-mode voltages V_{CM} in the motor shaft due to the imperfect addition of the three signals, as figure 1.2 shows. For comparison: The superposition of ideal sine waves would result in a zero-line compared to the shown PWM.

The shaft voltage manifests subsequently as current, which causes harmful mechanisms in bearings like Electric Discharge Machining (EDM) [4]. IIBCs introduce electric phenomena to rolling bearings, which Prashad described as tribology in electrical environ-

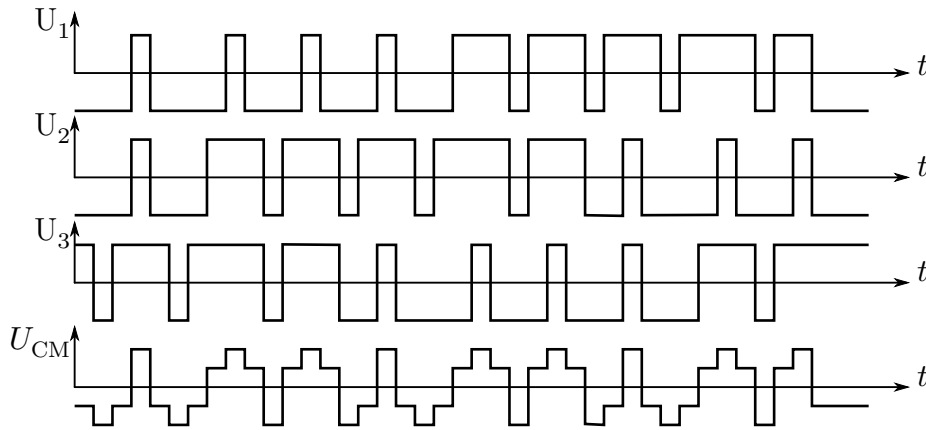


Figure 1.2.: Pulse Width Modulation (PWM) signals and superposition U_{CM} signal

ments [7]. These have been known for some time and have been under investigation since the 1990s, as Mütze [8, p.383] summarized. Research has focused on modelling, mitigating, and monitoring bearing currents since, according to Mütze [8]. While mitigation deals with preventing damaging discharges through design changes (like replacing standard bearings with ceramic ones), monitoring techniques detect electrical damage to adapt maintenance intervals of predictive maintenance. Monitoring is often done via structure-borne sound or torque measurement systems, which sense damage indirectly through increased vibrations or a reduced system efficiency as Cornel et al. [9] described. Modelling, however, focuses on describing the electrical condition of the bearing appropriately to predict harmful mechanisms. Therefore, the mechanical bearing system is equivalent to an electrical circuit with the rolling bearing as a network of electrical resistance $R_{\mathcal{E}}$, capacitance $C_{\mathcal{E}}$, and inductance $L_{\mathcal{E}}$ ¹.

Figure 1.3a illustrates a rolling bearing with its inner and outer ring, rolling elements, and the cage indicated by the bold dashed line. The space between the rolling elements is entirely (or partially) filled with lubricant (and air) or grease, respectively. The assembly is translated into electrical design elements, shown in figure 1.3b. The inner and outer ring acts as resistive contacts, connecting the electrotechnical equivalent for the tribological contacts as a parallel circuit. Since the tribological state is not specified yet, the circuit is generalized as impedance Z according to Harriehausen et al. [10, pp. 349, 353, 358]. Equation 1.1 shows the impedance's resistance, capacitance, and inductance contributions.

$$Z_{\mathcal{E}} = R_{\mathcal{E}} + 2\pi f j L_{\mathcal{E}} + \frac{1}{2\pi j C_{\mathcal{E}}} \quad (1.1)$$

Furthermore, it becomes clear that the AC resistance is frequency-dependent. A more straightforward representation of the circuit is shown in figure 1.3c. The representation in figure 1.3c might vary depending on the cage material since plastic materials insulate the rolling elements and metal cages connects them. The dashed line indicates the circuit for conductive bearing material.

¹The variables are assigned according to section 2.2 by the indices \mathcal{E} , \mathcal{T} , \mathcal{S} and \mathcal{F} .

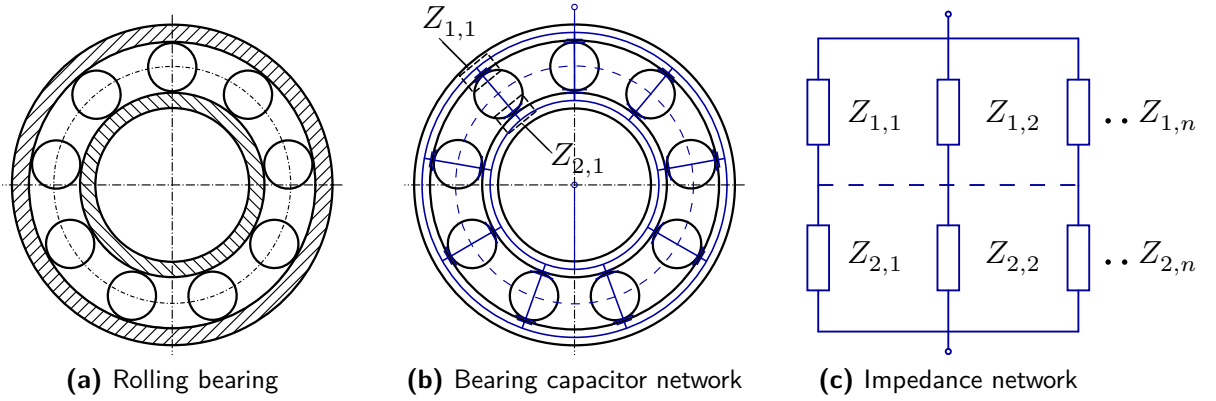


Figure 1.3.: Capacitor analogy for rolling bearings by Schirra et al. [11] based on Bader et al. [12] and Gemeinder et al. [13]

The operating conditions and tribological state determine the properties of the circuit analogy. Latter determines whether the contact between rolling elements and the ring is described by resistance for metal contact or capacitance for hydrodynamic lubrication according to Prashad [7, pp.116-129]. Dependent on the bearings operating condition for lubricated contacts, its tribological regime can be a combination of capacitance $C_{\mathcal{E}}$ and resistance $R_{\mathcal{E}}$. Knowledge about the correlation between electric properties and tribological states allows statements about one another. Magdun et al. [14], for example, used the capacitor analogy of a separating lubricant film to predict EDM events. However, many parameters govern the tribological system, and its description is complex, especially if electric phenomena are introduced. Experimental techniques for analysing single rolling bearing contacts are not upgraded for the additional analysis of electrical properties yet, so hardly any data are available for characterization.

A description is typically based on the Reynolds equation and the Hertzian contact theory to estimate the mean lubrication film thickness h_0 and the contact area A_{Hz} , respectively. These parameters were used by Gemeinder et al. [13] to calculate the capacity $C_{\mathcal{E}}$ of single rolling bearing contacts. The context between a bearings capacity and hydrodynamic lubrication is given according to equation 1.2.

$$C_{\mathcal{E}} = \varepsilon_0 \cdot \varepsilon_r \cdot \frac{A_{\text{Hz}}}{h_0} \quad (1.2)$$

Equation 1.2 implies that the capacity $C_{\mathcal{E}}$ of a plate capacitor equivalent to the tribological contact has a surface area A_{Hz} , spacing of h_0 , and is filled with a dielectric (lubricant) which has a specific permittivity ε . It is calculated from the vacuum permittivity ε_0 and a material-specific relative permittivity ε_r . Determining the electrical properties in this way must take various parameters into account, like temperature T , dynamic viscosity η , the overall bearing kinematics, the external frequency of the electric signal f , and others. Inaccuracies in one of these descriptions lead to significant deviations between theory and experiment. While the analogies used to approximate the contact region might be sufficient to estimate the likelihood of harmful mechanisms, an in-depth understanding

of how parameter changes impact the signal is hard to include in this model. Schirra [15] recently presented an impedance measuring approach for a bearing in an electric circuit to monitor radial loads and thus realized a sensory function. This novel approach which exploits the inverse causal relationships of equation 1.2 as a sensory technique, requires more accurate descriptions. It showed that the approach by Furtmann [2], and Gemeinder [16], which were the starting point for the signal analysis, is not suited to the contact description based on analytical film thickness regressions by Dowson et al. [17], [18] are too limited. Schirra [11] improved the models' accuracy by taking secondary effects like unloaded rolling elements into account but did not overcome the underlying limitations. It seems like analytical descriptions are insufficient for analysing electro tribological problems, which is why this work intends to approach the topic via numerical calculations.

1.2. A Short History of Elastohydrodynamics

Before diving into the fundamentals necessary to describe Elastohydrodynamic Lubrication (EHL) contacts numerically, one should revisit the history of EHL to identify the need for research. Therefore it is mandatory to understand why the actual description of the electrical properties through regression equations for the film thickness h and the Hertzian contact area A_{Hz} are insufficient.

A first numerical solution for the lubrication film thickness was presented by Dowson and Higginson [19], based on the work by Petrusevich [20], through iterating the Reynolds equation and the Hertzian contact calculation until convergence was reached. They also derived the regression equation for the minimum film thickness from their solutions in [17], [18]. However, the most known work, being a basis for regression equations, was published by Hamrock and Dowson [21]–[24]. They proposed not only an improved solution to the numerical approach but also derived regression equations from it. Moes et al. [25] later improved those regressions based on the numerical work by Lubrecht [26] and Venner [27].

The Reynolds equation does not correctly describe the actual EHL contact, especially for high loads, as Bair et al. [28] and Schäfer et al. [29] pointed out. Accordingly, Almqvist and Larsson [30][31] carried out their work differently and changed the numerical approaches in EHL calculation. They used a Navier-Stokes approach instead of the Reynolds equation to solve the EHL regime thermally. The improved convergence stability led to an increased number of CFD-based calculations. Following works coupled Computational Fluid Dynamics (CFD) to finite volume-based solid mechanics. Hartinger et al. [32] increased the pressure range for which CFD-based calculations were accurate. Hajishiafief et al. [33] and Hartinger et al. [34] exceeded the previous results by Hartinger et al. [32] afterwards. Lately, Tomic et al. [35] followed up on this work. Besides the achievement of Thermal Elastohydrodynamic Lubrication (TEHL), Venner et al. [36] and Habchi et al. [37] improved the description accuracy by adding sophisticated models for the lubricant compressibility.

Before the turn of the millennium, regression equations were still derived directly from

the numerical results with the help of dimensionless variables; this changed afterwards. The influences of compression and thermal calculations were taken into account by correction factors. Marian et al. [38] lately published a review on those dimensionless regression equations. They also stated strategies to account for compressibility and temperature impact. If one looks up the equations used by Schirra [15] or Gemeinder [16] to calculate the central and minimum lubricant film thicknesses, one finds the equations by Hamrock and Dowson [39]. Schirra used a thermally corrected viscosity by Murch and Wilson [40] to increase the accuracy towards different temperatures. Nevertheless, the equations currently used for modelling electrical properties reveal a gap in state-of-the-art numerical approaches. These old-fashioned descriptive equations need to be replaced with the modern theoretical framework in experimental research on tribological systems. This short excursion into the history of EHL calculations is far from complete but emphasizes the discrepancy between the calculation approaches available in numerics and those used to interpret of experimental data. The necessity to close this gap clarifies the need for research.

In order to catch up on literature, the author recommends the paper by Marian et al. [38] and Hou et al. [41]. The latter is a review of numerical methods for FSI, which is explicitly mentioned by Tukovic et al. [42], the most recent paper from the creators of the FSI toolbox in OpenFOAM. The following implementations are based on this as a platform.

1.3. Need for Research

As the previous section 1.2 made clear, it would be in line with past successful practices to use a numerical description of the electrical TEHL system to obtain a data basis for accurate regression equations for the capacitance $C_{\mathcal{E}}$. Therefore, this work offers a numerical framework using the theoretical approaches available based on state-of-the-art numerical calculations with an extension to electrostatics.

In order to show its functionality and limitations, the framework is applied to different examples. The aim is to carry out calculations which are comparable to experimental results based on the procedure introduced by Jablonka et al. [43]. Therefore, the numerical case setup has to represent the experimental conditions properly. The transfer of up-to-date EHL calculations into the research on electrical properties shall close the outlined gap.

Even though mitigation techniques are most prominent to prevent IIBCs, scientific insight into the physics of an electrically burdened tribological system is worthwhile. Not only because emerging technologies like sensory applications have become of increasing interest but also because an idea and visualization of the actual processes that take place are an added value.

This work starts with reviewing the existing theory on the description of rolling bearing tribology and electrical phenomena. Based on this theoretical foundation, the concepts closest to first principles are integrated into a multi-physical simulation based on the CFD code OpenFOAM. Naturally, this is not the first attempt to calculate tribolog-

ical contacts of bearings with a finite volume method, and the existing solutions like Hartinger et al. [32] and Hajishafiee et al. [33] are taken into account and serve as a starting point and reference. Typically those calculations are academic and just loosely related to real bearing applications. Thus, this work is distinct from previous ones by focussing on the application side of things. Therefore, the targeted calculations take experimental parameters in terms of load, geometry, and surface velocities as a basis. The attempt to extend the numerical framework to electrodynamic / -static calculations to derive macroscopic properties like capacity from the resolved contact geometry and compare them to experimental data is crucial for validity. Developing the procedure and successfully applying the program to experimental data promises more accurate descriptions for varying parameters and offers a starting point for future research.

2. Fundamentals

This chapter states the necessary fundamentals and introduces a mutual terminology between reader and author regarding variable definitions, equations, and models since these vary significantly across the literature. First, the research object, namely ball bearings, is characterized, the kinematic is determined, and the operating conditions and the mechanical loads investigated during this work are clarified. Then Fluid-Structure Interaction (FSI) is generally described, followed by specific descriptions of EHL. Afterwards, the deep groove rolling bearing tribology is analysed in this context.

In section 2.3, the underlying transport phenomena are introduced, necessary to describe the tribology of rolling bearings and their lubrication. The phenomena include a general outline of the continuity hypothesis towards mass, impulse, and energy transport, equations of state, and models for material properties like dynamic viscosity η or electric permittivity ε . In section 2.4, the equations to describe the deformation of solid bodies (rolling elements and bearing rings) are stated together with the calculation of temperature distributions in these components. Therefore mentioning the fundamentals of elastomechanics is mandatory, together with Hertzian contact mechanics and the heat conduction equation for solids. Section 2.6 offers information about the electrical properties of tribological systems to close out the description for all participating physical, so-called domains.

The term domain is used regularly throughout this work and describes a specific, self-contained area of physics. One speaks of solid, fluid, thermodynamics, and electro-dynamics. There is an overlap for variables and constants across the different domains, their affiliation to a domain is clarified through an identifier subscript introduced in section 2.2. Furthermore, all equations are stated in symbolic writing. This first part represents the state of research and states the relevant literature. It contains some considerations that might seem taken out of context at first glance but show their significance later during the calculation methodology in sections 4.1, 4.2, 5.2, and chapters 6 and 7 on interpretation and outlook.

2.1. Ball Bearing Systems

Rolling bearings are one of the most fundamental parts of a moving technical system and are present in nearly every engineering area. Although rolling bearings are crucial to the function by suppressing multiple degrees of freedom except for the needed ones, they are usually not recognized until they fail to operate. The proper design of the bearings determines whether or not a system works efficiently and sets the maintenance interval. These intervals and efficiency were the focus of research in the past, infusing nearly

every aspect connected to rolling bearing research. Starting with its kinematics and the operating conditions up to the choice of adequate materials and lubricants according to Dowson [44]. As a result, the operational limits of rolling bearings have shifted significantly, and the total lifetime has improved. However, research has not come to an end yet, but the focus of attention shifted severely due to new phenomena emerging from the fields of application bearings. As already indicated in the introduction, a new physical domain has taken a significant role in most research, especially in rolling bearing tribology, as the lubrication between rolling elements and inner/outer ring raceways is a source of failure.

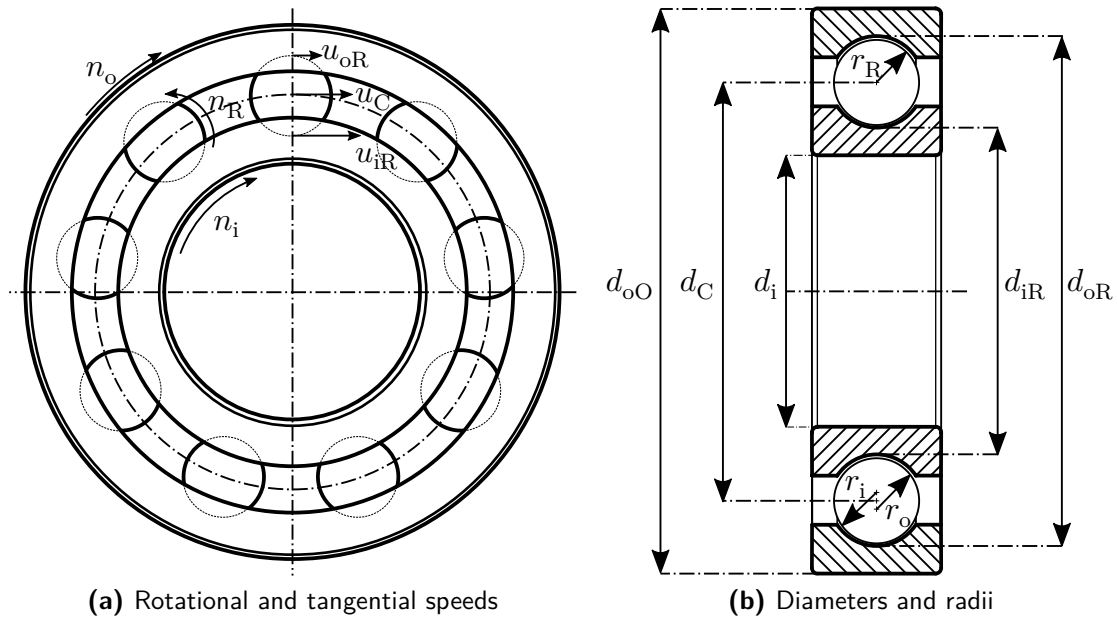


Figure 2.1.: Rolling bearing geometry, based to Harris et al. [45, pp.49, 310]

Since this work takes the rolling bearing as a system of interest for developing the numerical toolbox on TEHL lubrication and electrical phenomena, it is evident first to introduce the operating principle, kinematics, and characteristic quantities.

2.1.1. Kinematics

Rolling bearings consist of four major components. The inner- and outer ring between which multiple rolling elements are distributed evenly over the circumference. A cage indicated as a dashed line between the rings in figure 2.1a ensures the even distribution of the rolling elements. Pockets are provided in the cage to take in the rolling elements. The number of rolling elements and their geometry (spherical, cylindrical, or tapered) vary, leading to various designs. The rolling bearing kinematic is described in detail by Harris [45] and varies significantly for different assembly situations and bearing designs. Calculations carried out in this work are based on a deep groove, rolling bearing, which is radially loaded. Specifically, the rolling bearing of type 6205C3, shown in figure 2.1, was

chosen because the analysis of the results is done based on prior numerical works and experimental data gathered for this bearing design. For most applications, the inner ring rotates with the rotational speed n_i while the outer ring is not in motion. However, there are cases where the outer ring also has a rotational speed n_o unequal to zero. Therefore, figure 2.1a shows the most generalized situation of an inner- and outer ring in motion, according to Harris [45]. Given a no-slip condition between the rolling elements and the raceways, a state of pure rolling is assumed, which implies that the relative surface velocity at the contacting point is zero. The raceway velocity of the inner/outer raceway is calculated through equations 2.1 and 2.2.

$$u_{iR} = \frac{\pi}{60} n_i (d_C - 2r_R \cos(\alpha)) \quad (2.1)$$

$$u_{oR} = \frac{\pi}{60} n_o (d_C + 2r_R \cos(\alpha)) \quad (2.2)$$

The raceway velocities u_{iR} and u_{oR} , result from the mean-/cage diameter d_C by adding/-subtracting the rolling element radius r_R and multiplication with the angular velocity calculated from the rotational velocity of the corresponding ring. The velocities u_{iR} and u_{oR} represent the absolute tangential surface velocities in azimuthal direction for the contact point (red point figure 2.2a). If axial loads are present, the point of contact shifts away from the raceway centre by the angle α . This so-called contact angle α is shown in figure 2.2b and impacts the surface velocities as it alters the effective radius.

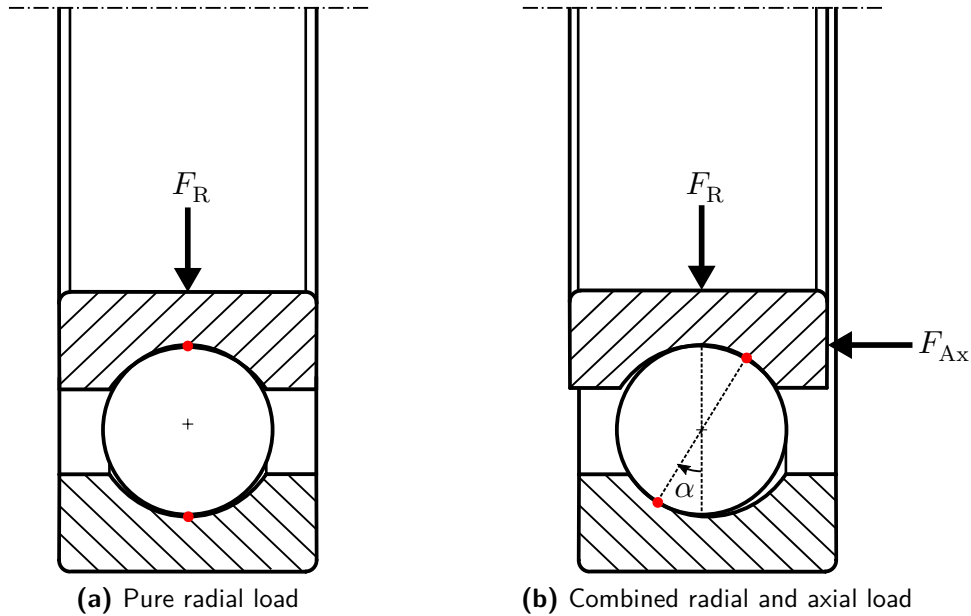


Figure 2.2.: Contact angle α as a result of axial load and play according to Harris et al. [45, p.53]

The initial contact angle α varies with the bearing type and is sometimes called the nominal contact angle. The alternation due to the operating loads is accordingly called

operating contact angle. For mere radial loads, which is the reference situation in this work, the contact angle α is zero. This situation leads to a simplification of equations 2.1 and 2.2. The cage velocity u_C , and its rotational speed n_m are calculated according to equations 2.3 and 2.4.

$$u_C = \frac{1}{2}(u_{iR} + u_{oR}) \quad (2.3)$$

$$n_m = \frac{1}{2}[n_i(1 - \frac{2r_R}{d_C} \cos(\alpha)) + n_o(1 + \frac{2r_R}{d_C} \cos(\alpha))] \quad (2.4)$$

Harris et al. [45, p.310] derived the rotational speed of the rolling elements, as equation 2.5 describes.

$$n_R = \frac{1}{2} \frac{d_C}{2r_R} (1 - \frac{2r_R}{d_C} \cos(\alpha))(1 + \frac{2r_R}{d_C} \cos(\alpha))(n_o - n_i) \quad (2.5)$$

The presented kinematic couplings between the rolling elements and rings have been determined for a pure rolling condition. However, a combination of sliding and rolling is more likely for tribological contacts in general. Therefore, the velocity of the slower contacting surface u_B belonging to the so-called base body and the velocity of the faster surface u_C belonging to the so-called counter body differ. The mean velocity of $0.5(u_B + u_C)$ and the differential velocity $u_B - u_C$ characterize the actual state of motion between the base and counter body. Their ratio is the Slide-to-Roll Ratio (SRR), shown in equation 2.6.

$$\text{SRR} = \frac{2(u_B - u_C)}{(u_B + u_C)} \quad (2.6)$$

The SRR is one of the significant dimensionless quantities in tribology. The numerical or experimental tribological analysis must state it during evaluation. The tribological contacts between the rolling elements and rings have a minimal $\text{SRR} = 0$ since pure rolling is assumed throughout this work. The actual SRR between rolling elements and rings can be somewhat between $\text{SRR} = 0$ and the maximum of $\text{SRR} = 2$, which mainly depends on the load acting on the contact. Therefore, manufacturers specify a minimum load to ensure a pure rolling condition. Nevertheless, sliding is also crucial since sliding bearings operate at $\text{SRR} = 2$. For radial loads, the circumference of the bearing is segregated into the load zone, characterized by the angle φ , and an unloaded zone, shown in figure 2.3a.

The radial load F_R ensures a pure rolling condition for the load zone. Elements outside the load zone might lose rotational velocity n_R due to inertia and friction. This loss results in an SRR unequal to zero towards the inner and outer ring. As the rolling elements re-enter the load zone, their rotational velocity n_R increase until the state of pure rolling establishes again. The SRR is used as the primary characterization feature for tribological contacts as it significantly determines the outcome of a calculation and how the actual contact will be shaped.

Numerical cases are known from the literature dealing with $\text{SRR} = 0, 1, 2$. The different SRRs are calculated in section 5.3 to compare the calculation accuracy, mainly based on

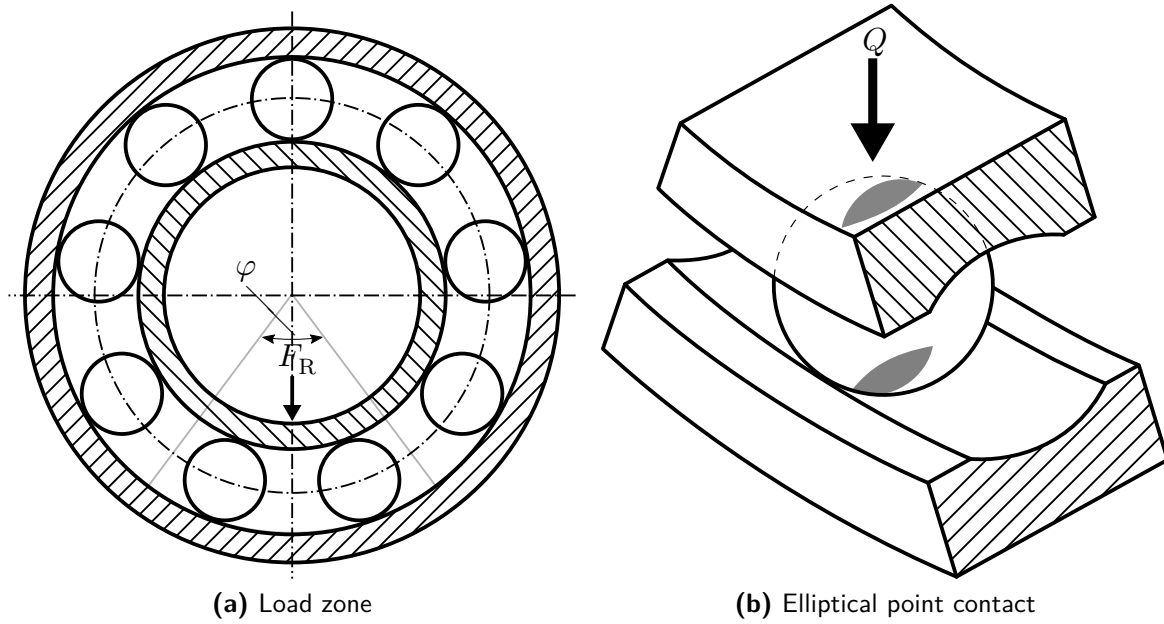


Figure 2.3.: Radial load F_R and load zone φ according to Harris et al. [45]; Point contact load Q for a single rolling element according to Hamrock et al. [39]

characteristics like the Petrushevish [20] peak, which only arise for specific SRRs. Concerning the application for rolling bearings, SRR close to zero or exactly zero is most relevant.

Contrary to what the theoretical load zone suggests, radial loads F_R only transfer through the contracts between the inner-/outer ring and the rolling elements and consequently into the housing by the backside of the outer ring. Because only a portion of the total surface area participates in the load transfer, the contact is characterized as concentrated contacts. These pairings of surfaces are also often referred to as non-conformal contact. Hence, Hertzian contact zones develop, distributing the load over a broader area by an elastic flattening of the contacting surfaces. Figure 2.3b qualitatively shows an example of such an area for a single rolling element in the centre of the load zone. The size and shape of the contact zone depend on the material properties and the load Q acting on it.

In principle, one distinguishes between line and point contacts. Due to the osculation ϕ , the primary form of the contact zone corresponds to an elliptical shape. ϕ is the radii ratio of the inner-/outer raceway (r_o/r_i) towards the radius of the rolling element (r_R), described by equation 2.7 according to Harris et al. [45, p.50].

$$\phi = \frac{r_R}{r_{o/i}} \quad (2.7)$$

As already indicated, the radial load F_R is distributed over multiple rolling elements in the load zone. It is, therefore, worthwhile to calculate the maximum load Q , which acts on a single rolling element, which is located in the centre at any given time. Therefore,

Harris et al. [45, p.238] offered an approximation based on Stribeck [46]. The maximum load for radially loaded deep groove rolling bearings without clearance is calculated according to equation 2.8.

$$Q = \frac{4.37F_R}{Z \cos \alpha} \quad (2.8)$$

Hereby, Z is the number of rolling elements and α the contact angle. The 6205-C3 bearing has seven rolling elements, and the contact angle is zero for pure radial loads. Later on, the discussed kinematic relationships and quantities will determine the velocity boundary conditions and the geometry for the calculation setup. The conversion of an external radial load F_R to the maximum load on a single contact Q is needed to translate test bench settings to the numerical case. The SRR sets different literature sources in perspective to the calculations carried out in this work.

2.1.2. Hertzian Contact

The Hertzian contact theory is one of the critical aspects of tribology and calculation of concentrated rolling bearing contacts. As shown in figure 2.4, the pressure becomes infinite at the point contact of the two contacting curved surfaces since the point has no spacial expansion.

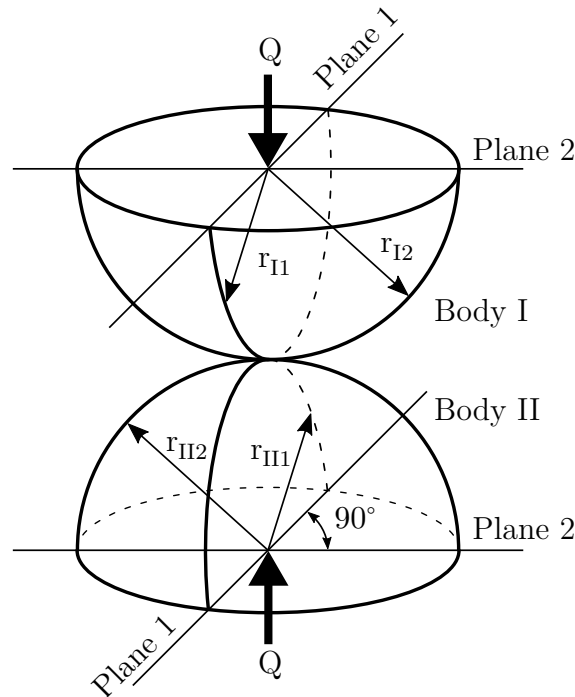


Figure 2.4.: Geometry for Hertzian contact according to Harris et al. [45, p.61]

The Hertzian theory proposes a load-dependent deformation of the bodies, which results in a flattening and, therefore, an area A_{Hz} with finite strain and stress. This region is

called the Hertzian contact area A_{Hz} . The Hertzian solution to the contact problem is essential in tribology since every analytical or numerical calculation of concentrated tribological contacts is based on or compared to the Hertzian solution. The numerical calculations presented in this thesis are also compared to the Hertzian solution for benchmark and interpretation of results. Figure 2.4 displays two solids (Body I, Body II) in mechanical contact, taken from Harris et al.[45, p.61]. Both bodies *I* and *II* each have two defining radii r_1, r_2 . The curvature sum $\Sigma\rho$ is defined as the sum of curvatures according to equation 2.9 and the respective curvature difference $F(\rho)$ by equation 2.10. While the radius of curvature is positive by definition, the curvature itself can be negative or positive, depending on whether the contact is convex or concave. The contact shown in figure 2.4 and described via equations 2.9 and 2.10 represents an ideal point contact for ball bearings.

$$\Sigma\rho = \frac{1}{r_{I1}} + \frac{1}{r_{I2}} + \frac{1}{r_{II1}} + \frac{1}{r_{II2}} \quad (2.9)$$

$$F(\rho) = \frac{(\frac{1}{r_{I1}} - \frac{1}{r_{I2}}) + (\frac{1}{r_{II1}} - \frac{1}{r_{II2}})}{\Sigma\rho} \quad (2.10)$$

All radii are unequal to zero and finite for the ideal point contact. For a line contact, the radii in one plane, for example, r_{I1} and r_{II1} , orthogonal to the rolling direction, become infinite. Harris also offered specific solutions for spherical rolling bearings [45, p.71], radial cylindrical rolling bearings [45, p.73], and tapered rolling bearings [45, p.77], which will not be further elaborated on here since those are derived from the presented one. In this work, the point contact is described in detail based on the work by Harris [45, pp.189]. Details on the line contact are also found in Harris et al. [45, pp.202]. A projection of the area A_{Hz} is illustrated in figure 2.5. While the contact between two spheres leads to a circular projection (as figure 2.4 indicated), the actual contact has an elliptical shape.

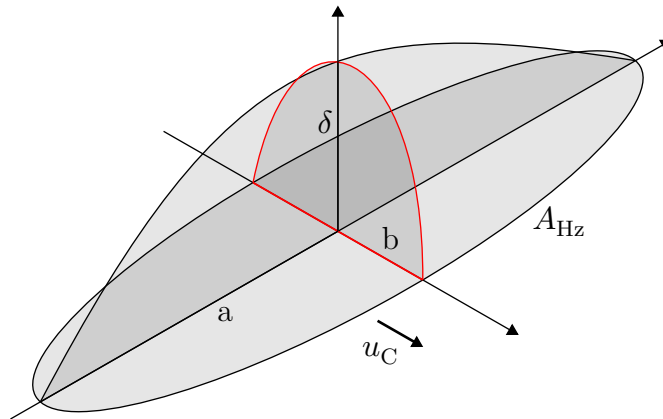


Figure 2.5.: Elliptical point contact

This ellipsoid is the consequence of the concave/convex inner and outer ring geometry (compared to figure 2.3b for visualization). The semi-axis b aligns in the direction of

motion u_C , while the semi-axis a is oriented perpendicular to b . The length of both half axis depends on the load Q , which is imposed on the bodies as depicted in figure 2.4. Furthermore, Young's modulus E , and the Poisson ratio ν impact the size of the contact and the deformation δ . Equations 2.11 and 2.12 are calculation rules for a and b from the dimensionless semi-axis parameters a^* and b^* , tabulated in Harris et al. [45, p.196].

$$a = b^* \cdot \left[\frac{3Q}{2\Sigma\rho} \cdot \left(\frac{(1 - \nu_{II}^2)}{E_{II}} + \frac{(1 - \nu_I^2)}{E_I} \right) \right]^{\frac{1}{3}} \quad (2.11)$$

$$b = b^* \cdot \left[\frac{3Q}{2\Sigma\rho} \cdot \left(\frac{(1 - \nu_{II}^2)}{E_{II}} + \frac{(1 - \nu_I^2)}{E_I} \right) \right]^{\frac{1}{3}} \quad (2.12)$$

Figure 2.5 also shows the total deformation δ of the bodies described in the Hertzian contact theory according to equation 2.13. The dimensionless deformation δ^* , also depends on the curvature difference $F(\rho)$, which is also a tabulated value by Harris et al. [45, p.196].

$$\delta = \delta^* \cdot \left[\frac{3Q}{2\Sigma\rho} \cdot \left(\frac{(1 - \nu_{II}^2)}{E_{II}} + \frac{(1 - \nu_I^2)}{E_I} \right) \right]^{\frac{2}{3}} \cdot \frac{\Sigma\rho}{2} \quad (2.13)$$

The deformation has related surface stress which is described by equation 2.14.

$$\sigma = \frac{3Q}{2\pi ab} \cdot \left[1 - \left(\frac{x^2}{a} \right) - \left(\frac{y^2}{b} \right) \right]^{\frac{1}{2}} \quad (2.14)$$

The equations in section 2.1.2 cover the necessary fundamentals of the Hertzian contact theory. The approximations available through this are used to predict expectable orders of magnitude for load and contact deformation. Equations 2.11 - 2.14 are needed to transfer radial loads F_R from the experiments into point contact load Q used during numerical calculations. The area of the contact to be simulated is highlighted in figure 2.5. The length of the semi-axis is also needed for discretization purposes. The subsurface stress distribution, often discussed in Hertzian theory since it is highly relevant for damaging mechanisms like pitting formation, is not covered.

2.1.3. Load Ratio

Another keyword in rolling bearing research is "load ratio." It describes the ratio between the dynamic load parameter C and the equivalent dynamic bearing load P and is the basis for the statistical bearing lifetime L_{10} calculation. While L_{10} is of subordinate relevance to this work, the load ratio C/P is useful.

Rolling bearing design and available sizes vary over orders of magnitude. Assessing whether a rolling bearing fails needs consideration of the difference in size and design. The load ratio is an adequate quantity to do so. Additionally, a minimum load is described through the load ratio to ensure the correct kinematic motion of the bearing, as assumed in section 2.1.1. The dynamic load parameter C is determined by the manufacturer, who calculates it from the Hertzian contact stresses. According to equation

2.15, the equivalent dynamic bearing load P needs to be calculated from the radial- and axial load F_R and F_{Ax} .

$$P = X \cdot F_R + Y \cdot F_{Ax} \quad (2.15)$$

The dynamic radial factor X and axial factor Y determine how radial- and axial loads F_R , F_{Ax} impact P depending on the bearing design. In the case of mere radial load, X becomes unity while Y is zero. For more detailed information on the calculation and lifetime estimation, it is referred to Niemann [47].

2.1.4. Operating Conditions and Lubrication Regimes

The correct function of a rolling bearing is ensured if several criteria are met. So far, the solid body kinematics of the rolling bearing has been explained, but the lubricant has a crucial role in the durability of rolling bearings according to Hamrock et al. [48]. The lubricant is supposed to reduce the friction coefficient μ of the tribological contact. μ is defined as the ratio of normal force F_N acting on the tribological contact and the friction force F_{fr} acting against the direction of relative motion. Lubricants are differentiated into solid and liquid.

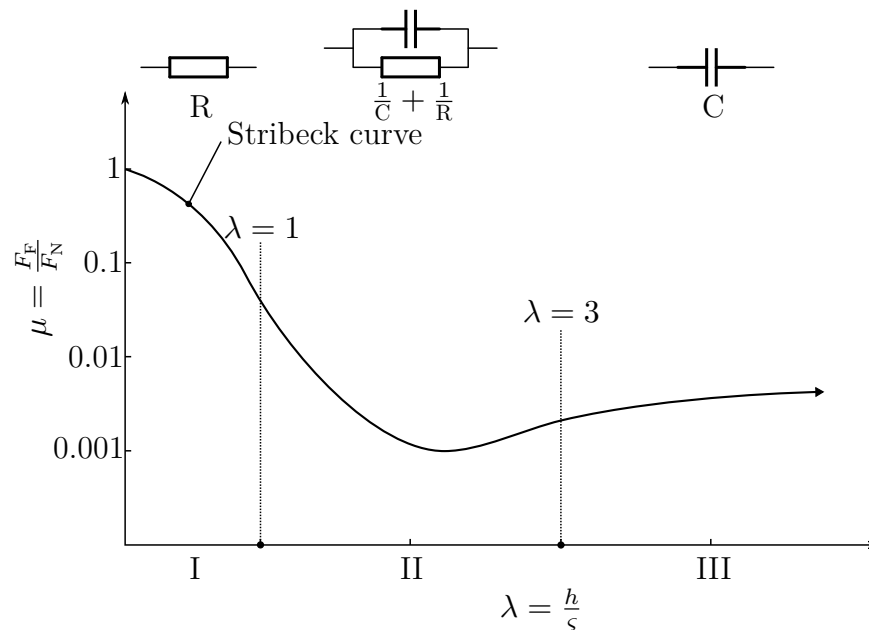


Figure 2.6.: Change in friction coefficient μ with specific lubrication film thickness λ ; Frictional regimes: I - solid-/boundary-friction; II - mixed friction; III - elastohydrodynamic-/hydrodynamic friction; Electrical analogy for comparison; Image adapted from Czichos [49], based on Stribek [46]

A solid lubricant is Polytetrafluoroethylene (PTFE) inlays for plain bearings or carbon dust. Most applications, however, run on liquid lubricants, typically greases or oils. These separate the surfaces through a hydrodynamic fluid film, introducing a positive pressure in the contact, which pushes them apart and counteracts the applied load Q .

A lubricating film h is formed, which carries the load together with the asperities of the surfaces. The ratio of lubrication film thickness h to the mean surface roughness ς is called specific lubrication film thickness λ . λ and the friction coefficient μ are qualitatively related. Figure 2.6 illustrates this relationship in the form of a Stribeck diagram. It allows determining the main frictional regimes. Regime I attributes solid body and boundary friction which means that the surfaces are in touch, and the mechanical contact ultimately carries the load. It is usually defined for λ from zero to unity. Regime II represents mixed friction as the lubricant separates the surfaces so that only the rough asperities are still in touch. The load distributes between the lubricating film and the mechanical contact areas. Regime III describes pure hydrodynamic friction as the lubrication film entirely separates the surfaces. For this to happen, a relative motion of the base and counter body is needed so that the lubrication film height suffices. While this is intuitively plausible for conforming contacts, the exact mechanism applies to concentrated contacts but introduces much higher pressures. This difference in pressure for conforming and concentrated contacts covers several orders of magnitude and leads to elastic deformations of the participating surfaces. This effect is called Elastohydrodynamic Lubrication (EHL) and accounts for part of the hydrodynamic lubrication regime III near the transition area from II.

The electrical analogy shown in figure 1.3 represents a rolling bearing that operates in this third regime. If rolling bearings operate in conditions associated with regime I and II, premature failure usually follows due to damage mechanisms associated with these tribological conditions. While there are exceptions, this rule holds for most bearings and lubricants. However, the previous analogy applies to the first and second lubricant regimes with different electrical components. Therefore, the capacitance is replaced with an electrical resistance for regime I representing the resistivity between two solid bodies in mechanical contact even though the mixed and boundary friction is of severe relevance for rolling bearings and the objective to research as reviewed by Spikes [50] and later by Zhu et al. [51], the desired operational state is regime III according to Czichos [49].

A relevant question for this thesis is, which Regimes become part of the simulation framework? If the transition from second to third (and vice versa) is considered, it impacts the numerical approach and descriptions in the background. The changes reach from the equation modelling process in chapter 2.2 to the architecture of numerical workflows in section 4.1.3. Therefore it is mandatory to declare in advance whether or not this transition should be considered or not. As already mentioned, regime III is the desired state of operation for the bearing. Since the focus is on the research on this native state and the electric phenomena there, the calculations and analyses performed in this work are strictly limited to EHL and hydrodynamic lubrication regime. Even if an extensive description is always the idealized goal, this limitation is necessary to manage the problem. The focus lies on the extension of EHL numerics with a fourth, electrodynamic, domain. To what extent the coupling between domains, mentioned in the beginning, introduces complexity to this work will be explained in section 2.2 and justifies the decision made here retrospectively.

2.1.5. Bearing Materials and Lubricants

In addition to geometry and operating conditions, the selected materials determine the tribological state of operation (see Stribeck diagram 2.6). Typical rolling bearing materials are steel, steel-based alloys, and ceramics. The most relevant properties of these materials for the following simulations are their Young's modulus E , Poisson ratio ν , density ρ_S , heat conductivity κ_S , and coefficient of thermal expansion α . While the properties of steel and its alloys only differ by nuances, the actual difference comes from ceramics. Table 2.1 lists typical values for those properties. The values for steel are taken from publications about EHL by Almqvist et al. [52] and Hajishafiee et al. [33]. Values for ceramics (for example, silicon carbide) are added for comparison from Tietz [53, p.5].

Table 2.1.: Bearing material properties for steel and ceramics
Solid Material Properties

Parameter	Variable	Unit	Value		
			Steel[33]	Steel[52]	SiC
Young's modulus	E	Pa	$210 \cdot 10^9$	$206 \cdot 10^9$	$450 \cdot 10^9$
Poisson ratio	ν	-	0.3		0.18
Density	ρ_S	kg m^{-3}	$7.85 \cdot 10^3$		$3.2 \cdot 10^3$
Heat conductivity	κ_S	$\text{W m}^{-1} \text{K}^{-1}$	47	46	3.8
Thermal expansion	α	K^{-1}	not considered		4.3
Specific heat capacity	c_S	$\text{J kg}^{-1} \text{K}^{-1}$	450	470	510

The lubricant properties are as relevant for the detailed description of an EHL contact. Namely, the dynamic viscosity η , density ρ , thermal conductivity κ_S , and specific heat capacity $c_{\mathcal{F}}$ of the lubricant determine the EHL contact significantly. Table 2.2 lists these properties at reference conditions. The values refer to the pressure p_{ref} and temperature T_{ref} that were present when the property was measured. The thermodynamic reference pressure p_{ref} and temperature T_{ref} vary as some of the measured quantities come from different sources. Again the parameters used by Almqvist et al. [52] and Hajishafiee et al. [33] are listed together with values for the FVA 3 reference oil. This lubricant is added to the list because the experimental results presented in section 5.4.2 were carried out.

The values for FVA 3 were taken from Bartel [54] for reference pressure $p_{\text{ref}} = 0$ Pa and temperature $T_{\text{ref}} = 303$ K. Appendix A offers the whole dataset by Bartel [54] for viscosity, density, specific heat capacity, and thermal conductivity for typical tribological pressure and temperature range which are used to fit the viscosity model and EoS parameters for the FVA oil. It should already be noted that the temperature and pressure dependency of the specific heat capacity and thermal conductivity is neglected throughout this work. These changes are insignificant for the tribology compared to changes in density and viscosity, as the datasets in appendix A outline.

Unlike metals and ceramics, lubricants have a wide range of properties, especially their reference density ρ_{ref} and viscosity η_{ref} varies in magnitudes. This diversity results from

Table 2.2.: Lubricant material properties in comparison based on Bartel [54]
Fluid Material Properties

Parameter	Variable	Unit	Value		
			[33]	[52]	FVA 3
Dynamic viscosity	η	Pa s	0.01 – 1	0.14	0.14
Density	ρ	kg m ⁻³	850	870	875
Heat conductivity	$\kappa_{\mathcal{F}}$	W m ⁻¹ K ⁻¹	0.15	0.14	0.13
Specific heat capacity	$c_{\mathcal{F}}$	J kg ⁻¹ K ⁻¹	2300	2190	2150

the attempt to establish the EHL or hydrodynamic regime (III in figure 2.6) as the operating condition. The choice of lubricant is the only way to tune the rolling bearing tribology since the size is determined and rotational velocity changes depending on the operational situation.

Besides the reference value for viscosity and density listed in table 2.2, the description of pressure and temperature-dependent changes of these values is crucial for accurately predicting of the tribological contact. Over time, various viscosity models and Equation of State (EoS) have been established to depict this behaviour correctly. In sections 2.3.5 and 2.3.4, some lubricant models and EoS are presented.

2.2. Multi-Physics

As already indicated in the introduction to this chapter, multiple physical domains are necessary to describe the rolling bearing tribology precisely. Multi-physics is the attempt to couple Partial Differential Equations (PDE) of different disciplines to accurately characterise a system or effect rather than relying on approximations at the point of interaction. The already introduced domains are described by their unique set of first principles (transport equations, conservation equations, and constitutive laws), which adequately describe one of the systems' physical aspects according to Keyes et al. [55]. The number of domains involved in the description varies, but some often occur together, see Bird et al. [56].

Unlike isolated topics like finite element calculations, which can be summarized to deal with mechanical challenges constantly, multi-physical simulations can rarely be summarized or generalized under one topic. Therefore, the most effective way of characterization is to highlight the involved domains and elaborate on their interactions. Figure 2.7 offers a schematic overview of the domains necessary to describe the TEHL phenomena combined with electrostatics and how they interact.

The necessary basics for each domain are stated in the following sections, and the interactions are explained. However, some general statements can already be made in advance without stating any equations.

The whole calculation domain Ω is divided into segments, or subdomains, whose boundaries are either the domain boundaries Γ or some mutual boundary Γ with other subdomains. Latter ones are usually called an interface. Figure 2.7 already features several

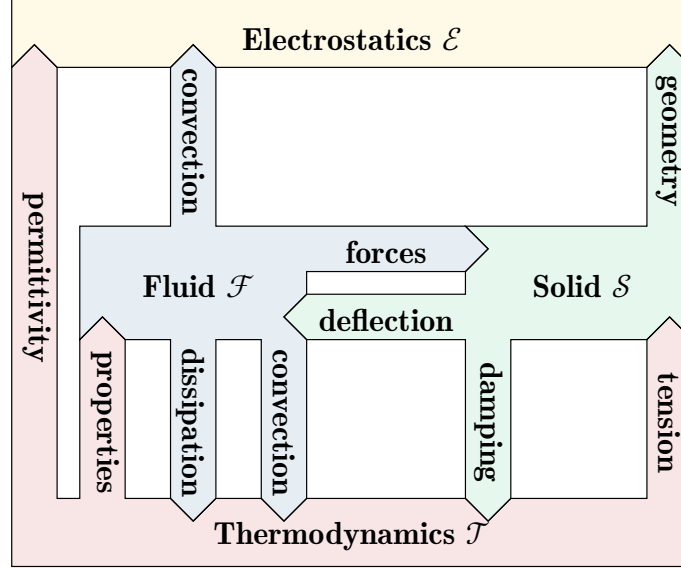


Figure 2.7.: Schematic domain representation and their interaction; Thermodynamics \mathcal{T} (red), fluid-mechanics \mathcal{F} (blue), structural-mechanics \mathcal{S} (green) and electrostatics \mathcal{E} (yellow)

interactions. Everything is centred around the primary interaction between the lubricant (fluid domain \mathcal{F}) and the tribological pairings of the rolling elements and rings (solid domain \mathcal{S}). A corresponding description of the FSI can be found in Richter [57]. The electrostatics subdomain \mathcal{E} is an extension to the classical FSI framework and matches the fluid subdomain \mathcal{F} with the same interface to the solid domain $\Gamma = \partial\mathcal{E} \cap \partial\mathcal{S}$. The thermodynamics subdomain \mathcal{T} covers the whole domain Ω and, therefore, the structural and lubricant subdomain.

While fluid, structure, and electrostatics are handled, more or less, independently, the thermodynamics is incorporated into the fluid and solid calculations as it interacts. This integration leads to the feature that the thermodynamic subdomain has an interface with itself as temperature and heat flux information need to be handed over at the FSI interface. Details on this are given in this work's associated sections, especially during comments on the implementation. Before detailed explanations of the subdomains \mathcal{F} , \mathcal{S} , \mathcal{E} , and \mathcal{T} start, a characterization of the FSI for the specific case of rolling bearings is given in section ?? to point out some restrictions.

Fluid-Structure Interaction FSI describes the reciprocal influence of fluids and solids on each other at some mutual interface according to equation 2.16.

$$\Gamma_{\text{FSI}} = \partial\mathcal{F} \cap \partial\mathcal{S} \quad (2.16)$$

The interaction at this interface Γ_{FSI} is mainly described by three coupling conditions, according to Richter [57, pp.80-82]. The geometric condition states that the fluid domain \mathcal{F} and structure domain \mathcal{S} do not intersect according to equation 2.17.

$$\mathcal{F} \cap \mathcal{S} = \emptyset \quad (2.17)$$

The non-intersection is intuitive since the lubricant can not penetrate the metallic rings and rolling elements. The mutual interface Γ does not detach at any point in space or time, leading to an equilibrium of position and velocity at the interface Γ . This restriction is referred to as the kinematic condition and has implications for the calculation procedure in chapter 4 later on. Equation 2.18 represents the kinematic condition.

$$\mathbf{u}_{\mathcal{F}}(\mathbf{x}, t) = \mathbf{u}_{\mathcal{S}}(\mathbf{x}, t) \quad (2.18)$$

The dynamic condition, equation 2.19, completes the FSI description and thus enables the calculation described in section 4.1.3. It states that the forces acting on the interface have to be permanently at equilibrium. Shear stresses and pressure exerted by the fluid on the solid lead to deformation and, thus, stresses in the solid, which counteracts the deforming forces. Equation 2.19 illustrates this.

$$\mathbf{n}_{\mathcal{F}} \cdot \sigma_{\mathcal{F}} = -\mathbf{n}_{\mathcal{S}} \cdot \sigma_{\mathcal{S}} \quad (2.19)$$

Example applications for FSI are countless and reach from large scales like the oscillation response of skyscrapers to small scales like microparticles in a flow. While examples for FSI problems are vast, the list of authors proposing numerical solution strategies is comparably short. Reviews like Hou et al. [41] illustrate this circumstance - most publications focus on divergence phenomena and run-time optimization. Identify possible fatal conditions and disqualify a particular approach for the problem. Still, fortunately, there are some characteristics to file the EHL contact and anticipate these problems. Those are explained now and applied to the described rolling bearing contact to determine which kind of FSI needs to be modelled. Building upon this classification, the mathematical description of the single domains regarding the tribological task is subsequently derived.

Density Relation For FSI problems, the density $\rho_{\mathcal{F}}$ of the fluid and $\rho_{\mathcal{S}}$ of the solid subdomain take a significant role, as van Brummelen [58] showed conveniently. The density ratio of equation 2.20 offers insight into the FSI problem and is a stability condition for numerical calculations.

$$\frac{\rho_{\mathcal{F}}}{\rho_{\mathcal{S}}} \leq 1 \quad (2.20)$$

Problems in which the fluid density is higher than that of the solid tend to diverge in numerical calculations. The so-called added mass effect is the primary reason for this instability. It describes an additional, yet virtual, mass that adds to a solid body as it moves through a fluid since the inertia of the fluid counteracts this movement. Although this is a physical principle, it results in an instability of numerical FSI methods due to errors in calculating forces at the interface Γ_{FSI} .

Van Brummelen [58] pointed out that compressible and especially incompressible FSI calculations can diverge due to this effect. While compressible approaches tend to stabilize with decreasing time-steps Δt , incompressible computations worsen so that the

interaction is miss-predicted. This fact is explained by the instantaneous changes in pressure for incompressible calculations in the whole domain, leading to the whole fluid's contribution to the added mass effect. In contrast, compressible calculations are limited to a local space corresponding to the time-interval regarded as the propagation of waves can be resolved. However, as long as inequality 2.20 stays valid, the danger of divergence due to the coupling of domains is small. By recalling the density parameters in tables 2.1 and 2.2, it is indicated that the added mass effect should not be of greater relevance for rolling bearing FSI calculations. This statement holds even for increases in fluid density due to pressure changes in the orders of magnitude. Nevertheless, the density ratio should be checked before setting up a simulation. The reader can find more details about the density ratio stability condition in Richter [57].

Elastohydrodynamics Rolling bearing contacts are Elastohydrodynamic Lubrication (EHL) problems, which means that a pressurized lubricant separates loaded non-conformal surfaces in relative motion. The pressure exerted by the oil deforms these surfaces, which leads to a Hertzian-like contact. Johnson [59] and Myers [60] identified four significant types of EHL to which concentrated point and line contacts can be assigned. They introduced a metric based on two parameters to distinguish different EHL cases. Therefore, the dimensionless viscosity parameter g_v (equation 2.21) and the dimensionless elasticity parameter g_E (equation 2.22) are introduced.

$$g_v = \frac{\left(\frac{2}{3}\pi^3\right)^3 \cdot \alpha_{\mathcal{F}} \cdot p^9 \cdot R^2}{E'^6 \cdot \eta_0^2 \cdot u_e^2} \quad (2.21)$$

$$g_E = \frac{\left(\frac{2}{3}\pi^3\right)^{\frac{8}{3}} \cdot p^8 \cdot R^2}{E'^6 \cdot \eta_0^2 \cdot u_e^2} \quad (2.22)$$

They are defined through basic properties of the EHL contact and imply the type of behaviour for a given pressure p acting in the tribological system. Also, the lubricant dynamic viscosity η_0 is known, and the solids reduced Young's modulus E is determined. The reduced Young's modulus E' is introduced in section 2.52 later on. Furthermore, the pressure-viscosity index $\alpha_{\mathcal{F}}$ is needed, which will be presented in section 2.3.5 in more detail as part of some viscosity models. The equivalent radius R takes into account the geometric condition of the tribological system, while the entrainment velocity u_e describes the mean speed of the surfaces. Explained clearly, g_E describes the transition from stiff towards elastic deformation in the solid due to pressure. Likewise, g_v describes the increasing impact of pressure on viscosity and, therefore, the change from an iso-viscous to a piezo-viscous behaviour. If both are plotted against each other, four characteristic EHL configurations are identifiable in figure 2.8. The four areas can be visualized clearly, by plotting the parameters over the ordinate (g_E) and abscissa (g_v) of a coordinate system. Multiple tribological states can establish depending on the material pairings, bearing size, and operating condition. While a sizeable rolling bearing with a lubricant of high viscosity and a low load may lead to an allocation in the iso-viscous-rigid area, the piezo-viscous-elastic corridor is likely to apply for most combinations as it is in this work.

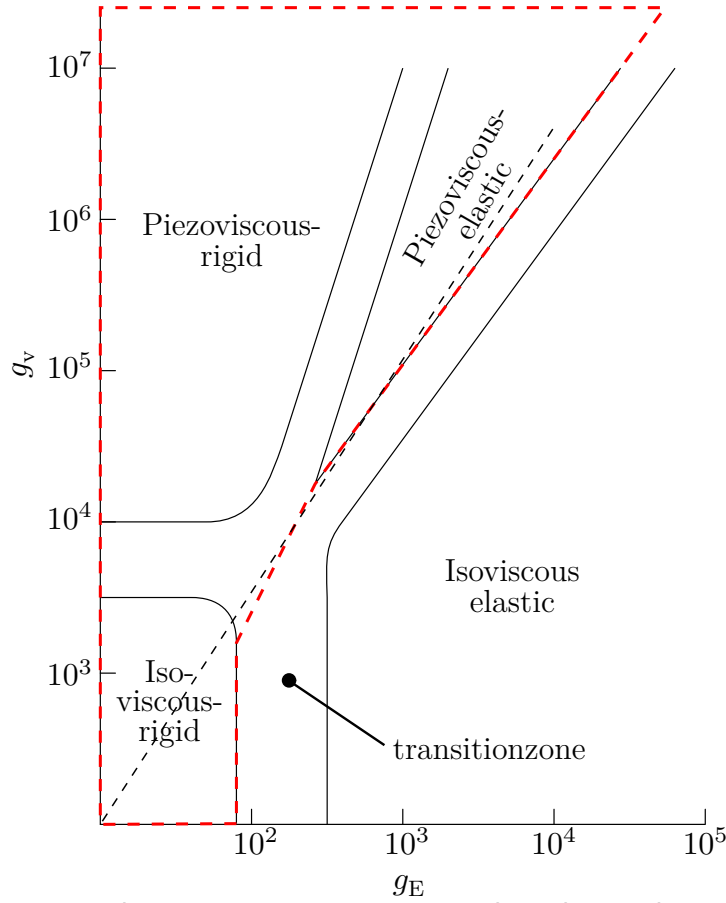


Figure 2.8.: Dimensionless viscosity parameter g_v plotted over dimensionless elasticity parameter g_E ; FSI regimes according to Hamrock et al. [48, p.508]; Dashed red line indicates regions relevant to EHL; Dashed black line indicates expected conditions calculated in this work

A rolling-element radius of $R = 3.96$ mm, ambient viscosity $\eta_0 = 0.14$ Pa s, entrainment velocity of $u_e = 2.5$ m s⁻¹, reduced Young's modulus $E' = 1.15 \cdot 10^{11}$ Pa and pressure viscosity coefficient $\alpha_{\mathcal{T}} = 1 \cdot 10^{-7}$ Pa⁻¹ is a typical parameter set for the bearing under investigation in this work. The dashed black line in figure 2.8 for elevated pressures between $p = 1 \cdot 10^8$ Pa and $p = 5 \cdot 10^8$ Pa outlines that the tribological contact in this work is expected to be found in the piezo-viscous-elastic lubrication regime. Although this is just an estimate, it has already become eminent that the piezo-viscous-elastic regime is only reached as the maximum pressure establishes. Before this, the solid body acts rigidly. This note should be kept in mind for the upcoming calculations as it explains some of the results found.

2.3. Fluid

An Eulerian view of the fluid domain describes the differential equations. Therefore, the volume is separated into elements, which are kept constant in space and time, so that the properties like mass, impulse, and energy can be balanced over volume element surfaces in the form of ingoing and outgoing fluxes. Generally speaking, the primary transport equations are nothing less than a balance. Bird et al. [56] have converted this balancing into the generic equation:

$$\left\{ \begin{array}{c} \text{rate of} \\ \text{accumulation} \end{array} \right\} = \left\{ \begin{array}{c} \text{flow} \\ \text{in} \end{array} \right\} - \left\{ \begin{array}{c} \text{flow} \\ \text{out} \end{array} \right\} + \{\text{production}\} - \{\text{elimination}\} + \left\{ \begin{array}{c} \text{external} \\ \text{forces} \end{array} \right\}$$

The measure of interest, for example, mass m , accumulates in the considered volume over time due to the fluxes over the volume's surfaces by transport processes like convection and diffusion. Some quantities like reactants for chemical processes can be produced/eliminated from the volume through reaction rates, which leads to source/sink terms inside a volume (rate of production/elimination). Nevertheless, the balance needs to stay intact as the production term of one reactant needs to equal the sink of one or numerous others. For some properties like the impulse forces, acting on the area of consideration might be of importance for the balance as well. The most renowned force field is the gravitational acceleration vector field g , which adds to the impulse balance. Other relevant volume forces like magnetism or dielectric forces might also contribute. It becomes clear that not every term applies to the balance of a measure of interest, and therefore the specification of necessary quantities for the multi-physical description of a ball bearing contact is stated now. The following remarks on the PDEs for describing a lubricant flow are based on the book "Transport Phenomena" by Bird, Stewart, and Lightfoot [56], which systematically derived all sorts of differential equations for fluids from this balance with unique clarity.

2.3.1. Continuity Equation

The starting point is the continuity equation or law of mass conservation, also called alternatively. As already mentioned, the lubricant is considered to undergo compression due to the high pressure to be expected. Therefore, a compressible formulation is necessary, so the balance reads according to equation 2.23.

$$\frac{\partial \rho}{\partial t} + \nabla \cdot (\rho \mathbf{u}) = 0 \quad (2.23)$$

Equation 2.23 states that the rate of change in density ρ with time $\partial/\partial t$ equals the mass flux in/out of the reference volume across its surface $\nabla \cdot \rho \mathbf{u}$ (see Moukalled et al. [61, p.657]). Contrary to an incompressible fluid, where the rate of change over time is zero, mass can accumulate in the volume, representing the needed compressibility accurately to describe lubricant behaviour in the tribological contact.

2.3.2. Momentum Transport Equation

Together with the continuity, the momentum transport formulated in equation 2.24 forms the basis for all calculations in the fluid domain according to Moukalled et al. [61, p.57].

$$\frac{\partial}{\partial t}(\rho \mathbf{u}) + \nabla \cdot \{\rho \mathbf{u} \mathbf{u}\} = -\nabla p + \nabla \cdot \boldsymbol{\tau} \quad (2.24)$$

Equation 2.24 describes how momentum $\rho \mathbf{u}$ changes over time. The contributions to this rate of change are convective and molecular transport. The second term on the left side $\nabla \cdot \{\rho \mathbf{u} \mathbf{u}\}$ describes the impulse carried by the mass flux that enters and leaves the volume over its surfaces. The molecular transport is a bit more deficient in the description as it represents the diffusion of impulse through the surfaces described by the divergence of the stress tensor $\nabla \cdot \boldsymbol{\tau}$. Lastly, differences in pressure at two points in a volume are also a driving force for momentum represented by the pressure gradients ∇p . Field quantities like gravitational acceleration or magnetic fields add directly, as they act on the volume but are omittable for the rest of this work because external forces are of a subordinate size.

The most complicated term to describe is the stress tensor $\boldsymbol{\tau}$. It consists of nine components, where the main diagonal elements describe the normal stresses and off-diagonal elements the shear. These stresses are present due to the velocity gradients in the fluid called the strain rate $\dot{\boldsymbol{\gamma}}$ and its viscosity η . How to describe this tensor correctly depends on how the fluid behaves for high gradients in velocity. A linear description of this dependency is equation 2.25 for so-called Newtonian fluids.

$$\boldsymbol{\tau} = \eta \{\nabla \mathbf{u} + \nabla \mathbf{u}^\top\} - \frac{2}{3} \eta (\nabla \cdot \mathbf{u}) \mathbf{I} \quad (2.25)$$

If equation 2.25 is inserted into equation 2.24, it results in the famous Navier-Stokes Equation (NSE) for Newtonian fluids. Using the NSE as a basis contributes to the work by Almqvist et al. [31] and those following, like Tasic et al. [35].

While most modern publications on rolling bearing TEHL numerics are based on equation 2.24, not all rely on a Newtonian fluid to describe shear behaviour. There was an intense discussion about whether the influence of shear-thinning in lubrication is distinguishable from a reduction in viscosity due to heat produced through shear stresses. Usually, a shear-thinning lubricant needs a description different from the Newtonian approach, where the most common descriptions are the Carreau-, Eyring, and Yasuda models, which were reviewed by Spikes and Jie [62] a couple of years ago. Since the viscosity depends on pressure p and temperature T , the strain rate $\dot{\boldsymbol{\gamma}}$ adds to three parameters that might impact how the shear stress tensor has to be modelled. Commentaries by Bair et al. [63] on the statements made by Spikes and Jie [62] on how these influences are distinguishable experimentally at elevated pressures have started a controversy. Czichos [49, p.419] mentioned, contrary to this discussion, that the Newtonian assumption holds for mineral- and synthetic oils as long as no additives are present. These opposing positions indicate how complex the correct rheological determination of lubricant properties is. Accordingly, a fundamental decision must be made at this point

regarding the consideration of strain rate $\dot{\gamma}$ dependency for the modelling of the stress tensor $\boldsymbol{\tau}$ and the dynamic viscosity η . While intuition tells that the impact of high gradients in velocity, especially at the convergent inlet region of the TEHL, is relevant, this work sticks to the Newtonian description for two reasons. The first one is practical since this work is the first of its kind on tribology at the Institute for Product Development and Machine Elements (pmd); every extension towards more unknowns makes it more difficult to pinpoint problems and derive relations between input quantities and outcome. The second one concerns the cases studied later during the results section 5. The experiments that were carried out establish an SRR close to/precisely zero and therefore have nearly no differential velocity in the contact region. For example, Hartinger et al. [32] have utilized a shear-thinning model that is only enabled for a limiting strain rate. Below this limit, the considered cases in their work were calculated with the Newtonian assumptions.

The cases in Hartinger et al. [32] used the Newtonian assumption correspond to the ones in this work concerning the SRR and lead to coherent results. Hence, only small velocity gradients are present in the region of interest (the contact itself), so the focus is on a sophisticated description of the viscosity. Therefore, this is also called low-shear viscosity, as it determines the shear behaviour of the fluid in the region of low strain rates. However, it is necessary to keep in mind that this restriction to the Newtonian description leads to errors if the calculations are done for higher SRR. Fortunately, the simulations in this work are for radially loaded bearings, for which a pure rolling and, therefore, SRR of zero is expected. Before turning the attention to the viscosity description for the lubricants, a formulation for the temperature T and enthalpy h_e evolution is necessary.

2.3.3. Energy Transport Equation

Although thermodynamics is a domain in itself and illustrated in figure 2.7, it is closely coupled to the fluid, and the solid domain, leading to temperature and enthalpy, is calculated as part of the fluid solution. Thus, thermodynamics has no separate chapter but is covered during fluid and solid domain explanations.

If compressibility is part of the investigation, thermodynamic descriptions are implemented in CFD calculations. The way energy and heat are approached varies, depending on the task to be solved. For simple calculations, the transport of temperature T is described directly in the fluid domain, while for more sophisticated calculations, the specific energy e or enthalpy h_e is calculated. An example of a problem requiring the latter is sound wave propagation or transitions between subsonic and supersonic regions of calculation, where the conversion of kinetic energy into heat is imminent according to McDonald [64]. If calculated with the temperature transport equation, such a task would be cumbersome to handle.

Usually, the specific enthalpy h_e is chosen for tasks involving compressibility and dissipative processes, which are both expected for TEHL rolling bearing contacts. Equation 2.26 shows the enthalpy transport derived from Bird et al. [56] and Versteeg et al. [65,

p.20].

$$\frac{\partial}{\partial t}(\rho h_e) + \nabla \cdot [\rho \mathbf{u} h_e] - \frac{\partial p}{\partial t} = \nabla \cdot [\boldsymbol{\tau} \cdot \mathbf{u}] - a_{\mathcal{F}} \Delta h_e \quad (2.26)$$

Equation 2.26 balances the specific sensible enthalpy h_e according to Moukalled et al. [61, p.62]. Unlike mass (2.23) or impulse (2.24), thermodynamics distinguishes different forms of energy, like mechanical energy, the energy of formation (during phase change), and internal energy, which are balanced partly or entirely dependent on the task. This distinction leads to multiple versions of the energy transport equation, all found in Bird et al. [56]. The sensible specific enthalpy h_e is the part of the total enthalpy that contributes to an actual change in temperature. It does not contribute to the enthalpy of formation like phase changes from ice to liquid, where a change in total enthalpy of the system is observable, but the actual temperature does not change.

In this work, no phase change or chemical reaction which leads to the enthalpy of formation contributions is considered, and therefore the specific sensible enthalpy h_e is accurate to use. Nevertheless, the rate of change in specific enthalpy $\partial h_e / \partial t$ obeys the same rules as it also changes with convection $\nabla \cdot [\rho \mathbf{u} h_e]$ and diffusion $a_{\mathcal{F}} \Delta h_e$. The diffusive heat transport describes the way energy is distributed from areas of high enthalpy to low enthalpy, ultimately leading to an equal distribution. The thermal diffusivity $a_{\mathcal{F}}$ is a material property determining the molecular transport of heat (as Brownian motion) through the fluid.

Another adaption made to equation 2.26 is the consideration of viscous heating. The source $\nabla \cdot [\boldsymbol{\tau} \cdot \mathbf{u}]$ is an irreversible increase in enthalpy inside the area of consideration due to the shear strain. It couples the enthalpy equation 2.26 to the impulse transport 2.24 as it is the complementary term for the dissipation of impulse into heat found in the NSE. Usually, such a contribution is of minor importance and therefore omitted. Though, it becomes of severe relevance if high strain rates or a high viscosity is present. Depending on the SRR and resulting shear strains, viscous heating must be considered, especially as viscosity changes in orders of magnitude in the contact, as explained in section 2.3.5. Therefore this dissipative effect is used while other source terms are omissible.

A final contribution to the balance is the change of pressure p over time, the so-called compression heating. It describes the thermodynamic work done to the balance volume for increasing its pressure and hence increases its enthalpy. The definitions for enthalpy might vary. For example the enthalpy of formation can be taken into account, which changes the total enthalpy of the volume, but does not contribute to temperature changes. Viscosity models and equations of state are typically formed with changes in absolute temperature, thus utilizing the enthalpy instead is troublesome. Therefore the enthalpy is translated to a temperature distribution by equation 2.27.

$$\Delta h_e = c_p (T - T_{ref}) \quad (2.27)$$

This equation defines the change in temperature due to an increase in enthalpy via the specific heat capacity $c_{\mathcal{F}}$ of the fluid. Thus the temperature distribution is available for other calculations. The thermodynamics domain takes a special place in the area

of multi-physical calculations. It overarches physical spaces typically associated with a single kind of physics and therefore needs description not only for the fluid region but also for the structural regions. Special attention is thereby drawn to the matching conditions at these regions' interfaces as it significantly determines the outcome of a calculation.

The heat produced in the contact due to viscous heating and compression is dissipated through the rings and rolling elements. A heat transfer through the interface has to occur for this to happen. The amount of heat transferred to the solid determines the local fluid temperature. Errors in the enthalpy calculation lead to an over-/under prediction of the film thickness and therefore diminishes the accuracy according to Kaneta et al. [66]. The description of this interface condition impacts the accumulation of heat in the tribological system. It is determined by the heat transported into the solid and will be discussed in chapter 4.

2.3.4. Equations of State and Compressibility

Compressibility is a delicate topic for numerical calculations due to the instability it introduces. Explanations about the stability of compressible flows can be found in any standard book on numerical flow simulation such as Ferziger et al. [67, p.505]. Luckily for most engineering applications, the standard assumptions of incompressible fluids apply, and therefore an Equation of State (EoS) is unnecessary. TEHL calculations do not offer this kind of simplification.

The lubricant has to be handled compressibly to calculate the lubrication film thickness accurately described by Larsson et al. [68, p.21] regarding Höglund et al. [69]. Therefore an EoS must be introduced in addition to the set of PDEs already given. The EoS sets pressure p , specific volume v , and temperature T (so-called PVT relations) into a relationship. Equation 2.28 shows the ideal gas law, the most famous EoS described by Baehr et al. [70, p.457].

$$p \cdot v = R_s \cdot T \quad (2.28)$$

The perfect gas EoS states that the specific volume v does increase with a rise in temperature T and decreases with a rise in pressure p . The correct unit is ensured by adding the specific gas constant R_s describing how different gases behave.

As was already evident from the formulation of the previous differential equations, most numerical implementations rely on density descriptions. The specific volume v and density ρ are inversely proportional to each other, according to equation 2.29, which allows a reformulation of equation 2.28, replacing the specific volume v with the density ρ .

$$v = \frac{1}{\rho} \quad (2.29)$$

The change of density with pressure is called compressibility K or bulk modulus. Equation 2.30 shows the derivation of the bulk modulus K for an ideal gas after replacing the specific volume with the density. Analogue derivatives are possible for the EoS to follow. Detailed derivations of bulk moduli for the implemented models are found in

appendix C.

$$K = \frac{\partial \rho}{\partial p} = \frac{\partial}{\partial p} \frac{p}{R \cdot T} = \frac{1}{R \cdot T} \quad (2.30)$$

The rearrangement of equation 2.28 plus a reference density ρ_{ref} is a perfect fluid EoS. Equation 2.31 states the most basic EoS for approximating a compressible fluid.

$$\rho = \rho_{\text{ref}} + \frac{p}{R \cdot T} \quad (2.31)$$

All EoS for fluids similarly describes compressibility. A given reference density ρ_{ref} at temperature T_{ref} and pressure p_{ref} is modified with the actual p and T values.

Several EoS have been provided over the years, but only a few are commonly used for EHL applications. There is a distinction between empirical EoS and those based on theoretical models¹. Dowson et al. [71, p.89] introduced a widely used EoS for compressible calculations of liquid lubricants shown in equation 2.32.

$$\frac{V}{V_0} = \frac{\rho_0}{\rho(p)} = \frac{1 + \frac{K'_0 - 1}{2K_0} \cdot p}{1 + \frac{K'_0 + 1}{2K_0} \cdot p} \quad (2.32)$$

Equation 2.32 accounts for an empirical type of EoS. The relative isothermal change of volume V/V_0 (and density ρ_0/ρ respectively) with increasing pressure is described via the bulk modulus at ambient pressure K_0 and its rate of change K'_0 . The Dowson and Higginson EoS, shown in equation 2.32, is made temperature dependent by expressing the ambient bulk modulus K_0 as a function of temperature T . The rate of change K'_0 is considered to be temperature independent. There are different ways to describe the change in bulk modulus K'_0 . Bair [72, p.69] states a linear form with an inverse dependency on temperature T according to equation 2.33.

$$K_0 = K_\infty + \frac{K'_0}{T} \quad (2.33)$$

Another possible description for the temperature dependency of the bulk modulus was mentioned by Fakhreddine et al. [73, p.3, eqn.3]. They offered an exponential approach, which led to satisfying results, according to Bair [72]. The exponential description of the temperature-dependent bulk modulus is stated in equation 2.34.

$$K_0 = K_{00} \exp(-\beta_K T) \quad (2.34)$$

A less empirical EoS is the Tait equation introduced to rheology by Bair [28, p.69] based on Hirschfelder et al. [74, p.261] and the related, less known, EoS by Murnaghan [75]. The Tait EoS is considered accurate for most liquids, even for very high pressures, as

¹Latter ones are advantageous, as they are closer to so-called first principles and easier to interpret, since a physical meaning backs them up.

Bair [72] pointed out regarding Castro et al. [76]. The Tait EoS is shown in equation 2.35 and the Murnaghan EoS in equation 2.36.

$$\frac{V}{V_0} = \frac{\rho_0}{\rho(p)} = 1 - \frac{1}{1 + K'_0} \ln \left[1 + \frac{p}{K_0} (1 + K'_0) \right] \quad (2.35)$$

$$\frac{V}{V_0} = \frac{\rho_0}{\rho(p)} = \left(1 + \frac{K'_0}{K_0} \cdot p \right)^{\left(-\frac{1}{K'_0} \right)} \quad (2.36)$$

These equations also utilize the bulk modulus according to equation 2.33 and equation 2.34 alternatively. Both equations provide valid results across a considerable pressure and temperature range, as McDonald [77] reviewed. Even though these two EoS are used to describe the pressure-volume-temperature relation more analytically, some fits to a specific lubricant are still necessary. The relative change in density can be adjusted to match experimental data, like Bair [72] examined extensively for many liquid lubricants. Though temperature and pressure-dependent density values are not always available, Bair [72, p.123] stated idealized parameters for lubricant behaviour. These are listed in table 2.3.

Table 2.3.: Free volume theory parametrization for equation 2.35 for ideal lubricant according to Bair [72, p.123]

Tait Equation Parameters								
	K'_0	Unit	K_{00}	Unit	β_K	Unit	a_V	Unit
Model liquid	11	—	9	GPa ⁻¹	$6.5 \cdot 10^{-3}$	K ⁻¹	$8 \cdot 10^{-4}$	°C ⁻¹

The relative volume change through pressure can be fitted for some lubricants, shown in figure 2.9 for the lubricant Low Viscosity Index (LVI) 260 oil.

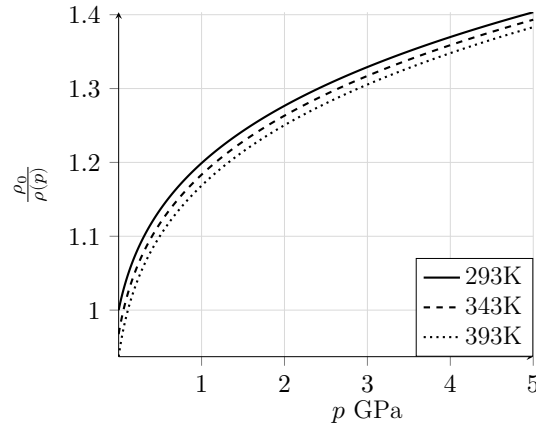


Figure 2.9.: Relative density $\rho_0/\rho(p)$ plotted over pressure p for Tait equation 2.35 using parametrization from table 2.4 at $T_R = 313K$ according to Bair [72]

The plot results from the Tait EoS according to equation 2.35 and the temperature-dependant bulk modulus modelling according to equation 2.34. The parameter set listed in table 2.4 was used to visualize the relative density for different temperatures and pressures. The change in density is plotted for a large pressure range just to illustrate the compression. Relevant for the present calculation is a pressure change up to $\Delta p = 2$ GPa. While the changes with pressure are apparent, the change with temperature is less dominant, especially for very high compressions. However, for the pressure range up to $p = 1$ GPa the temperature impact is significant. So does the volume change by ten percent for a temperature increase of $\Delta T = 100$ K at ambient pressure which corresponds to a pressure change of $\Delta p = 0.5$ GPa and should therefore not be neglected according to Bartel [54, p.109].

Table 2.4.: Tait equation 2.35 parametrization using bulk modulus equation 2.34 according to Bair [72]

LVI 260 Parameters			
Parameter	Variable	Unit	Value
Bulk modulus pressure rate of change	K'	—	12.38
Thermal expansion ratio	a_v	K^{-1}	$7.158 \cdot 10^{-4}$
Bulk modulus at reference pressure	K_{00}	$\text{kg m}^{-1} \text{s}^{-2}$	$9.534 \cdot 10^9$
Temperature density coefficient	β_K	K^{-1}	0.005728

The oil used during the experiments in this work is a reference oil named FVA 3. It is a base oil without additives, often used for academic research, even though data sets are not that extensive. The temperature dependence of density is documented in Table 2.5. Fortunately, LVI 260 and FVA 3 are pretty similar, and the parameters given by Bair

Table 2.5.: Temperature-density data for FVA 3 reference oil

FVA 3 $\rho(T)$			
T	Unit	ρ	Unit
313	K	865	kg m^{-3}
333	K	853	kg m^{-3}
353	K	841	kg m^{-3}
373	K	829	kg m^{-3}
393	K	816	kg m^{-3}

[72, p.70] for LVI 260 oil fit those of FVA 3 if equation 2.34 is used for either EoS. The EoS is needed to estimate the lubrication film thickness since compression of 20 percent or more is expected, which translates to an equivalent error for the lubrication film thickness if not considered. Different EoS are suited for specific tasks. Therefore, all the stated models are implemented in the numerical toolkit for future work, even though only the Tait EoS is used for the relevant calculations in section 5.5. The same applies to the viscosity models presented next.

2.3.5. Viscosity

Besides density, the fluid viscosity also impacts the TEHL contact significantly. Unlike regular fluid mechanics, where viscosity is either a constant or just slightly affected by temperature, the rheology of technical oils is much more complicated. For concentrated TEHL contacts, the pressure changes by orders of magnitude so that the viscosity might increase. The shear stresses introduced to the enthalpy balance in section 2.3.3 lead to a significant local temperature increase in the contact area. Differences of 200K are possible, which decreases the viscosity and acts as a balancing measure to the pressure-based increase. The change of viscosity with pressure and density for the FVA 3 oil is documented in appendix A. In the following multiple viscosity models are presented. Analogue to the density models, not all of them are used in this work, but all are integrated into the transport library of the numerical tool presented in chapter 4 for future work. A general relationship of viscosity with pressure p and temperature T is described by relation 2.37 according to Bair [28, p.101].

$$\eta \propto \eta_{\text{ref}} e^{\alpha p - \beta \Delta T} \quad (2.37)$$

Viscosity models can be classified as empirical or analytical equations. The free volume approach, an analytical model, requires an EoS of the type Tait or Murnaghan for calculation. The relation of equation 2.37 already showcases most empirical models' key characteristics. An exponential pressure or temperature expression is used to adjust a known viscosity η_{ref} at reference conditions $p_{\text{ref}}, T_{\text{ref}}$. An early but widely used description of the sole pressure dependence is the Barus equation 2.38, first published in 1893 [78].

$$\eta = \eta_0 e^{\alpha_{\mathcal{F}} p} \quad (2.38)$$

The change with pressure is fitted to experimental data by the pressure-viscosity-coefficient $\alpha_{\mathcal{F}}$. The missing temperature dependence was added by Wilson et al. [79], which established a widely accepted description according to equation 2.39. The temperature dependence is fitted with the temperature-viscosity-coefficient $\beta_{\mathcal{F}}$.

$$\eta = \eta_0 e^{\alpha_{\mathcal{F}} p - \beta_{\mathcal{F}} (T - T_{\text{ref}})} \quad (2.39)$$

This description of viscosity has been used by Murch et al. [40] to correct the film thickness calculations based on the Reynolds equation in 1975, taking the temperature into account. Recently the estimates by Murch et al. have been utilized for semi-analytical calculations of electric rolling bearing properties by Schirra et al. [11]. Several more empirical models have been developed for medium to high-pressure applications over the past decades. The equations presented by Roelands et al. [80], [81], especially the temperature-dependent formulation stated in equation 2.40, have been the foundation for several numerical calculations like those by Hajishafiee et al. [33].

$$\eta = \eta_p \left(\frac{\eta_R}{\eta_p} \right)^{\left[\left(\frac{p_p - p}{p_p} \right)^Z \left(\frac{T_R - T_{\infty}}{T - T_{\infty}} \right)^S \right]} \quad (2.40)$$

Both the temperature corrected Barus viscosity model, and the Roelands viscosity model is implemented in the transport model library to allow comparative calculations to known numerical, and analytical solutions like Hajishafiee et al. [33] and Schirra et al. [11]. The free volume approach, a more analytical description, was presented by Doolittle in a series of publications [82]–[84]. The free volume $V - V_\infty$ calculated from the total volume V and occupied volume V_∞ is the basis for this approach, presented in equation 2.41.

$$\eta = \eta_{\text{ref}} \exp \left[BR_0 \left(\frac{\frac{V_\infty}{V_{\infty\text{ref}}}}{\frac{V}{V_{\text{ref}}} - R_0 \frac{V_\infty}{V_{\infty\text{ref}}}} - \frac{1}{1 - R_0} \right) \right] \quad (2.41)$$

It is noticeable that equation 2.41 neither depends on temperature T nor pressure p , directly. The actual viscosity η is calculated from the viscosity η_{ref} at reference pressure p_{ref} and reference temperature T_{ref} .

The exponential change in viscosity is calculated through the relative volume fraction (total volume V divided by total volume at reference state V_{ref}) and the occupied volume fraction (occupied volume V_∞ divided by occupied volume at reference conditions $V_{\infty\text{ref}}$). In order to express the temperature T and pressure p dependence, Bair et al. [72, p.117] assumed that the volume V_0 at ambient pressure p_0 follows equation 2.42.

$$\frac{V_0}{V_{\text{ref}}} = 1 + a_V(T - T_R) \quad (2.42)$$

Analogue to this, the occupied volume changes in the same linear fashion according to equation 2.43.

$$\frac{V_\infty}{V_{\infty\text{ref}}} = 1 + \varepsilon(T - T_{\text{ref}}) \quad (2.43)$$

Equations 2.42, 2.43 and an EoS, like Tait (equation 2.35) or Murnaghan (equation 2.36) calculate viscosity for large temperature and pressure ranges. Bair [72] presented several parameters for authentic lubrication oils and ideal strong/fragile behaviour, complementary to the parameter set for the Tait model in table 2.3². The associated parameters for the Doolittle-Tait-viscosity model by Bair [72] are listed in table 2.6.

Table 2.6.: Fragile/strong parametrization for equations 2.41 and equation 2.43 according to Bair [72, p.123]

Doolittle Equation Parameters										
	η_{ref}	Unit	T_{ref}	Unit	B	Unit	R_0	Unit	ε	Unit
Fragile	-	Pa s	293	K	1.8	—	0.82	—	$-10 \cdot 10^{-4}$	K^{-1}
Strong	-	Pa s	293	K	4	—	0.7	—	$-15 \cdot 10^{-4}$	K^{-1}

Figure 2.10 visualizes the logarithmic change in relative viscosity with pressure for different temperatures for this models. The change of viscosity with pressure utilizing the

²The terms strong and fragile liquid were popularized by Angell [85] and are visualized by so called Angell plots

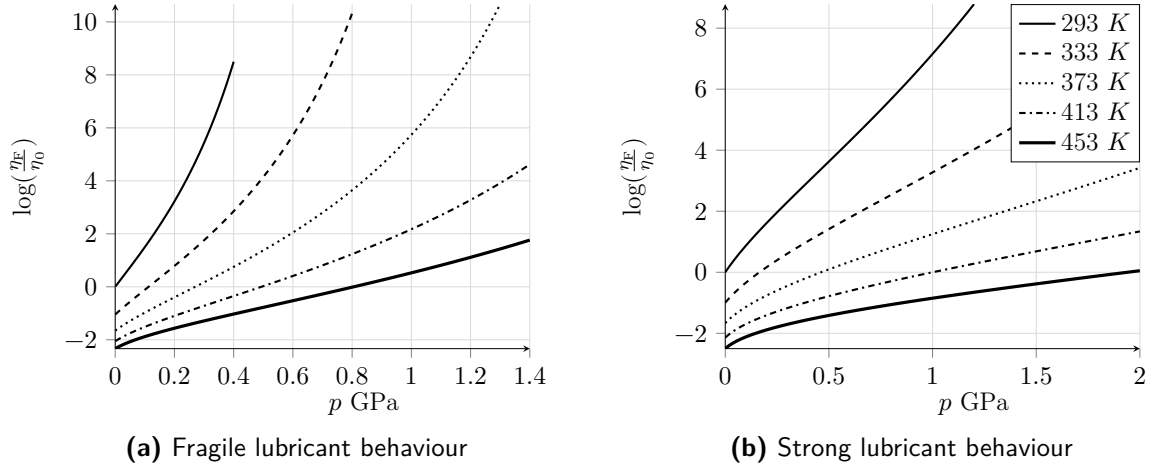


Figure 2.10.: Relative viscosity η_F/η_0 plotted over pressure p for Doolittle-Tait model with fragile/strong parametrization from table 2.6)

parameters listed in tables 2.3 and 2.6 is significant. The more progressive increase in viscosity with pressure in figure 2.10a is associated with a fragile lubricant, while the more linear change with pressure is called a strong lubricant behaviour. Also noticeable is the impact of temperature on the overall viscosity for the whole pressure range.

2.3.6. Glass Transition

A critical aspect of the description of lubricants has not been considered. Analogue to the fluid to gas transition for low pressures and elevated temperatures, lubricants can undergo a solidification. While the regular phase change is crystallization, a solid-state typical for most materials, the transition to an amorphous solid state is also possible if the temperature quench (cooling rate) is high enough. The amorphous solid-state is glass. It is worth mentioning that the glass transition temperature T_G differs from the crystallization temperature. A renowned glass transition is the solidification of silicate melts resulting in window glasses. The process described applies to melts whose actual state at ambient temperature is solid and to various liquids like lubricants. However, the glass transition temperature for most those liquids is somewhat below ambient conditions, as pointed out by Hansen et al. [86, p.250].

Lubricants are differentiated according to their origin into mineral- and synthetic oils, which belong to the class of hydrocarbons. While there are some water-based and liquid metal lubricants, most applications use mineral oils based on paraffin, naphthalene, and aromatic components. Synthetic oils, mainly polyesters, carbonaxidesters, or phosphoraxidesters, are usually used in high-temperature environments like internal combustion engines according to Czichos [49].

While the actual glass transition is a matter of fact, the details of a theory to describe glass transition are subject to intense research on dense matter physics. The number of explanatory approaches is extensive in that most review papers only cover a fraction of

it and refer to other reviews for completeness, such as Berthier and Biroli [87] or Karmaker et al. [88] did. But despite the number of explanations, several authors pointed out the relevance of glass transition for lubrication in TEHL contacts for example Bair et al. [89].

While a deep dive into the theory of glass formation in amorphous media is not the scope of this work, an explanation based on the free volume theory by Turnbull and Cohen [90], [91] is given. The Doolittle viscosity model described earlier is based on this theory. The free volume theory is considered the basis for a group of Kinetically Constraint Models (KCM) [87, p.33-37], whose approach can be described by a rigid sphere model for molecular movement. The premise for the following explanation is that the rigid spheres are not penetrable. The molecular composition might be represented by the mentioned rigid spheres for a space filled with lubricant. The total space, or volume, is considered to be V , while the space occupied by the lubricant spheres, represented as black dots, is the occupied volume V_∞ . The white space between the spheres is considered empty or free, which gave the theory its name. The free space is just the difference of total and occupied volume $V - V_\infty$. The viscosity of a lubricant depends on the possibility of a single sphere altering its position. The probability for such a change in place was calculated by Cohen and Turnbull [90], [91].

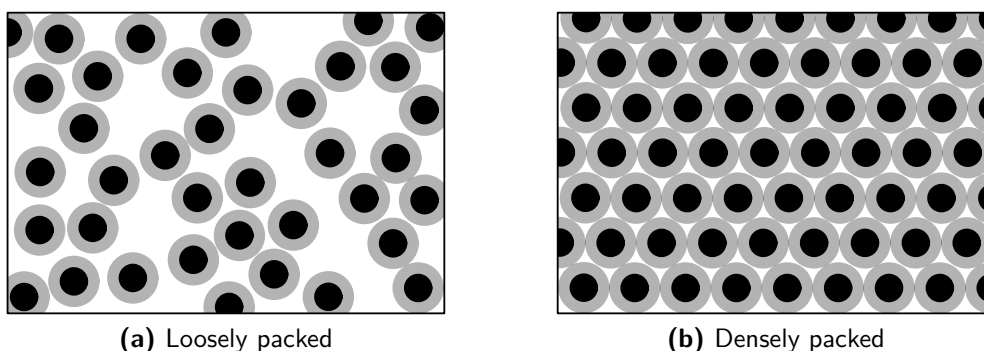


Figure 2.11.: Visualization of the free volume concept.

Black - rigid molecule space; Grey - temperature dependent free space; White - free space

The state at ambient conditions is visualized in figure 2.11a. If the volume is subjected to elevated pressure, it undergoes compression, reducing the total volume. Since the lubricant elements do not change in size or number, the occupied volume V_∞ stays the same, reducing the free space. The compressibility reaches its limit as the free space becomes zero $V = V_\infty$, which has two implications.

First, viscosity increases towards infinity as no sphere movement is possible, and second, the maximum compression of the fluid is reached. The lubricant is now in a glassy state, shown in figure 2.11b. Strictly speaking, the occupied volume V_∞ is not constant but changes with temperature. Williams, Landel, and Ferry [92] described it as a function of volume V_g during glass transition and the glass transition temperature T_G at ambient pressure p_0 according to equation 2.44. It is considered that glasses undergo a thermal

expansion with the expansivity α_G .

$$V_\infty = V_G[0.975 + \alpha_G(T - T_G)] \quad (2.44)$$

The grey areas in figure 2.11 represent the impact of this consideration on the concept of free volume. With decreasing temperature, the occupied space increases, leading to increased viscosity and a decreased compressibility. The Doolittle 2.41 model is based upon this theoretical framework, and the impact of temperature on viscosity can be seen in figures 2.10a and 2.10b. The same applies to the Tait equation 2.35, the Murnaghan equation 2.36, and the density in figure 2.9.

2.4. Solid

One of the first attempts to calculate solid deformation with a finite volume method in FSI was described by Demirdzic and Muzaferija [93], [94] based on equation 2.45 for linear elastic deformations.

$$\rho_s \frac{\partial^2 \mathbf{D}}{\partial t^2} = \nabla \cdot \boldsymbol{\sigma} + \rho_s \mathbf{f}_b \quad (2.45)$$

Here \mathbf{D} is the displacement vector, ρ_s is the constant solid density, $\boldsymbol{\sigma}$ is the stress tensor, and \mathbf{f} external body forces acting on the solid volume.

The displacement vector \mathbf{D} is the difference between the actual spatial position \mathbf{x} of a surface or volume element at a given time and its reference position \mathbf{X} in a Euclidean space, illustrated in figure 2.12.

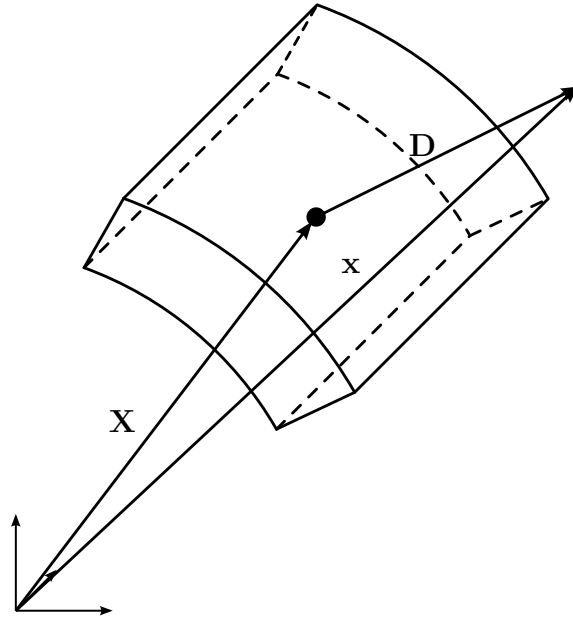


Figure 2.12.: Displacement vector \mathbf{D} indicating current position \mathbf{X} from initial position \mathbf{X}

The position \mathbf{X} typically coincides with the time $t = 0$, but not necessarily. The description of displacement as a vector can be done according to equation 2.46 .

$$\mathbf{D}(x_1, x_2, x_3, t) = \mathbf{x}(x_1, x_2, x_3, t) - \mathbf{X}(x_1, x_2, x_3, t_0) \quad (2.46)$$

While the Eulerian point of view dominates for fluid mechanics, except maybe for the description of streamlines, this Lagrangian point of view is established for solid mechanics and implemented for FSI calculations in OpenFOAM by Tukovic et al. [42].

The Stress tensor $\boldsymbol{\sigma}$ is defined by Hooke's law, shown in equation 2.47 as Jasak and Weller [95] described in their publication for the initial implementation of a solid mechanic's solver in OpenFOAM.

$$\boldsymbol{\sigma} = 2\mu_s \boldsymbol{\varepsilon} + \lambda_s \text{tr}(\boldsymbol{\varepsilon}) \mathbf{I} \quad (2.47)$$

Here μ_s and λ_s are the Lamé coefficients. They relate the material properties of Young's modulus E and Poisson ratio ν to the stress tensor $\boldsymbol{\sigma}$. Equations 2.48 and equation 2.49b are the definitions for Lamé coefficients.

$$\mu_s = \frac{E}{2(1 + \nu)} \quad (2.48)$$

$$\lambda_s = \begin{cases} \frac{\nu E}{(1 + \nu)(1 - \nu)} & \text{for plain stress} \\ \frac{\nu E}{(1 + \nu)(1 - 2\nu)} & \text{for plain strain and 3D cases} \end{cases} \quad (2.49a)$$

$$(2.49b)$$

Equation 2.50 describes the strain tensor $\boldsymbol{\varepsilon}$ with the displacement \mathbf{D} .

$$\boldsymbol{\varepsilon} = \frac{1}{2}[\nabla \mathbf{D} + (\nabla \mathbf{D})^\top] \quad (2.50)$$

The expected deformations of rolling bearing contacts are small compared to the total dimensions of the bearing, and no permanent deformation should occur since this equals a failure of the machine element. Therefore the deformation is assumed to be elastic and compressible. Inserting equation 2.50 into equation 2.47 offers a description for the stress tensor $\boldsymbol{\sigma}$ dependent on the displacement vector \mathbf{D} . Neglecting the time derivative and body forces leads to the differential equation needed to calculate the solid displacement locally according to equation 2.51.

$$\nabla \cdot [\mu_s \nabla \mathbf{D} + \mu_s (\nabla \mathbf{D})^\top + \lambda_s \text{tr}(\nabla \mathbf{D}) \mathbf{I}] = 0 \quad (2.51)$$

The Eulerian description for the fluid domain and a Lagrangian approach for the solid led to the renowned Arbitrary Lagrangian-Eulerian (ALE) formulation of FSI. The basic equations and theory described here can be found in Richter [57, pp.37-48].

Reduced Young's Modulus Typically EHL calculations of rolling bearings are simplified by mapping deformations of the base body, usually the rings, onto the deformation of the rolling elements. Therefore only a single Hertzian deformation area needs to be calculated. This reduction is made by assuming that the base body is ideally stiff and the counter body has, in turn, a modified stiffness or Young's modulus, which is calculated according to equation 2.52.

$$E' = \left(\frac{1 - \nu_1^2}{E_1} + \frac{1 - \nu_2^2}{E_2} \right)^{-1} \quad (2.52)$$

The resulting reduced Young's modulus E' includes the stiffness of base body E_1 and the corresponding Poisson ratio ν_1 and values for the counter body E_2 and ν_2 . With the help of this conversion, the calculation effort of empirical equations, like Dowson and Toyoda [96], and the modelling effort for the numerical EHL calculation is reduced, as only a single body has to be calculated elastically in this way. ³

Heat Transport in Solids Analogue to the heat transport in fluids, the solid parts also participate in the overall energy transport. Heat transfers from the lubricant to the solid region and vice versa. The discussion of transfer conditions, for heat and kinematic coupling and exchange of forces is explained later in chapter 4.2. However, calculating temperature distributions in the solid itself is relatively simple. Fourier's law of heat conduction for isotropic material is sufficient to calculate the temperature distribution in bearing rings and rolling elements according to equation 2.53.

$$\frac{\partial T_s}{\partial t} = a_s \Delta T_s \quad (2.53)$$

The transient change of temperature T in the solid parts is governed by the heat conduction κ_s and the temperature divergence. While there exist effects like tensional heating, the deformations faced in TEHL are, on the one hand, small and, on the other hand, nearly steady, which is why these effects are expected not to impact the result at all. The temperature development of the solid is mainly determined by its surrounding temperature, the interface temperatures due to heat transfer between lubricants and the solid region, and the temporal change due to conduction, covered by equation 2.53.

2.5. Dimensionless Quantities

The description of an EHL contact is challenging, as the stated PDE already indicates. Therefore, comparing experiments of varying geometry, material properties or operating

³It should be noted here that the description of the reduced Young's modulus E' differs greatly in published numerical calculations. As an example, Hajishiafee [33] and Singh's [97] input values differ by a factor of three. The author has not yet been able to find a reason for these differences. The upcoming calculations are based on the reduced E modulus according to the recent work by Singh et al. [97].

conditions with changing parameters is therefore rather complicated.

Dimensionless quantities like the Reynolds number Re are used to enable such comparisons. Some dimensionless quantities are presented in the following parts, starting with the Reynolds number Re . Its definition is shown in equation 2.54, according to [98, p.101].

$$Re = \frac{\rho UL}{\mu} \quad (2.54)$$

The Reynolds number is formed using the fluid density $\rho_{\mathcal{F}}$, velocity \mathbf{u} , dynamic viscosity η , and a length scale L characteristic for the domain. In the case of lubrication, the expected film thickness h might be used as a characteristic length scale. The Reynolds number is used as an example here because of its high prominence in engineering and to verify that turbulence phenomena are irrelevant ($Re > 2300$) for EHL simulations in rolling bearings. In anticipation of the information from tables 4.2 and 4.1, the Reynolds number is calculable to $Re \leq 500$. This value varies depending on the inputs (especially the characteristic length) but never exceeds a value that might indicate turbulence to occur, which is why this topic is laid aside for the course of this work. Since the relationship between velocity \mathbf{u} and dynamic viscosity η is also of fundamental importance to EHL contacts, it is worth mentioning the Reynolds number. Concerning heat transfer and heat conduction/diffusion, the Fourier Fo and Biot number Bi are needed for analysis purposes. The Fourier number is defined in equation 2.55, according to Baehr et al. [70, p.129].

$$Fo = \frac{\lambda_S \cdot t}{c_S \cdot \rho_S \cdot L^2} \quad (2.55)$$

It is formed using the solid heat conductivity κ_S , the time t , specific heat capacity c_S , and density ρ_S . Contrary to the Reynolds number Re and the Biot number, the Fourier number is a dimensionless time to characterise cooling or heating processes. It is needed in paragraph 5.2 for the interface coupling tests to verify the correct functioning of the heat transfer. Additionally, the already mentioned Biot Number is also required. It is defined in equation 2.56 according to Baehr et al. [70, p.130]

$$Bi = \frac{a_{\mathcal{F}} L}{\kappa_S} \quad (2.56)$$

The Biot Number is formed using the solid heat conductivity κ_S , the thermal diffusivity $a_{\mathcal{F}}$, and the characteristic problem length L . It describes the tangential temperature development at an interface. It is also needed for the upcoming heat transfer tests in paragraph 5.2.

Besides the Reynolds, Fourier, and Biot numbers, comparing different EHL contacts is usually impossible. Dowson et al. [99] defined a dimensionless velocity, load, and material parameter.

First of all, the dimensionless velocity is defined according to equation 2.57.

$$\bar{U} = \frac{u_e \eta_0}{E' r_R} \quad (2.57)$$

The dimensionless velocity \bar{U} is formed with the entrainment velocity u_e , which describes the mean velocity of the contacting surfaces, which in turn is determined by the SRR and overall velocity. The viscosity at ambient conditions η_0 , the reduced Young's modulus E' , and the radius of the rolling element r_R . These quantities lead to the dimensionless velocity \bar{U} .

The second key parameter for determining tribological contacts is the load carried by the EHL contact. Therefore, a dimensionless load parameter \bar{W} has been established, divided into a two and three-dimensional formulation shown in equations 2.58.

$$\bar{W} = \frac{Q}{l \cdot E' \cdot r_R} \quad (2.58a)$$

$$\bar{W} = \frac{Q}{E' \cdot r_R^2} \quad (2.58b)$$

The differentiation is made because most EHL calculations are done as two-dimensional approximations of line/ point contacts. The load Q , as an integral of the pressure p exerted on the surface of an EHL zone, is again de-dimensioned with the reduced Young's modulus E' and the rolling element radius r_R .

The third and final parameter utilized throughout tribology literature describes the material properties of both fluid and solid domains and is defined in equation 2.59.

$$\bar{G} = \alpha_{\mathcal{F}} E' \quad (2.59)$$

The dimensionless material parameter \bar{G} is formed with the pressure-viscosity coefficient $\alpha_{\mathcal{F}}$ used to characterize the change in viscosity with increasing pressure p and the reduced Young's modulus E' .

Due to the comparability of different systems through the described parameters, they have been used to describe film thicknesses as recently worked up by Marian et al. [38]. As an example, equation 2.60, according to Dowson and Toyoda [71], is mentioned here, which will also serve as an estimate for the quality of numerical solutions concerning the central lubricant film thickness in the following.

$$\bar{H} = \frac{h_c}{R} = 3.06 \cdot \bar{G}^{0.56} \cdot \bar{U}^{0.69} \cdot \bar{W}^{-0.1} \quad (2.60)$$

Equation 2.60 is the formulation of the dimensionless lubrication film thickness \bar{H} by utilizing the material \bar{G} , load \bar{W} , and velocity parameter \bar{U} . It corresponds to the central lubrication film thickness h_c divided by a characteristic radius of the contact. In the case of the rolling bearing under investigation in this work, the rolling element radius r_R is utilized.

2.6. Electrostatics of Tribological Systems

The electrostatics of tribological systems is a relatively new topic compared to the FSI research in the past. It is investigated due to the changed conditions discussed during the

introduction in chapter 1. A primary task for this work is to find an adequate description of the electrical phenomena. Therefore, the material properties like permittivity ε and characteristics like capacity $C_{\mathcal{E}}$ need to be determined. The electrostatic theory covers the need for rolling contact scenarios. The following explanations on electrostatics and electric charge transport complete the necessary theoretical framework of this work and closes chapter 2.

2.6.1. Electro Quasi Static Assumption

The phenomena relevant to EHL take place at different speeds and time-scales. Therefore, the shortest occurring time-scale determines the temporal resolution of a numerical calculation. This circumstance becomes more restrictive for multiple interacting domains as the number of considerable phenomena increases. It sets boundaries, for example, to the time increment that can be used to perform numerical calculations and needs to be analysed in advance. This topic is dealt with as part of the implementation explanation in chapter 4.

The particular time-scale for the electric phenomena is discussed here because it is needed for deciding how the electric phenomena are represented. For the application to rolling bearings, magnetic interaction has not been found of relevance in previous descriptions. Thus, it remains to clarify if electrodynamics, electrostatics, or a hybrid, called the quasi-static approach, suffices to describe the electric domain \mathcal{E} . K uchler [100] stated that the decision for what is permitted depends on the electrodynamic time-constant τ_{em} , stated in equation 2.61.

$$\tau_{\text{em}} = \frac{L}{u_{\mathcal{E}}} \quad (2.61)$$

According to Melcher [101], the specific time τ_{em} determines how long it takes to propagate an electromagnetic wave over the characteristic length L . Therefore the phase velocity $u_{\mathcal{E}}$ of the travelling media is determined. In this case, the lubricant. Equation 2.62 is an approximation for the electromagnetic wave velocity $u_{\mathcal{E}}$ for a media of known permittivity ε and mobility $\mu_{\mathcal{E}}$.

$$u_{\mathcal{E}} = \frac{1}{\sqrt{\mu_{\mathcal{E}}\varepsilon}} \quad (2.62)$$

The time-constant τ_{em} is compared to the time-step Δt of the numerical calculation. The electric field undergoes an instantaneous change for the temporal resolution used during the calculation. The reason is supplied later as soon as the necessary information is given in chapter 4. In other words: The propagation of an electromagnetic wave through the tribological contact takes place within a single time-increment of the numerical calculation and is therefore not resolved.

A static equilibrium is reached in each incremental moment in time, which permits quasi-static calculations and allows the description of dynamic phenomena. This approach is called Electro-Quasi-Static (EQS) approximation or Magneto-Quasi-Static (MQS) respectively, depending on the dominant field of description, and is described in detail by Melcher [101].

2.6.2. Electrostatics

The electric field \mathbf{E} , for EQS, is described as the gradient of the electric potential Φ stated in equation 2.63.

$$\mathbf{E} = -\nabla\Phi \quad (2.63)$$

Equation 2.64 describes the potential Φ of the electric field \mathbf{E} , which changes with the charge density $\rho_{\mathcal{E}}$ inside the calculated region. This link leads to the Poisson formulation of the electrostatic problem.

$$\Delta(\varepsilon\Phi) = -\rho_{\mathcal{E}} \quad (2.64)$$

The electric field \mathbf{E} is mainly determined by the potential boundary conditions established for the region considered.

Metallic surfaces are considered equipotential with a fixed value so that the electric field \mathbf{E} is always perpendicular to such metallic surfaces. As a boundary for the electric domain, metals have fixed voltage U , and the electric field has no gradient at such a surface. If the media in question has an electric conductivity $\kappa_{\mathcal{E}}$ Fourier's law can be established 2.65, leading to equation 2.65 with the electric conductivity $\kappa_{\mathcal{E}}$.

$$\frac{\partial\rho_{\mathcal{E}}}{\partial t} = \kappa_{\mathcal{E}}\Delta\Phi \quad (2.65)$$

The conduction of charges through the media alters the electric field. However, the lubricants used in this work are expected to act as ideal dielectrics and therefore have a vanishing electric conductivity $\kappa_{\mathcal{E}}$ which leads to a charge density $\rho_{\mathcal{E}}$ of zero inside the lubricant. This assumption simplifies the electrostatic differential equation 2.64 to a Laplace equation. Puchtler et al. [102] used the Laplace equation successfully for calculating the capacity of rolling bearing contacts analytically.

2.6.3. Electric Species Transport

While the detachment of charges from the metallic surfaces is rather unlikely for lubricants like FVA 3, the occurrence of ions due to discharge or similar events is more likely. The occurrence and transport of charges bound to chemical species or ions are relevant for the electric calculations of tribological contacts, mainly because it significantly impacts the electric field and leads to a coupling between the fluid domain and electric domain. For example, Prashad [7, p.81] encountered increased ionization of grease lubricants for discharge phenomena and stable potential differences, leading to a deterioration of the lubricant.

The charge transport equation 2.66 shows how the scalar transport is described. It is often referred to as Nernst-Planck or convection-diffusion-migration equation and is found in textbooks on electrokinetics like Masliyah et al. [103, p.190]. Among other things, the charge density of a species $\rho_{\mathcal{E}}$ changes in time according to the flux by convective transport due to the velocity \mathbf{u} of the background flow. Furthermore, a diffusion of the species is taken into account via its respective diffusivity $D_{\mathcal{E}}$, as well as migration due

to the electric potential Φ .

$$\frac{\partial \rho_{\mathcal{E}}}{\partial t} = -\nabla \cdot (\rho_{\mathcal{E}} \mathbf{u} - D_{\mathcal{E}} \nabla \rho_{\mathcal{E}} - \rho_{\mathcal{E}} \mu_{\mathcal{E}} \nabla \Phi) \quad (2.66)$$

The migration of charges through the electric field is described as velocity per electric field unit. Therefore, an mobility $\mu_{\mathcal{E}}$ is defined according to equation 2.67, also called the Nernst-Einstein Equation.

$$\mu_{\mathcal{E}} = \frac{zqD_{\mathcal{E}}}{k_{\text{B}}T} \quad (2.67)$$

$\mu_{\mathcal{E}}$ is formed through electric charge zq_{E} , the Boltzmann constant k_{B} , the absolute temperature T , and the diffusivity $D_{\mathcal{E}}$ of the charge carrying ions, which is also used to describe the diffusive contribution to the temporal change in charge density $\rho_{\mathcal{E}}$. The diffusivity $D_{\mathcal{E}}$ can be determined via the Stokes-Einstein relation shown in equation 2.68, which was derived by Einstein [104] and Sutherland [105] independently.

$$D_{\mathcal{E}} = \frac{k_{\text{B}}T}{6\pi\eta a} \quad (2.68)$$

The diffusivity $D_{\mathcal{E}}$ is formed with the Boltzmann constant k_{B} , the absolute temperature T , which describes how a species diffuses due to Brownian motion. It is divided by an expression for the fluid's resistance to this motion based on viscosity. Equation 2.68 and the explained context are described in Melcher [101, pp. 5.27-5.28].

While equation 2.68 might be used to determine an approximate value for the diffusivity, usually tabulated values are used, and the implications of a changing viscosity or increasing temperature are neglected. The same applies to influences of compressibility on the charge density. In principle the diffusion of charges needs individual handling for every charge carrying species, since their diffusivity varies. For this first approach to integrate the topic it is assumed that only one species is present, thus only one diffusivity is needed. This is of course a very strong simplification because not only varying species are left out but also their interaction and reaction to each other. Strictly speaking a positive and negative charge density would have to be present and their superimposition should be added to the calculation of the electric field.

Equation 2.68 has only been mentioned for completeness. A detailed discussion of future research is given in chapter 6, which will pick up this topic again. However, even without this aspect, the transport of charge carrying species will significantly impact the electric field, as can be seen in chapter 5, and thus the quantities under integration, like the overall capacitance of the tribological system.

2.6.4. Clausius Mossotti Equation

Elevated temperatures T and pressures p affect the viscosity and require a compressible description of the fluid domain. Additionally, the increase in the state variables, like the permittivity ε , also impacts the electric domain.

The Debye equation describes the dependency of permittivity on pressure and temperature. Therefore, the equation is simplified by neglecting the impact of permanent dipoles, which results in the Clausius-Mossotti equation 2.69.

$$P_m = \frac{\varepsilon_r - 1}{\varepsilon_r + 2} \frac{M_m}{\rho} = \frac{N_A}{3\varepsilon_0} \alpha \quad (2.69)$$

Equation 2.69 is an EoS for describing polarizability ξ via the relative permittivity ε_r , molar mass M , density ρ of the lubricant. Alternatively, it is described via the Avogadro constant N_A , the free space permittivity ε , and the polarizability ξ . Schrader [106] used a formulation of the Clausius-Mossotti equation to describe the relative permittivity ε_r through the density ρ . This implicit dependency on temperature and pressure analogue to the Doolittle equation for viscosity suits the canon of equations very well. 2.70 shows the Schrader equation.

$$\varepsilon_r' = \frac{\varepsilon_r + 2 + 2 \cdot (\varepsilon_r - 1) \frac{\rho'}{\rho_0}}{\varepsilon_r + 2 - (\varepsilon_r - 1) \frac{\rho'}{\rho_0}} \quad (2.70)$$

The formulation 2.70 fits the description of lubricant properties via the equation of state and justifies why an analytical approach for the equation of state was favoured. Equation 2.70 shows how the thermodynamic state in the contact might be altered due to pressure. The impact of this equation on the actual values will be discussed in the numerical results section as the permittivity is calculated for all simulations of tribological contacts.

3. Research Questions

The primary goal of this thesis is to obtain insights into the mechanisms of electrical phenomena acting in tribological rolling bearing contacts. Therefore, a numerical approach to the mechanisms underlying these phenomena is developed and applied to offer a new perspective. The main research question for this work is, therefore, as follows:

To what extent can the properties of Elastohydrodynamic Lubrication systems in rolling contacts be reproduced numerically by implementing the existing theory on electrostatics and charge transport?

Since the theoretical framework has already been given in chapter 2 and relevant equations and descriptive models were covered, the next step is to structure and implement the simulation approach. The implementation described in chapter 4 is tested to ensure the successful integration of the theory.

In chapter 4, multiple approaches and programs are available as the basis for the implementation. The available programs and different architectures are revisited briefly to identify suitable candidates. By comparing the requirements to the capabilities of the individual programs, taking the possibilities for expansion and modification into account, one is selected. Then, the modelling of EHL systems is implemented into the existing framework. As will be shown in section 4.1 the resulting numerical model meets all imposed requirements. After the successful implementation, the design of a reference calculation example follows, which is a complex topic and needs special attention. Therefore, the second research question concerns the case setup and is prerequisite for answering the first one:

How should the tribological contact of a rolling bearing be set up in the presented framework, to calculate all quantities relevant for the characterization of electric phenomena?

To ensure the validity of the single implementations, isolated aspects are tested by comparing numerical results with known solutions to problems as a benchmark in section 5.2. With the confirmation that all individual aspects work correctly, the rolling bearing case, presented in 4.2, is approached in section 5.3. Based on these calculations, the basic functionality of the numerical modelling is demonstrated. However, some limitations are found, so that the comparison between fully coupled numerical calculations to experimental data is not possible at the time of submission. Since the experiments to collect these data were carried out specifically as part of this work, they are nonetheless presented in section 5.4 for future research. Whereas the descriptions from section 5.3

answer the second research question in outlines, the calculation approach is used on two examples from experimental tribology research at the pmd.

Because approaches based on the Reynolds equations and Hertzian contact theory are strictly limited to ideal geometries, which categorically excludes an investigation of deviating surfaces like pittings, spallings, or ripples, the numerical model helps to investigate those problems, even within the limitations found. Thus, numerical calculations for such perturbed surfaces are carried in section 5.5.1. Subsequently, the temporal development of charge densities in the tribological contact is investigated for discharge prevention in section 5.5.2. The third research question therefore deals with the application of the developed program to real problems of tribology:

How does the numerical approach support the description of experimental research on electrical phenomena in tribological systems?

In answering this third and final research question, the capabilities of a numerical perspective on electrical phenomena in EHL contacts becomes apparent for achieving new scientific insights. A brief discussion of the results from chapter 5 is held in chapter 6. Subsequently, this discussion also answers the research questions in inverted order, since the answer to research question three contributes to research question two and same to the main research question one.

The possibilities and restrictions that were found for the implemented theory are evaluated and assessed to conclude the scientific progress made in this work in chapter 7. The discussion and critical appreciation will also contribute to the answer of the primary research question. Addressing the ability to reproduce electrical phenomena in EHL systems, this work concludes with a discussion of advantages, disadvantages, uncertainties, and inaccuracies as a vital part of the scientific process, and outlines possible future work.

4. Calculation Methodology

Before explaining the overall program structure, it is worthwhile to straighten some terms/definitions and work out the purpose to be achieved with the implementations. Therefore, the primary function of the program is defined. According to Roth [107, p.110], the formulation of the primary function should be neutral to the actual solution but describe the causal relationship between input quantities and intended outputs.

The primary function is divided into partial functions to accomplish this goal, which leads to a functional structure whose individual tasks are easier to handle, according to Feldhusen et al. [108, p.41]. The partial functions process input quantities, like forces and deformations, and provide their outputs to subsequent functions. According to Gramlich [109, p.64], specific processes realize these partial functions. The actual implementation in the programme can be understood as a process. Figure 4.1 shows the relationships.

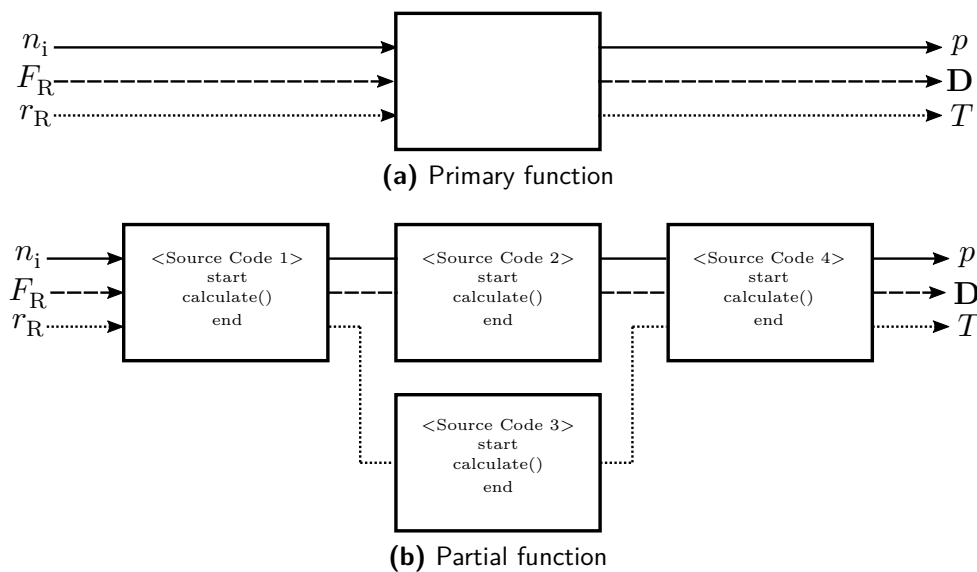


Figure 4.1.: Schematic visualization of a functional structure realizing a primary function following Feldhusen et al. [108, p.45]

Since the sequence, interaction, and iteration of the partial functions is permutable and multiple processes are available, variants of the functional structure exist. The processes that underlie the partial functions utilize models for calculation. In the sense of product development, according to Feldhusen et al. [108, p.80], models are simplified representations of a complex reality with an accuracy corresponding to the purpose of modelling. In addition, Stachowiak [110, p.132] stated that only a fraction of the

attributes of the system to be described is relevant to the modelling task. Therefore, the model's validity is limited, according to Stachowiak [110, p.133].

Transferring this methodological descriptions to numerics means defining the primary function first. It could be formulated as follows:

Calculate a locally resolved converged solution for all quantities needed to characterize a single rolling bearing contact and its electrical properties for given specifications to the geometry, operating conditions, and material quantities

The coarsest form for the structure of partial functions, in the context of multi-physical simulations, is along with the physical domains and their interactions. Processes, realizing the partial functions, are accordingly solvers and solution algorithms for the specific domains. These processes handle objects like pressure p , temperature T or deformation \mathbf{D} as their input and output quantities and process them using models. In the context of numerics, the term model comprises differential equations, EoS, and equations for describing material properties like viscosity η , permittivity ε , or Young's modulus E . The models necessary for this work are described in chapter 2.

The following chapter is concerned with the functional structure and its implementation. First of all, the program framework is selected from the available options in section 4.1.1. For a better understanding of the following remarks on the implementation, some additional information on the programming language are given prior in section 4.1.2. The complete functional structure which was implemented into the selected framework is presented in section 4.1.3 for an overview. The individual programme modules, aka partial functions and processes are addressed in detail from section 4.1.4 to 4.1.6. The partial functions and underlying processes are explained and linked to the models after explanations on the functional structure. In the last part of this chapter, the reference case for application of the functional structure is explained in detail. The explanations in section 4.2 transitions directly to the presentation of the results in chapter 5.

4.1. Programme Architecture and Implementation

4.1.1. Program Selection

Numerous source codes and commercial programs are available for multi-physical simulations, including FSI. The question is, which one is most suited for the task. The program choice as a basis for tackling the tasks of this thesis and is based on a few requirements. First, there is the requirement that a program should already incorporate relevant domain interactions. Since the presented models, especially for viscosity and the EoS, are rarely used in conventional CFD, a programming interface to embed those models is a second requirement. A simple disclosure of the source code is the third requirement, since scientific reproducibility needs to be ensured, which is only possible to a limited degree for commercial code.

The question of the most suitable programme is answered by elaborating on the main

distinguishing features between them. A few programs cover the theory stated in chapter 2. On the commercial side, COMSOL™ and ANSYS™ have to be mentioned as all-in-one solutions for computations governing multiple physical domains. These include FSI, electromechanics, and thermodynamics. OpenFOAM, SOFA, and Kratos are examples of open source approaches to multi-physics. Outlining advantages and disadvantages compared to the requirements led to OpenFOAM as the program of choice. The following paragraphs will give a short explanation for this decision.

Typically, licensed code is only used as a front-end tool, while the access to programming interfaces for those programs restricts the customer side. This restriction is uncritical as long as the program is solely used to compute tasks that the implemented models and solution algorithms cover. Commercial code means time and resource savings for this prerequisite. If models and solution algorithms need implementation via user interfaces, these tools can become inefficient and hard to handle. The required transparency is often not given for licensed code because the developer keeps the underlying processes a business secret. This circumstance is sometimes called "license limitation," around which the pro and contra discussion of open-source codes versus licensed programs in scientific work arises as Ince et al. [111] discussed. Open-source tools cover the requirement for transparency better since every part of the program is accessible and can be published alongside the scientific findings.

Apart from the commercial vs. open-source distinction, the approach to covering multiple domains is the main distinctive feature. While programs like COMSOL™ or ANSYS™ cover all domains within one modular framework and a Graphical User Interface (GUI) for all of its features, some codes operate abstractly by connecting individually specialized programs. Those approaches, called Application Programming Interface (API), are used to join tools developed for a single domain via their Input and Output (I/O) interface. Figure 4.2 visualizes the API- and stand-alone approach.

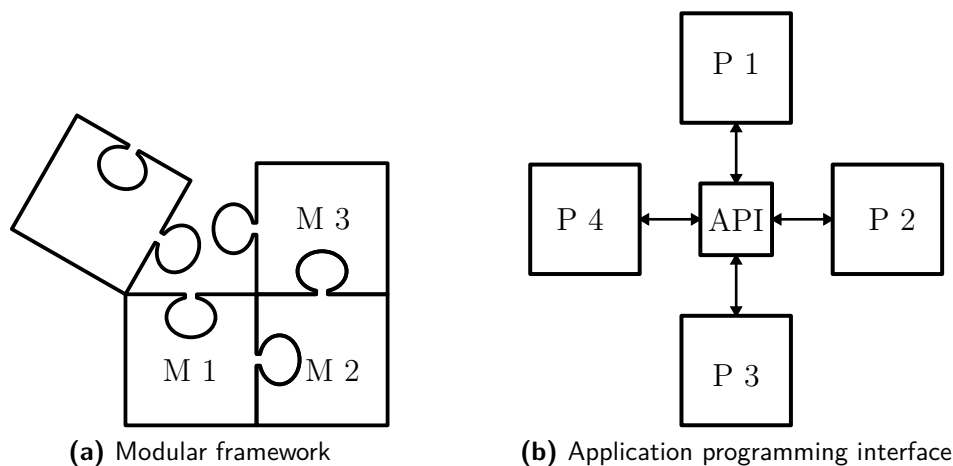


Figure 4.2.: Visualisation multi-physics programme architecture; Complete framework consisting of modules M 1-3; API connecting individual programs P 1-4

APIs can use highly specialized tools suited best for their individual domain and thus

offer the vastest solver libraries compared to all-in-one solutions. On the downside, those approaches often lack efficiency since the I/O is time-consuming compared to runtime-based data exchange in a single framework. The incoherence in data management between different tools adds to this problem, as intermediate translations of datasets for the input into another program become necessary. Attachment of a new system is a problem because most software is not designed to operate in this context. Therefore, I/O gateways have to be scripted, if that is even possible in the first place.

As one of the most prominent source codes for CFD, OpenFOAM has been established as a researcher-oriented open source code. The complete accessibility of the source code with extensive documentation and the support of a vast research community is beneficial. Open source offers the opportunity to adapt every line of the code, for good or bad.

An exclusion criterion for many programs is the solution strategy for the linear equation systems during the calculation. A linear equation system is built when calculating differential equations on finite volumes, which can be expressed in the form of equation 4.1.

$$\mathbf{J} \cdot \mathbf{x} = \mathbf{r} \quad (4.1)$$

The Jacobian \mathbf{J} incorporates the coupling terms between the unknown variables \mathbf{x} . The right side of the equation summarises quantities that do not explicitly depend on the unknown variables, like external forces or boundary conditions.

Either a single system of equations is formed across all domains or multiple, one for every domain, according to Degroote et al. [112]. A distinction is therefore made between a monolithic and a partitioned strategy. The monolithic approach only requires the solution of a single linear system of equations, which ensures convergence as long as the system is not under-determined. The consecutive partitioned approach cannot guarantee this. If the totality of the equation systems is only solved once, one speaks of a loosely coupled procedure. While such an approach is typically rapid, it also tends to diverge as described by Richter [57, p.283]. The equation systems are sub-iterated, therefore solved implicit and strongly coupled to prevent this. While this reduces the divergence tendency significantly, it is also time-consuming. Three basic approaches can therefore be identified as monolithic, weakly coupled and strongly coupled.

However, monolithic approaches are rare. The reason is found in the computational expenses to solve the linear equations system. Partitioned approaches draft their boundary conditions from the previous solution and achieve interaction between domains. Boundary conditions are always found on the right-hand side of equation 4.1. The coupling matrix \mathbf{J} of a single domain is sparsely occupied and thus less expensive to solve. An exemplary coupling matrix 4.2. The sparseness and size of the Jacobian determine the computational expenses.

$$\begin{pmatrix} j_{1,1} & j_{1,2} & 0 & 0 & 0 \\ j_{2,1} & j_{2,2} & \ddots & \ddots & 0 \\ 0 & \ddots & \ddots & \ddots & 0 \\ 0 & \ddots & \ddots & j_{m-1,n-1} & j_{m-1,n} \\ 0 & 0 & 0 & j_{m,n-1} & j_{m,n} \end{pmatrix} \cdot \begin{pmatrix} x_1 \\ x_2 \\ \vdots \\ x_{m-1} \\ x_m \end{pmatrix} = \begin{pmatrix} r_1 \\ r_2 \\ \vdots \\ r_{m-1} \\ r_m \end{pmatrix} \quad (4.2)$$

Sparseness, in the sense of all entries are near the main diagonal, is absent from the monolithic approach. While coupling terms are on the right-hand side of equation 4.1 for partitioned approaches, the coupling can be located all over the Jacobians for monolithic systems. Equation 4.3 illustrates this circumstance.

$$\begin{pmatrix} \dot{j}_{1,1} & \dot{j}_{1,2} & \cdots & \dot{j}_{1,n-1} & \dot{j}_{1,n} \\ \dot{j}_{2,1} & \dot{j}_{2,2} & \cdots & \vdots & \dot{j}_{2,n} \\ \vdots & \vdots & \ddots & \vdots & \vdots \\ \dot{j}_{m-1,1} & \vdots & \cdots & \dot{j}_{m-1,n-1} & \dot{j}_{m-1,n} \\ \dot{j}_{m,1} & \dot{j}_{m,2} & \cdots & \dot{j}_{m,n-1} & \dot{j}_{m,n} \end{pmatrix} \cdot \begin{pmatrix} x_i \\ \vdots \\ y_n \\ \vdots \\ z_k \end{pmatrix} = \begin{pmatrix} r_1 \\ r_2 \\ \vdots \\ r_{m-1} \\ r_m \end{pmatrix} \quad (4.3)$$

In addition, the matrix system grows over-proportionally with an increasing number of unknown variables \mathbf{x} . These two aspects lead to fully occupied systems of huge matrices, which are disproportionately expensive to solve. While this might be acceptable for small tasks with only a few degrees of freedom, either because fewer domains are under consideration or the problem has only a few mesh points, it is computationally unfavourable.

To summarize, the savings in computational costs is the main benefit of explicit partitioned calculations, but only if convergence is achievable. If this is not the case, an implicit, partitioned approach is inevitable. In case even reiteration between the domains does not lead to convergent solutions, a monolithic approach can ensure convergence at extremely high computational costs. For calculating a bidirectional effect, like fluid-structure interaction, a monolithic approach seems disadvantageous as the coupling occurs across time-steps. In addition, the goal of coupling a total of four domains at a necessary medium to high temporal resolution, which is discussed in section 4.2, disqualifies a monolithic approach ultimately. Previous approaches have also shown that implicit partitioned calculations are most effective. Since a monolithic solution procedure cannot be implemented in the aforementioned programs anyway, a partitioned approach is realizable with API and all-in-one solutions. API becomes less attractive for an implicit partitioned approach as the bottleneck for parameter transfer between the individual programs becomes exceptionally time-consuming.

To decide which program should be used, an overview of programs used in the the literature offers some insight to narrow down the selection. Focussing on previously utilized programs provides the advantage of exploiting the experience gathered in literature. The numerical calculation of EHL contacts has been carried out with commercial software early on by Almqvist et al. [30] and lately by Tomic et al. [35]. At the same time, there is an equal number of publications using OpenFOAM for the numerical calculation of EHL contacts like Hartinger et al. [32], [34], Hajishafiee et al. [33] or lately Singh et al. [97].

As already mentioned, the open-source program OpenFOAM is used for this work. It is an all-in-one application that uses a partitioned approach. The main reason for this, except the fact it matches the mandatory requirements mentioned before, is its transparency due to the disclosed source code and the adaptability this offers. Since for both commercial programs and OpenFOAM implementations of EoS, viscosity models,

and calculation procedures for the electric properties are necessary, the accessibility of OpenFOAM is superior to programs like COMSOL™ or ANSYS™.

4.1.2. C++

OpenFOAM is written in C++, an Object-Oriented Programming (OOP) language. Therefore, the terminology and structure used for the descriptions in OpenFOAM originate from the basic terms used in C++ programming, so it is helpful to explain those in advance. Since this work is not about programming language and its syntactic finesses, only the most relevant aspects of C++ are stated shortly, essential for understanding the program architecture of OpenFOAM. For example, Lippman et al. [113, pp.58-60] offer a structured introduction to the fundamentals of C++ on which the following explanations are based.

The significant advantage of object orientation is its extensible nature of programming. Procedural code typically offers a predefined set of variable types from which single instances are defined at run-time. Such a type might be a piece of text (Character (char)) or numbers (Integer (int), Floating Point Number (float)). The meaning of instance is taken from informatics and defines an allocation of memory at the Hard Disk Drive (HDD) and defines which type of information is stored. The type determines a set of allowed operations on the single instances.¹

OOP is different since it offers the possibility to define new, more complex types based on existing ones. These definitions of types are called classes. Their description is done in advance during the code compilation to introduce new classes to the compiler. Listing 4.1 shows an example of a generic class definition.

Listing 4.1: C++ class definition example

```
class class_name {
    public :
        member_function_1;
    private :
        member_function_2;
    ...
};
```

The class consists of multiple functions (so-called member functions) that define operations done by it on input data or its own allocated data. Those functions are divided into public and private. Private functions are only accessible from within the class, while public member functions are callable from outside the class.

If a class is introduced to a C++ code, its new type becomes available so that it can be instantiated. These instances are called objects and become callable in the program run-time. C++ has some basic classes for object definitions like the mentioned number types int and float or text types like char. Those types are more or less universal for

¹For example a char does not allow any mathematical operation since a piece of text is inadequate for calculus but allows word searches

other languages too. A class should not be misunderstood as data since it also provides functions that define the allowed and forbidden operations performed with/on the class. The class itself will be instantiated as one or multiple objects in the process of a C++ executable. The actual program with its procedural code is also existent in C++. Listing 4.2 shows the rudimentary structure that represents the actual program executed.

Listing 4.2: C++ executable example

```
#include "fvCFD"
using namespace FOAM;

int main()
{
    some_procedural_code;
    return some_value;
}
```

Usually, such a program includes multiple libraries that introduce classes used during the program's run. An example of such a library is included in listing 4.2. The *fvCFD* library introduces all the classes necessary to set up the primary finite volume fields which OpenFOAM uses for calculation. Other vital libraries are the *fvSchemes* and *fvSolutions*. They contain functions for discretization of differential equations and solution procedures to calculate the linear systems of equations.

With this basic understanding of C++, it is easy to describe what OpenFOAM is. It is nothing less than a set of libraries which provide classes like geometric fields, scalars and vectors. These libraries are supplemented by executables which can be understood as the actual procedural programs that perform numerical calculations on the fields. These are solvers and introduce iterative calculation procedures that follow predefined patterns.

During the initialization, all required variables are declared. The geometric data given by the user are transformed into fields in the form of arrays containing listings of point and cell coordinates together with face and neighbouring relationships between each discrete cell, shown in figure 4.3.

On this basis, all scalar and vector fields are built. From the geometric data, fields are derived, assigning data like temperature, pressure, and velocity information to each cell centroid p_C .

These fields are then processed according to numerical principles. If convergence is reached, the data is written to the hard drive and post-processed.

To realize the program needed to fulfil the primary function defined earlier, it uses several of the available OpenFOAM functionalities. Such functionalities include grid generation (*fvFields*), multiple fluid/structural solvers and utility libraries like thermophysical properties. However, functions are supplemented to the existing classes and libraries to get the needed functionality. The next part of this work deals with the architecture, changes and additions to OpenFOAM. For compactness of this thesis, only the final version is explained, without detailing the overall development process.

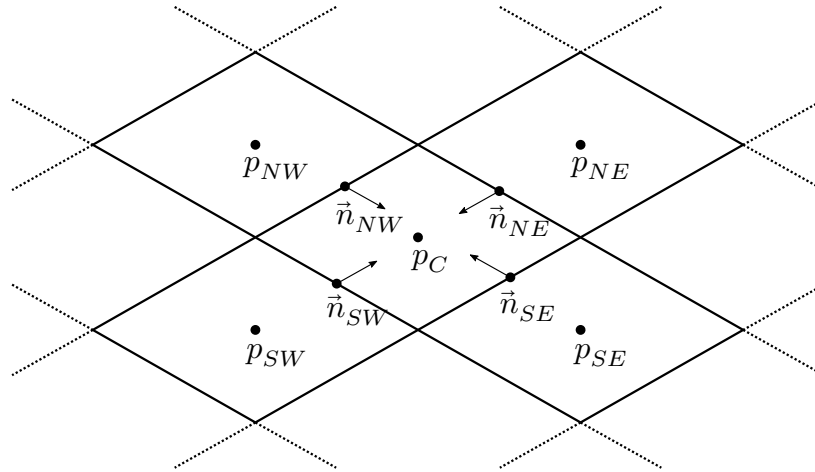


Figure 4.3.: Example for geometric field information; The neighbouring relations (p_i) and surface normals (\vec{n}_i) for a single cell centroid serve as the basis for calculating the balance equations

4.1.3. Overarching Implementation

Now that the program choice has been clarified, the implementing of all models and processes to realize the partial functions is the centre of attention. The architecture discussed in the following is built based on the foamExtend 4.0 FSI toolbox, described by Tukovic et al. [42]. Since its publication, several researchers have adapted and applied it to many problems, for example Khodaei et al. [114] for a medical technology application. The foamExtend version of OpenFOAM is a developer's environment for research purposes. Contrary to OpenFOAM, which only includes release solvers tested extensively and are therefore state of the art, foamExtend also has practical applications like the mentioned FSI toolbox.

Since the FSI application does not extend to TEHL applications yet, several implementations are needed to cover physics needed. Therefore, the differential equations and material models stated in chapter 2 must be included. To ultimately draw valid conclusions from results obtained with the modified program, all these integrations must be tested before calculating an actual task. In the following, the overall architecture program in its latest version is described first to give an overview. Some parts that needed adaptation are described in detail. Crucial elements of the program architecture are used in specific isolated tests to verify their correct functioning in section 5.2. This approach is called Test-Driven Development (TDD), an essential procedure during program as Beck [115] explained.

Flowchart Visualization Reproducing program architectures within print media in a comprehensible way is challenging, and only a few diagrams are established for such a task. The most common is the flowchart, whose symbols are standardized in the DIN-EN-66001 [116]. Even though flow visualization is a standard tool for programming, it can result in elongated graphics. Some more extensive routines are hidden behind single

blocks for a tidier structure. Such a sub-routine representation, shown in figure 4.4d, is used to stagger the level of complexity.

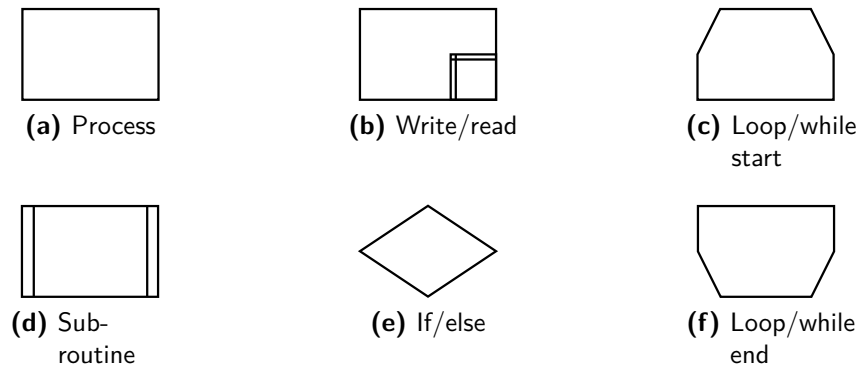


Figure 4.4.: Flowchart symbols according to DIN 66001 [116]

Subroutines are accessed, visualized, and discussed throughout this chapter or referenced in the corresponding appendices. Apart from the process and sub-routine blocks, "if" and "if-else" statements, shown in figure 4.4e, are also needed. The third type of structure are loop limiters, shown in figure 4.4c and 4.4f. Beyond these essential elements, the writing process has been added to show where data is written from run-time to the hard-drive represented by figure 4.4b.

This last aspect is vital since OpenFOAM only writes to the hard drive if instructed to. Otherwise, variables and fields are stored in allocated spaces in the Random Access Memory (RAM) and administrated via a run-time library. It coordinates the starting and termination of an application. This also includes, for example, the instantiation of objects during the start and the handling of services through libraries which are included via dynamic linking.

The term "field" is used for every form of mathematical array filled with scalar and vectorial quantities, where an entry corresponds to a cell of the underlying grid during calculation as described in subsection 4.1.2. As these fields can have a size of multiple MegaByte (MB), writing and reading processes become computational expensive, so it is used as rarely as possible.

Before going into detail on the programme sequences, a synopsis on the implementations is given. This synopsis should help the reader allocate the different fundamentals to their representation in the program.

Directory Structure Based on state-of-the-art approaches, like [32]–[34], an implicit, strongly coupled, partitioned calculation procedure is the declared objective, which is also advantageous concerning new implementations. Figure 4.5 delivers an overview of the FSI toolbox organization, including all the extensions and changes made during this thesis.

Shown are its executables and libraries with their main functionalities. *Italic words* indicate elements that were added, transferred from OpenFOAM, or adapted somehow.

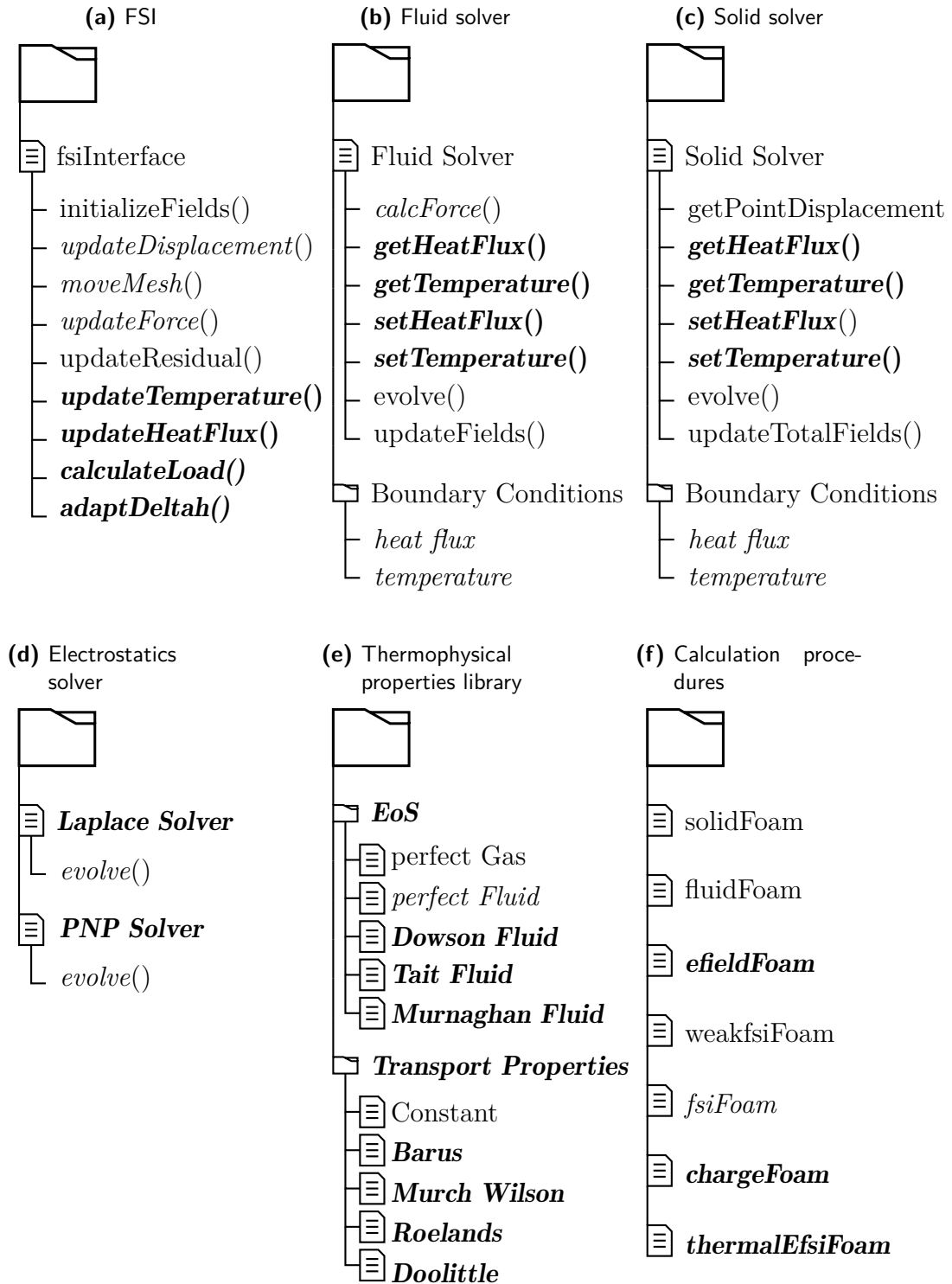


Figure 4.5.: Synopsis of the program architecture;
Upright terms - unchanged; Italic terms - adapted; Bold terms - newly created

Non-italic words mean the parts were already present in the FSI toolbox by Tukovic et al. [42]. The program is divided into six components. The central part is the FSI functionality in figure 4.5a, which handles the communication between the domain-specific solvers and includes all overarching FSI functionalities like mesh control and data exchange. Everything related to a single domain is dealt with by their respective solvers, illustrated in figures 4.5b, 4.5c and 4.5d. The models and EoS needed for the fluid solver are provided in the thermophysical properties library, shown in figure 4.5e. Multiple EoS and viscosity models were added, and the whole library was made available to the FSI toolbox. The sequence by which FSI functions and solvers are called is provided within the calculation procedures listed in figure 4.5f.

Due to this structure, implementing new calculation procedures is relatively simple, which is advantageous for future work. Appendix E.1 shows the source code for the `thermalEfsiFoam` calculation procedure. The architecture becomes clearer by explaining how thermal information is handed over, exemplary.

So does, for example, the `updateTemperature()`-function call from the `thermalEfsiFoam` solution procedure requests temperature information by calling the `getTemperature()`-function of a specific domain solver. The received data is translated to the opposing domain by the `updateTemperature()`-function via a General Grid Interface (GGI), which is detailed below. The transformed temperature information is then written to the temperature field of the target domain by calling its `setTemperature()`-function. The updated data comes into effect during the following solution of the domain via the `evolve()`-function. The actual solution procedure, i.e. the solver, for the domain is stored in the `evolve()`-function. Source code examples for the domain specific `evolve()`-functions can be found in the corresponding appendices.

General Grid Interface The transfer of information at the interface of two domains is essential for the function of any coupling. A GGI, first presented by Beaudoin et al. [117], is used to couple non-conformal interfaces of a contiguous region for data handover. Initially developed for turbomachinery simulation, it allows different grid resolutions for interacting domains. Figure 4.6 shows an exemplary GGI.

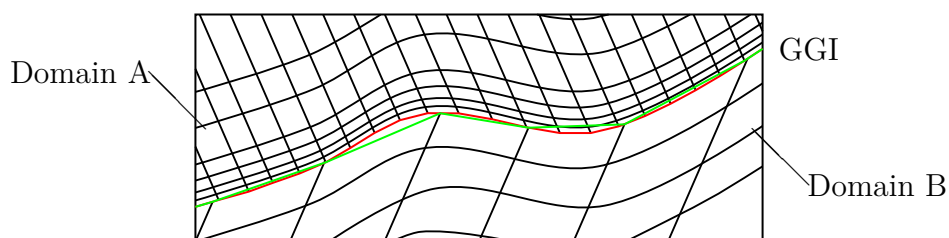


Figure 4.6.: General Grid Interface (GGI) connecting domains A and B of different resolution at a circular interface

Shown are two exemplary domain grids (A and B) with different resolution. The deviation at their mutual boundary interface is emphasized by colour. The red contour represents A and the green one domain B. What is striking is the poor consistency of

the lines. Hence, to exchange data at the interface, an interpolation is needed. With the help weighting functions, based on the surface area fraction of the cell contours, information are transferable from domain A to B.

The GGI is helpful to keep computational costs low because the resolution of mesh regions at interfaces is not necessarily equal, as figure 4.6 indicates. Figure 4.6 also shows a drawback of GGIs at curved surfaces with deviating resolution at the interface because overlap errors occur. Beaudoin et al. [117, p.6] also identified this problem and solved it by recalculating the weighting factors to enforce continuity at the interface. This weight adjustment reduces the error to a magnitude of 10^{-3} . The error can be reduced to zero for matching resolutions if necessary. For example if the remaining error induces instability². The GGI functions are used implicitly, for example for the `getTemperature()` and `setTemperature()` functions.

Mesh Movement The second significant coupling provided by the `fsiInterface` executable is the mesh deformation with the `moveMesh()` function. It translates the deformation **D** of the solid solver onto the fluid-solid interface. Subsequently, the dynamic mesh movement procedure is invoked by the `moveMesh()` function to distribute the interface deformation over the complete fluid grid. Such a distribution prevents too massive distortions of single fluid cells. The `moveMesh()` function ensures domain continuity, and the FSI coupling is realized. This approach of adjusting the boundary conditions of a domain based on the previous solution is a form of the partitioned procedure described at the beginning of chapter 4.1.1.

Solver Implementation The fluid, solid, and electrostatics classes are very similar in their architecture and contain, as the names indicate, the actual domain solvers. The `evolve()`-functions of the fluid, solid and electrostatic classes contains the domain specific solution procedure. In the literature multiple approaches are available for solving the differential equations associated with each domain. Therefore, not only one but multiple sub-classes are available per domain, each following another solution paradigm. Each solver sub-class is inherited from the basic class. Thus, the sub-classes own the general functions listed for the basic class in figure 4.5 which are needed to make the solver work as part of the framework.³

The toolbox's fluid, solid and electrostatics components consist of a generic solver class that already incorporates all necessary constructors and functional declarations that the `FSIInterface` class might request during the initialization of a calculation procedure. The derived sub-classes are named after the original solver whose source code is

²An example for this is mentioned later if the case setup is explained in section 4.2

³At this point, a conceptual ambiguity should be clarified. Typically the term solver is used to describe the overall calculation procedure for the solution of a specific task such as the `main()` function. For example the PISO algorithm is called a solver. However, this description fits multiple procedures implemented for the several domains but also the sequences in which these are executed in the whole EHL calculation procedure. Therefore, the term solver is exclusively used for the solution inside of the domains, which is in line with regular CFD literature, while for EHL loops the terminology calculation procedure is used.

embedded into the `evolve()`-function. For example, the PISO executable, first described by Issa [118], fills all the declarations made in the base class with definitions and equations. In the case of the `evolve()`-function, this means the actual procedural solution algorithm as it is known from the regular OpenFOAM release executable. The core information to be taken away from these explanations is, that established solvers known from the main OpenFOAM release are made available in the FSI framework.

Thermophysical Properties Implementation The material models like dynamic viscosity η and EoS are grouped in the fifth part of the toolbox, the thermophysical properties library. It contains various classes, including functions for calculating density, viscosity, compression modulus, several mixing rules for chemical species, and others. The basic implementation for this library and the turbulence model library are also taken from OpenFOAM. Latter is not elaborated here because it is irrelevant for the following calculations. The turbulence library was implemented for future work and to keep the structure close to the original from OpenFOAM. The thermophysical properties library allows the implementation of new models. This property comes in handy, as the pre-implemented ones do not include those models described in the fundamentals in sections 2.3.4 and 2.3.5. These models, however, are mandatory for state-of-the-art EHL calculations. Multiple EoS and viscosity models were added to this library, anticipating future research and offering a selection from which to choose. In the following, mainly the Tait (2.35) and Dowson (2.32) EoS and the Doolittle (2.41) and Roelands (2.40) viscosity models are used.

Calculation Procedure The sixth and final part of the program contains multiple calculation executables, defining the actual procedural code. While parts one to five cover all necessary functionalities, the sequence in which these functions are processed during simulation is defined here.

Besides the pre-implemented FSI calculation procedure, special procedures for EHL and TEHL calculations were added, alongside some for single domain calculations. These single domain procedures reduce the calculation to their underlying solvers, allowing comparison to reference cases and simplifying the process of implementation verification and validation later in chapter 5.

To keep this work straightforward, only the TEHL calculation procedure, named `thermalEfsiFoam`, is reviewed in detail. The actual source code of the `thermalEfsiFoam` executable is attached in appendix E.1. Figure 4.7 illustrates the program sequence in a flowchart representation. The calculation procedure starts by creating all needed quantities like grids and parameter fields while reading library information (1). At the beginning of a new cycle, the program updates pressure forces at the FSI interface and evolves a predictive solution for the displacement vector \mathbf{D} of the solid domain based on the pressure values from the last time-step (2).

With this initial guess for the local solid displacement, the main FSI calculation (3) is entered. At first, the fluid mesh boundary is adjusted based on the residual information (4). The residual is an array calculated as the distance between the surface elements

of the fluid- and solid domain at their FSI interfaces. The residual arises because the fluid mesh has not followed the new solid deformation yet. After adapting the fluid boundary, the internal fluid mesh is distorted to distribute the deformation over multiple cells. The fluid solution is evolved, so the topological changes take effect, leading to changes in pressure p , temperature T and velocity \mathbf{u} (5). Then the boundary forces are recalculated (6), and the solid is evolved with the newly calculated boundary forces (7). The residual is updated and convergence checked(8). If the residual drops below the convergence criterion, the calculator leaves the FSI sub-iteration. Otherwise, the FSI calculation starts again by imposing the solid displacement \mathbf{D} on the fluid side of the interface. The previously calculated residual serves directly as a convergence criterion. A residuum between fluid and solid grid, smaller than 10^{-8} μm is considered standard for EHL calculations.

Up to this point, the depicted procedure equals an implicit partitioned FSI coupling approach, with the addition of thermal calculations (5,7) and handovers between fluid and solid. The electrostatic domain is calculated right after the FSI sub-iteration (9). After that, the calculation of the time-step is complete and data are written to the HDD. Also, the force Q acting on the system is calculated (10). The system's state is evaluated at the end of each time-step (11). Therefore, the acting force Q is compared to the target value Q_{aim} . The aim, for the whole calculation, is to find a solution, where the forces exerted by the pressurized lubricant are at equilibrium for a predefined load Q_{aim} . Since this is a fundamental description, please refer to figure 4.8 for details.

If the target load is not reached yet, the calculation continues (12). This corresponds to an increase in the time-step. It is aimed for a steady state, where $Q=Q_{\text{aim}}$ is reached . To find an EHL configuration that counteracts the target load is the primary goal for this FSI coupling. So, the calculation is interfered with after each time-step for adjustment (13). The position of the solids in relation to each other is adjusted by Δh . If the target load has not yet been reached, the original distance h is reduced as shown in figure 4.8a, otherwise it is increased shown in figure 2.3b.

Load Calculation Previous work on the numerics of EHL contacts showed that the most challenging task is to reach this balance. The underlying problem is, that an equilibrium for the domains, reflecting pressures in an EHL magnitude, is not possible from the initial configuration. Figure 4.8c emphasizes this problem. An EHL contact is created according to the principles of Hertzian theory described in section 2.1.2. The solids deformation δ corresponds to the total distance covered during the calculation. This is a value that is greater than the initial lubrication film thickness, so that a negative value would be necessary to calculate the EHL contact right from the beginning. For this reason, it is not possible to calculate EHL contacts in one sweep but through gradual adjustments.

The total force exerted by the fluid onto a rolling element depends heavily on the local viscosity, lubrication film thickness, and the entire area of deformation. In turn, the latter two depend on the external load, which presses the solid surfaces together and reduces the height of the lubrication film. Therefore, the balance of forces is not just a

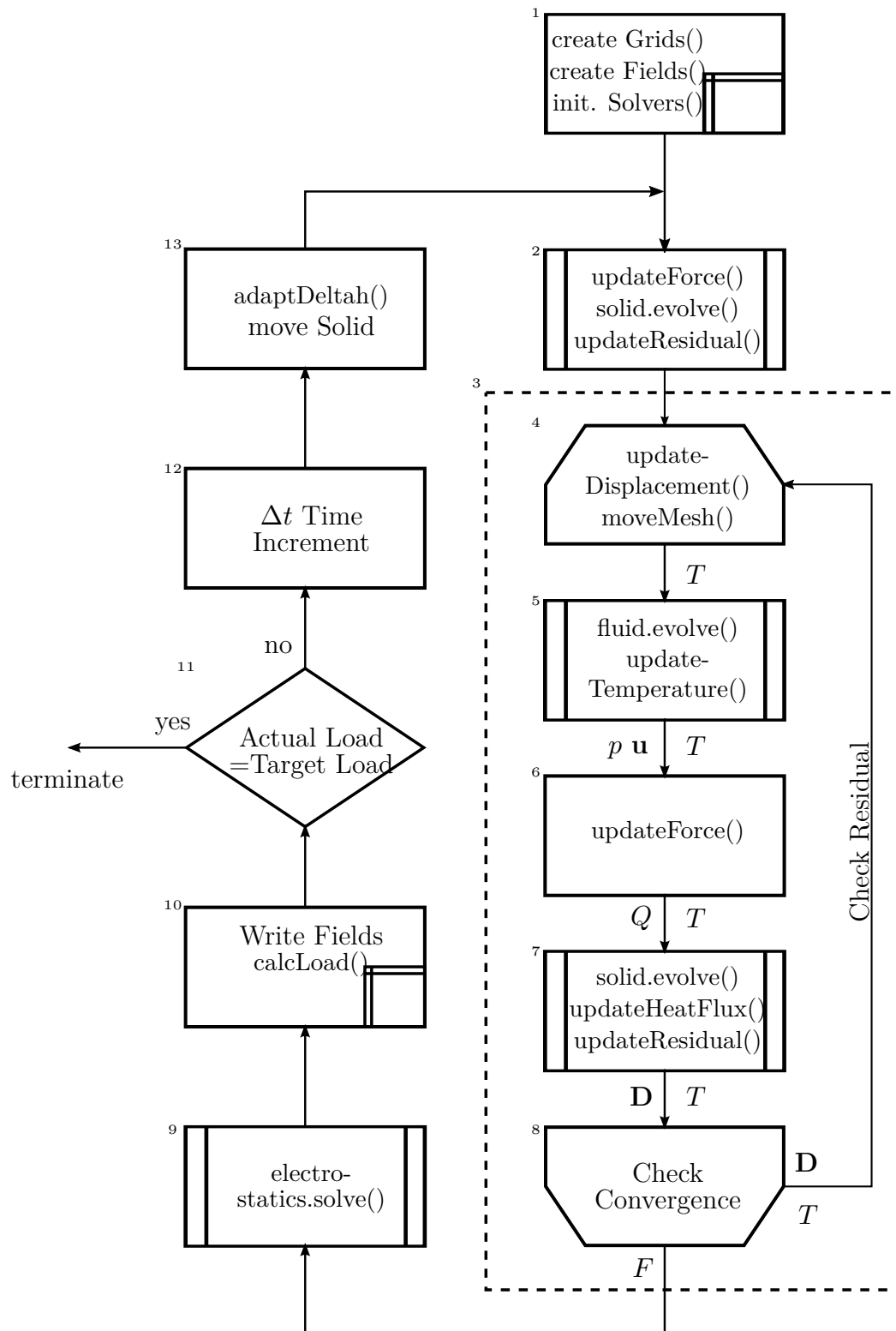


Figure 4.7.: Flowchart representation of the *thermalEfsiFoam* calculation procedure

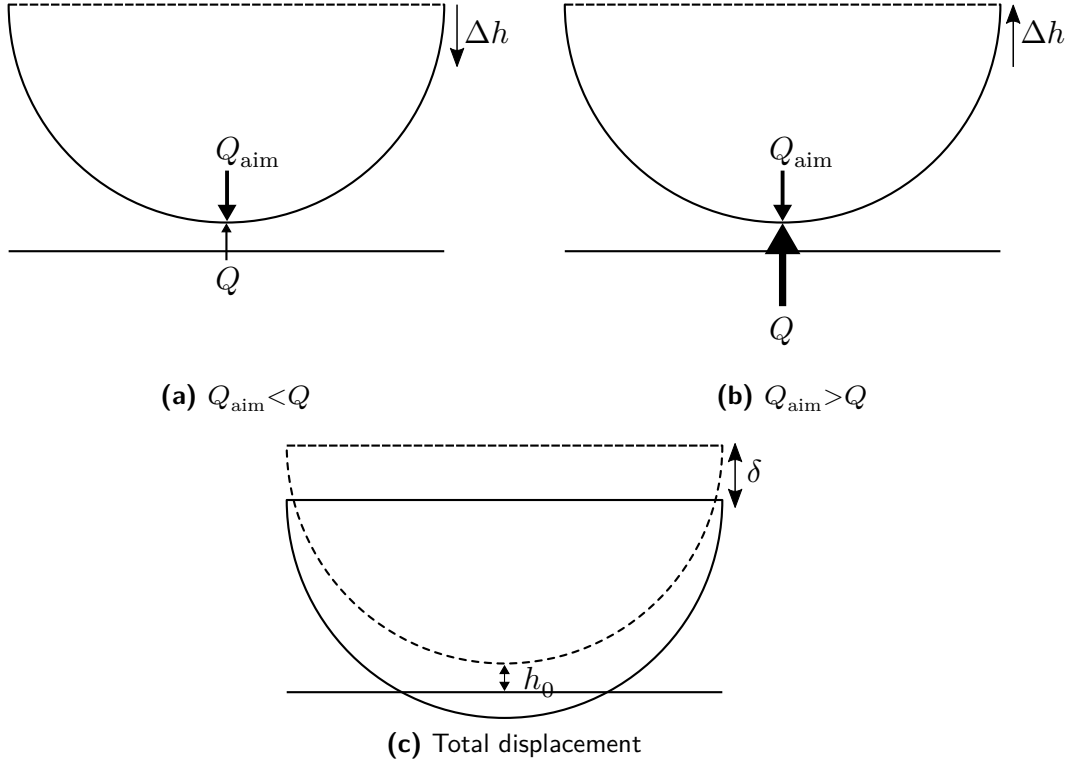


Figure 4.8.: Visualisation of lubrication film thickness adaption function *adaptDeltah()*

stable pressure versus external force equivalence but also the stationary equilibrium of those other properties.

It has been proven to be effective to adapt the calculation after each step to reach the target load. The actual load calculation with the `calcLoad()`-function is executed directly before entering the FSI predictor in the next time-step. If the calculated load matches the target load, the computation is terminated; otherwise, an adaption is made for the next time-step.

Hartinger et al. [32, p.5] suggested changing the initial distance between the rolling element and ring surface h_0 as an adaptive measure. Therefore, the initial distance between the surfaces is changed by Δh , according to equation 4.4.

$$\Delta h = (D_{\max} - D_{\min}) \cdot \frac{Q_{\text{aim}} - Q}{Q_{\text{aim}}} \cdot \frac{\Delta t}{t_{\text{cd}}} \cdot R_{\text{ref}} \quad (4.4)$$

The change of h in this equation is dependent on the actual load Q and the target load Q_{aim} . To stabilize the process, it is necessary to take the time-increment Δt into account as well. The time-step size is de-dimensionalised by relating it to the characteristic deformation-time t_{cd} , defined according to equation 4.5.

$$t_{\text{cd}} = \frac{r_{\text{R}}}{c_{\text{solid}}} \quad (4.5)$$

The characteristic deformation-time t_{cd} calculates from the typical problem length and the sonic velocity of the solid material. For the characteristic problem length, the rolling element radius r_R is used. The reference bearing for the case, described in section 4.2, is a 6205 deep groove rolling bearing. Table 4.1 lists all geometric information for the calculations. The sonic velocity c_{solid} for rolling bearing materials, listed in table 4.2, calculates to 5170 m s^{-1} using equation 4.6.

$$c_{solid} = \frac{E}{\rho} \quad (4.6)$$

Apart from the time-dependency, the calculation also depends on the actual deformation of the system $D_{max} - D_{min}$. Although equation 4.4 considers several effects, Hartinger et al. [32] and Hajishafiee et al. [33] propose a relaxation factor R_{ref} for adaptation, depending on the problem definition. Ideally the relaxation is close to one⁴.

The adjustment is embedded in the new time-increment procedure before entering the next iterative FSI cycle. Since the change in height is minimal, an initial h which leads to a load far below the target load, results in high computational expenses. Therefore, a prediction for h via equation 2.60 is helpful to start the calculations close enough to the actual result to spare time. If h_0 is chosen too large, a possible problem was the susceptibility to vibration between height change and simulated force response. If the initial guess is too small, there may be problems with the grid. Both issues are relevant later.

Schwartz Domain Decomposition Figure 4.7 shows that the only variable passed through directly from the solid to the fluid domain, and vice versa, is the temperature T . It is apparent that the transition between fluid and solid domain needs handling. The Schwartz Domain Decomposition (SDD) method is used to realize the coupling at the FSI interface, based on the work by Schwarz [119, pp.133-143].

The temperature distribution is calculated in both domains $\mathcal{T} = \mathcal{S} \cup \mathcal{F}$. The SDD is applied to the interface $\Gamma_{FSI} = \partial\mathcal{F} \cap \mathcal{S}$. The SDD combines a Neumann (fixed temperature T) and a Dirichlet (fixed heat flux q) boundary condition. The method is divided into two steps which are both performed per FSI iteration k . Thereby, the Temperature or heat flux is calculated at one domain boundary and written on the other. Equation 4.7 shows the workflow of the decomposition at the boundary for a single FSI sub-iteration.

$$\begin{aligned} \text{STEP1 :} \\ \lambda_1 \cdot T_{\mathcal{F}}^k + (1 - \lambda_1) \cdot q_{\mathcal{F}}^k &= \lambda_1 \cdot T_{\mathcal{S}}^{k-1} + (1 - \lambda_1) \cdot q_{\mathcal{S}}^{k-1} \\ \text{STEP2 :} \\ \lambda_2 \cdot T_{\mathcal{S}}^k + (1 - \lambda_2) \cdot q_{\mathcal{S}}^k &= \lambda_2 \cdot T_{\mathcal{F}}^k + (1 - \lambda_2) \cdot q_{\mathcal{F}}^k \end{aligned} \quad (4.7)$$

⁴In this context it is important to note that the values mentioned by Hartinger et al. [32], [34] and Hajishafiee et al. [33] differ significantly from those estimated for the present calculations. An evaluation for reference cases and those for distorted surfaces later on did not allow any conclusion if there is a systematic influence which is still unconsidered.

λ_1 and λ_2 are binary constants with a possible value of one or zero. Depending on how λ_1 and λ_2 values are set, four different versions of the SDD exist to exchange thermal information. Typically a Neumann-Dirichlet combination is imposed in two steps according to equation 4.7. Thereby λ_1 is set to one, and λ_2 is set to zero. This way, the heat flux calculated for the fluid side of the FSI interface is used as a boundary condition for the solid side. Accordingly, the temperature distribution at the solid side is imposed as the boundary condition on the fluid side during its next calculation. While also different combinations are possible like $\lambda_{1,2} = 1$ or $\lambda_{1,2} = 0$ the Neumann-Dirichlet combination is used in the following.

With respect to figure 4.5 and 4.7, the corresponding functions are `updateTemperature()` and `updateHeatFlux()`, which collect the interface information by calling the `getTemperature()/getHeatFlux()`-function from one solver and overrides the boundary information with the `setTemperature()/setHeatFlux()`-function of the other. Due to this implementation, any combination of λ_1 and λ_2 is available in the framework. In this way, a flexible application of the SDD should also be made possible for future research.

It is usually necessary to iterate the SDD method within for convergence and thus solve the domains temperature fields multiple times. For the EHL calculation, this is not needed since the time-steps are small compared to the determined thermodynamic time-constant ⁵, so a calculation alongside the FSI cycle has proven to be sufficient.

Now that the general calculation procedure and parameter handling between the blocks in figure 4.7 is outlined, the sub-routines for fluid-solid- and electrostatic solver are detailed next. It should be pointed out again that in the actual implementation, different solvers are available for each domain. However, only those used in this work are discussed.

⁵See paragraph 4.2 for details.

4.1.4. Fluid Solver

The sub-routine block (5) from figure 4.7 is unfolded in figure 4.9 and displays the flowchart diagram for the fluid solver.

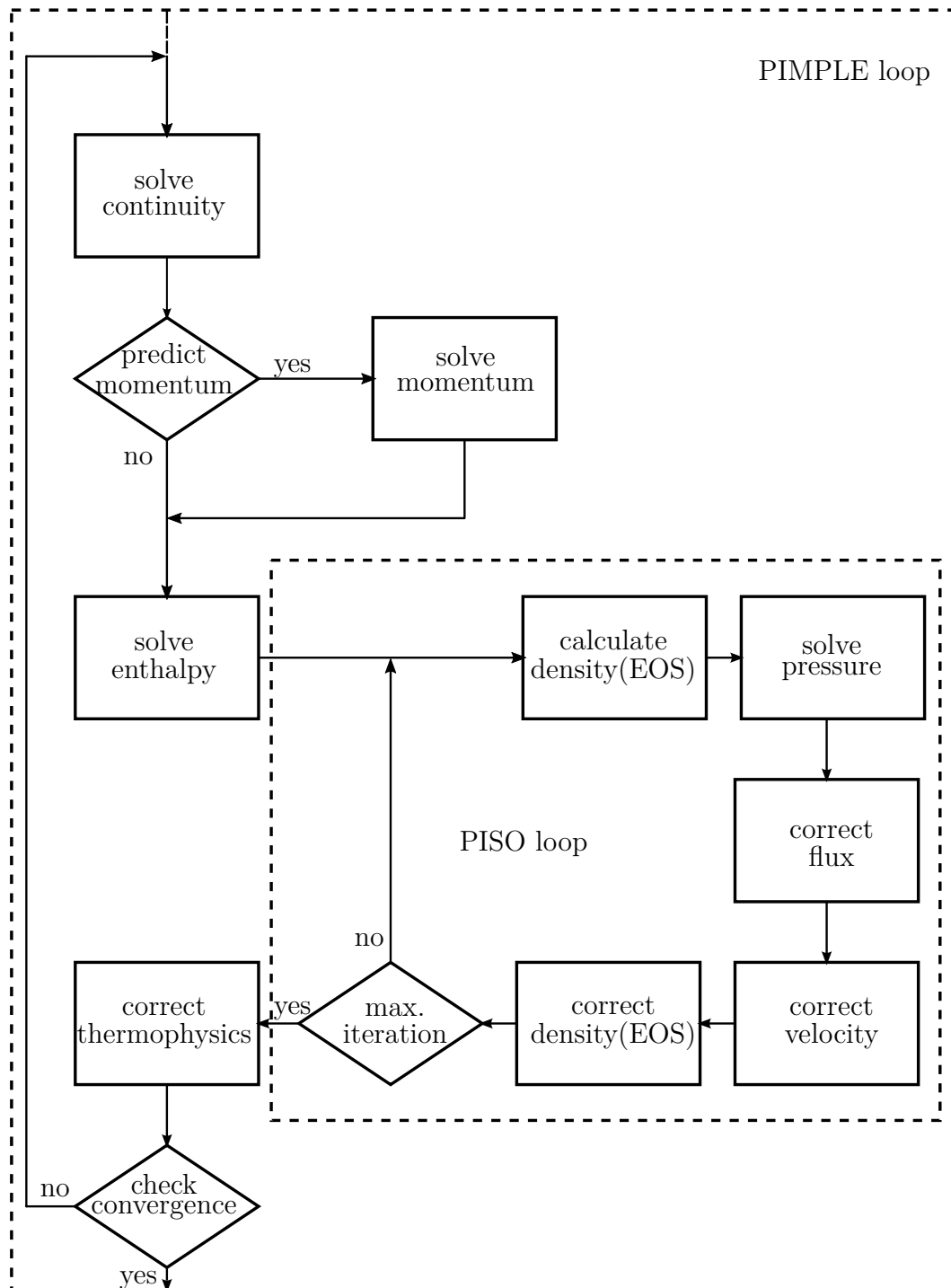


Figure 4.9.: Flowchart representation of the *pmdRelease* fluid solver

The fluid solver calculates the lubricants impulse and thus the velocity and pressure fields. In addition, it accounts for compressibility, temperature distribution, and realistic lubricant rheology, as specified in the fundamentals in section 2.3.

The pre-implemented Pressure Implicit with Splitting of Operators (PISO) algorithm does not meet these requirements, so another solver is necessary. Therefore, all fluid domain data in this work are calculated with a compressible, transient solver called "rhoPIMPLE." The term "PIMPLE" is not an acronym like PISO but a neologism to illustrate that it merges the PISO and Semi-Implicit Method for Pressure-Linked Equations (SIMPLE) algorithm. The initial version of the solver was developed and implemented to OpenFOAM by Patankar [120]. The prefix "rho" emphasizes that the algorithm uses a compressible calculation. The differential equations for the lubricant described in section 2.3 are found in the algorithm, as figure 4.9 shows schematically. The actual implementation, specifically the evolve function containing the rhoPIMPLE algorithm is added in appendix E.2. It consists of a predictor (PIMPLE loop) and corrector (PISO loop) step. Predictor-corrector methods are characterized by high calculation speed and a stable convergent rate, according to Ferziger et al. [67, p.193], and therefore often the first choice if no experience is present for approaching a problem. To better understand the procedure, it is helpful to decompose the variables involved. The lubricant velocity \mathbf{u} , pressure p , density ρ , and mass flux \dot{m} are spit into predictor values (*) and correction values ('), respectively. Equation 4.8 lists the decomposition for mentioned variables.

$$\begin{aligned}\mathbf{u} &= \mathbf{u}^* + \mathbf{u}' \\ p &= p^n + p' \\ \rho &= \rho^* + \rho' \\ \dot{m} &= \dot{m}^* + \dot{m}'\end{aligned}\tag{4.8}$$

The superscript n instead of (*) for the pressure indicates that the current value is based on a correction from the previous iteration since the PISO corrector step is executed multiple times. The enthalpy h_e is not listed here, because does not participate in the predictor corrector procedure.

Returning to the diagram illustrated in figure 4.9, the outer loop starts by determining the mass flux \dot{m} (via equation 2.23) first. Optionally, a predictive value for the velocity \mathbf{u}^* (via equation 2.24) is evaluated before the enthalpy h^{n+1} (equation 2.26) is calculated based on the intermediate variables available. So the calculation utilizes either a solution from the last time-step or the previous iterative result.

The predictive solution for the velocity does not yet satisfy the conservation of mass, as can be proven by inserting it into the discrete continuity equation, which is why this step is called predictor. To reach flux consistency, the velocity solution $\mathbf{u} = \mathbf{u}^* + \mathbf{u}'$ is corrected to establish the conservativeness of the solution. The velocity correction value \mathbf{u}' is calculated with the pressure corrector p' .

The pressure correction is calculated during the PISO sub-iteration. Therefore, the solver calculates the density ρ with one of the EoS introduced in section 2.3.4. Then, the pressure p' is computed. A correction equation is required for this, which has to be

obtained from the fundamental equations. As a starting point for the pressure correction, the discretised compressible continuity equation is taken, according to equation 4.9.

$$\frac{\rho^* + \rho'}{\Delta t} \cdot V + \Sigma(\dot{m}) = 0 \quad (4.9)$$

It displays the change in mass inside a control volume V according to the mass flux \dot{m} entering and leaving through the control volume's surface. However, these fluxes are much more complicated than the incompressible continuity because of the density and velocity decomposition. Equation 4.10 shows this circumstance.

$$\begin{aligned} \dot{m} &= (\rho^* + \rho')(\mathbf{u}^* + \mathbf{u}') \cdot S \\ &= \underbrace{\rho^* \mathbf{u}^* \cdot S}_{\dot{m}^*} + \underbrace{\rho^* \mathbf{u}' \cdot S + \rho' \mathbf{u}^* \cdot S + \rho' \mathbf{u}' \cdot S}_{\dot{m}'} \end{aligned} \quad (4.10)$$

The second-order correction $\rho' u'_i$ is dropped as it decreases much faster during the correction sub-iteration than the other terms, that contain a correction value. Providing a Rhie-Chow interpolation for the velocities \mathbf{u}^* and \mathbf{u}' ultimately leads to the discretised pressure correction equation.

$$\frac{V}{\Delta t} K p' + \Sigma K \left(\frac{\dot{m}^*}{\rho^*} \right) p' - \Sigma \rho^* D \left(\frac{\partial p'}{\partial x_i} \right) \cdot S = - \frac{\rho^*}{\Delta t} \cdot V - \Sigma \dot{m}^* \quad (4.11)$$

With the help of the compression modulus K and the diffusion constant D , equation 4.11 was adjusted, so that the pressure correction p' now is calculable. A detailed derivation of equation 4.11 is not provided here, as the predictor-corrector procedure for compressible fluid flow calculation is a CFD standard solver. An in-depth and easy-to-follow derivation is given by Moukalled et al. [61, pp.660-663]. The actual implementation utilizes the compressibility, derived from the EoS. The derivations for the Tait and Mur-naghan equations are added in appendix B for completeness.

Next, the pressure correction p' is calculated, and surface fluxes, velocity, and density are corrected. This correction procedure is sub-cycled for better convergence and increased stability. While the number of corrector iterations is usually less relevant for the overall computation time in CFD, it is impactful for FSI numerics. The calculation time increases considerably for more corrector iterations, because the number of iterations multiplies with each outer correction and each enclosing FSI iteration per time-step.

Particular attention should be drawn to the density calculation inside the corrector loop, where the implemented models from section 2.3.4 come into play via a call to the thermophysical properties library. Since the momentum equation is not calculated until the next iteration, the viscosity is only corrected once after the corrector step as part of the overall corrections for every variable modelled through the library, summarised as "correct thermophysics." In addition, thermal conductivity is adjusted at this point, depending on the new pressure and temperature. While the corrector is executed a fixed number of times, the overall predictor-corrector loop is left based on convergence criteria for pressure, enthalpy, and velocity.

The iteration is terminated if the residuals have dropped below the target threshold. Otherwise, the whole loop is repeated until the termination conditions are met, or a maximum number of iterations is exceeded. Especially during the start of an FSI calculation, it happens that the fluid solution does not drop below the convergence criteria. The reason for this is the time-dependent development of the fields within the domain until the stationary solution is established. Results from this section of the simulation are not wrong per se, but they represent a start-up behaviour that is not relevant for the further analyses. To avoid endless iterations, the number of runs of the fluid solver is therefore limited.

4.1.5. Solid Solver

Compared to the fluid flowchart, the solid chart, which figure 4.10 shows, is more simplistic and straightforward. Figure 4.10 represents the sub-routine (7) from figure 4.7. The calculation consists of two parts, which are iterated to convergence sequentially. The first iterative procedure calculates the temperature distribution in the solid according to Fourier's Law (equation 2.53), and the second one calculates the deformation \mathbf{D} .

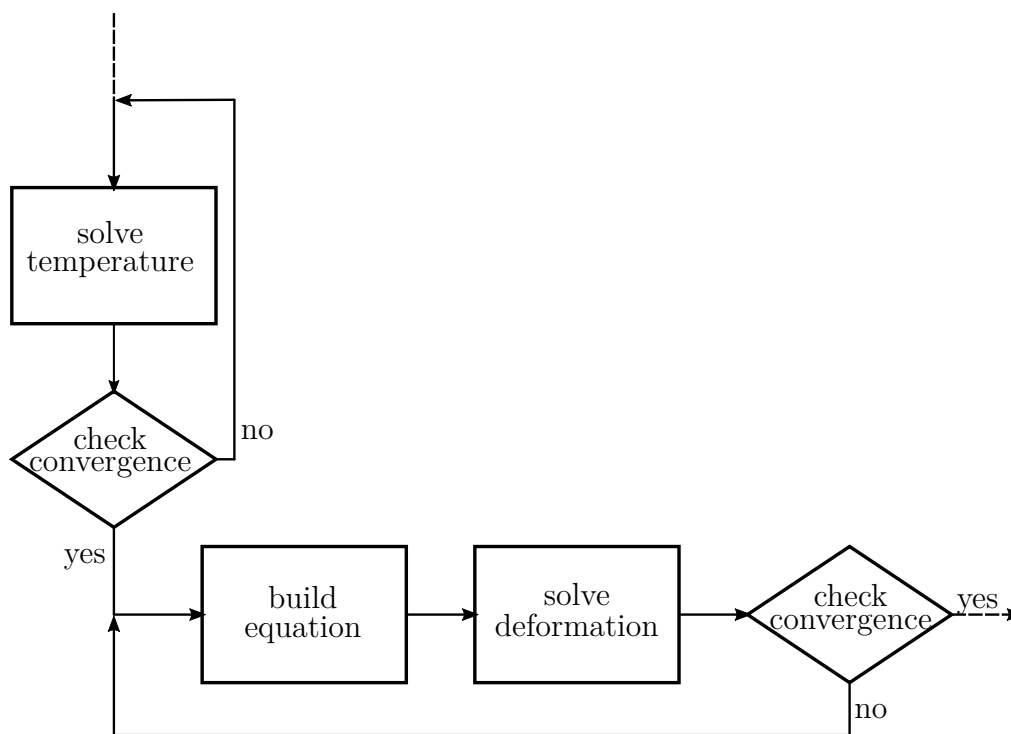


Figure 4.10.: Flowchart representation of the *temperatureuntotalLagrangian* solid solver

The used solver is equivalent to the *untotalLagrangian* implementation described by Tukovic et al. [42], which is based on the work by Demirdzic et al. [93], [94]⁶. How-

⁶At this point, it should be pointed out once again that the solution procedure is also a finite volume

ever, a preliminary temperature calculation was added, since the problem to be solved requires knowledge of the thermal evolution in the solid. Basically, the differential equations from section 2.4 are discretised directly and solved regarding the target variables displacement \mathbf{D} and temperature T . However, there is the possibility to add multiple terms for the calculation of displacement. For example, thermal stresses and non-linear material behaviour can be taken into account. For this reason it should be pointed out, that especially thermal stresses and non-linear materials were disabled in the modified *temperatureunstoalLagrangian* solid solver, which is used for the following calculations. Thermal stresses are of subordinate relevance for the calculation since pressure-induced stresses exceed these by orders of magnitude in EHL. Similar applies for the opposite direction. The total deformation does not exceed elastic deformation so that heat dissipation through plasticity is irrelevant. The source code for the *temperatureunstoalLagrangian* solver associated with figure 4.10 is provided in appendix E.3.

4.1.6. Electrostatics Solver

Finally, the electrostatics solver is described, which is responsible for the calculation of charge distributions and the resulting electric field. Figure 4.11 shows the implementation.

Preliminary to the iterative solution procedure, the relative permittivity is updated with the modified Clausius-Mosotti equation 2.70 so that local changes due to pressure and temperature are taken into account. Afterwards, the fluid flux is read because it is needed to calculate the convective part of the charge transport.

There are two versions of the electrostatic field calculation implemented. The simple Lagrange solver solely calculates the electric field based on the applied potential (voltage difference) and the relative permittivity. Charge carrying species and thus a charge density within lubricant is not considered. The electric field is derived from the solution to the potential differential equation, since the electric field is its gradient. The calculation follows differential equations 2.64 and 2.63. The blocks for reading the fluid fluxes and solving the charge transport are dropped for this solver. The source code for this solver is provided in appendix E.4.

The second, more complex solver incorporates the presence of charged species inside the oil. The complexity arises from the convective and diffusive motion those charges perform due to the mentioned fluid flux and gradients in the electric field. Since the fluid only imposes a motion on the charged species but is not affected, since phenomena like electro-osmotic flows are negligible, the fluid and electrostatic calculations are linked weakly. The convective part along the electric field gradient, however, is bidirectional. While charged species are subject to a force exerted by the electric field, their presence also impacts the electric field strongly. Therefore, the differential equation for charged species transport 2.66 and electric potential 2.64/2.63 are solved iteratively until both reach convergence. The source code for this more complex solver is provided in appendix

approach which is fundamentally different from an Finite Element Method (FEM). Works that have already successfully used this approach in OpenFOAM are for example [37], [95], [121] and [122]

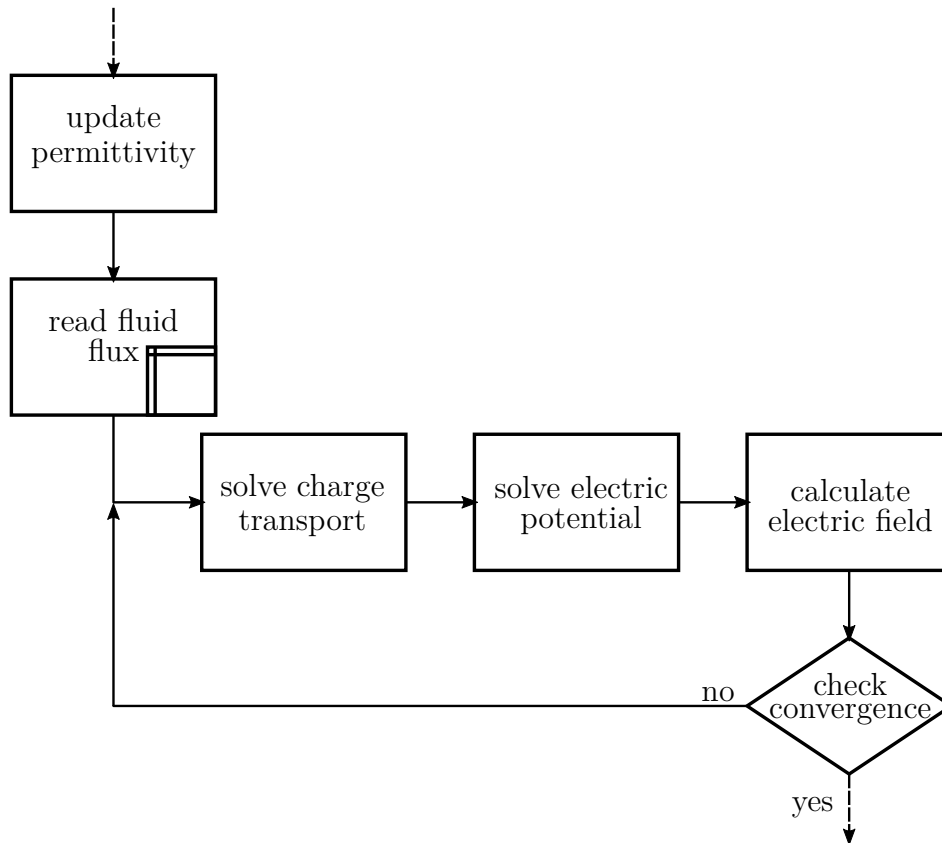


Figure 4.11.: Flowchart representation of the *ionicChargeSolver* solver combining charge transport (PNP solver) and electric field calculation (Laplace solver)

E.5.

This more complex calculation procedure is introduced in anticipation of future research towards electric damaging mechanisms and is applied later in some simple examples. In section 5.5.2, the charge density transport is used to interpret some remarkable phenomena observed during discharge experiments of another research project by Harder et al. [123].

4.2. Calculation Setup

In this second part of chapter 4, the ball bearing system from section 2.1 is set up as a numerical reference case for calculation, using the framework which was just presented. Setting up a reference case is a delicate task, and numerous aspects need consideration. The explanations start with a discussion of temporal resolution, since this is of significant importance to numerical EHL calculations. Afterwards, the reduced, two-dimensional geometry is derived from the real rolling bearing point contact, and the grid strategy is explained. Then, discretization schemes and solution procedures for the discretised systems are stated. All necessary boundary conditions are also identified and explained.

This section and the whole of chapter 4 close with explanatory notes on the used model parameters, especially for viscosity and density. Whenever possible, used parameters are set into perspective to other numerical approaches known from the literature.

Time Resolution EHL calculations are resource-demanding due to a high grid resolution in the tribological contact, and a problem that develops across scales. Latter refers to the transition towards the EHL region, called inlet, and away from the EHL region towards the surrounding lubricant, called outlet. The extent becomes clear, looking at figure 4.13. While the overall fluid domain height Y is in the range of 1 – 10 mm, the EHL lubrication film h is $< 0.2 \mu\text{m}$. Both, inlet and outlet are assumed to partially determine the quantities of interest, as Schirra [15] elaborated. High-resolved numerical meshes always need a temporal resolution corresponding to the maximum occurring flow velocities. The relationship between temporal resolution and cell size of a grid is described via the prevailing flow velocity using the Courant-Friedrichs-Lewy (CFL) number, according to equation 4.12.

$$\text{CFL} = \frac{u \cdot \Delta t}{\Delta x} \quad (4.12)$$

Detailed information on the CFL number and its implications is found in every CFD numerics textbook, like Ferziger et al. [67, p.271]. The CFL number describes how the grid resolution captures the convective transport of information through the calculation domain. The distance travelled because of the velocity \mathbf{u} per time-step Δt must not exceed the cell length Δx in that direction. Otherwise, information skips a cell, and numerical errors, like checkerboarding, might occur. Typically, the CFL number is differentiated for the coordinate directions.

Especially the pressure correction, equation 4.11, is susceptible to such errors. Therefore, CFL numbers are calculated locally from the mentioned quantities and should stay below 1 for the whole calculation domain. While some algorithms can correctly operate with CFL numbers exceeding 1, it usually aims for maximum values of less than 0.7. Equation 4.13 rearranges equation 4.12 for a CFL number of 0.7, directly indicating a maximum Δt , which ensures numerical stability.

$$\Delta t_{\mathcal{G}} = \frac{0.7 \cdot \Delta x}{u} \quad (4.13)$$

Anticipating the information from paragraphs *Grid Strategy* and *Parametrisation*, equation 4.13 yields a Δt for the fluid domain between $1 \cdot 10^{-7}$ and $1 \cdot 10^{-9}$, based on the grid resolutions and surface velocities. Information on the grid resolution is stated in table 4.3.

Comparable limitations also prevail for the solid domain. Here, aliasing during a transient calculation is the concerning effect to prevent. Analogue to the fluid region, the solid's sonic velocity u_s , and the grid resolution determine the maximum time-step Δt_s , according to Melcher et al. [101, p.26]. In equation 4.14, the sonic velocity u_s is already replaced by a definition via the Lamé constants, introduced in equations 2.48 and 2.49b

earlier.

$$\Delta t_s = \frac{\Delta x}{\sqrt{\frac{\lambda_s + 2\mu_s}{\rho_s}}} \quad (4.14)$$

The density and Young's modulus are chosen according to table 4.2. Thus, the time-step Δt results in $1.5 \cdot 10^{-10}$ s, for explicitly calculating the transversal sound propagation in the solid.

It is also possible to define a time-step for the thermodynamic domain. Equation 4.15 shows the time-step calculation for the solid domain.

$$\Delta t_{\mathcal{T}} = \frac{\Delta x}{\frac{k_s}{c_s \cdot \rho_s}} \quad (4.15)$$

The maximum time-step $\Delta t_{\mathcal{T}}$ is calculated with the solids' specific heat capacity c_s , thermal conductivity a_s and the solids density ρ_s . Only the solid thermodynamic time-step is needed. The reason is that the thermal evolution in the solid is independent of the deformation and thus decoupled. For the fluid domain, the convective contribution to the temperature change is dominant, and so it coincides with the time-step already determined via the CFL number. However, the time-step for heat conduction (diffusive transport) is in the same order of magnitude for solid and fluid. The values from table 4.2 results in a time-step of > 1 s, indicating that the thermodynamic domain is not a factor for temporal calculation stability.

Figure 4.12 illustrates the relevant time-steps.

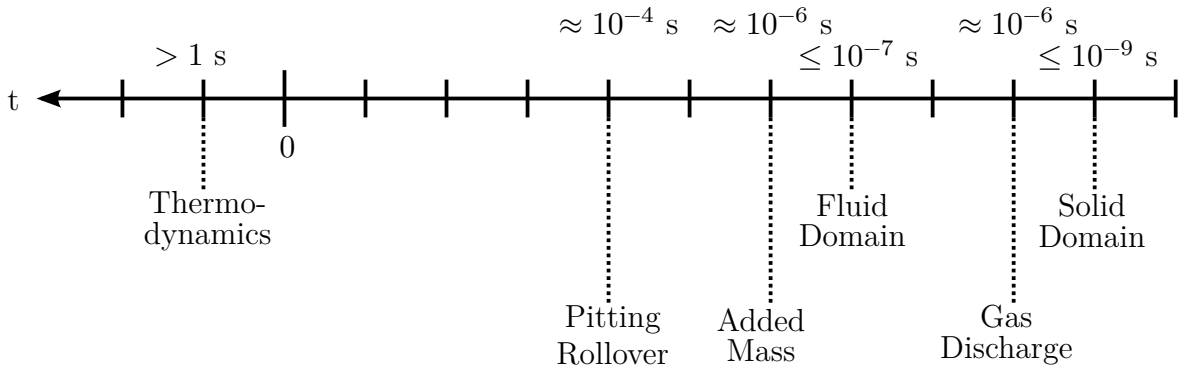


Figure 4.12.: Visualisation of the maximum time-steps for the individual domains

In addition, the characteristic time for pitting rollover and gas discharges are added for comparison and indication for future research. The added mass effect, discussed in paragraph 2.2 is shown. In the fundamentals, a quasi-static definition for calculating electric fields was assumed. Now that the actual geometry is discussed and necessary temporal resolutions are related, a justification for this is finally provided.

Contrary to a dynamic calculation, a static approach does not resolve the propagation of electromagnetic waves inside an area of interest. The limiting time increment Δt from which wave propagation processes are resolved can roughly be estimated using the wave

propagation speed for electromagnetic waves over a characteristic distance, according to Melcher et al. [101, p.26]. Equation 4.16 illustrates the characteristic time-increment.

$$\Delta t_{\mathcal{E}} = \frac{h}{u_c} \quad (4.16)$$

The lubrication film thickness h is used as reference distance, while the electromagnetic propagation velocity $u_c = \sqrt{(\epsilon \cdot \mu)^{-1}}$ in the lubricant represents the problem-specific velocity. Latter is defined via the media-specific permittivity ϵ and permeability μ . Inserting values in the typical range for polymeric lubricants result in a characteristic time of less than $1 \cdot 10^{-14}$ s, which falls below the target calculation times for the fluid, solid and thermodynamic domains by six orders of magnitude. Simply put, the simulation does not capture dynamic changes in the electric field, and it is assumed at all times that wave propagation processes have entirely decayed. However, this fact does not flaw the two-way interaction of electric field and charge carrying species, according to Melcher et al. [101, p.22].

Calculation Geometry Calculating EHL contacts has proven to be very resource-demanding throughout literature, so reducing the calculation geometry is imperative. The same goes for this work, so that the Ball Bearing contact, presented in section 2.1, is reduced from three to two dimensions. Similar to most of the works known from the literature, like Hartinger et al. [32] or Almqvist et al. [31], the elliptical point contact is only calculated for its centreline, as indicated in figure 2.5 by the red outer line. This reduction is an immense saving due to the high resolution that must be achieved in the contact zone. Furthermore, recalling figure 2.3b, two elliptical contacts exist per rolling element. The ring surfaces are considered flat for simplicity since the raceway radii are significantly bigger than the rolling element radius. Therefore, the inner and outer tribological contact are identical and carry the same load, as they are connected in series regarding the force flow of the bearing. Figure 4.13 displays the two-dimensional calculation domain resulting from these reductions.

The resulting structure of the whole domain Ω corresponds to known approaches like Hartinger et al. [32], Hajishiafee et al. [33], and Almqvist et al. [30]. Singh et al. [97] lately introduced a smaller calculation domain that only covers the area close to the EHL region, indicated by the thin dotted lines. The domain is split into the solid subdomain \mathcal{S} and the fluid \mathcal{F} , which coincide with the electrical subdomain \mathcal{E} , respectively. The thermal \mathcal{T} domain covers the whole calculation region and needs to hand over information at the interfaces Γ_{FSI} and Γ_{Raceway} .

The Γ_{FSI} surface represents the fluid-structure interface with its FSI typical boundary conditions, as discussed in section 4.1.3. The solid rings domain is rigid according to literature and the reduced Hertzian contact model. It is discretised and modelled because of its temperature evolution and thus contribution to the overall thermal balance.

To realize the FSI calculation, three coupling conditions are needed, according to Richter [57, pp.80-83]. Although the coupling conditions have already been introduced in section 2.2, they will be discussed here with reference to the actual calculation geometry. First,

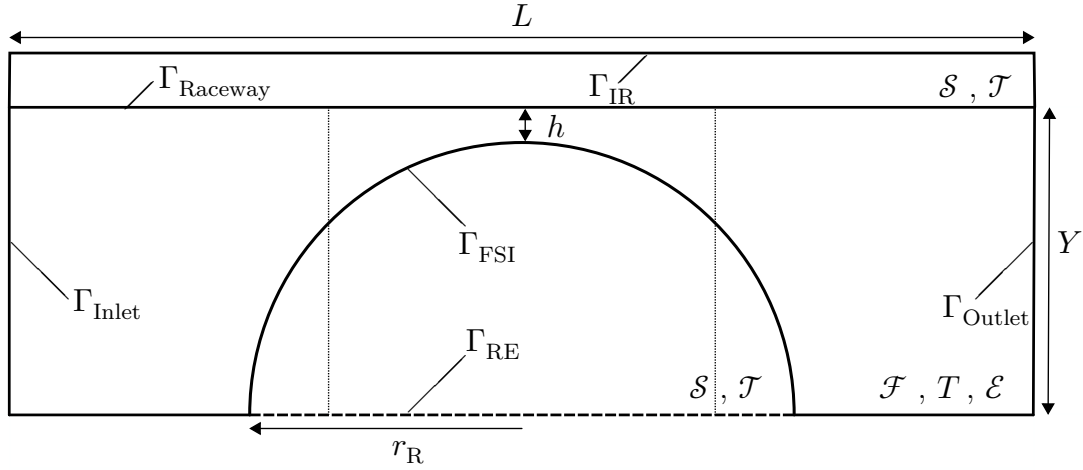


Figure 4.13.: Two-dimensional point/line contact representation for EHL rolling bearing numerics

there is a kinematic coupling between the solid and fluid domain, which enforces equal velocities. Equation 4.17 tells that the fluid moves at a velocity $\mathbf{u}_{\mathcal{F}}$ always matches the solid's velocity $\mathbf{u}_{\mathcal{S}}$ during the whole calculation at all points \mathbf{x} along the mutual interface Γ_{FSI} .

$$\mathbf{u}_{\mathcal{F}}(\mathbf{x}, t) = \mathbf{u}_{\mathcal{S}}(\mathbf{x}, t) \text{ at } \Gamma(t)_{\text{FSI}} \quad (4.17)$$

Besides the kinematic condition, there is also an equilibrium of forces at the mutual interface. This dynamic condition states that the stresses $\boldsymbol{\tau}$ exerted by the fluid equal those present in the solid region. This circumstance is taken into account by using the fluid stress tensor $\boldsymbol{\tau}$ as a boundary condition to calculate solid elastic deformations \mathbf{D} . Equation 4.18 represents this equilibrium.

$$\mathbf{n}_{\mathcal{F}}\boldsymbol{\tau}_{\mathcal{F}} = \mathbf{n}_{\mathcal{S}}\boldsymbol{\tau}_{\mathcal{S}} \text{ at } \Gamma(t)_{\text{FSI}} \quad (4.18)$$

The condition also implies geometric coupling, which is the third condition. It states that the solid subdomains \mathcal{S} do not detach from the fluid subdomain \mathcal{F} and also do not overlap with them. The same goes for the thermal and electric sub-domains, respectively. This statement is expressible for numerical purposes as an equivalence of the normal vectors for each face according to equation 4.19.

$$\mathbf{n}_{\mathcal{F}} = -\mathbf{n}_{\mathcal{S}} \quad (4.19)$$

The fluid domain follows the solid deformation to keep the interface in touch. The implementation of this follow-up movement has already been explained in paragraph 4.1.3 based on figure 4.7.

Geometrical dimensions for published EHL calculations by Hajishiafee et al. [33] and Almqvist et al.[30], both using an analogue case geometry as shown here, are listed in table 4.1. Additionally, parameters for an realistic rolling bearing used for the experiments described in section 5.4.2 are added for comparison. It quickly becomes clear that the geometry deviates from established calculation setups. As a result, much higher

Table 4.1.: Parameters for the two-dimensional numerical case by Almqvist [30] and Hajishiafee [33] compared to the present work

Case Parameters					
Parameter	Variable	Unit	Value		
			Almqvist	Hajishiafee	present
Radius	r_R	mm	10	10	3.96
Length	L	mm	-	120	40
Lubrication film thickness	h	μm	-	0.1	0.1 – 1
Entrainment velocity	u_e	m s^{-1}	0.5	2.5	1 – 2.5
Target load	Q	kN m^{-1}	100 – 150	10 – 450	10 – 100
Slide-to-roll ratio	SRR	-	0 – 0.5	0.4 – 2	2
Dim.-less velocity	\bar{U}	-	$9 \cdot 10^{-12}$	$0.006 - 1.1 \cdot 10^{-9}$	$0.1 - 3.9 \cdot 10^{-9}$
Dim.-less load	\bar{W}	-	-	$0.09 - 2.7 \cdot 10^{-4}$	$2.76 - 16.5 \cdot 10^{-4}$
Dim.-less material	\bar{G}	-	-	$3.9 - 14 \cdot 10^3$	$0.23 - 13.8 \cdot 10^3$

fluid pressures and solid deformations are to be expected. The geometrical information provided in standard papers does not correspond to any bearing geometry.

Typically the radii of rolling elements for two-dimensional line contact calculations in numerical simulations is 10 mm, which differs significantly from the 3.96 mm radius of the 6205-C3 bearings used by Martin [124]. A diameter of 10 mm does not apply to any standard bearing and should be considered of academic nature. However, the smaller radius causes some problems for the calculation, as seen later. For a better comparison between the listed approaches, the dimensionless velocity, load, and material parameters are also listed since those values allow a comparison between the publications, despite different geometries, materials, and speeds.

The calculations are carried out in two dimensions, as presented in figure 4.13, leading to an infinite line contact approximation. Therefore, the forces calculated for the geometry are per unit depth kN m^{-1} . Since CFD methods in OpenFOAM are volume-based, there is no actual two-dimensional calculation. The workaround used in CFD reduces the number of cells in the third dimension to one and leaves the boundary conditions for this direction empty. Therefore a two-dimensional calculation is realized. The actual load is calculated by multiplying the force per meter by the cell's length in the empty direction, typically from 1 mm to 1 μm . Unfortunately, the size for which the calculations were performed is not always stated in the literature to recalculate the real force for easier comparison. So that the force per metre is stated throughout this work, as in table 4.1, the other characteristic geometric dimensions are those listed in table 4.1. Accordingly, the material parameters from table 4.2 are taken for the calculation.

Parametrisation Aside the geometrical quantities, the used materials also play a crucial role in EHL calculations. Table 4.2 lists those for comparison across mentioned publications and the values used for this work. In contrast to the geometrical parameters,

Table 4.2.: Material parameters for the two-dimensional numerical case by Almqvist [30] and Hajishafiee [33] compared to the present work

Material Parameters					
Parameter	Variable	Unit	Value		
			Almqvist	Hajishafiee	present
Density	$\rho_{\mathcal{F}}$	kg m^{-3}	870	850	$865(313K)^{[125]}$
Viscosity	η	$\text{g m}^{-1} \text{s}^{-1}$	40	76	$77.5^{[125]}$
Heat capacity lubricant	$c_{\mathcal{F}}$	$\text{m}^2 \text{s}^{-2} \text{K}^{-1}$	2190	2300	$2480^{[125]}$
Thermal conduc- tivity	$\kappa_{\mathcal{F}}$	$\text{kg m s}^{-3} \text{K}^{-1}$	-	0.15	$0.138^{[125]}$
Density	$\rho_{\mathcal{S}}$	kg m^{-3}	7800	7850	7850
Young's modulus	E	$\text{kg m}^{-1} \text{s}^{-2}$	$2 \cdot 10^{11}$	-	$2.1 \cdot 10^{11}$
Poisson ratio	ν	-	-	-	0.3
Reduced Young's modulus	E'	$\text{kg m}^{-1} \text{s}^{-2}$	-	$3.45 \cdot 10^{11}$	$2.3 \cdot 10^{11}$
Heat capacity solid	$c_{\mathcal{S}}$	$\text{m}^2 \text{s}^{-2} \text{K}^{-1}$	-	-	464
Thermal conduc- tivity	$\kappa_{\mathcal{S}}$	$\text{kg m s}^{-3} \text{K}^{-1}$	45	47	42

material quantities match more closely and correspond to realistic data, also for reference publications. The most significant difference can be found in the reduced Young's modulus, which is attributable to diverging definitions on calculating this value.

Due to the different approaches, not every parameter is found in the literature. Especially the actual Young's modulus and the Poisson ratio are rarely stated, so only the reduced Young's modulus is mentioned, which is problematic due to the diverging definitions. Lubricant properties for the present work are taken from Schuler [125] and correspond to the properties of the FVA 3 reference oil. This lubricant was used for the experiments by Martin et al. [126] and the hybrid bearing tests.

Grid Strategy The success of a numerical simulation heavily depends on the grid quality, so this topic will now be discussed.

The overall calculation region from figure 4.13 is split into two grids, shown in figure 4.14.

For simplicity, it is always referred to as the solid grid (4.14a) and the fluid grid (4.14b), although the electrostatic calculations, for example, are performed on the fluid grid.

The solid grid consists of two discontinuous grids, one for the inner ring and one for the

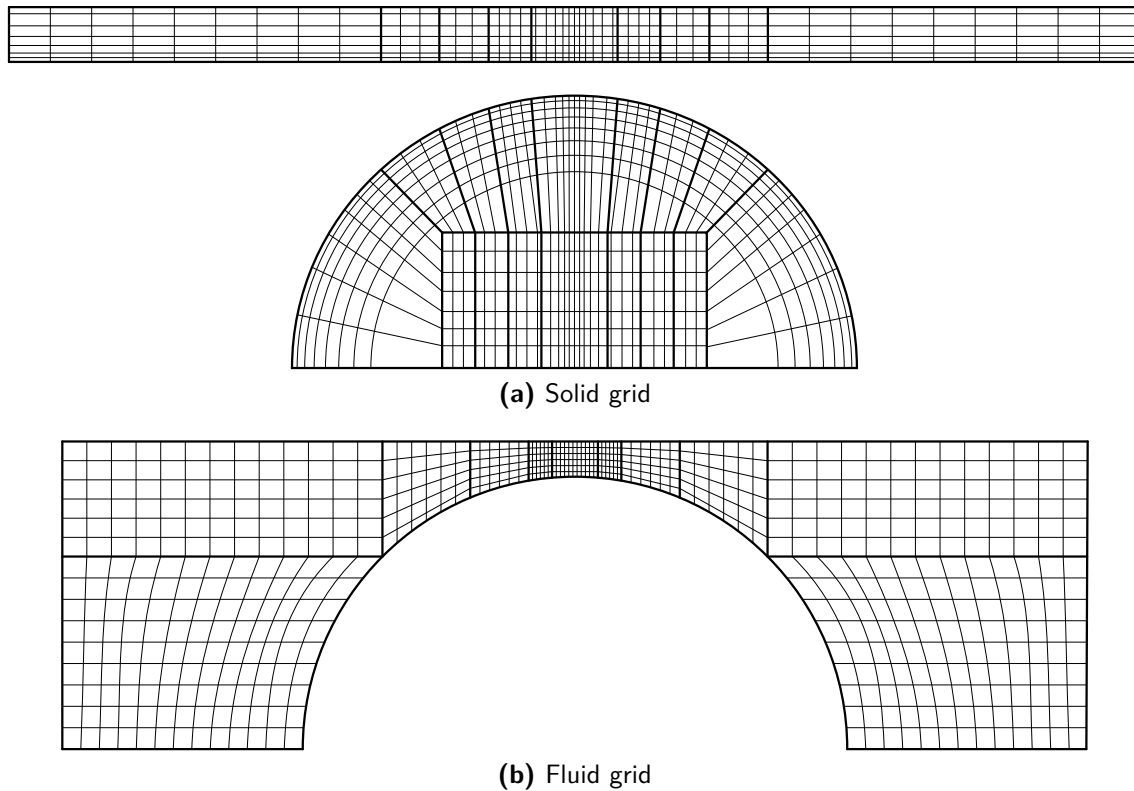


Figure 4.14.: Schematic grid designs; Reduced presentation

rolling element half circle. While the inner ring grid has a reasonably coarse approximation with a grading towards the EHL region to capture temperature changes, the rolling element grid is finer and related to the fluid grid discretization. The resolution along the rolling element perimeter equals that of the fluids grid, precisely to approximate any deformation of the imposed fluid forces. This measure is necessary to avoid instabilities in the FSI calculation examined by Feldermann et al. [127, p.8]. They encountered that a drop in resolution along the perimeter of a factor of two or more against the fluid grid resolution leads to oscillations in the FSI coupling.

A cause for failure in Finite Volume Method (FVM) based calculations is a high cell non-orthogonality. Typically, meshes are checked before the start of a calculation to ensure that no cell has non-orthogonal surfaces exceeding 70 degrees. In FSI, the solid and fluid mesh is distorted throughout the calculation so that the initial mesh quality needs to be very high to tolerate changes in the non-orthogonality. High aspect ratios are a driving factor for mesh non orthogonality in dynamic meshes. Figure 4.15 shows how a cell with a high aspect ratio (4.15b) is more prone to the same distortion than the low aspect ratio cells (4.15a).

The goal is to prevent the individual cells from high non-orthogonality during the calculation. Therefore, the single cells must have a nearly square geometry, especially near the surface and the EHL zone. The goal of discretization and grading is to ensure an aspect ratio close to one. Thus, the perimeter resolution also determines the radial

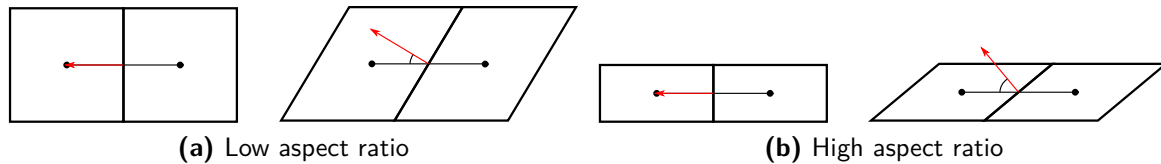


Figure 4.15.: Visualization of severity of cell non-orthogonality due to distortion

resolution partially. The solid grid is graded towards the EHL region and in a radial direction towards the surface. This objective of a low aspect ratio also holds for the fluid grid discretization.

The fluid grid is oriented on the block structure that Hajishiafee et al. [33] and others introduced. Here the domain gets steadily finer towards the EHL region. Hajishiafee [128, p.55] aimed for an aspect ratio of less than five for the whole fluid grid. The blocks are parametrized, as figure 4.16 shows.

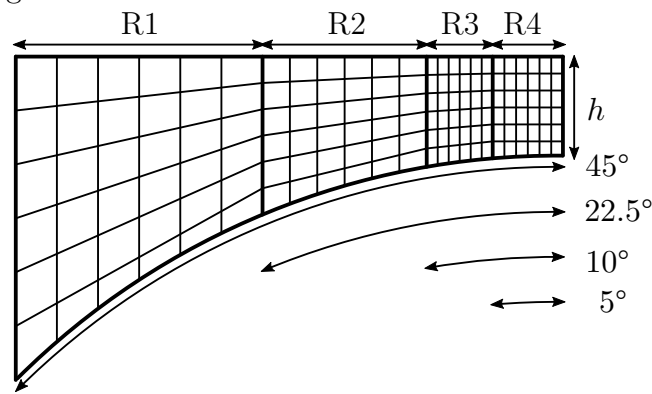


Figure 4.16.: Detailed representation of the contact zone; Fluid grid shown

The most central patch resolves the Hertzian contact area, which is the most critical region with large deformations and high gradients inside the lubricant. The Hertzian contact area corresponds approximately to an angle of five degrees. Assuming ideal aspect ratios and a given number of cells for the height, the resolution in the x direction is determined by the initial lubrication film thickness. Table 4.3 lists grid resolutions for the crucial area from figure 4.16 for different radii and y resolutions for an initial film thickness $h = 0.1 \mu\text{m}$.

From the values in table 4.3, the grid resolution for the solid domain is derivable accordingly. With the ensured ideal aspect ratio and a one-to-one resolution around the perimeter between fluid and solid grid, the mesh is expected to deliver a grid-independent solution with minor non-orthogonality correction necessary. The calculated number of cells closely corresponds to the grid-independent resolution found by Hajishiafee et al. [33, p.265] in their grid study. Accordingly, a grid study is not included here.

Discretization Schemes and Solution Procedures The system's boundary conditions serve as a starting point for the simulation. Starting from there, all scalar and vectorial quantities evolve into the calculation region until a stationary solution establishes in the

Table 4.3.: Number of cells in perimeter direction for an aspect ratio of 1 and given number of cells in height direction

$h = 0.1 \mu\text{m}$	Grid Resolutions			
	$r_R = 3.96 \text{ mm}$		$r_R = 10 \text{ mm}$	
Y-Cells	10	20	10	20
X-Cells				
R1	20	40	20	40
R2	55	110	55	110
R3	105	210	105	210
R4	1161	2298	1367	2736

case of EHL. Thus, the final result heavily depends on the choice of boundary conditions. For the fluid grid, the enclosing boundaries which need specification are the inlet Γ_{Inlet} and outlet Γ_{Outlet} boundary. Added to this are the interface boundaries with the solid grid Γ_{FSI} and Γ_{Raceway} . Table 4.4 lists all quantities for which boundaries need definition, including the fluid and electrostatic calculation.

Table 4.4.: Boundary and interface conditions for the fluid domain

Boundary	Fluid Boundary Conditions				
	p	\mathbf{u}	T	U	$\rho\epsilon$
Γ_{in}	fixedValue 10^5 Pa	zeroGradient	fixedValue 353 K	zeroGradient	zeroGradient
Γ_{out}	fixedValue 10^5 Pa	zeroGradient	fixedValue 353 K	zeroGradient	zeroGradient
Γ_{FSI}	zeroGradient	rotatingWall Velocity	<i>heatFlux/</i> <i>temperature</i>	fixedValue 0 V	fixedValue 0 A s m^{-3}
$\Gamma_{\text{SurfaceIR}}$	zeroGradient	movingWall Velocity	<i>heatFlux/</i> <i>temperature</i>	fixedValue 7 V	fixedValue 0 A s m^{-3}

Strictly speaking, only for the temperature calculation the interface characteristic to the solids comes into play directly. For every other scalar or vectorial quantity listed in table 4.4, the boundaries Γ_{FSI} and Γ_{Raceway} are treated as conventional boundary conditions and, therefore, the actual limit of their domain. The indirect FSI coupling via forces and deformations is the reason for this.

The pressure is set to a zero gradient boundary condition at the solid walls $\Gamma_{\text{FSI}}/\Gamma_{\text{Raceway}}$ and preserves ambient pressure at the inlet and outlet. For temperature, heat exchange boundary conditions are used, as discussed earlier. The inlet and outlet ambient temperature is preserved, where the value given is only an example. The ambient oil temperature adapts according to the calculated cases, considering the experimental setup in section 5.4.2.

Quantities not mentioned here, like viscosity η or permittivity ϵ are modelled based on pressure and temperature during the solution procedure. The boundary behaviour of

the resulting scalar fields is thus dependent on the boundary behaviour of pressure and temperature.

Table 4.5 is the corresponding table for the solid grid. Displacement \mathbf{D} and temperature T are the quantities to be defined. The point displacement is added for completeness. While the displacement \mathbf{D} represents the cell centre, as shown in figure 2.12, the point displacement describes the position of the focal points of the cell surfaces. The pointDisplacement always corresponds to the cell displacement vector through the neighbouring relationships (see 4.3).

Table 4.5.: Boundary and interface conditions for the solid domain
Solid Boundary Conditions

Boundary	\mathbf{D}	T	pointDisplacement
Γ_{fix}	fixedValue 0 m	zeroGradient	fixedValue 0 m
$\Gamma_{\text{FixInnerRing}}$	fixedValue 0 m	zeroGradient	fixedValue 0 m
Γ_{FSI}	tractiondisplacement	<i>heatFlux/</i> <i>temperature</i>	traction displacement
$\Gamma_{\text{SurfaceIR}}$	fixedValue 0 m	<i>heatFlux/</i> <i>temperature</i>	fixedValue 0 m

The symmetry plane of the rolling element Γ_{RE} and the ring surfaces Γ_{IR} and Γ_{Raceway} do not undergo any displacement. A movement of the solids is prevented, and stress builds up as the FSI surface Γ_{FSI} deforms. The traction displacement condition specifies pressure and shear stresses on the Γ_{FSI} boundary, which are overwritten from the fluid pressure and stress solution. The solid temperature condition at Γ_{FSI} corresponds to the fluid boundary according to the SDD. If, for example, the temperature boundary condition is chosen for the fluid, the solid boundary is set to a heat flux condition. Since only a section of the solid is represented in the solid domain, the boundaries in the direction of the remaining structure apply a zero gradient condition.

Most of these boundary conditions are consistent with approaches from the literature, while the temperature conditions are already an extension. However, the conditions for the electrostatic field and the charge transport, also need some explanation. The boundary for the electrostatic field is the voltage difference Φ which exists between the inner and outer ring, due to the reasons made in chapter 1. The value of seven volts, however, comes from the artificially imposed potential difference used in the experiments by Harder et al. [123] and Martin et al. [126], which are the basis for the experiments done in this work (section 5.4.2).

The charge density boundary condition implies, as it is listed here, that no charged species are carried into the fluid domain from outside or vice versa, which would ultimately correspond to a source and, therefore, potential equalization. While such processes, for example, due to creeping currents, might be of interest, this work only deals with charges through sources inside the domain and how they move in the fluid due to the influences presented in the fundamentals in section 2.6.2. The charge density of the internal field is changed locally to do so, and the system's development is observed

thereafter. Details are provided in section 5.5.2 on these tests.

4.3. Assumptions and Simplifications

The descriptions of the numerical grid already indicates that the main simplification is the reduction of the calculation domain to a two-dimensional space. The increase in computational expenses for realizing a three-dimensional analysis is the main reason for this measure. It also keeps the calculation time within reasonable limits, especially because massive parallel processing approaches are not efficient for the described numerical grid due to extreme differences in resolution dependant on the direction.

The problem here is that this simplification makes a comparison with experimental data difficult since those data are always three-dimensional. Hartinger et al. [34, p.151] recently dealt with this same difficulty for their analysis of a ball on disc tribometry experiment (three-dimensional point contact) with numerical calculations done in two dimensions with a case setup similar to the one in this work. While the transfer of velocities and geometric parameters is fairly simple (compare to section 2.1) the most complicated part is the recalculation of the radial load acting on a three-dimensional Hertzian contact into a two-dimensional force. Hartinger et al. [34] calculated the maximum Hertzian pressure p_{max} for the point contact and translated this into a load for the numerical line contact, which leads to similar maximum pressure. For the experimental studies that were done for this work, described in section 5.4.2, the same calculation needs to be done. Therefore, the point contact load Q is calculated from the radial loads F_R applied in the test-rig. The maximum occurring point contact load in the centre of the load zone, compare to figure 2.3, is calculated with equation 2.8. Equation 2.14 presented in subsection 2.1.2 is subsequently to calculate the Hertzian contact pressure for the point contact. Afterwards, the two dimensional force Q_{2D} is calculated with equation 4.20.

$$Q_{2D} = \frac{Q_{max}}{l} = \frac{\pi \cdot \sigma_{max}^2}{\Sigma \rho} \cdot E' \quad (4.20)$$

Here, the equation for calculating a Hertzian line contact was rearranged according to the force per length Q_{max}/l . Inserting the point contact stress delivers a two-dimensional load which equals the contact lengths and pressures for the point contact.

The experimental radial load F_R , the maximum loads Q for the single rolling element in the centre of the load zone, and the two-dimensional load for numerical calculations are listed in table 4.6. In addition to this simplification, some assumptions should also be mentioned at this point which have already been implicitly used during the fundamentals. First of all, it is assumed that the bearing spaces are fully flooded with lubricant. This implies for the fluid domain a single phase system since no wetting and de-wetting of surfaces needs consideration and no second phase like air needs to be incorporated. This assumption is valid in that the experiments, explained in section 5.4.1, are carried out with a high lubricant flow through the bearing. This assumption should be kept in mind since it will be revisited later for discussion of the results in chapter 6. While the rolling elements pass through the load-zone for a real bearing and thus the radial load changes

Table 4.6.: Conversion of loads from experimental setup, in section 5.4.2 via the single contact onto the two-dimensional numerical case

Two-dimensional Load Values					
Radial load F_R	Unit	Load Q	Unit	Line contact load	Unit
-	N	20	N	61700	N m^{-1}
1000	N	453	N	136290	N m^{-1}
2000	N	907	N	216340	N m^{-1}
3000	N	1360	N	283490	N m^{-1}
4000	N	1813	N	343430	N m^{-1}
5000	N	2266	N	398510	N m^{-1}
6000	N	2720	N	450020	N m^{-1}

with time, the radial load is calculated as a steady quantity for this work. This is more like the behaviour of a ball-on-disc EHL contact as described in the work by Hartinger et al. [34]. This is a rather strong simplification which, however, makes it possible to neglect the time dependency of the load for the time being and is typically usual for numerical tribology so far. Only when transient processes are investigated would the assumption have to be abandoned. The last aspect is the pure rolling assumption (SRR= 0). Strictly speaking, this assumption can only be made for elliptical contacts at the centre of the contact ellipse (compare 2.5). For all other areas, there is differential slip present due to the bearing kinematics. A consideration of differential slip is possible if the SRR is changed via the surface velocity boundary conditions (see table 4.4).

5. Results

Next, the elaborated implementations are tested and applied. In section 5.1 changes to the original code are tested, before it is applied to the introduced EHL case setup in section 5.3. Subsequently, as already indicated, some experimental data are stated in section 5.4. Part of the explanations is also a short description of the experimental setup. This chapter concludes with a discussion of calculations related to experimental research in section 5.5. Those results also serve as the basis for answering the third research question and as an entry to the following interpretation of the results in chapter 6.

5.1. Code Verification and Simulation Validation

Numerical calculations are always an approximation and are therefore prone to error. For these calculations to be trustworthy, it must be ensured that the error is low especially if changes have been made. So the changed code and its application to the research topic must first be tested. The tests are divided into those for verification and those for validation.

Verification ensures that changes in the source code are syntactically correct so that no errors occur during compilation. Nevertheless, even clean source code may not work because it is incorrect in context of the program's task. While the syntax is correct as the compilation runs without errors, which can be taken for granted in all the presented changes, the proper embedding must be checked for every function.

Validation is a more challenging task compared to verification. Although a program or source code is verified, this does not mean that the results obtained during a simulation are correct. A confirmation of the correctness is equal to its validation. However, it remains to be considered that the validation for a specific calculation task does not also validate other ones. The more different the tasks are, the less meaningful validation of one is for the other. While divergence, a complete failure of the calculation, is an apparent falsification, discretization errors in space and time are harder to identify if the calculation converges towards a particular solution.

How close a particular solution is to the exact result is called the absolute error. For most problems in which numerical methods are used, no exact solution is known and the determination of this absolute error is hardly possible. Thus, it is often only feasible to determine the error relatively in order to get a feeling for the accuracy of a numerical approximation. A validation, in the numerical sense, is the estimation of errors from different approximations, like grid resolution, discretization model and cumulative errors during iteration. If the sum of these errors drops below a tolerable limit with increasing

iterations in reasonable time, the simulation can be considered validated.

The validation task is split into multiple tests, each validating a single domain with a calculation for which either experimental data are available with a low margin of uncertainty or other numerical results which are generally considered accurate as Ferziger [67, pp.534-539] described. The calculation for which the implementation work has been done is usually not available so that the accuracy is validated for the several types of error by testing. For example, the discretization error due to the finite number of grid points is calculated multiple times with increasing number of grid cells (typically called grid resolution) to find a solution independent of it. This so-called grid-independent solution is considered sufficiently accurate and usually the minimum form of validation conducted for numerical investigations. Since the underlying grid corresponds to the grid studies by Hajishafiee et al. [33], a grid study is not necessary for this work.

5.2. Test-Driven Development

Verification and validation are usually carried out in parallel with program development in a Test-Driven Development (TDD) approach, presented by Beck [115]. Once a new program section is integrated, a suitable test scenario is immediately planned to verify and validate this implementation. Such a procedure is necessary because a final joint validation is almost impossible since interactions, for example, between a new solution algorithm and a new model library can hardly be resolved afterwards, as in the present case.

As the next step, some tests are presented to verify that the various changes and extensions to the original code by Tucovic et al. [42] are operating correctly. Therefore, the validation and verification examples follow the original order of implementation. First of all, each extension is tested individually, starting with the material models. Then the single solution algorithms of the domains are tested via simple calculations of acknowledged numerical references or by comparison to analytical solutions, if possible. Subsequently, the domain coupling is put to the test. Finally, a transition is made to TEHL contacts. The values for pressure and deformation are compared to the literature results. The chosen reference calculations are expected to have a characteristic like the Petrusevich peak for certain SRRs, which should also show in the numerical results and increase the calculation's trustworthiness.

Whenever appropriate, the SRR, and other dimensionless quantities introduced in subsection 2.5, are stated for the calculations. This information increases the comparability with literature solutions and simplifies the discussion of similarities and discrepancies. The use of dimensionless velocity-, load- and geometric parameters is necessary because numerical calculations in tribology are carried out with varying setups. For example, the actual geometry might vary significantly for two setups, while the calculated stresses are nearly the same indicating differences in the target load and regarded tribological regime. Refer to the geometric data compared in table 4.1 as an example. Thereby, comparisons between different publications is only possible to a limited extend, especially if no reference to a real geometry is established anyway. Dimensionless quantities,

introduced in section 2.5, overcome this lack of comparability at least partly.

Density Model Verification The TDD approach starts with the material models. Two aspects are tested to ensure they are working correctly. First, the correct implementation is checked, which means that the code is free of errors and operates as part of the thermophysical properties library. The second aspect is that an equation and all the given constants used to compute the solution are read correctly, and the results match expected values. While it is possible to activate a single function in a C++ program (or library) to test them, this does not necessarily mean the function/implementation works accordingly in the program's context. Therefore a one-dimensional test case is set up, shown in figure 5.1.

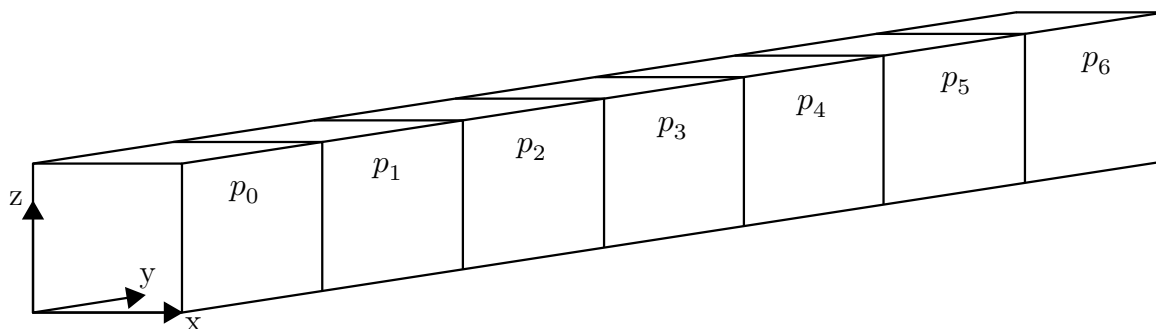


Figure 5.1.: Finite volume one-dimensional ($[1,5000,1]$ cells) calculation region with predefined pressure and temperature values per cell to recreate viscosity and density curves for validation

The case counts 5000 cells in the x-direction. Values for temperature and pressure are assigned to every cell in advance according to the expected pressure and temperature range presented in the fundamentals (compare figure 2.9). The case is run with a calculation procedure that initializes all fields, solvers, and the thermophysical properties library as it is done for the main program, which was presented in section 4.1.3. Then the density is calculated by executing the corresponding EoS function from the thermophysical models library. So the defined model is executed for the cells. This way, it is ensured that the functions execute correctly as part of the library and within the whole program context. The results for viscosity and density are written to the hard drive. Figure 5.2 shows an excerpt from the calculated case.

First, the equations of state are gone through. Unlike an actual numerical calculation, fixed pressure and temperature values are assigned to every cell. The pressure covers the complete range expected for TEHL systems from environmental pressure of $p = 10^5$ Pa to double the expected EHL pressure of $p = 5 \cdot 10^9$ Pa. The calculation is repeated multiple times with constant temperature at each cell but with different values. By plotting the resulting relative changes in density together with the assigned pressure and temperature, the curves equal those from figure 2.9. This way, the model implementation and the correct embedding of the library are verified. The results for the Tait (equation 2.35) and Murnaghan (equation 2.36) EoS are shown in figure 5.3.

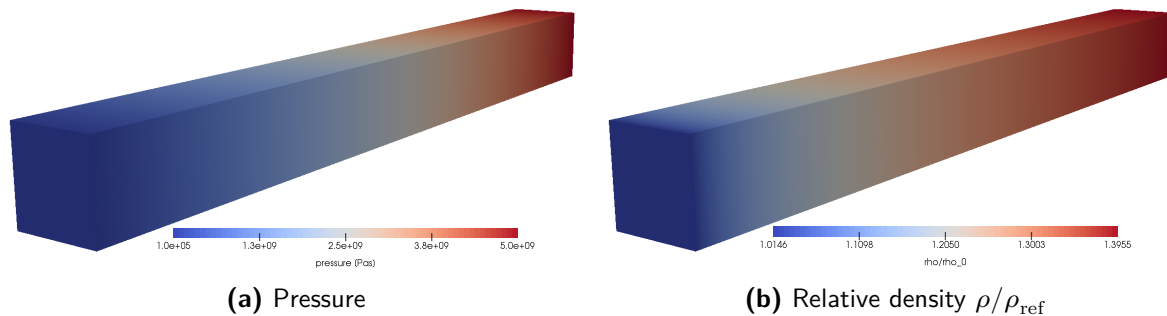


Figure 5.2.: Finite volume pseudo one-dimensional ([5000,1,1] cells) calculation region OpenFOAM case visualization via ParaView

The other implemented models, like perfect fluid (equation 2.31) and Dowson-Higginson (equation 2.32) have not been presented here but were tested in the same way. The graphs for the Tait and Murnaghan density models were calculated with both equations 2.34 and 2.33 for the bulk modulus. The results match those in the literature taken from Bair [28]. Therefore the implementation of the EoS is considered to be trustworthy. The model parameters are changed for the actual EHL calculations later in this work since the oil used during the experiments (FVA 3 reference oil) does not match those described in the literature. Therefore, the curves only image the graphs' qualitative course but deviate from their actual values. However, these changes do not compromise the validity and verification of the models in general, which was proven here.

Viscosity Model Verification So that the verification and validation of the thermo-physical models' library are completed, the same procedure is repeated for the implemented viscosity models by Wilson-Wong (equation 2.39), Roelands (equation 2.40), and Doolittle (equation 2.41). Unlike the first two, the Doolittle model needs density values assigned to each cell for calculation since the viscosity changes through the ratio of density ρ to ambient density ρ_0 , instead of being calculated through the state variables temperature T and pressure p directly. Therefore, the results are shown once for the Tait and once for the Murnaghan model from figure 5.3. The EoS parameters are similar to the density verification. Figure 5.4 depicts the Doolittle viscosity model for different parametrizations and EoS. The viscosity changes in the order of magnitudes for increasing pressure and is therefore depicted with an exponential y-axis scaling. The recognisable changes in viscosity with pressure p and temperature T can also be seen for comparison from table A.1 in appendix A. To classify the values, it should be pointed out at this point that the representation is the dynamic viscosity η . The choice of the modelling parameters leads to over-exponential viscosity curve with increasing pressure, called a fragile lubricant. A strong lubricant in contrast has a parametrization which shows a more linear viscosity curve with increasing pressure on an exponential scale. The curves in figure 5.4 match those from the literature with the corresponding model parameters, which verifies and validates the implementation. The original graphs are

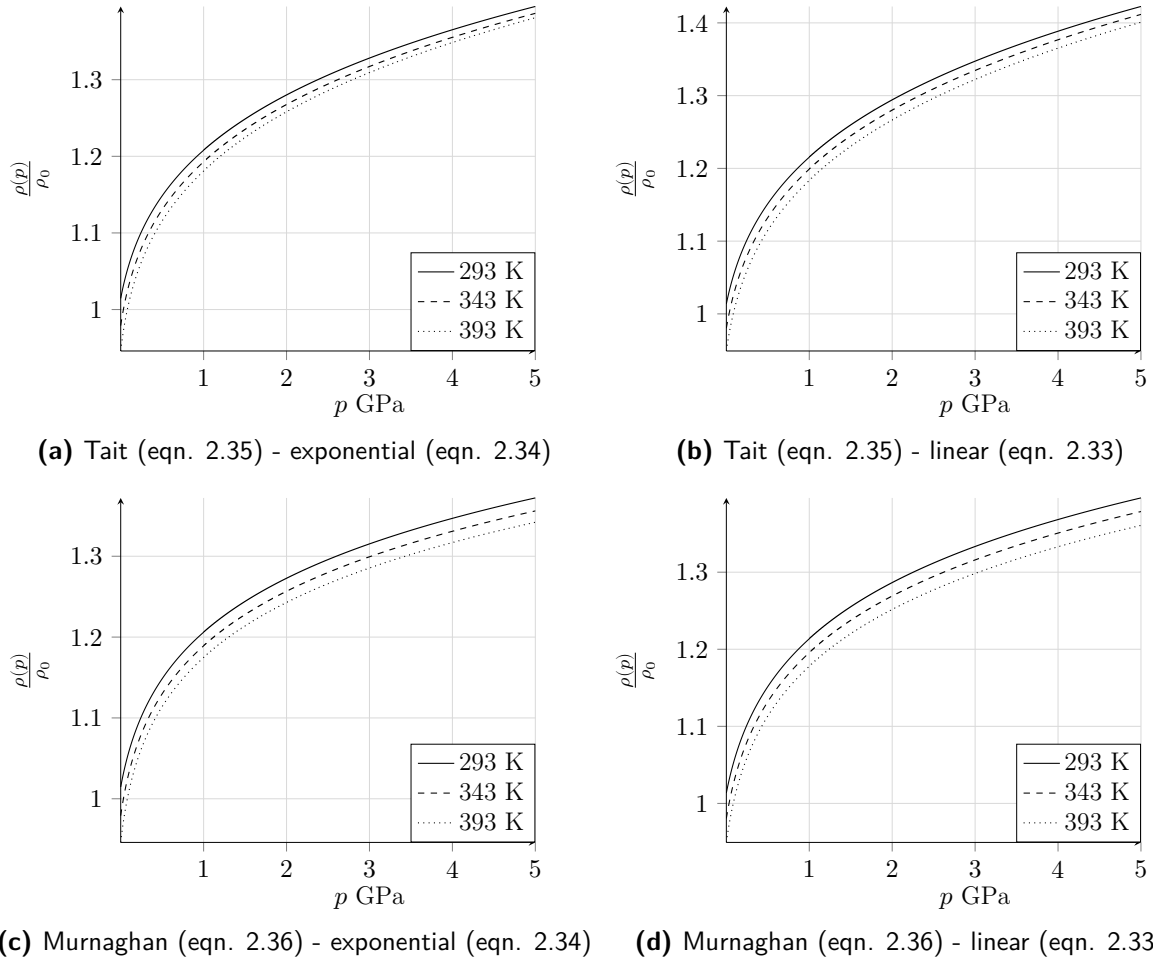


Figure 5.3.: Relative density $\rho(p)/\rho_0$ plotted over pressure p for different temperatures based on the parametrization for LVI 260 reference oil according to Bair [28], results from OpenFOAM; (a) Tait equation, exponential change in bulk modulus with temperature; (b) Tait equation, linear change in bulk modulus with temperature; (c) Murnaghan equation, exponential change in bulk modulus with temperature; (d) Murnaghan equation, linear change in bulk modulus with temperature

not shown here since they are identical but can be found in the book by Bair [28, p.124]. A closer look at the graphs for the Doolittle viscosity models shows that the values do not cover the whole pressure range for low temperatures. The reason lies in the unique coupling between EoS and viscosity.

The Doolittle model is based on the free volume theory. Thus, it should cover the transition from a liquid to a glassy state for temperatures below the glass transition temperature at elevated pressures. The glass-forming of a lubricant is regarded as an elastic solid, and the flow behaviour comes to a standstill, theoretically. This state is equivalent to an infinite viscosity. Close to the glass transition pressure, which decreases

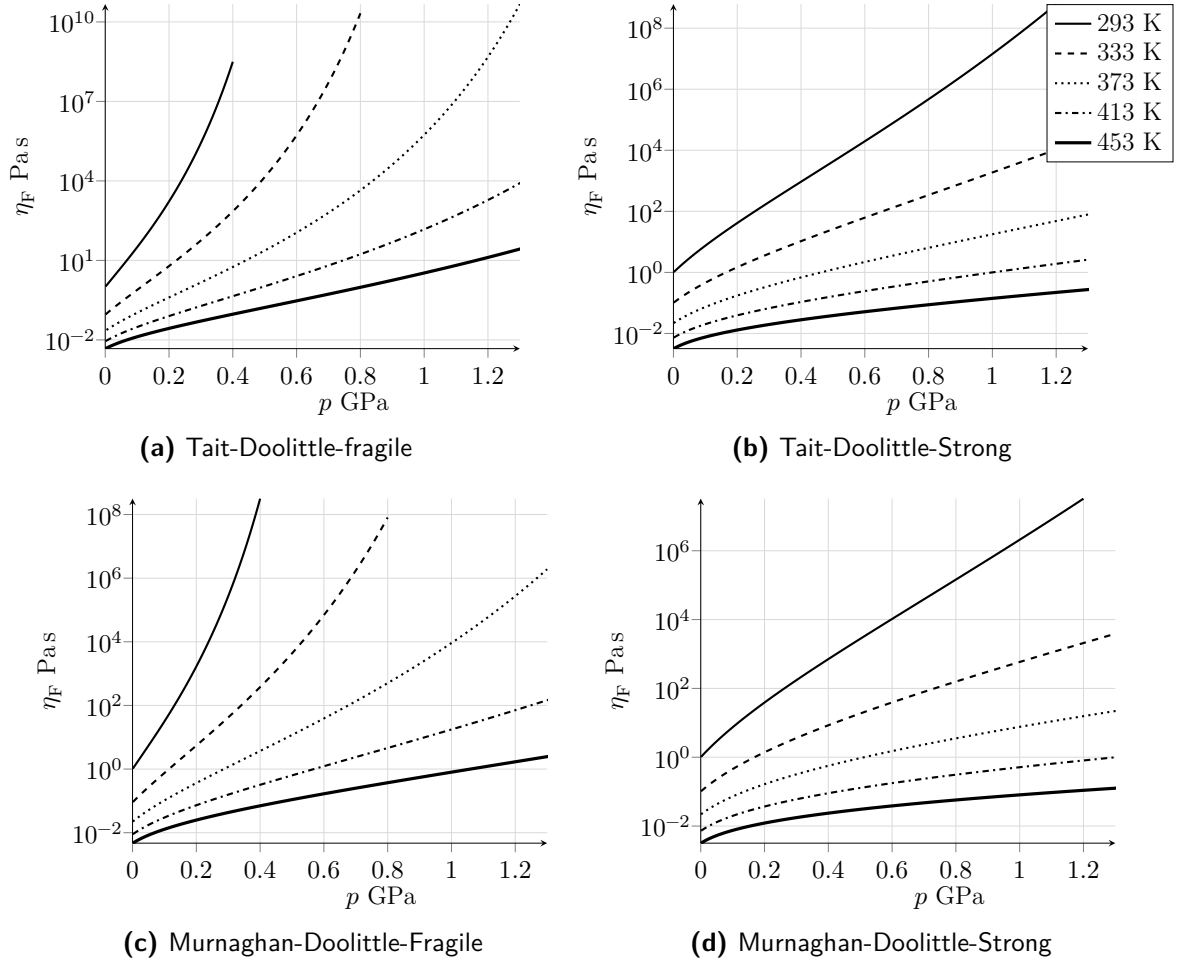


Figure 5.4.: Dynamic viscosity $\eta_F(p, T)$ plotted over pressure p for different temperatures T (legend applies to all graphs); (a) Tait-Doolittle verification results from OpenFOAM based on parametrization for ideal fragile/strong lubricant according to table 2.6

with temperature, the viscosity strives towards infinity asymptotically. The coupling between EoS and the Doolittle model does not account for that correctly. Thus, the models valid scope of application for the model is limited to the pressure ranges shown. Figure 5.5 illustrates the problem.

First of all, the free volume theory described in section 2.3.6 implicates that for a given temperature, there is a limiting density/maximum compression to be reached asymptotically as the free volume vanishes with elevated pressures. Therefore, graph 5.5a should reach a plateau, which it does not. Looking back at figure 5.3, neither the Tait nor the Murnaghan EoS does reach such a plateau even for extreme pressure like $p = 5 \cdot 10^9$ Pa. While the free volume theory suggests that this asymptotic limit varies for changing temperature, it has to exist somehow. The second inaccuracy of these models is linked to this directly. The Doolittle viscosity model accounts for the glass transition so that the

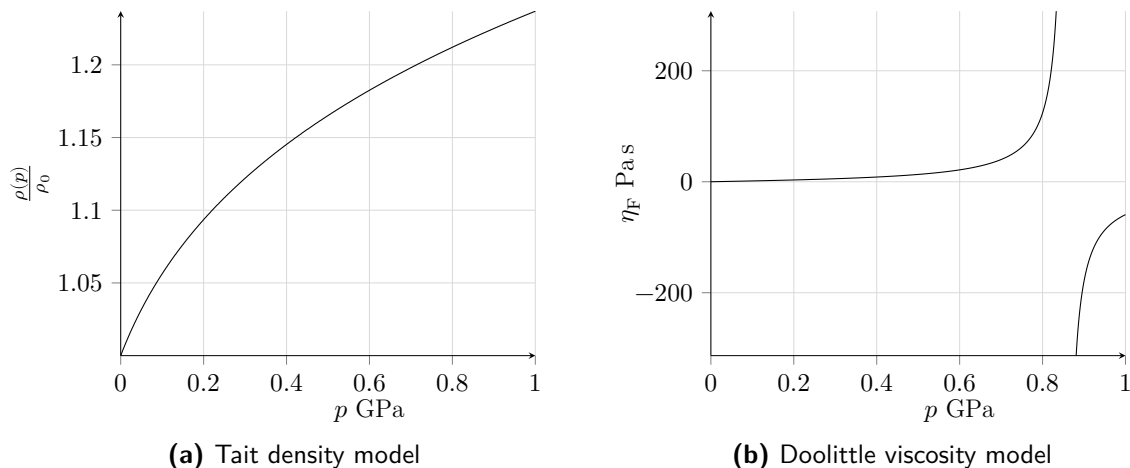


Figure 5.5.: Tait Doolittle model singularity and unboundedness; (a) Relative Density $\rho(p)/\rho_0$ plotted over pressure p ; (b) Dynamic viscosity η_F plotted over pressure p

viscosity increases exponentially as the inverse density approaches the occupied volume. However, if the viscosity is calculated beyond the pressures given in the literature (for a specific temperature), graph 5.5b is the result. A singularity in the viscosity description occurs. The graph's position and exponential development towards this point heavily depend on the model parametrization.

This singularity does not have any physical meaning and has implications for the use in numerical calculations because the occurrence of a value beyond the asymptotic limit, only for a single cell, leads to a fatal error during calculation and has to be prevented. Preventing this was done for the implementation in two ways. First of all, the increase in density is limited to a predefined relative change in volume corresponding to the occupied volume V_∞ (equation 2.44) according to Bair [63, p.117]. If the viscosity model is parametrized correctly, the singularity lies beyond the glass transition pressure-temperature combination so that the limitation of density also sufficiently prevents singularities in viscosity. The pressure at which the singularity occurs therefore changes with the parametrisation of the model. Ideally, the model strives towards a realistic glass transition, thus singular, value without reaching it during calculation. Then the model's validity is ensured for non glass forming conditions. A case that implies glass transition at any point in the calculation domain however impairs the validity and is therefore out of scope. However, it is also limited to five orders of magnitude change to stabilize the numerical iterative procedure. While the actual glass transition as hybrid modelling of the oil as fluid and solid at the same time is out of scope for this work, the viscosity limitation is a necessary approximation.

Contrasting to this combination of EoS and viscosity model, figure 5.6 shows the referencing calculation to the literature case published by Hartinger et al. [32] using the Dowson density model and a modified version of the Roelands viscosity model, which were explained in the fundamentals.

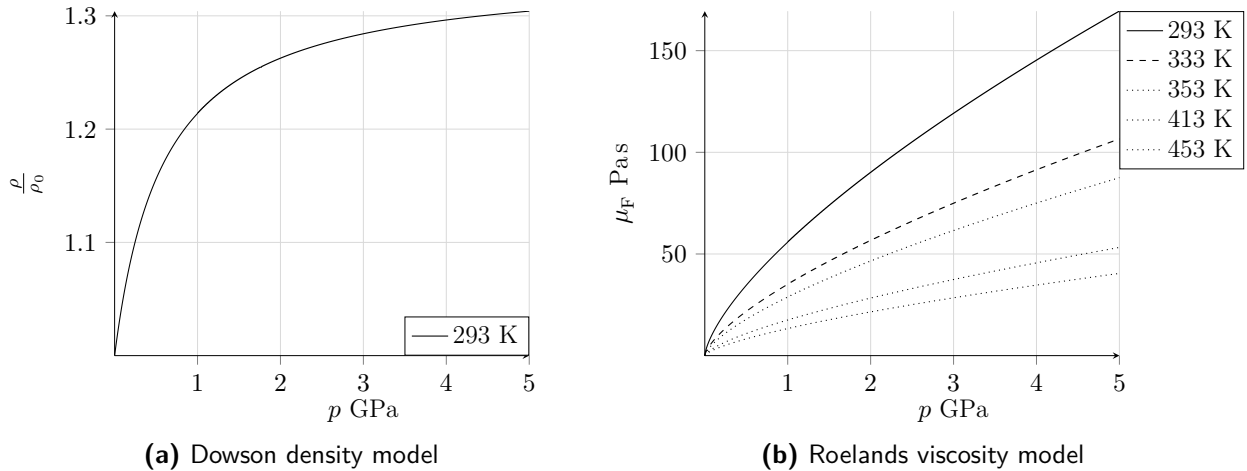


Figure 5.6.: Dowson model implemented and parametrized according to Hartinger et al. [32]; (a) Relative Density ρ/ρ_0 plotted over pressure p ; (b) Dynamic viscosity μ_F plotted over pressure p

These exact models with the parameters are used later and differ significantly from those discussed before. It can be seen clearly, that the Dowson model strives asymptotically towards a limiting value consistent with the premise of free volume theory. The Roelands viscosity model is different from the Tait and Murnaghan model as it evolves over proportionally strong with pressure, compared to Tait and Murnaghan. Hartinger et al. [32] used this combination of Dowson and Roelands model successfully to calculate two-dimensional EHL contacts concerning shear thinning and phase change.

The resulting curves and the values for density match those expected from the literature. Therefore the implementation of the new viscosity models into the framework presented in this work is considered to be correct. However, it should be mentioned that the viscosities strongly depend on model parametrization. Small changes can shift the pressure dependant viscosity change from strong to weak behaviour and also alter the glass transition singularity for the Doolittle model.

Fluid Solver Verification and Validation The verification and validation of the implemented fluid solver is more complicated than justifying that EoS and viscosity models reproduce literature values correctly. The solver contains multiple differential equations to calculate the velocity \mathbf{u} , pressure p , and temperature T , with an EoS, verified and validated before. While the compressible PIMPLE solver itself is not a new development, it has undergone a significant rewriting to fit the structure of the underlying program as described in section 4.1.4. Demirdžić and Perić [129] published benchmark solutions for flow and heat transfer problems in non-orthogonal grids. Figure 5.7 displays their calculation setup.

The calculation is based on an equilateral grid of length L forming a parallelogram with an opening angle of 45° degree. The sides have a length of $L = 1$ m. Due to the inclination, the applied block-structured grid is highly non-orthogonal, which corresponds to

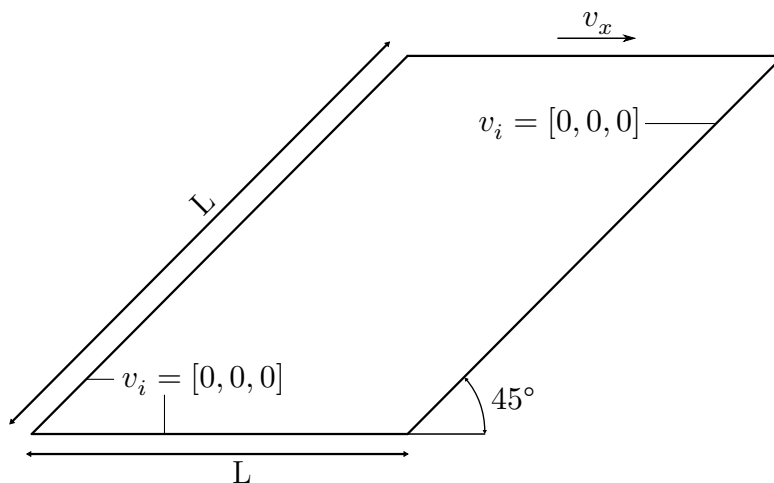


Figure 5.7.: Non-orthogonal cavity geometry based on the C1 benchmark test case by Demirdžić and Perić [129]

the grid states of the target calculation shown earlier in section 4.2, so that the validation also translates to the target case. All sides of the case are defined as walls. Only the top wall has a velocity of $v_x = 1 \text{ m s}^{-1}$. Density $\rho = 1 \text{ kg m}^{-3}$ and viscosity $\eta = 0.01 / 0.001 \text{ Pa s}$ were chosen to match certain Reynolds numbers.

Figure 5.8c shows the case calculated for $\text{Re} = 100$. Figure 5.8a is the corresponding original case by Demirdžić and Perić [129] for the same Reynolds number. Figures 5.8b and 5.8d show the results for $\text{Re} = 1000$, respectively.

The colour-map for figure 5.8c and 5.8d represents the velocity magnitude. Streamlines are added for comparison to the reference case. The reproducibility of the change from one primary circular flow in figure 5.8a to two circular flows for a higher Reynolds number in figure 5.8b is used for verification of laminar flows. Transience or turbulence is not visible as it is not considered for the reference calculation and the test case here. The calculation is incompressible to avoid interactions with the equation of state. The similarity of streamlines for both cases is commonly used for validation. An in-depth evaluation of these simulations is not provided here, since the match between current implementation and reference case is visible.

Solid Solver Verification Even though the solid solver has only been adapted slightly by including the heat conduction equation without coupling to thermal stresses, the solid solver is also tested for the purpose of this work. The goal is to showcase that it operates correctly for the actual EHL calculation. Therefore, a simple analytical elastic deformation of a three-dimensional square beam is calculated numerically and compared to the available analytical solution. Figure 5.9 depicts the case.

A beam is given the length L of 2 m and the width/height of $H = 0.2 \text{ m}$. It is clamped on one end while a force is applied on the other. The analytical equivalent to this case is a uniaxial bending beam since the applied force is only acting in one direction. For the numerical calculation the beam is discretised into 10.000 square cells of length $L = 2/100 = 0.02 \text{ m}$ and width/height of $H = 0.2/10 = 0.02 \text{ m}$. The force F_y is

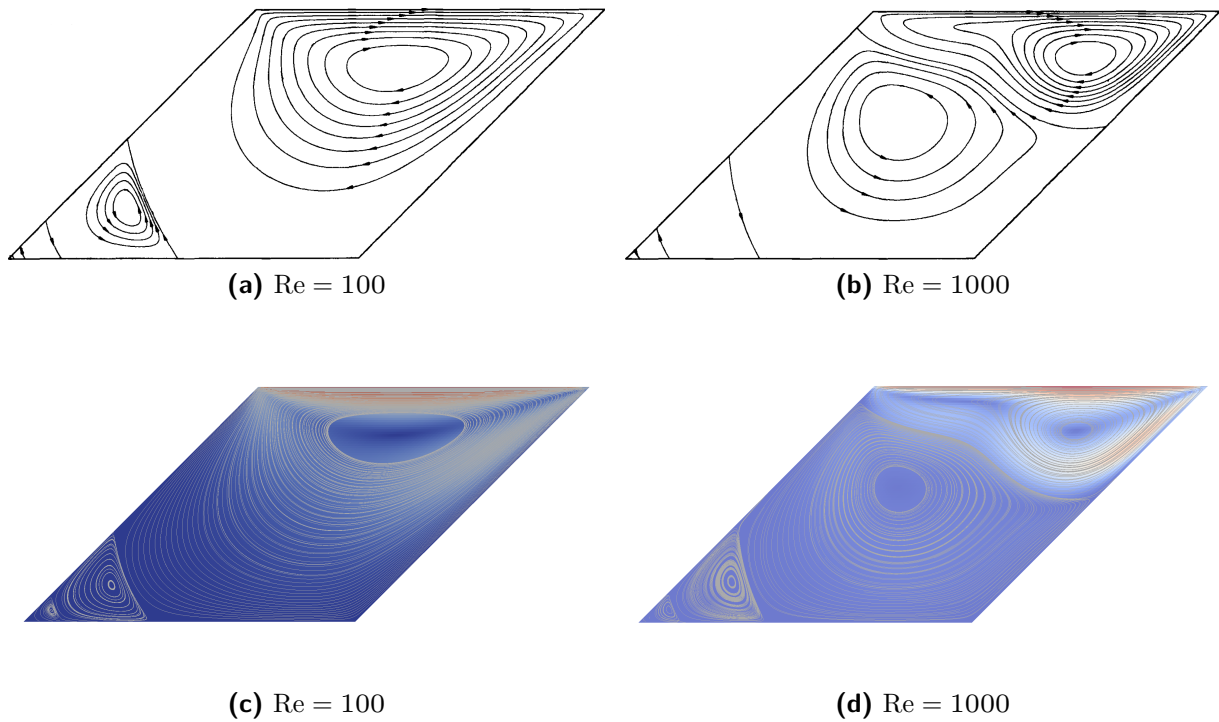


Figure 5.8.: (a), (b) Non-orthogonal cavity results, original images by Demirdžić and Perić [129]; (c), (d) Numerical results from OpenFOAM

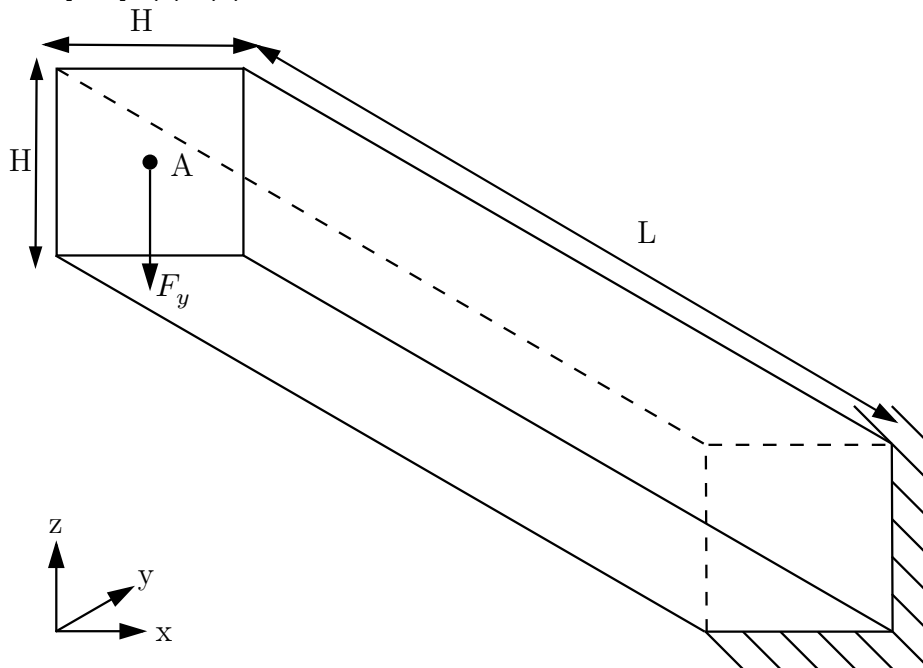


Figure 5.9.: 3D beam calculation setup

distributed across the beam's surface. The stationary displacement for a given force in

the numerical calculation is compared to the available analytical solution. This is done for loads from $F = 10$ N to $F = 800$ N. The solution for the uni-axial bending of a square beam is calculated according to Gross et al. [130, pp.119-220]. The resulting equation 5.1 calculates the maximum deformation D_{max} through Young's modulus E of 7000 N m^{-2} , the second moment of area I , by the beam's length L and the force F acting. For a square geometry, the second moment of area calculates to $I = 1.3\bar{3} \cdot 10^{-4}$.

$$D_{\max} = \frac{F_y \cdot L^3}{3 \cdot E \cdot I} \quad (5.1)$$

The analytical and numerical maximum deformations for point A (see figure 5.9) are listed in table 5.1.

Table 5.1.: Total deformation at point A for a uniaxial deflection of a square beam; Analytical solution compared to numerical results

Beam Deformation		
Force N	Analytical solution m	Numerical solution m
10	0.02	0.0208(0.0208)
40	0.08	0.083(0.083)
100	0.2	0.206(0.206)
400	0.8	0.75(0.7498)
800	1.6	1.204(1.2116)

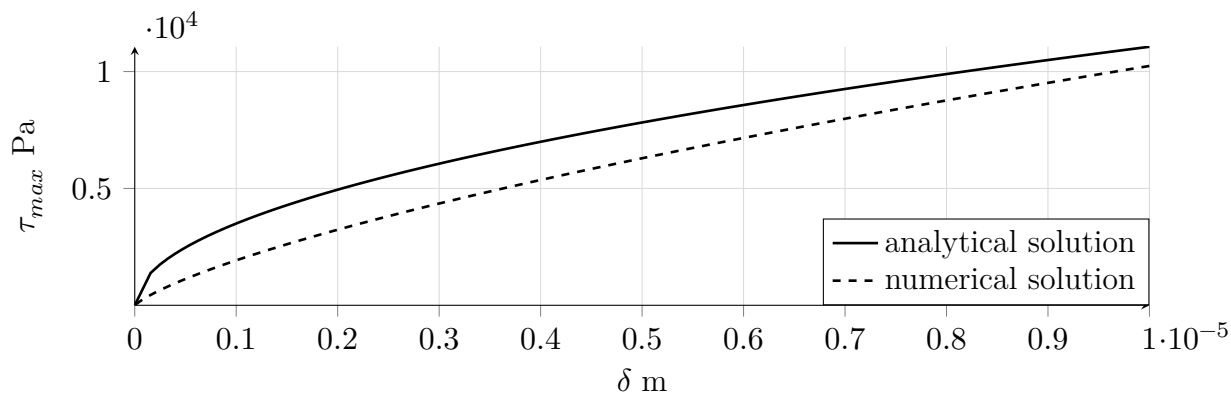
The results indicate that the numerical calculation underestimates the bending for large forces and thus large deformations. On the contrary, it over-predicts the bending for small loads (deformations). There are various reasons for such an error, with shear locking being the most probable.

Shear locking follows from the inability of the single elements to bent at the surface. Increasing the cell density in the numerical calculation leads to less over prediction for small deformations, but the deviation for large deformation is still significant. The results for the increased cell count are added in braces for table 5.1. The changes for small forces are below the accuracy of the significant digits.

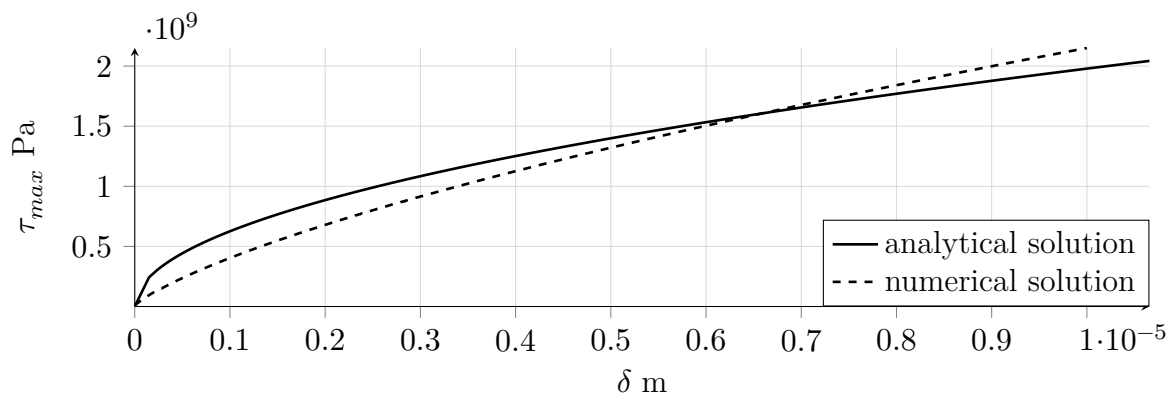
While the bending of a square beam indicates that the overall solver operates properly, a transition to a mechanical contact problem is purposeful to conclude the solid solver verification and validation. Therefore, a numerical equivalent to a Hertzian contact is calculated. This exact problem is calculated with analogy to the schematic two-dimensional simplification introduced in section 4.3, figure 4.14a.

Therefore a two-dimensional half-sphere is pressed onto a rigid, semi-infinite flat surface. The numerical grid implementation is equivalent to figure 4.14a. The rigid surface is constantly moved towards the half-cylinder. The deformation of the half-cylinder is calculated with a penalty method. The maximum contact stress and deformation δ , which matches the displacement, are plotted against each other in figure 5.10.

The analytical solution based on the Hertzian contact theory [45, p.61] is also plotted for comparison. Again, two different cases were calculated. One for a soft material



(a) Soft Hertzian contact



(b) Hard Hertzian contact

Figure 5.10.: Maximum stress τ_{max} plotted over displacement δ ; Numerical Hertzian contact solution and analytical calculation according to Harris [45, p.198-203]

($E = 1 \cdot 10^6$ Pa) shown in figure 5.10a and one for values that correspond to the actual EHL contact ($E = 2.1 \cdot 10^{11}$ Pa) in figure 5.10b. The maximum stress τ for the soft material is significantly smaller due to its linear dependence on the Young's modulus. By comparison, it becomes clear that the numerical solution seemingly under-predicts the displacement δ to stress relation for small deformations and starts to over predict those for large displacements. An evaluation of the grids showed that the used penalty method did not terminate the surface penetration entirely, which especially for small displacements, is significant in the results. Figure 5.11 shows the case setup and a detailed representation of the contact area.

Since there is no penalty method used during the actual EHL calculations because a force balance is established, the solid solver's handling of the mechanical contact task suffices for this work but might be revisited in the future.

Temperature and Enthalpy Coupling through Interfaces The last aspect that needs to be tested individually is heat exchange at the domain boundaries. This test is necessary to ensure the correct functioning of the overall temperature calculation described

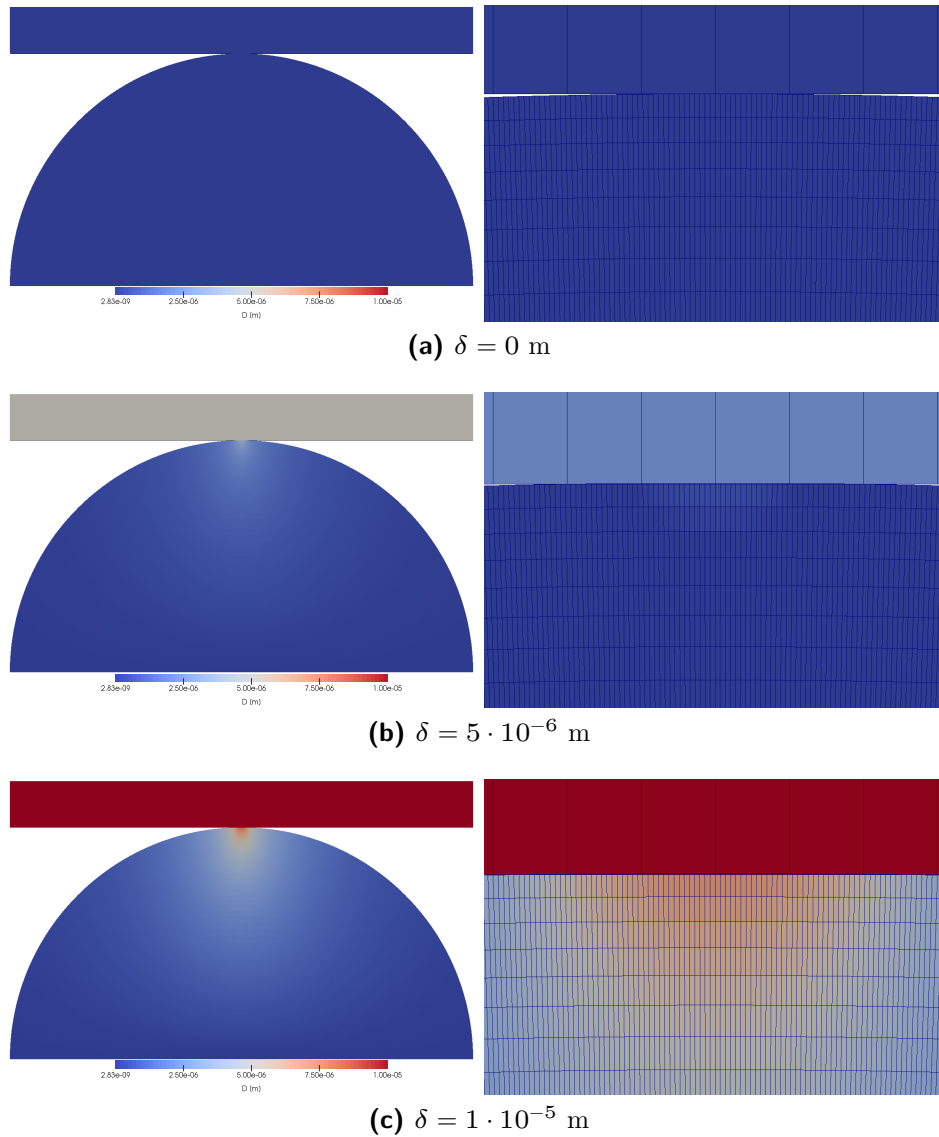


Figure 5.11.: ParaView visualization for the linear elastic Hertzian deformation for different deformations δ according to figure 2.5

for the implementation in section 4.1.3. The handling of the temperature balance in the tribological system is expected to be crucial for quantifiable results in the future.

As a validation case, the cooling of an infinite cylinder in a parabolic stream is considered. Figure 5.12 depicts the calculation setup and relevant dimensions.

The length L is set to 0.205 m, the height H to 0.05 m and the cylinder radius r to 0.01 m. For comparison, the dimensionless analytical solution for an infinite cylinder cooling is utilized. Equation 5.2 describes the dimensionless mean temperature evolution of the cylinder over time, according to Taler [131, pp.407-410].

$$\Theta = \frac{T(t) - T_{\infty}}{T_i - T_{\infty}} = \sum_{n=1}^6 \frac{4 \cdot \text{Bi}^2}{\mu_n^2 [\text{Bi}^2 + \mu_n^2]} e^{-\mu_n^2 \cdot \text{Fo}} \quad (5.2)$$

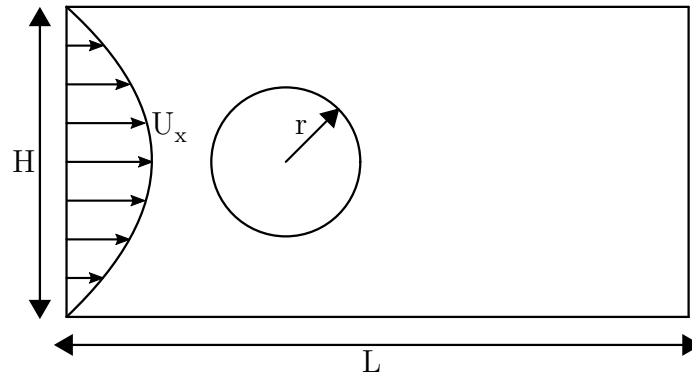


Figure 5.12.: Infinite cylinder cooling test case

Although the accurate formulation of equation 5.2 is an infinite sum, only the first six elements of the sum are usually evaluated. The values for μ_n are found in table 5.2 for different Biot numbers.

Table 5.2.: Parameters for the mean Temperature calculation for different Biot numbers according to Taler [131, p.406]

Biot Parameters						
Bi	μ_1	μ_2	μ_3	μ_4	μ_5	μ_6
0.1	0.4417	3.8577	7.0298	10.1833	13.3312	16.4767
1	1.2558	4.0795	7.1558	10.2710	13.3984	16.5312
4	1.9081	4.6019	7.5201	10.5423	13.6125	16.7073

The Biot number describes the relation between heat transfer α_F to the fluid and heat conduction λ_S . Details on the Biot number were provided in section 2.5. The radius r is used in the case of the infinite cylinder. The time dependency in equation 5.2 is represented by the Fourier number Fo , which was also introduced in section 2.5.

Since the heat transfer coefficient α_F for the fluid and thermal conductivity λ_S for the solid is known, the mean temperature decrease of the cylinder is calculable. The curves that result from the analytical calculation with equation 5.2 are shown in figure 5.13.

It should be noted that the ordinate is inverted, a unique feature of the graph. The analytical solution shown is based on a zero dimensional view of the cooling process which corresponds most closely to a measurement of the mean cylinder temperature. For increasing Bi numbers the time to cool the cylinder from its initial temperature to environmental temperature reduces by magnitudes. The significance of a temperature mean is reduced for lower Biot number since the non-uniformity in cooling along the radius increases due to a lower heat conductivity. However, for this calculation, the averaging suffices. Comparing the temperature decrease during the transient calculation with the estimated course for temperature provides information if the numerical implementation behaves conclusively for the implemented Schwartz decomposition method. Therefore the calculation case parameters were set to match the Biot numbers of $Bi=0.1, 1$ and 4 listed in table 5.3.

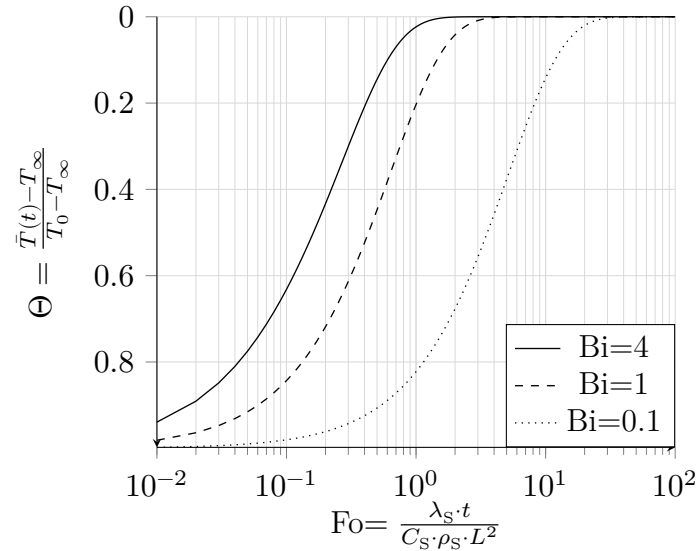


Figure 5.13.: Dimensionless temperature Θ plotted over Fourier time Fo for increasing Biot numbers Bi - analytical solution

Table 5.3.: Thermal parameters for the infinite cylinder test for different Biot numbers

Case Parameters				
Biot-Number	Bi	0.1	1	4
Thermal conductivity	λ_S	1	0.1	0.025
Density	ρ_S	100	100	25
specific heat capacity	c_S	100	10	10
Heat transfer coefficient	α_F	10	10	10
Characteristic length	r	0.01	0.01	0.01

Furthermore, the chosen parameters result in a match between Fourier time and calculated real-time. The temperature is de-dimensioned to match Θ with the initial cylinder temperature $T_0 = 305$ K and the far-field fluid temperature of $T_\infty = 300$ K. The results of the numerical calculations are plotted in figure 5.14.

First of all, it can be stated qualitatively that the temperature curves develop comprehensibly following the analytical solution and that the shortening in cooling time is visible for increasing Biot numbers. However, it becomes apparent that the overall cooling time deviates quantitatively from the analytical. A possible reason for this deviation is the numerical setup difference, which calculates the local heat transport on the surface from the temperature difference at the wall and the heat transfer coefficient. The temperature difference is governed by the convective transport of the fluid, which depends on the flow field. The analytical solution is zero dimensional and implies an ideal constant heat transport through the interface. In addition the heat conductivity becomes of increasing importance for low Biot numbers since it leads to an inhomogeneous temperature profile in the cylinder which is not captured by the analytical solution. If

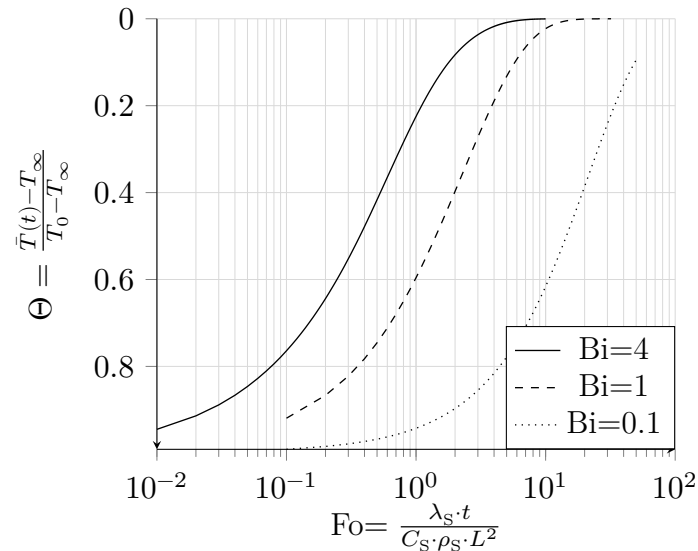


Figure 5.14.: Dimensionless temperature Θ plotted over Fourier time Fo for increasing Biot numbers - numerical solution

one considers these differences between numerical calculation and analytical solution the calculated curves indicate verification of the correct operation of the SDD and thus the heat transfer. It should be noted, that only the Dirichlet-Neumann version of the SDD was tested as it is the relevant implementation for this work.

5.3. Comparative Calculation with Literature Cases

Now that the individual parts of the program are verified to work as intended, the next step is to start the coupling and see whether the calculation matches renowned FSI solutions. Three calculations are presented here. The first is a standard FSI case by Turek and Hron [132]. Afterwards, the transition to calculations with the EHL geometry, presented in section 4.2, is done. The third case modifies the calculation to an EHL case known from the literature. At the end of this section, the transition to the target geometry is complete.

FSI Validation While the individual parts might be convergent, the FSI interaction is a different story and might lead to divergence of single program parts. Therefore, tests against literature cases are needed to ensure that the coupling works as intended. Luckily, there are some references usually used to test fluid-structure interaction. The most prominent one has been introduced by Stefan Turek and Jaroslav Hron [132] for an elastic beam in an incompressible laminar flow. Two out of three characteristics, namely a laminar flow and elastic deformation, are met to calculate TEHL rolling bearing contacts for electrical phenomena. The difference is that a compressible calculation aimed for was not included in the original calculations, which has to be considered

during comparison. The case geometry is shown in figure 5.15.

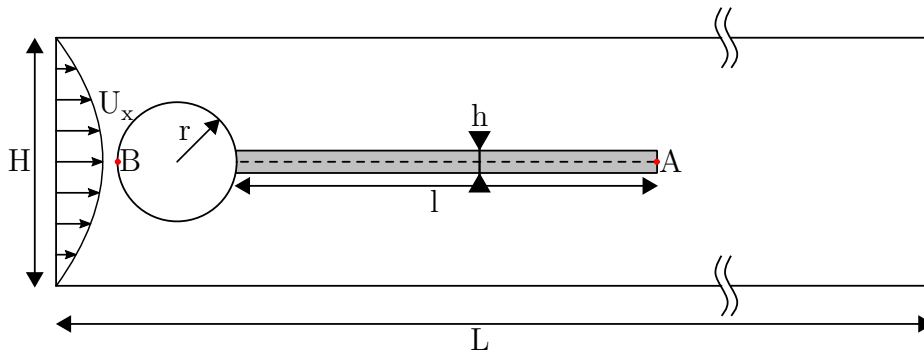


Figure 5.15.: Calculation scheme proposed by Turek and Hron [132, p.249] for FSI benchmark; Parabolic inflow U_x triggers periodic oscillations. Displacement amplitude and frequency of point A relative to B used for benchmark

Depicted is a rigid cylinder with an elastic two-dimensional beam attached to it. Like the heat exchange verification, a parabolic inflow is applied as a boundary condition for the fluid domain. In response to the stream resulting from this slightly asymmetric inflow, the traction forces and pressure differences on the upper and lower side of the beam evoke an oscillation, which reaches a stationary equilibrium. Excerpts from the simulation are shown in figure 5.16 for different points in time throughout the calculation.

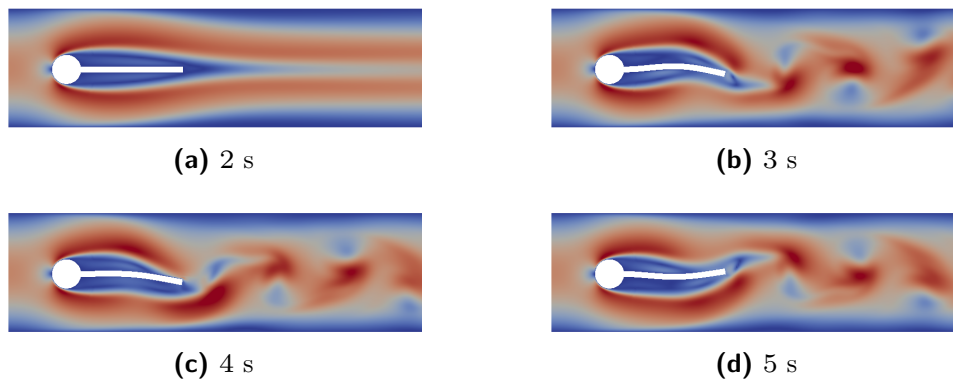


Figure 5.16.: Extract from the Hron Turk Simulation

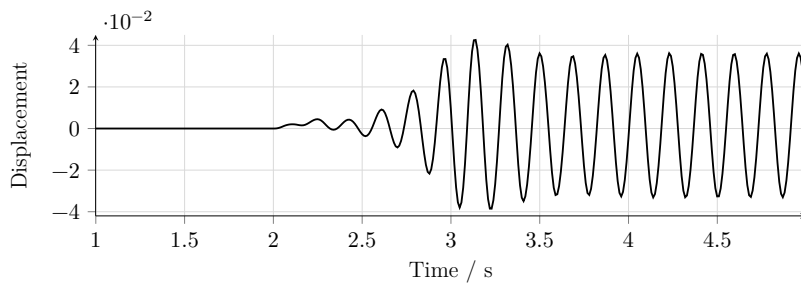
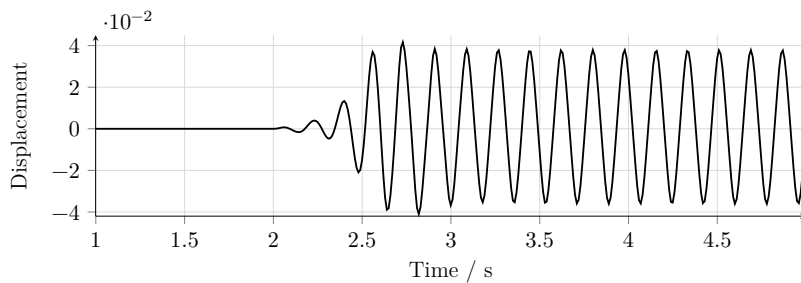
For comparison with the original case, the case must be parameterised analogously. Table 5.4 lists the fluid, solid and geometric parameters used calculation.

The characteristic for the analysis is the oscillation at the beams tip. The point under consideration, named A, is highlighted with a red dot in figure 5.15. Figure 5.17a displays the result for the reference case over a time-interval of five seconds.

The amplitude and frequency of the vertical deflection relative to point B indicate the accuracy of the FSI calculation. Thus, its position was tracked and written to the hard drive during execution of the program. This tracking was done for the reference case and the new fluid solver. The graphs course shows that the calculation divides into two

Table 5.4.: Characteristic parameters for the Turek-Hron test

Case Parameter			
Parameter	Variable	Unit	Value
Viscosity	η	$\text{kg m}^{-1} \text{s}^{-1}$	1
fluid Density	$\rho_{\mathcal{F}}$	kg m^{-3}	1000
maximum Velocity	\mathbf{u}	m s^{-1}	3
solid Density	ρ_S	kg m^{-3}	1000
Young modulus	E	$\text{kg m}^{-1} \text{s}^{-2}$	$5.5 \cdot 10^6$
Poisson ratio	ν	-	0.4
length beam	l	m	0.35
height beam	h	m	0.02
radius cylinder	r	m	0.05
length domain	L	m	2.5
height domain	H	m	0.41

**(a)** consistentICO**(b)** pmdisothermRelease**Figure 5.17.:** Solution of the Hron and Turek FSI calculation performed by Tukovic [42] and isothermal compressible *pmdRelease* solver

stages. For the first two seconds, the fluid calculation is decoupled from the solid so that the flow solution can evolve through the calculation domain. Afterwards, the FSI coupling is engaged, and the oscillation emerges until periodicity is reached.

Figure 5.17b shows the results for the modified solver and calculation procedure. The first difference is the time it takes until the oscillation reaches its stationary equilibrium. Case 5.17b reaches it at 2.5 seconds, while for case 5.17a, it takes 3 seconds. This

deviation results from the PIMPLE algorithm, which develops much faster through the fluid domain, and an already stationary flow situation exists during coupling. The oscillation frequency is identical to 5.5 Hz for both calculations. The same statement can be made about the oscillation amplitude, which deviates by five percent. The difference might be attributed to the added mass effect and thus to the compressibility. Therefore, the FSI coupling is considered verified and validated for macroscopic deformations so that only the transition towards EHL contacts remains to be investigated.

Comparative Lubrication Film Thickness Calculations The transition towards EHL calculation is done next. This investigation determines if the central film thickness h calculated with the new framework matches the expected values. According to Dowson and Toyoda [71], the calculation presented in section 2.5 in equation 2.60 is used as a reference for comparison.

The used case setup for the fluid and solid domain is finally the one introduced earlier, depicted in figures 4.14a, and 4.14b. The calculation is brought to convergence for varying target loads Q , temperatures T , and surface velocities u_e . For this calculation, the Doolittle-Tait equations were used. Based on Bair [72, p.121], the parametrization is listed in table 5.5 and corresponds to SAE 20 mineral oil.

Table 5.5.: Parameters for the free volume theory model based on equation 2.41 and Tait model based on equation 2.35 and 2.33

Doolittle Equation Parameters										
	η_{ref}	Unit	T_{ref}	Unit	B	Unit	R_0	Unit	ε	Unit
SAE 20	0.109	Pa s	293	K	3.52	—	0.698	—	$-1.03 \cdot 10^{-3}$	K^{-1}
Tait EoS Parameters										
	ρ_{ref}	Unit	K'	Unit	a_v	Unit	K_∞	Unit	K_0	Unit
SAE 20	878	kg m^{-3}	10.4	—	0.0008	K^{-1}	-0.928	GPa	580.7	GPa K

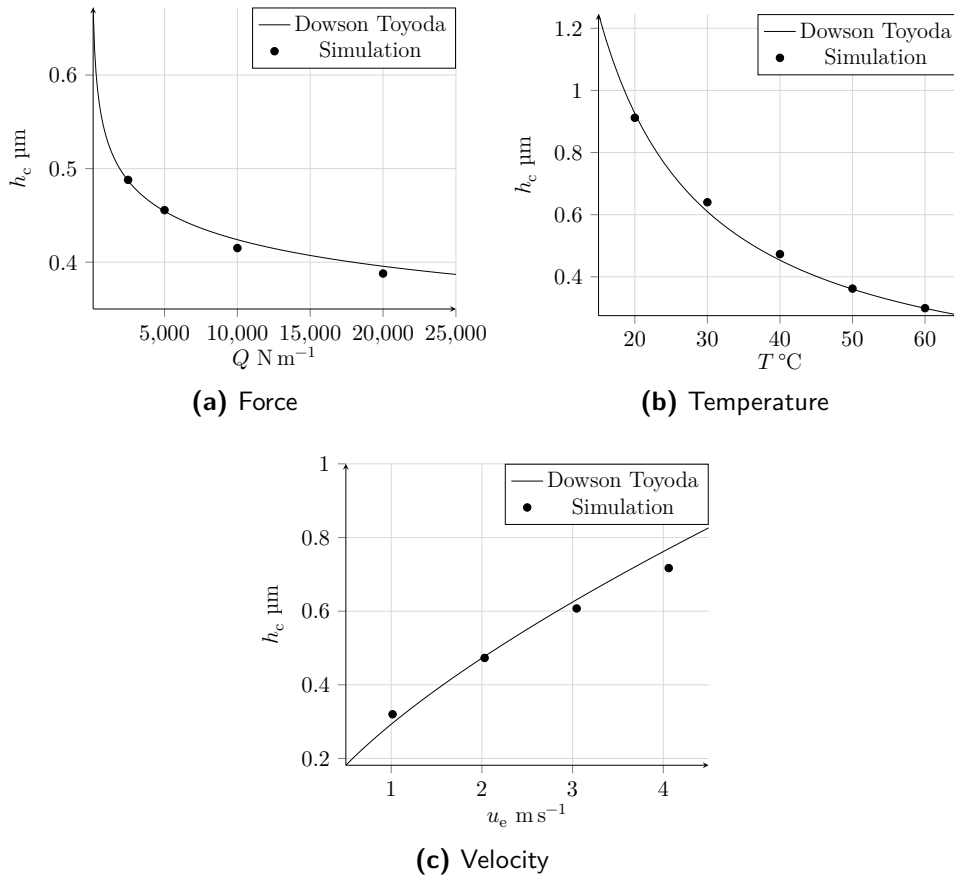
Therefore, the distance between the solid domain rolling element and the semi-infinite surface is adapted to equation 4.4 until the target load is reached. The resulting lubrication film which carries the applied load is compared to the analytical calculation of the EHL lubrication film thickness of the same parameter combination. The aim is to get a first benchmark on how close the setup and program can reproduce known approximations for the main property h that is necessary to calculate the overall system's capacity accurately. For the calculation, load, entrainment velocity, and temperature were varied according to table 5.6.

All calculations were carried out with an $\text{SRR} = 0$. Figure 5.18 shows three graphs with an approximation for the central lubrication film thickness according to Dowson and Toyoda with varying force 5.18a, ambient temperature 5.18b, and entrainment velocity 5.18c. While one parameter was changed, the others were kept at the initial value.

The Dowson-Toyoda approximation accurately reproduces the central lubrication film thickness and considers the characteristic changes in h for the varied parameters. With increasing load, the central lubrication film thickness decreases as expected. The same

Table 5.6.: Parameters for central film-thickness calculations

Case Parameters					
Load Q	Unit	Velocity u_e	Unit	Temperature T	Unit
[2.5; 5; 10; 20]	kN m^{-1}	2.03	m s^{-1}	293	K
5	kN m^{-1}	[1.01; 2.03; 3.04; 4.06]	m s^{-1}	293	K
5	kN m^{-1}	2.03	m s^{-1}	[293; 303; 313; 323; 333]	K

**Figure 5.18.:** Central film-thickness h_c plotted over force, temperature and velocity; Comparison between Dowson-Toyoda reference calculation and numerical results

goes for the overall oil temperature. A reduction in temperature decreases the dynamic viscosity η and thus the film thickness h . On the contrary, an increase in velocity increases the central lubrication film thickness h , which follows the theory.

Some selected values over the range of parameters calculated with Dowson Toyoda were also calculated numerically with the developed approach, and the stationary solution for the central lubrication film thickness h is added to the plots. As shown in figure 5.18, the central lubrication film thickness, taken from the calculations matches the expected values well. A slight underestimation for increasing surface velocities is detectable in figure 5.18c. The same observation is made for increasing forces in figure 5.18a. The

simulation, however, behaves accurately for increasing temperatures, which is essential. The calculation approach delivers the tested range of parameters compared to the film thickness calculation. However, one must consider the results under one restriction. The load applied to the contact is not yet in the range of actual EHL numerical calculations. The calculated lubricant film thicknesses might be according to the approximation but results in very high film thicknesses of at least $0.3 \mu\text{m}$ corresponding to pressures in the lubricant of 500 MPa .

Table 5.7.: Dimensionless parameters for the central film-thickness comparisons to Dowson-Toyoda reference calculation and numerical results

Dimensionless Quantities			
Parameter	Variable	Unit	Value
Dimensionless load parameter	\bar{W}	-	$0.343 - 2.75 \cdot 10^{-5}$
Dimensionless velocity	\bar{U}	-	$1.2 - 4.78 \cdot 10^{-10}$
Dimensionless geometry	\bar{G}	-	$0.0575 - 6.9 \cdot 10^3$

Compared to known solutions from EHL numerics, this just reaches the relevant area. The deformations known from the literature are obtained for high loads. Thus, the lubrication film thicknesses decrease to $0.1 \mu\text{m}$, increasing the deformation. Only then do phenomena such as a Petruszewski peak become visible. The load applied here corresponds to a dimensionless load parameter $\bar{W} = 0.343 - 2.75 \cdot 10^{-6}$. Therefore, a last comparative calculation with literature is carried out next.

Isothermal EHL Contact Before entering the results concerning experiments and other aspects, this last case is based on a publication by Hartinger et al. [32, p.6]. An isothermal EHL simulation with a $\text{SRR} = 0$ is presented.

Even though the work is concerned with the impact of shear-thinning on the lubricants behaviour, a SRR of zero leads to a case that does not consider shear dependence, especially since this behaviour is only considered above a limiting shear rate, as discussed in section 2.3.2. A modified version of the Dowson EoS (equation 2.32) is used throughout the calculations presented in Hartinger's work. The viscosity description at low shear rates follows the second Roelands model 2.40 due to an isothermal simulation. Those models for density and viscosity are also included in the present calculation framework and are used to keep the comparability high. The case geometry coincides with the one presented in figure 4.13. The parameters used for the comparative calculations were set identically and are listed in table 5.8.

The listing is subdivided into geometrical properties, those for the EoS, low shear viscosity model η , and solid properties, respectively. It has to be pointed out that the calculation differs in solid domain handling. The reference case was calculated with a deflection method, based on the Hertzian contact back in the days, while the current calculation is performed with the finite volume approach as discussed in the fundamentals. The calculation was divided into three steps. First, the fluid solution was calculated until a stationary solution was reached. This result was then used as the initial guess

Table 5.8.: Hartinger et al. [32] reference case parameter list; Compare to figure 4.13

Case Parameters			
Parameter	Variable	Unit	Value
Geometry			
Radius	r_R	mm	10
Initial lubrication film	h_0	μm	0.1
Entrainment velocity	u_e	m s^{-1}	2.5
SRR	-	-	0
Fluid			
Density	$\rho_{\mathcal{F}}$	kg m^{-3}	850
Dynamic viscosity	η	m^2s^{-1}	0.01
Roelands reference pressure	p_{ref}	Pa	$1.98 \cdot 10^8$
Roelands pressure index	z	-	0.6
Solid			
Reduced Young's modulus	E'	$\text{kg m}^{-1} \text{s}^{-2}$	$3.45 \cdot 10^{11}$
Load	Q	N m^{-1}	$1 \cdot 10^5$
Dimensionless Quantities			
Dimensionless load parameter	\bar{W}	-	$0.09 \cdot 10^{-4}$
Dimensionless velocity	\bar{U}	-	$7.25 \cdot 10^{-12}$
Dimensionless geometry	\bar{G}	-	$8 \cdot 10^3$

for the coupling problem. Finally boundary displacement was applied in the third step to bring the solution closer to the target load.

While the initial coupling, at around ten percent of the target load, converged satisfactorily, instabilities occurred during the adaption of the solution. As the pressure approached actual EHL regions, larger than $p > 2 \cdot 10^8$ oscillations set in between the fluid solution and the displacement of the solid, ultimately leading to divergence above twenty percent of the target load, needed for comparison to the Hartinger calculation. Results for the different stages are shown in figure 5.19.

The problem can best be visualized via the pressure integral at the FSI interface. The force acting on the surface was tracked for each solver iteration. Figure 5.20 shows the build-up in force for the initial fluid solution without FSI coupling.

As expected, the pressure build-up during the fluid solution develops without problems. After the coupling between fluid and solid was activated, oscillations already occurred within a time-step, which subsides over several FSI iterations. However, the initial coupled solution reached convergence with a pressure distribution corresponding to the calculations before. The increase in pressure, and stronger deformations due to the reduced distance between the inner ring and the rolling element, also led to increased vibrations in the FSI sub iteration until divergence occurred due to a detachment of the interface due to excessive distortions. The course of the interface pressure force for this situation is shown in figure 5.21.

Figure 5.21a shows the same starting procedure towards an initial stationary state as

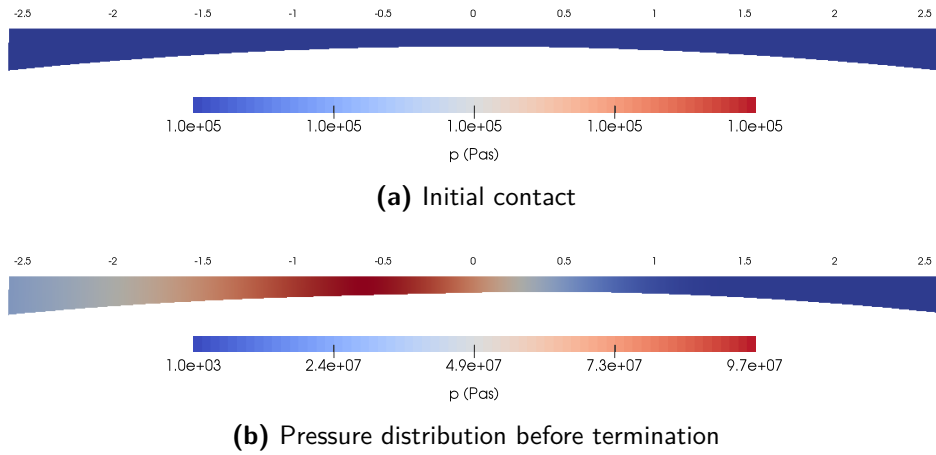


Figure 5.19.: ParaView visualization for the Hertzian deformation

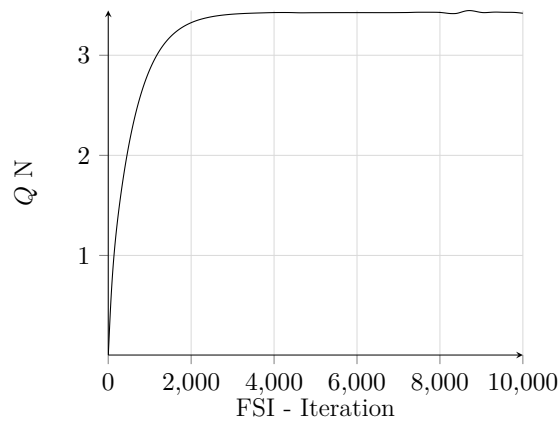


Figure 5.20.: Load Q plotted over FSI - Iteration for fluidFoam

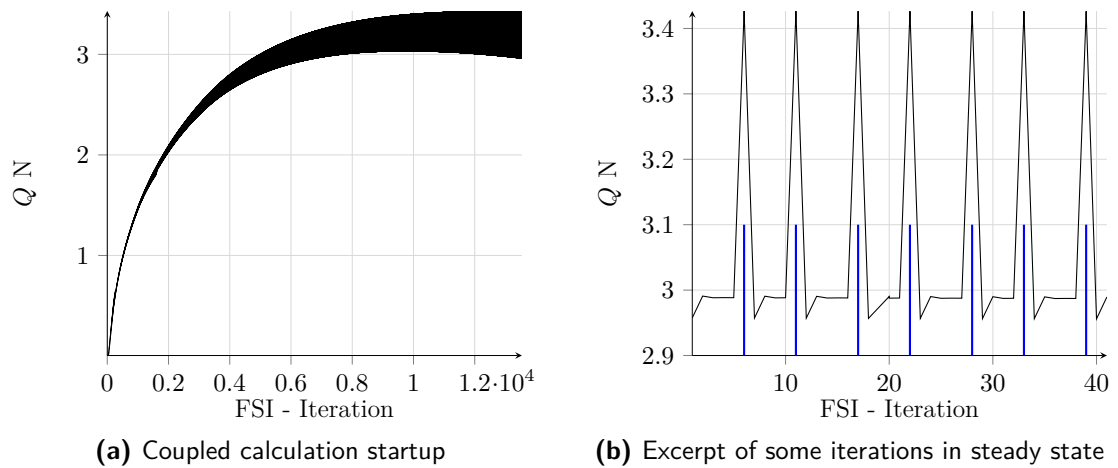


Figure 5.21.: Load Q plotted over FSI - Iteration for *fsiFoam*

for the uncoupled case in figure 5.20. For a better illustration of the problem, some FSI cycles at the end of the calculation are extracted in figure 5.21b. Blue lines are added to indicate where a new time-step was entered. The problem presented here could not be overcome despite various approaches. Unfortunately, the experimental data's parameter combinations also fall above the calculable contact pressures. However, it is nevertheless presented as this data is precious and can be used for future reconciliation with EHL calculations.

5.4. The Capacity of Rolling Bearing Contacts

Now that the program's primary verification and validation are complete and limits for applicability are determined, the actual calculation of capacities and charge transport processes is approached. The first step is calculating single rolling bearing capacities compared to experimental data.

The problem is the availability of experimental data suited for comparison. Most investigations are concerned with regular rolling bearings and overall life-time estimations in electric signals like Gemeinder [16] or Schirra [15]. Even if such data are available, the electric signal is the sum of multiple capacities from undetermined operating conditions, leading to capacity data representing a network of different capacities, as indicated in figure 1.3 during the introduction of this work. Since these experiments do not allow signal separation and thus inference to the individual contact, these data are troublesome for investigating a single contact.

Such data are hard to interpret with a tool designed to resolve only a single contact. In addition to this, only a few experiments are concerned with electrical phenomena, and most of these are only concerned with damaging mechanisms, which adds to the problem of finding appropriate data. For the above reasons, experiments were carried out to generate data suited to compare numerical results. The primary requirement was reducing the signal to a single rolling element. The experimental approach to achieve this is presented next. Afterwards, the data collected with the setup are introduced. The test-rig parameters are then translated to the numerical setup, and finally, the experimental results are compared to the numerical data.

5.4.1. Hybrid Bearing Experiments

Jablonka et al. [43] designed an experimental setup to estimate lubrication film thickness through capacity measurements and coincidentally created a reference experiment that allows for the comparison to numerical data obtained by the approach presented here. Figure 5.22 shows a schematic representation of the experimental setup used by Jablonka et al. [43, p.15].

The test-rig consists of an electrically insulated hybrid rolling bearing. The inner and outer rings are wired to an electric circuit so that the entire rolling bearing is connected in parallel to a reference capacitance. Also connected is a Lubcheck system, which imposes an electric signal on the circuit and receives the response signal. An oscilloscope

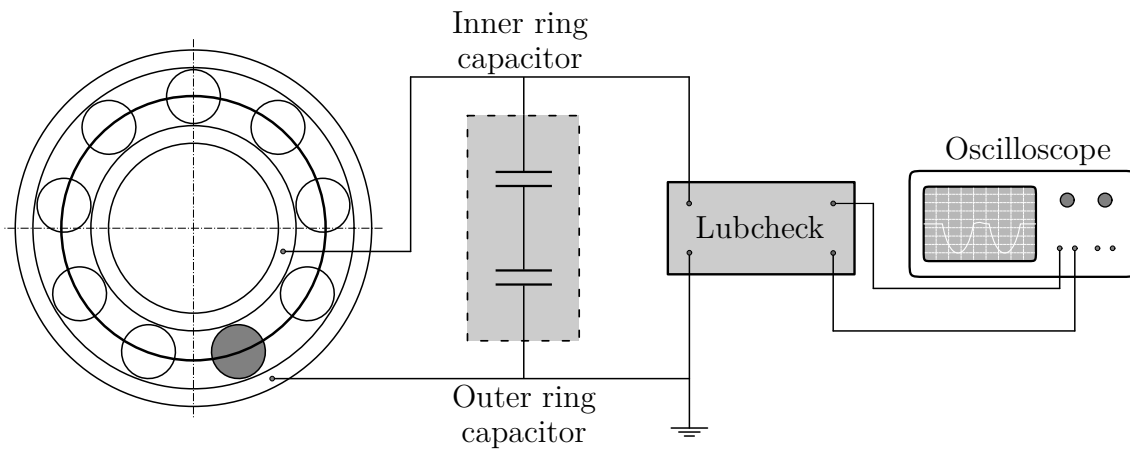


Figure 5.22.: Experimental setup according to Jablonka et al. [43]

is connected to the Lubcheck system to read the voltage and current signals and save them for post-processing.

Hybrid bearings are rolling bearings in which the metal rolling elements were replaced with ceramic ones. Typically ceramic rolling bearings are used only for special applications like corrosive environments. Ceramic components are very expensive and complicated to handle. The advantage of ceramics, based on silicon carbide, is that it is an insulator and thus, can be neglected for the bearings' capacity. To get information about the lubrication film thickness for radially loaded rolling bearings during its revelation, Jablonka et al. [43] measured the difference in capacity between the inner and outer ring of the bearing. They installed a single rolling element made of steel so that the measured signal only corresponds to this rolling element. Together with a plastic, non-conducting cage material, the measured signal was reduced to two corresponding rolling bearing contacts.

Due to rotational speed and radial load, the rolling bearing capacity in the circuit carries information about the operating condition. Experiments were carried out by Jablonka et al. [43] for different radial loads $F_R = 1 - 6$ kN. The tests were carried out for a 6306 ETN9 deep-groove ball bearing and a Schell Turbo T100 lubricant. Since this is a different rolling bearing and a different lubricant as considered in this work, the non-dimensional load and velocity are listed instead of the absolute values to establish comparability. Since test-rigs and bearings differ for different publications, it is reasonable to calculate the dimensionless velocity and geometrical parameter to increase comparability. The experimental parameters were de-dimensionalised according to equations 2.58 and 2.57. The dimensionless velocity \bar{U} calculates to $15.4 \cdot 10^{-12}$; the dimensionless radial load \bar{W} is found in table 5.9.

A crucial part of this setup is the correct interpretation of the signal. Therefore, a model for the lubrication film thickness based on the dynamic viscosity and compressibility is needed. Furthermore, the lubricants' permittivity must be known. The calculation of the dielectric constant to calculate the capacitance in the experiments by Jablonka et al. [43, p.241] was done density-dependent, based on Tait's equation of state with parameters provided by Bair et al. [28] for a mineral oil-based lubricant which therefore

Table 5.9.: Test parameters for the Jablonka et al. experiments and the according temperature corrected values

Dimensionless Quantities	
Velocity \bar{U}	Load \bar{W}
$15.4 \cdot 10^{-12}$	$4.3 \cdot 10^{-5}$
	$8.60 \cdot 10^{-5}$
	$1.30 \cdot 10^{-4}$
	$1.73 \cdot 10^{-4}$
	$2.16 \cdot 10^{-4}$
	$2.59 \cdot 10^{-4}$

increases the comparability of these experimental data to the ones performed for this work. Also, the equation of state is already present in the calculation framework. While the approach is quite intriguing, a significant flaw comes with it. Ceramic materials and rolling bearing steel differ in Young's modulus, heat expansion and Poisson ratio. These differences lead to an abnormal, temperature-dependent load-carrying behaviour. This circumstance was not taken into account in the experiments since the load capacity of the ceramic ball varies with the applied force. For this reason, but also due to a deviating bearing geometry, and lubricant choice, the experiments were repeated.

5.4.2. Temperature Corrected Hybrid Bearing Experiments

Because not all experimental parameters are traceable from the work of Jablonka et al. [43], and due to the identified flaw of the setup, their experiments were repeated for this work. Therefore, a slightly different experimental approach based on the work by Schirra et al. [11] was used¹. As it has just been described, the main difference in the experimental setup is using a Wheatstone bridge as an electrical circuit to measure the impedance of a 6205 C3 hybrid rolling bearing. The Wheatstone circuit is shown in figure 5.23.

Analogue to the experiments by Jablonka et al. [43], ceramic rolling elements were used in between the metallic bearing rings. The rolling elements were separated by an insulating plastic cage, which is a standard part for 6205 C3 rolling bearings. As can be seen in appendix D a total of four bearings were used in the test-rig. Three standard ceramic bearings and the hybrid bearing as test object. The test bearing was flooded with FVA 3 reference oil as an operating lubricant during the run. The test-setup is equipped with temperature control for the oil reservoir. By this means, the oil feed temperature is adjustable. This feature of the test-rig was used to compensate for the difference in stiffness between the ceramic rolling elements and the steel rolling element. The deviating deflection for different loads was compensated by thermal expansion to achieve an even load distribution. The thermally corrected test parameters are listed in table 5.10.

¹The schematic experimental setup is shown in appendix D

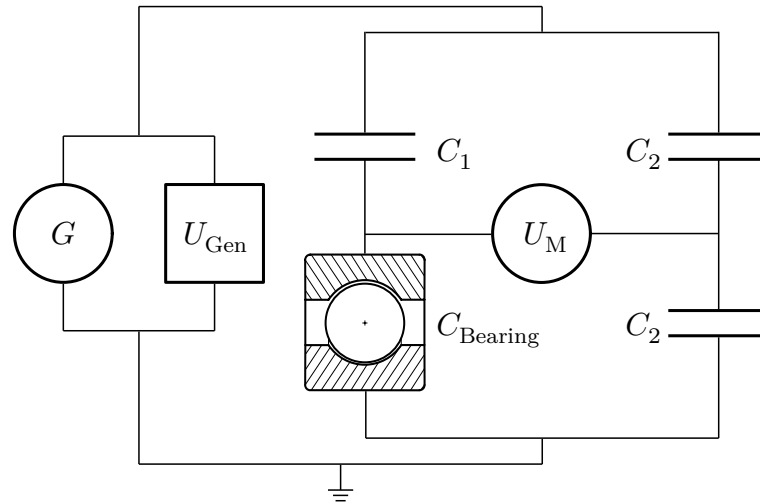


Figure 5.23.: Wheatstone bridge circuit diagram with test bearing capacity C_{Bearing} according to Puchtler et al. [102]

Table 5.10.: Input parameters for a full factorial experimental plan including temperature correction

		Experimental Quantities		
Voltage V	Frequency kHz	RPM (\bar{U})	Load kN (\bar{W})	Temperature K
6	5	2000 ($1.94 \cdot 10^{-9}$)	1 ($2.76 \cdot 10^{-4}$)	304.4
			2 ($5.52 \cdot 10^{-4}$)	312.3
			3 ($8.28 \cdot 10^{-4}$)	318.6
			4 ($1.10 \cdot 10^{-3}$)	324.97
			5 ($1.38 \cdot 10^{-3}$)	330.35
			6 ($1.65 \cdot 10^{-3}$)	335.45
	4000 ($3.88 \cdot 10^{-9}$)	1 ($2.76 \cdot 10^{-4}$)	304.4	
		2 ($5.52 \cdot 10^{-4}$)	312.3	
		3 ($8.28 \cdot 10^{-4}$)	318.6	
		4 ($1.10 \cdot 10^{-3}$)	324.97	
		5 ($1.38 \cdot 10^{-3}$)	330.35	
		6 ($1.65 \cdot 10^{-3}$)	335.45	

The radial loads F_R were applied in 1 kN steps. The 6205 C3 rolling bearing, rotated with 2000 RPM and 4000 RPM. From the bearing information and the operating conditions in table 5.10, parameters for the numerical case setup, presented in section 4.2 can be derived. The case parameters are listed in table 5.11.

In addition to the listed experimental parameters, a parameter set for the used FVA 3 reference oil is needed. The lubricant model parametrization for a Doolittle-Tait approach is listed in table 5.12. Each test was carried out with an oil feed temperature according to the compensation temperature needed for the applied radial load. The thermal adjustment was done prior to the measurements so that the oil feed temperature

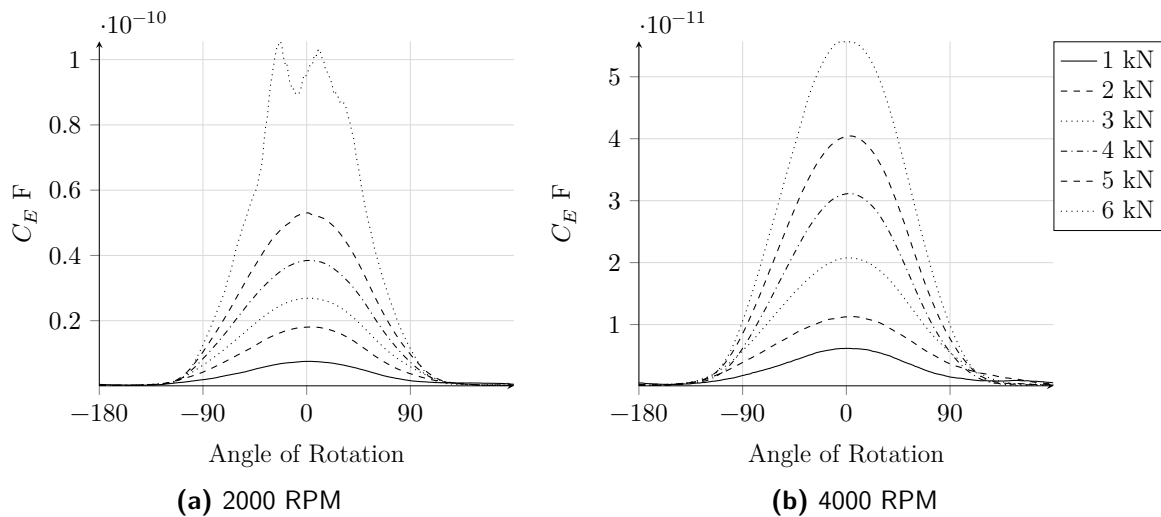
Table 5.11.: Geometry parameter for 6205 C3 rolling bearings

6205 C3 Bearing			
Parameter	Variable	Unit	Value
Geometry			
Radius	r_R	mm	3.69
Initial Lubrication film	h_0	μm	0.1
Entrainment Velocity	u_e	m s^{-1}	1.63, 3, 26
SRR	-	-	0

Table 5.12.: Parameters for the free volume theory model based on equation 2.41 and Tait model based on equation 2.35 and 2.34 for FVA 3

Doolittle Equation Parameters										
	η_{ref}	Unit	T_{ref}	Unit	B	Unit	R_0	Unit	ε	Unit
FVA 3	0.049	Pa s	288	K	2.7	-	0.8	-	$-0.8 \cdot 10^{-3}$	K^{-1}
Tait EoS Parameters										
	ρ_{ref}	Unit	K'	Unit	a_v	Unit	K_{00}	Unit	β_K	Unit
FVA 3	875	kg m^{-3}	11.5	-	0.0011	K^{-1}	-11	GPa	6.9	mPa

is expected to match the system's temperature. A 6 V AC voltage with a frequency of $f = 6$ kHz was used as a measuring signal. From the received voltage and current signals, the impedance Z and thus capacity C_ε were recalculated. Figure 5.24b shows the capacity change for one revolution of the steel ball.

**Figure 5.24.:** Capacity C_{Bearing} plotted over angle of rotation data gathered by Mulrav [133] for the hybrid bearing test-setup

Strictly speaking, the shown signal is the average over several rotations. With the knowl-

edge about the rotational speed and capacity relative to the rolling element position, the samples from the signal were averaged. While the curves are really smooth for eleven out of twelve parameter combinations, the highly loaded, low rotational speed combination in figure 5.24a deviates from this. The collapse in capacity can be interpreted as discharges during individual rotations as a consequence of exceeding the dielectric strength of the rolling contact or having asperity contacts, leading to an electric current. The dielectric strength describes the resistance of a capacitor to discharge via electric flashovers, thus the EDM process. The tribological condition is subject to statistical fluctuations and thus the discharge or contact only occurs during some rotations, leading to the shown graph after superposition. However, for the rest, a high statistical certainty was achieved. This can be seen when the peak values are plotted against each other with their statistical standard deviations. Figure 5.25 shows these plots for 2000 RPM and 4000 RPM.

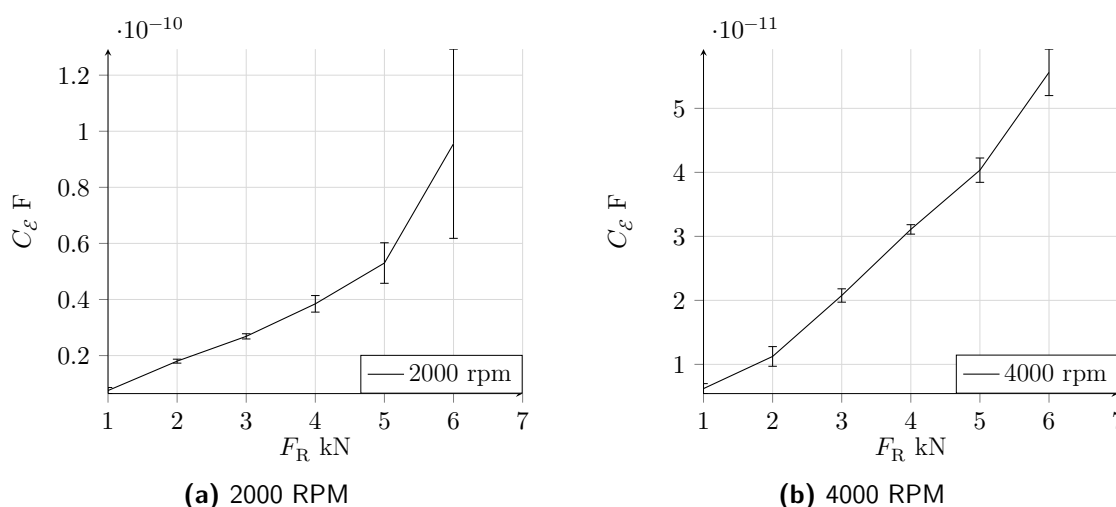


Figure 5.25.: Peak capacity C_ε plotted over radial load F_R ; Standard deviation added for the average over several rotations

Especially for smaller loads, the standard deviation is low. For increasing load, the standard deviation also increases. The irregularities for the 6 kN case at 2000 RPM now becomes apparent. A high load, paired with a slow rotational speed, led to a disadvantageous state, which is probably beyond what is replicable with the program architecture since solid body contact and actual discharge phenomena were not in the scope in the beginning. Either way, considering the limitations identified in section 5.3 it is currently not possible to validate the calculation framework against this experimental data. To illustrate this, it is worth comparing the loads used for validation in figure 5.18a with the 2D loads calculated in the table 4.6 for the experimental parameters. Currently, the whole solver is only validated for loads up to 20.000 N m^{-1} while the minimum value for comparing experimental data to numerical calculations requires at least 136.000 N m^{-1} . Applying such a load to the numerical calculation results in the oscillations as it was presented in section 5.3 during the comparison to the Hartinger

et al. [32] case. For the current state of affairs, calculations are therefore only possible for the areas of isoviscous-rigid and piezoviscous-rigid EHL behaviour (figure 2.8 for comparison). Thus, characteristics like the Petrusevish peek will not be found for the following calculations, since such Elastohydrodynamic Lubrication (EHL) phenomena are related to the piezoviscous-elastic lubrication regime.

5.5. Further Investigations

Even though the comparison to experimental data was not feasible, due to the reasons identified in section 5.3, two more aspects were investigated. In this way, the basic usability of the developed functions and implementations is elaborated more. Two examples from the field of experimental rolling bearing research at the pmd are used for this purpose.

The impact of surface imperfections on the electro-tribological condition of a rolling bearing contact was investigated by Martin [124]. For this, he engraved structures into the raceways of rolling bearings using laser lithography. These prepared bearings were run in the same test-setup as presented for the reference measurements in section 5.4.2. The structured surfaces were measured three-dimensionally to determine characteristics like mean surface roughness and asperity heights. Some of these data sets (Stereolithography (STL) data) were embedded into the numerical case for this work. The results that could be produced within the current limits of the framework are presented next. Some calculations for the transport of charges and their impact on the electric field are presented afterwards to answer the third research question from chapter 3. The results were produced in the context of experimental observations made by Harder et al. [123] and offer a first explanatory approach for their results. The findings by Harder et al. [123] are therefore summarized.

5.5.1. Surface Imperfections

Integrating surface features into the analysis is highly relevant for the research on electrical phenomena in tribological systems. While the predictability of an ideal contact is high with the expressiveness of analytical or empirical descriptions, it decreases rapidly for a tribological system with, for example, distorted geometries. Accordingly, an extension of the calculation to this topic is beneficial. Therefore, some available data from experiments with impaired geometries by Martin [124] were used. The data which are presented in the following section were gathered by Zaiat [134]. The measured geometric features, provided by Martin [124], were embedded into the case design presented in section 4.2. Figure 5.26 visualizes the surface textures as received from Martin [124].

The aim of this calculation is, on the one hand, to present a process for implementing such realistic data in the calculation framework and, on the other hand, to show the results of a complete, convergent, run with the calculation procedure presented in section 4.1.3, figure 4.7. The naming of the surface data was retained from the originator as L7 and K11 for simplicity. The main difference between these two surfaces is the depth

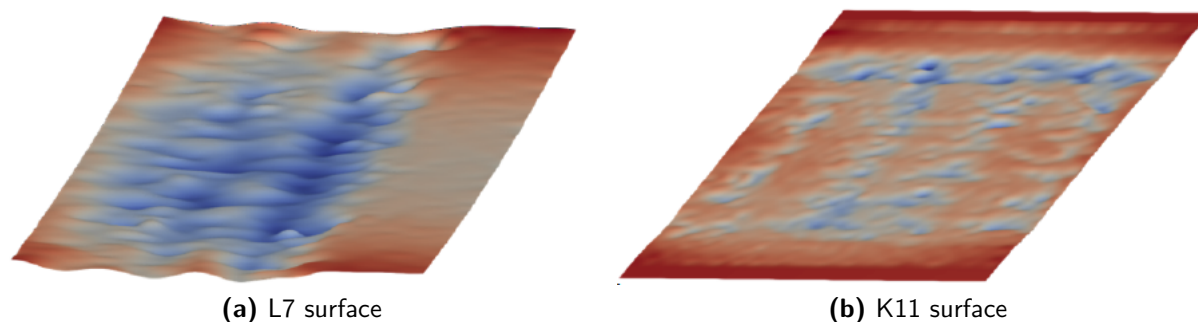


Figure 5.26.: Measured Surface imperfections by Martin [124]

of the damage. The calculations were conducted with a height profile taken from the centreline of each dataset, which was inserted into the two-dimensional grid. Figure 5.27 displays the resulting fluid and solid domain geometry.

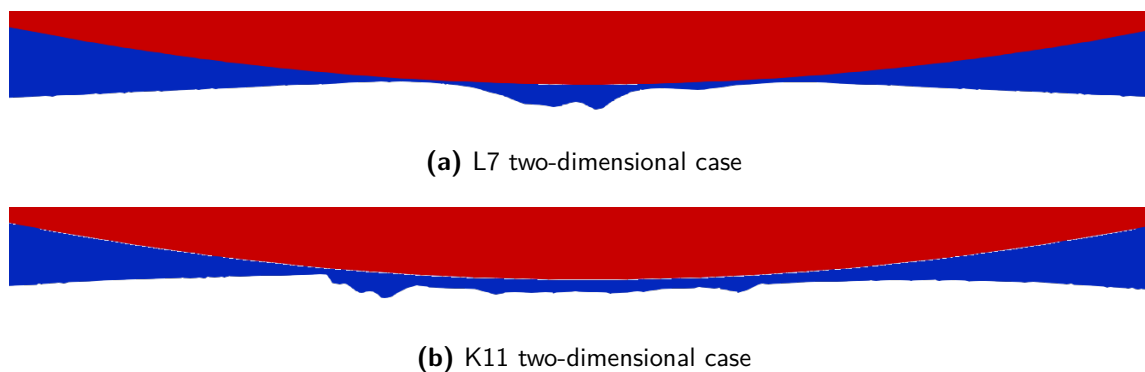


Figure 5.27.: Integration of 5.26a and 5.26b centerline into 2D numerical Grid

Figures 5.27a and 5.27b only show the calculation domain's inner region, matching the R4 section in figure 4.16 earlier on. Figures 5.27a and 5.27b display approximately $0.1 \mu\text{m}$ in the positive and negative direction of rolling. The red area in figure 5.27 represents the rolling element, while the contour line of the blue displays the surface profile of the fluid grid at the surface of the ring.

Based on this, calculations were carried out within the restrictions discussed in section 5.4.2. The pressure distributions for the converged calculations are shown in figures 5.28b and 5.28c. Figure 5.28a shows the pressure profile for the reference case for comparison. As already pointed out, the calculations were performed for load characteristics, small enough to ensure convergence. While initial tests failed to converge, the entrainment velocity was increased to obtain stable solutions. Thus, notice the maximum pressure p below $< 70 \text{ MPa}$ for the reference calculation. Especially for the K11 case, pressure peaks occurred at the asperities. As this does not result in a uniform pressure profile, the distances between rolling elements and asperities become very small as the load-bearing capacity is severely lowered. This reduction in load-bearing capacity added to the limits for the calculation. Accordingly, there was already an enormous pressure at

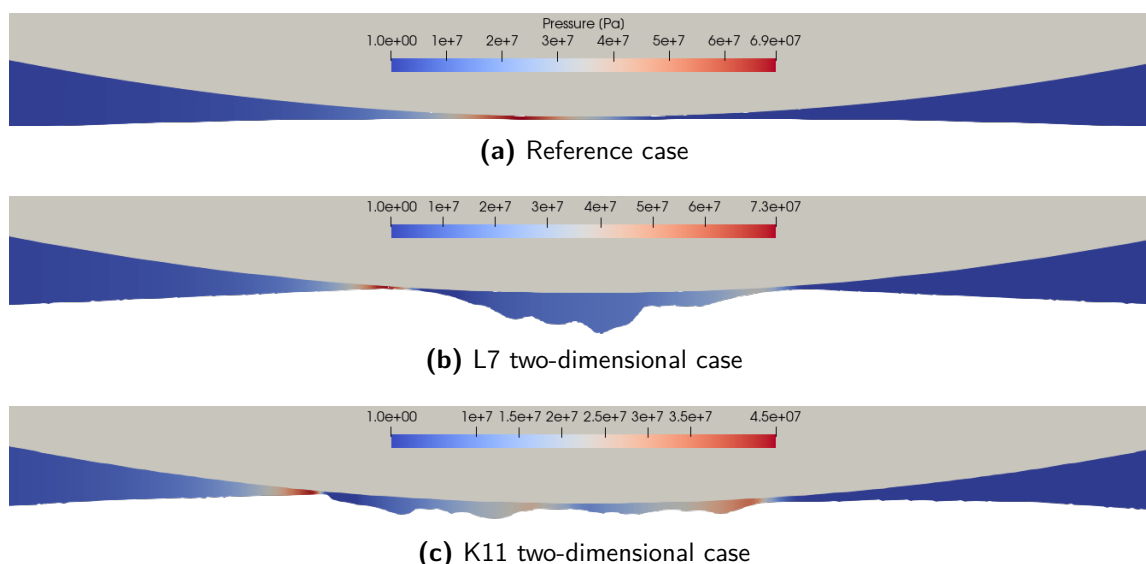


Figure 5.28.: Pressure distribution for $T= 313$ K, $u_e= 2.03$ m s $^{-1}$

this point for low loads, which quickly rose beyond the limits for convergence. Figure 5.29 visualizes this problem.

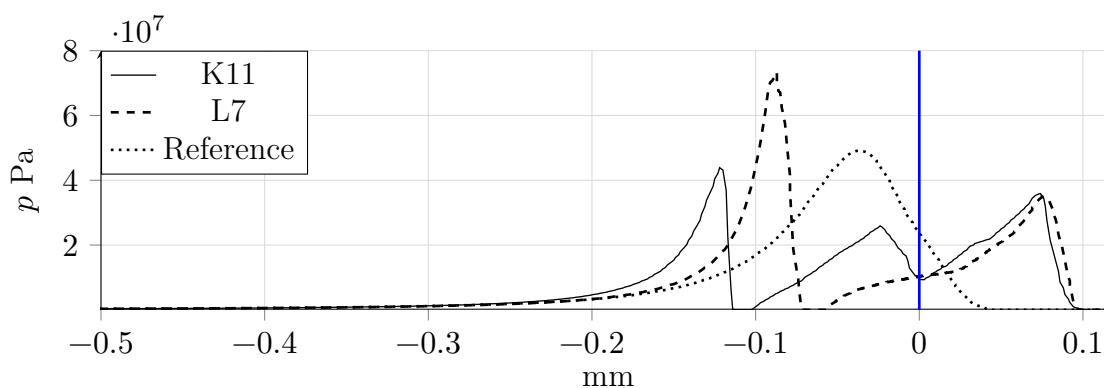


Figure 5.29.: Pressure p plotted over EHL contact length for the imperfections; Blue line - centre of the EHL contact

The pressure profiles for the K11 and L7 case shown deviate very firmly from the ideal pressure distribution. This deviation makes it understandable why a calculation based on an analytical theory like Dowson-Higginson cannot reproduce realistic results for distorted surfaces of any kind. However, the calculation could be stably conducted for the entire process for these low radial loads, as presented in chapter 4. Thus, the electric field was calculated, considering the density-dependant changes in permittivity ϵ . The result for the electric field is shown in figure 5.30.

What is exciting about figures 5.30b and 5.30c compared to figure 5.30a is the local increase in electric field strength. These local maxima indicate that non ideal surfaces are more likely to induce electrical damage mechanisms. The local pressure peak values

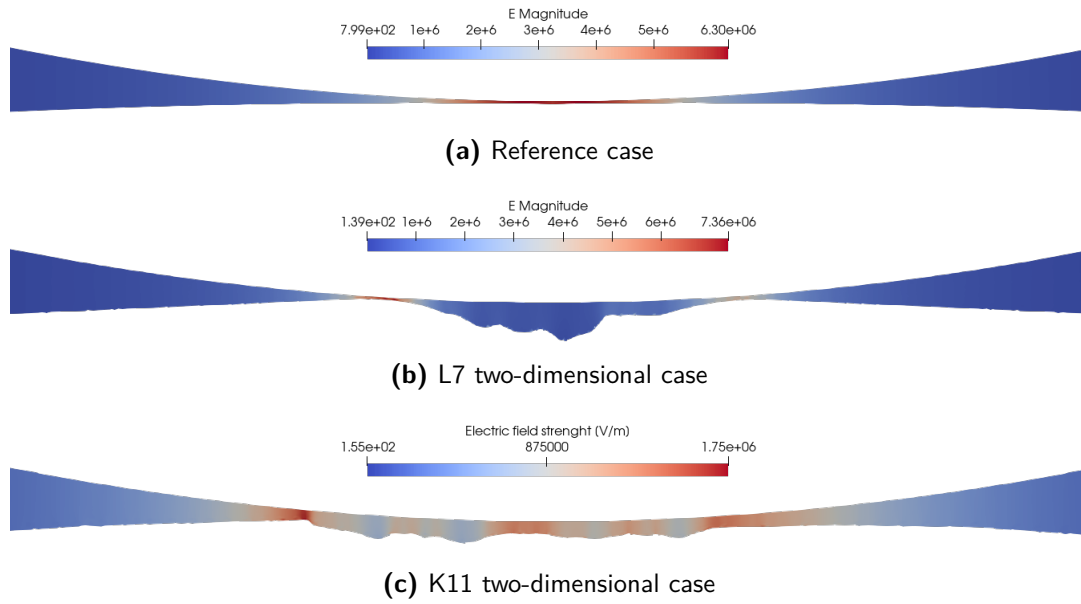


Figure 5.30.: Electric field for $T= 313$ K, $u_e= 2.03$ m s $^{-1}$

amplify this effect since the permittivity is affected directly. Figure 5.31 shows the local increase in permittivity as a state function of pressure p and temperature T , according to the explanations in section 2.6.4.

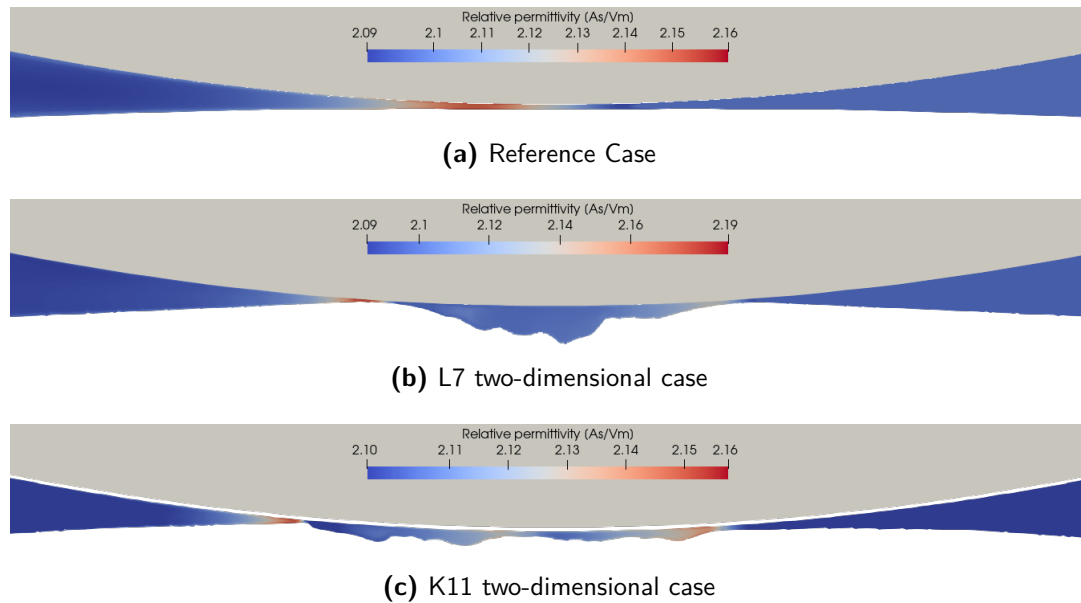


Figure 5.31.: Relative Permittivity ϵ_r for $T= 313$ K, $u_e= 2.03$ m s $^{-1}$

A quantitative evaluation of the results is not purposeful at this point since the solver has not been validated against experimental data jet. However, some qualitative statements are possible especially with regard to analytical considerations. Even for low loads,

the impact of the surface imperfections on the electric field strength is apparent. The asperities lead to local peak values in the electric field, and also, the pressure build-up is heavily distorted. Actually the pressure profiles are far from the reference solution which shows how little meaningful the reference solution or corresponding analytical considerations are in the context of non ideal conditions. In combination with the local changes in permittivity, onset points for damaging phenomena are identifiable. Therefore, it is inevitable to approach future investigations on the basis of numerical calculations. Even if a more in-depth evaluation of these calculations is not purposeful since no realistic EHL pressures were reached, it is a first step towards analysing electric fields in distorted rolling bearing contacts. Such analysis could be used for future research to adapt existing impedance models concerning degradation mechanisms.

5.5.2. Charges in Rolling Bearing Contacts

One important topic often addressed in research of rolling bearing tribology are damage mechanisms due to electric phenomena. One of the most prominent is EDM, which are held accountable for most bearing failures in the context of electricity. While the actual discharge is understood, considering some uncertainty, as described by Küchler [100], the aftermath of a discharge is unclear and its pertinence for the following events.

Harder et al. [123] aimed to estimate EDM currents on the bearing life-time in their experimental studies. The initial finding was that the damaging mechanism needed an initial discharge as a starting point, after which the damaging mechanism establishes. Their experiments suggest a decrease in dielectric strength after the initiation.

The explanatory approach for this observation is that ions reside in the EHL region. The existence of charge-carrying species close/in the EHL area impacts the dielectric strength. Another observation indicates that this state of decreased dielectric strength decays over time if the electric potential is removed from the system. After a specific period, the dielectric strength returns to its initial value.

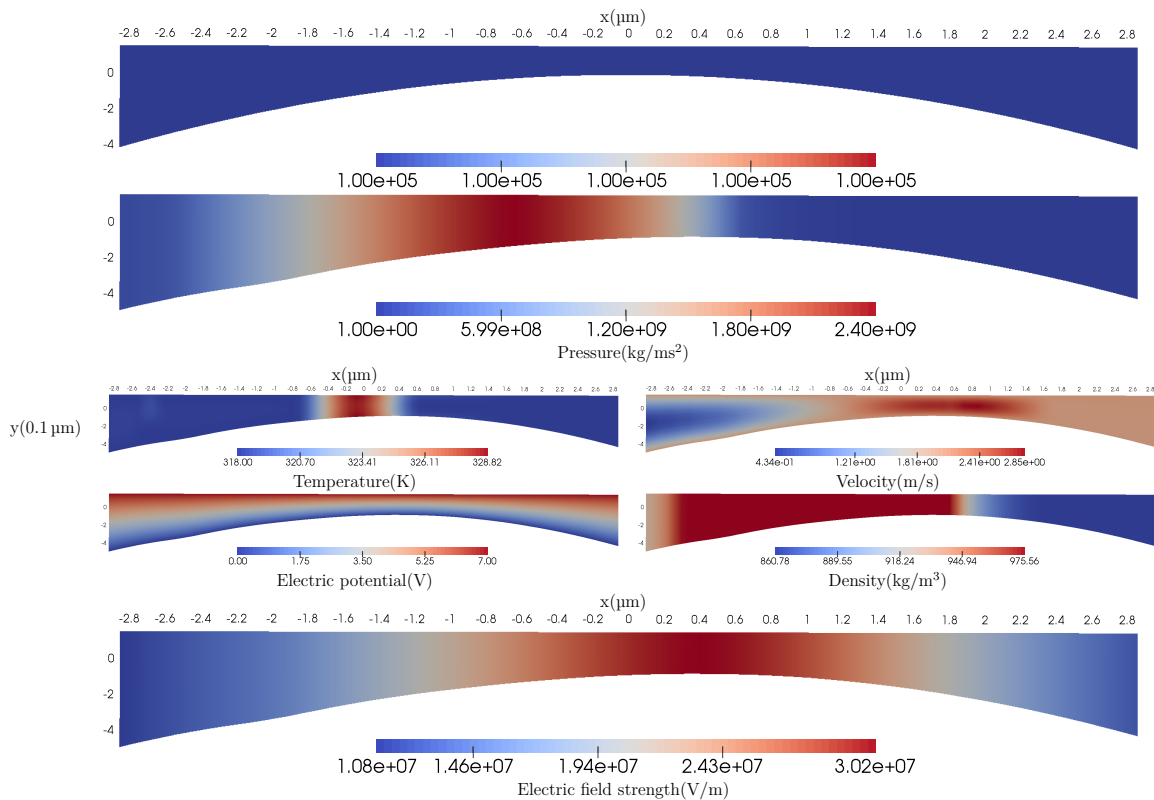
Therefore, tracking ions in the EHL contact as a test for the numerical framework was a natural choice. An example calculation is based on an experimental dataset, and the results are used to calculate the temporal progression of anionic species in contact with the far lubricant field. The shown procedure is intended to be a blueprint for future calculations of underlying electrochemical processes which might be connected to the phenomena of reduced dielectric strength during consecutive discharges. The experimental parameters by Harder et al. [123] are listed in table 5.13 and were used for the numerical case setup.

The fluid and solid parameters are chosen according to the SAE 20 lubricant already introduced in table 5.5. Calculations were carried out for an initial lubrication film thickness of 1 μm , declining until the target load was reached. The numerical results for the thermal FSI calculations are summarized in figure 5.32.

Due to some adaptations in the case setup, the calculations led to an over-prediction in the pressure profile. This is the consequence of the fact that the glass transition was reached in some regions of the calculation area. Subsequently, the density field shows the used limiter values of the density function, which stabilized the calculation but led

Table 5.13.: Experimental Parameters used by Harder et al. [123]

Experimental Parameters			
Parameter	Variable	Unit	Value
Geometry			
Temperature	T	K	318
Electric potential	Φ	V	7
Signal frequency	f	kHz	8
Radial load	F_R	kN	2
Bearing type	6205 C3	—	
SRR	-	-	0

**Figure 5.32.:** TEHL numerical calculation

to named overestimation of the lubrication film thickness. The geometry, thus the solid domain, was then frozen for the following calculation of the ion transport. Only the fluid domain was further calculated, coupled with the electrostatic domain. Before starting this calculation, an initial area was impinged with a charge density ρ_ϵ of one. in the area of highest electric field strength. The added charge could be followed in the process². Since the FSI coupling was deactivated, the time-step size could be increased drastically so that the actual convective transport in the area of lubrication could be followed.

²Sources and sinks were omitted for simplicity

Figure 5.33 displays the temporal development of the charges throughout 10 μs , which is a significant period, compared to the FSI calculations.

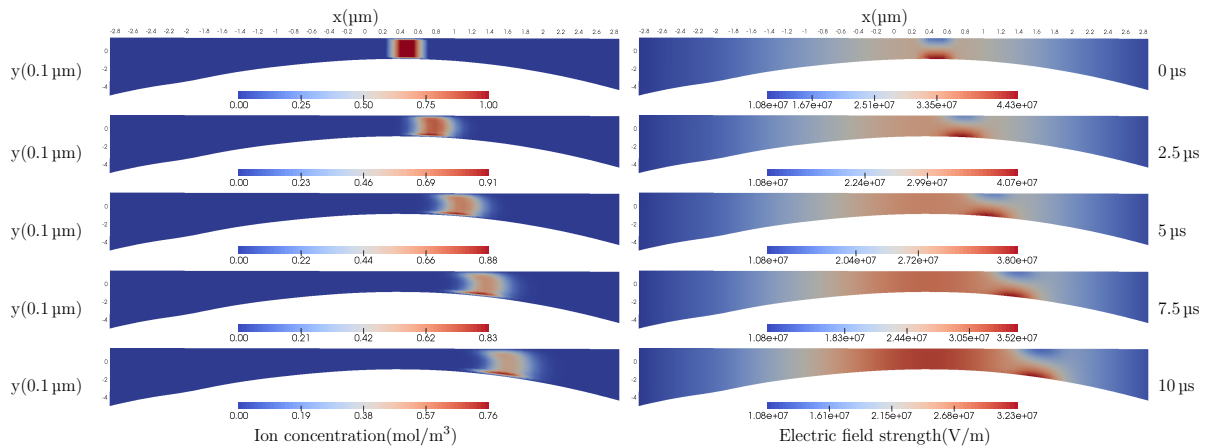


Figure 5.33.: Temporal development of ion concentration for low ionic mobility

The calculations were carried out twice, once for an idealized ionic species with low electric mobility ($10^{-10} \text{ m}^2 \text{ V}^{-1} \text{ s}^{-1}$) as shown and once for the same configuration with high electric mobility in figure 5.34 ($10^{-8} \text{ m}^2 \text{ V}^{-1} \text{ s}^{-1}$).

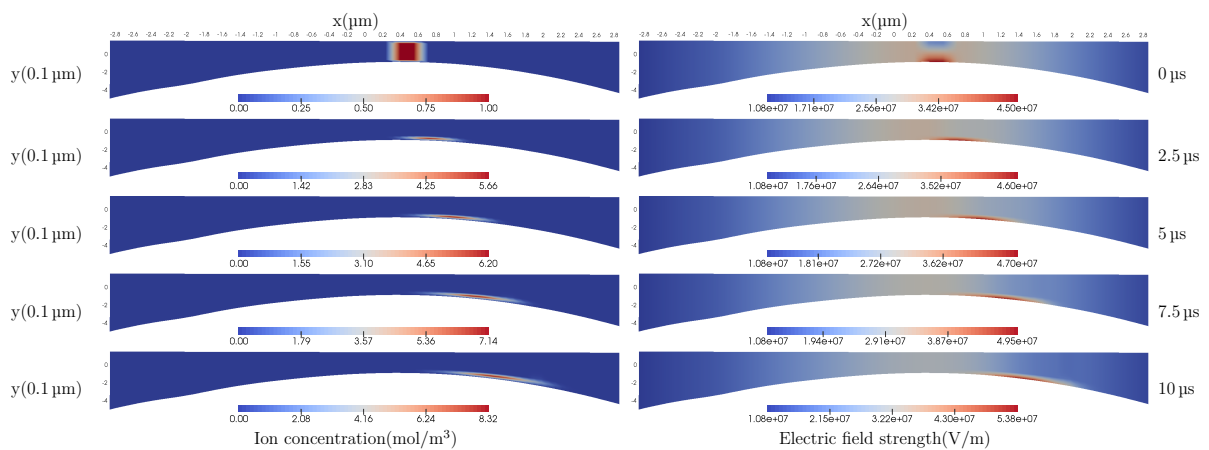


Figure 5.34.: Temporal development of ion concentration for high ionic mobility

Electric mobility describes how the electric field impacts the movement of a charge-carrying species. The change in two orders of magnitude amplifies the differences in the species movement. While ions with high electric mobility accumulate at the surface of the rolling element, the same process is far less dominant for the low mobility case. While this is not surprising, the agglomeration leads to a spike in the electric field strength, which is remarkable since such an increase might be an onset point for the subsequent discharges. The distance of 0.1 μm from the EHL contact is considered as reference for the residence-time, as discharging can no longer be assumed at greater distances. The residence-time for the high mobility case is estimated to be $7.5 \cdot 10^{-6} \text{ s}$ and $7.5 \cdot 10^{-6} \text{ s}$

for the low case.

The explanatory approach suggested by the underlying theory of EDM for lubricants concerns ions left in the contact region. If the dwell times of the hypothetical ions in the contact zone are compared with the frequencies of the applied signal, it becomes clear that an effect of the ions when the peak voltage is reached after a discharge can undoubtedly be expected.

6. Discussion

After presenting the results, the question arises whether the need for research, identified in section 1.3, is already covered. For this discussion, it is helpful to revisit the research questions formulated in chapter 3. Since the three questions build on each other, it is helpful to start with the third one because it also directly concerns the results presented at last. Discussing the third research question is mandatory before approaching the second and main research question review.

The third research question raised was how the presented approach can support the analysis of experimental research on electric phenomena in tribology. The presented numerical approach does support the experimental research on electrical phenomena in tribology. First and foremost, it allows the direct implementation of topological data into the calculation, which is impossible with idealized descriptions for the contact through Hertzian theory and medium lubrication film thicknesses via Dowson and Toyoda as presented in sections 2.1.2 and 2.5. The differences between those idealized contact descriptions and real contacts became apparent in section 5.5.1. Local maxima and the coupling of electrical properties to the state variables for the locally resolved contact is a new quality for the analysis and in no way describable with the help of mean values. A similar statement applies to the description of charges in the contact region and their interaction with the electric field by simultaneously considering the lubricant flow. Even though the calculations are only initial approaches and do not allow quantifiable conclusions to be drawn, the potential gets clear. The visualisation of physical interaction across domains and thus the possibility for evaluation against theory for explanatory attempts, as done in section 5.5.2, shows the opened up opportunities. Thus, the added value for experimental investigation was clearly illustrated, and the third research question was answered. Nevertheless, certain limitations prevail, as disclosed in section 5.3, leading to the discussion of the second and main research questions.

Although, the individual programme parts, which were considered critical for the functioning of the multi-physics calculation, were verified and validated individually during the TDD in section 5.2, the application to the tribological case in focus did not work out entirely. While calculations for low to medium loads did converge, the FSI coupling seems to be flawed beyond that. The identified limits of stability demonstrated in section 5.3 for the EHL case setup, introduced in section 4.2, did not allow validation against the experimental data collected, especially for this task. For this reason, only qualitative statements can be derived from the previous calculations. A separate discussion of the second and main research questions is not possible since attempts to explain aforementioned limitations might relate to the case setup and the overall calculation procedure. At the time of submission, it is only possible to speculate about the causes of the instabilities in the FSI coupling for realistic EHL parametrization and target loads. On the

one hand, model parameters and grid design can lead to instabilities, which relates to the discussion of the second research question. However, on the other hand, systemic errors like the set calculation procedure might also be responsible. Dependencies such as discretization schemes that only work in the context of specific calculation procedures increase the difficulty of solving the stated issues even further. The following findings can be noted for the time being before approaching an answer to the second and main research questions.

The individual functions implemented for the overarching implementation, presented in section 4.1.3, allow reproducing all calculation procedures the literature listed in section 1.2 states. It can also be noted that the overall case design and parametrization setup is close to publications known from the literature. However, during the testing, it became clear that especially the grid is prone to errors from non-orthogonality as a result of the deformation. The segmentation and related grid resolution and grading presented in 4.2 aimed to create an ideal aspect ratio of one for the converging and diverging region of the EHL contact. The aspect ratio was calculated for the initial lubrication film thickness and thus changed fast if the lubrication film thickness was adapted. As a minimal example, the grid, calculated for an initial lubrication film thickness of 0.1 μm , is applied to a case with a 1 μm initial lubrication film thickness. As a result, despite every other setting being kept constant, the fluid solution diverges only within the first few iterations due to a deterioration of the aspect ratio.

The susceptibility to such an error is extremely high due to the low cell volume in the EHL zone of the grid. In addition, the calculation was also very susceptible to oscillation in the fluid-structure coupling, as shown in section 5.3. Amplitudes in the actual load of 13 percent of the mean value at stationary equilibrium for a new time-step are problematic. However, the FSI coupling converged towards a stationary value over several iterations, and the oscillatory amplitude increases if the adjustment of the lubrication film thickness towards the target load and thus higher pressures and deformations is executed. It should also be noted that the electric domain implementation works without any problems and does not contribute to the reasons for the restrictions. Quite the opposite, as the discussion of research question three, showed.

The question arises which solution can be pursued to eradicate the prevailing problems. Besides discretization schemes and solution algorithms for the fluid and solid domain, the time-step size, choice of parameters, especially for the viscosity model and EoS, and the grid strategy are possible starting points for optimisation of the case setup. The solver choice and the procedural sequence for the calculation are starting points for optimisation of the overarching implementation. In addition, combinations of those adjustments can be made, which adds to the complexity of the analysis.

The answer to the second research question if the presented case setup is best suited for calculating relevant quantities to characterize electric phenomena in TEHL tribological contacts is rather no. However, it cannot be clarified whether it is only due to the implemented case or the calculation procedure that the proposed approach seems flawed. The unsatisfactory answer to the second research question initiates a similar discussion for the main research question. While the electric properties in rolling contacts are displayable in the framework and offer new insights, the actual calculation of EHL con-

ditions still does not reach the state of the art for numerical calculations as summarised in the beginning, in section 1.2. However, it cannot simply be said that the objective of the main research question was not achieved. In principle, a toolbox was created with the presented implementations that can map all necessary aspects for the simulation of electrical phenomena in tribological contacts. Analogue to the second research question, it is not clarified whether these tools were used in the ideal composition.

Concerning the need for research, it can be stated that this work offers starting points but does not cover the topic entirely yet. While a promising approach for describing electrical phenomena was extracted from the theory and applied to the task of rolling bearing analysis, the attempt to reach state of the art in TEHL numerics was not wholly successful. This was a little surprising, since the approaches are based on established solutions, and the architecture follows the best practice of renowned authors. The reasons for this are manifold, and there is much room for optimization left. Although there are several plausible causes and many possibilities for customisation, it is not possible to give a conclusive answer to the reasons for the limitation encountered in this work.

One possible cause regarding the overall framework lies in the partitioned approach chosen for the calculation. As mentioned in the presentation of the time-scales in section 4.2, the solid mechanical problem and the fluid problem develop at different speeds. While the solid solution followed the fluid solution and reached a stationary equilibrium within a time-step, the fluid solution did not. Therefore, the instability must be considered across the time-steps. While the fluid and solid solution are perfectly convergent within an FSI iterative process in one time-step, the temporal dependency of the fluid solution leads to a significant change in the next iterative cycle. This circumstance is seen in the spike values at the beginning of an iterative cycle. Subsequently, the spike pressures cause the solid to displace accordingly, leading to underestimating the fluid solution. The bigger the pressure spike, the more FSI sub-cycles are necessary to allow this behaviour to subside and converge the coupling.

While this phenomenon might decay for low-pressure problems in EHL and does not affect regular FSI calculations, it becomes increasingly dominant for a problem where minor adjustments were made. Accordingly, a change in deformation leads to significant changes in pressure. Even an under-relaxation for the coupling or the individual solvers did not overcome the instability issue on the systems level.

A comparison to state-of-the-art might also help identify problems by identifying differences in the assumptions made in the fundamentals. The most significant difference between the present approach and known numerical TEHL solutions is handling negative pressures behind the Hertzian contact region. Figure 6.1 shows the target geometry's the pressure distribution for an .

Hajishafiee et al. [33] did the same type of calculation for their grid independence study. The negative kinematic pressure is equivalent to the elevated pressure at the inlet zone and is encountered by most authors like Hartinger [32], Hajishafiee [128] or Singh [97]. Hartinger and others handled this phenomenon by introducing a phase-averaged cavitation model to the solution procedure. Every time the pressure drops below the cavitation threshold (typically 1000 Pa), a phase change towards the gaseous phase is added. The density and viscosity per cell are calculated based on the prevailing phase

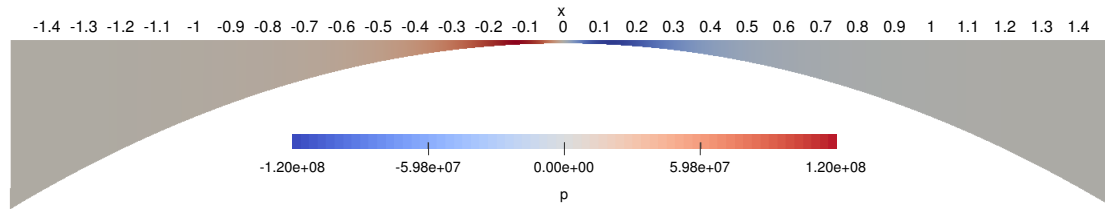


Figure 6.1.: Incompressible stationary calculation

fraction. The phase fraction is also considered for the continuity calculation leading to a total pressure above the cavitation threshold, and negative values are prevented. However, cavitation as an explanation for negative pressures seems unlikely regarding real rolling bearing applications. The occurrence of cavitation is typically synonymous with damage as described by Franc et al. [135, p.6]. To the author's knowledge, cavitation is not mentioned as a regular damage mechanism, for example, Sommer et al. [136, p.226]. One of the main inaccuracies for the numerical calculation of rolling bearing tribology is the assumption that lubricant is present wherever there is no rolling bearing material. In real applications, a closed surface film can be assumed. Figure 6.2 clarifies the difference.

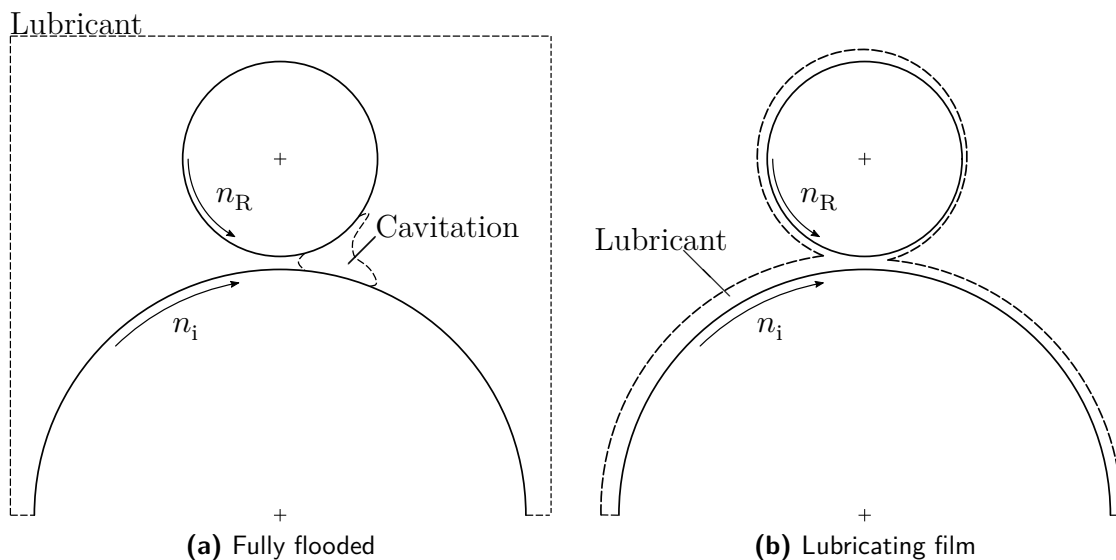


Figure 6.2.: Cavitation and two phase representation for the calculation region

If one drops the assumption of a wholly flooded bearing, shown in figure 6.2a, negative pressures could be attributed to a reduced height of the carried lubricant at the surfaces, shown in figure 6.2b. Such a description necessitates a two-phase flow description with consideration of the phase boundaries for the fluid solver. Neither a phase-averaged nor a two-phase solver was considered for this work since the extension towards multi-phase systems plus the consideration of electric fields and charge carrying species add a whole new dimension of complexity to the already complex problem. However, the introduction of a cavitation zone behind the EHL region or the considering of two-phase

flows might impact the result. The premise of this work was to limit the pressure at the cavitation region and stabilise the calculation by a higher relaxation and more robust discretization. Since this measure introduces a continuity error, it is also a possible reason why prior numerical approaches succeed where this one failed for the aspect of TEHL handling.

In conclusion, there remains a divided picture on how to interpret the success of this work. On the upside, some positive results were obtained regarding the third research question, and sound approaches for describing the electrical properties could be found and applied. Opposite that, the goals set with the main and second research questions were only conquered partially due to the discussed reasons. The ground covered in all four domains and the corresponding implementation work made will also be highlighted positively. The aspects discussed in this chapter allow numerous next steps. In chapter 7, some good points of departure will be discussed, reflecting the author's experience made throughout this work.

7. Conclusions and Outlook

Coming to the end, the work is summarized briefly and starting points for future research are stated.

In the present work, the numerical calculation of electrical phenomena in TEHL rolling contacts was the topic. Reasons for the relevance of this research were given during the introduction in chapter 1. The aim was to close the identified research gap between experimental practice, relying on empiric approximations, and available numerical possibilities. For this purpose, several approaches from different areas of numerics were assembled, and subsequently a theoretical framework was extracted from literature in chapter 2.

After a suitable programme architecture was identified in section 4.1, the theory was modelled within the chosen framework and a numerical reference case was set up in section 4.2 of chapter 4.

The implementations and changes to the initial framework were accompanied by the TDD, a methodological verification and validation process. Section 5.2, contains all the calculations done for validation and verification for the individual parts in this development process. In order to have a final validation for the overall system as it was described in section 4.1.3, reference experiments were carried out to create a database. The test-setup and the results were described in section 5.4. Due to the problems encountered for the final validation, a comparison of numerical results to the reference experiment was not possible, but the data were still included in this work for future research. Chapter 5 concluded with some exemplary calculations for experimental findings, made at the pmd. With the help of these calculations, the capabilities of the new numerical framework were emphasized and new insights in the electrical behaviour of tribological systems were achieved.

Beside the topic concerning the final validation and the corresponding issues with the actual EHL calculations, the results of this work open up numerous possibilities for future research.

Although the work was focussed on the subject of rolling bearings, an extension towards other tribological systems like gears and sealing technologies are imaginable for this framework. Especially gears are exposed to similar electrical phenomena as rolling bearings, so that an extension towards such systems is close by.

Another interesting topic which seems fertile is the extension of the charge density calculation towards multiple electric species. The aim could be to introduce a full fledged electro chemical calculation to the lubricant domain. Thus, an actual analysis of the situation during and after a discharge event becomes describable. The calculations made in section 5.5.2 lead towards this topic. However, when considering discharges at high field strengths, the input of heat through current flow must be considered, which introduces

another coupling between thermodynamic and electrostatics (then maybe electrodynamics) domain. The influence of such a heat on the load-bearing capacity of the lubricating film would be another interesting question. In order to be able to calculate approach these topics for the piezoviscous-elastic regime, the problems identified must first be overcome.

As a first measure, a transition within the openFOAM architecture from foamExtend towards the recent release of openFOAM 10 is desirable. The reason for this porting are the-state-of-art solver implementations which then become available, offering a greater freedom of choice and customizability. Alternatively a migration of the approach towards a capable all-in-one solution, as those mentioned in chapter 4, might also be an option, at least for cross-checking calculations to identify deviations and possible errors. If the here presented framework and implementations is to be kept, then it is recommended to revisit the main architecture of the solution procedure, as introduced in section 4.1.3 for improvement. Another adjustment would be to take into account aforementioned cavitation to see if high pressure EHL become computable like this.

From the author's point of view, the introduction of cavitation as a solution to the negative pressure problem does not reflect real rolling bearing tribology. The mere assumption of a fully flooded lubrication gap, which was also used here as described in section 4.3, is not realistic. A much more accurate representation would be a two phase system with phase boundary, consisting of air and lubricant. This way the actual lubrication, in the form of thin film on the surfaces of the rolling element and raceway are displayable as outlined in 6. Negative pressures would therefore not lead to cavitation, but to a film breakup behind the EHL region, which is more sound to realistic lubrication scenarios.

The introduction of a two-phase system however also implies a different, more complicated formulation of the electrostatic domain. Apparently the numerical description of electrical phenomena in Thermal Elastohydrodynamic Lubrication still offers much opportunities for research and development. So with this work the topic was merely opened up.

A. FVA 3 Reference Oil Data

FVA 3 Viscosity		
Viscosity η Pa s	Pressure p GPa	Temperature T K
0.14	0	303
0.05	0	323
0.03	0	333
0.02	0	343
0.017	0	353
0.015	0	363
0.001	0	433
15	0.5	353
45	0.6	353
75	0.65	353
150	0.7	353

Table A.1.: FVA 3 Viscosity Data taken from Bartel [54, p.120]

B. Compressibility

B.1. Murnaghan Compressibility Derivation

$$\begin{aligned}
 \psi_{\text{Murnaghan}} &= \frac{1}{\rho} \frac{\partial \rho}{\partial p} \\
 &= \frac{1}{\rho_0 \left(1 + \frac{K'_0}{K_0} p\right)^{\frac{1}{K'_0}}} \frac{\partial \rho_0 \left(1 + \frac{K'_0}{K_0} p\right)^{\frac{1}{K'_0}}}{\partial p} \\
 &= \frac{1}{\rho_0 \left(1 + \frac{K'_0}{K_0} p\right)^{\frac{1}{K'_0}}} \frac{\rho_0 \partial \left(1 + \frac{K'_0}{K_0} p\right)^{\frac{1}{K'_0}}}{\partial p} \\
 &= \frac{1}{\left(1 + \frac{K'_0}{K_0} p\right)^{\frac{1}{K'_0}}} \frac{1}{K_0} \left(1 + \frac{K'_0}{K_0} p\right)^{\frac{1}{K'_0}} \left(1 + \frac{K'_0}{K_0} p\right)^{-1} \\
 &= \frac{1}{\left(1 + \frac{K'_0}{K_0} p\right)^{\frac{1}{K'_0}}} \frac{1}{K_0} \left(1 + \frac{K'_0}{K_0} p\right)^{\frac{1}{K'_0}} \left(1 + \frac{K'_0}{K_0} p\right)^{-1} \\
 &= \frac{1}{K_0} \left(1 + \frac{K'_0}{K_0} p\right)^{-1} \\
 &= \left(K_0 + K_0 \frac{K'_0}{K_0} p\right)^{-1} \\
 &= \left(K_0 + \cancel{K_0} \frac{K'_0}{\cancel{K_0}} p\right)^{-1} \\
 \psi_{\text{Murnaghan}} &= \left(K_0 + K'_0 p\right)^{-1}
 \end{aligned} \tag{B.1}$$

B.2. Tait Compressibility Derivation

$$\begin{aligned}
\psi_{\text{Tait}} &= \frac{1}{\rho} \frac{\partial \rho}{\partial p} \\
&= \frac{1}{\rho_0 \left[\left(1 - \frac{1}{1+K'_0} \ln \left[1 + \frac{p}{K_0} (1+K'_0) \right] \right) \right]^{-1}} \cdot \rho_0 \frac{\partial}{\partial p} \left[1 - \frac{1}{1+K'_0} \ln \left[1 + \frac{p}{K_0} (1+K'_0) \right] \right]^{-1} \\
&= \left[1 - \frac{1}{1+K'_0} \ln \left[1 + \frac{p}{K_0} (1+K'_0) \right] \right] \cdot \frac{\partial}{\partial p} \left[1 - \frac{1}{1+K'_0} \ln \left[1 + \frac{p}{K_0} (1+K'_0) \right] \right]^{-1} \\
&= \left[1 - \frac{1}{1+K'_0} \ln \left[1 + \frac{p}{K_0} (1+K'_0) \right] \right] \cdot - \left[1 - \frac{1}{1+K'_0} \ln \left[1 + \frac{p}{K_0} (1+K'_0) \right] \right]^{-2} \\
&\quad \cdot \frac{\partial}{\partial p} \left[1 - \frac{1}{1+K'_0} \ln \left[1 + \frac{p}{K_0} (1+K'_0) \right] \right] \\
&= - \left[1 - \frac{1}{1+K'_0} \ln \left[1 + \frac{p}{K_0} (1+K'_0) \right] \right]^{-1} \cdot \frac{\partial}{\partial p} \left[1 - \frac{1}{1+K'_0} \ln \left[1 + \frac{p}{K_0} (1+K'_0) \right] \right] \\
&= - \left[1 - \frac{1}{1+K'_0} \ln \left[1 + \frac{p}{K_0} (1+K'_0) \right] \right]^{-1} \cdot \frac{\partial}{\partial p} \left[1 - \frac{1}{1+K'_0} \ln \left[1 + \frac{p}{K_0} (1+K'_0) \right] \right] \\
&= - \left[1 - \frac{1}{1+K'_0} \ln \left[1 + \frac{p}{K_0} (1+K'_0) \right] \right]^{-1} \cdot - \frac{1}{1+K'_0} \frac{\partial}{\partial p} \ln \left[1 + \frac{p}{K_0} (1+K'_0) \right] \\
&= - \left[1 - \frac{1}{1+K'_0} \ln \left[1 + \frac{p}{K_0} (1+K'_0) \right] \right]^{-1} \cdot - \frac{1}{1+K'_0} \left[1 + \frac{p}{K_0} (1+K'_0) \right]^{-1} \cdot \frac{1}{K_0} (1+K'_0) \\
&= \cancel{-} \left[1 - \frac{1}{1+K'_0} \ln \left[1 + \frac{p}{K_0} (1+K'_0) \right] \right]^{-1} \cdot \cancel{-} \left[1 + \frac{p}{K_0} (1+K'_0) \right]^{-1} \cdot \frac{1}{K_0} \\
&= \left[1 - \frac{1}{1+K'_0} \ln \left[1 + \frac{p}{K_0} (1+K'_0) \right] \right]^{-1} \cdot \left[1 + \frac{p}{K_0} (1+K'_0) \right]^{-1} \cdot [K_0]^{-1} \\
&= \left[1 - \frac{1}{1+K'_0} \ln \left[1 + \frac{p}{K_0} (1+K'_0) \right] \right]^{-1} \cdot \left[K_0 + \frac{pK'_0}{K_0} (1+K'_0) \right]^{-1} \\
&= \left[1 - \frac{1}{1+K'_0} \ln \left[1 + \frac{p}{K_0} (1+K'_0) \right] \right]^{-1} \cdot [K_0 + p(1+K'_0)]^{-1}
\end{aligned} \tag{B.2}$$

C. Compression Modulus

C.1. Dowson Higginson

$$K = K_0 \left(1 + \frac{K'_0 + 1}{2K_0} p \right) \left(1 + \frac{K'_0 - 1}{2K_0} p \right) \quad (\text{C.1})$$

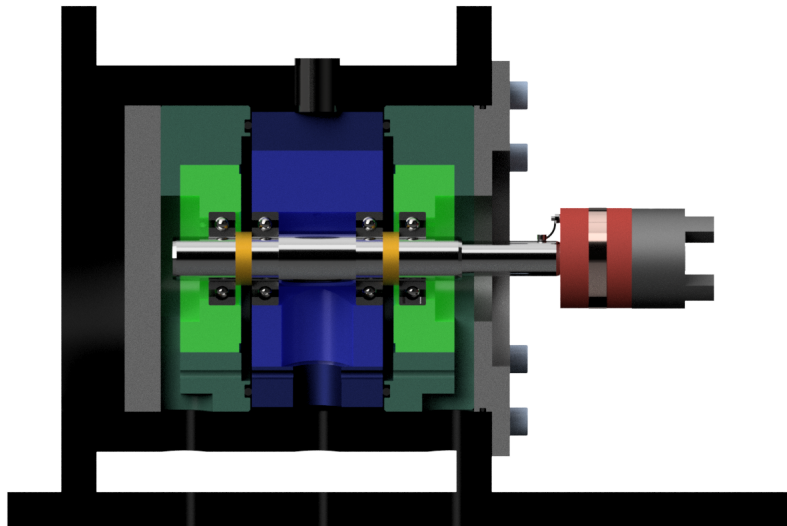
C.2. Tait

$$K = \left\{ 1 - \frac{1}{1 + K'_0} \ln \left(1 + \frac{p}{K_0} (1 + K'_0) \right) \right\} [K_0 + p(1 + K'_0)] \quad (\text{C.2})$$

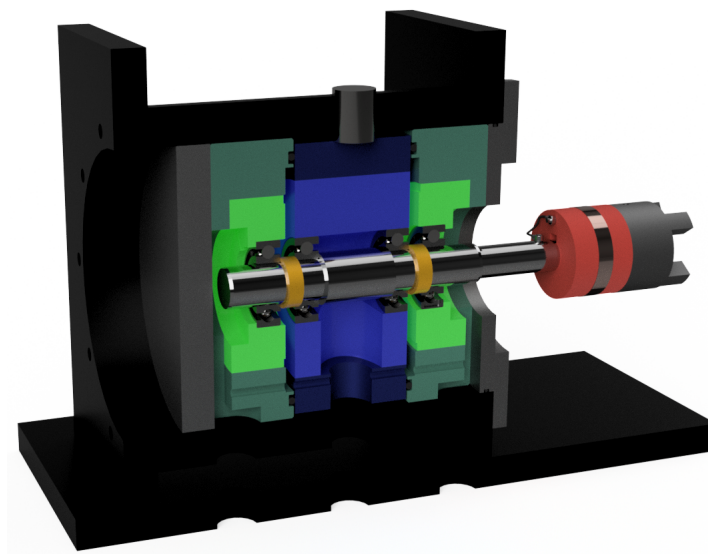
C.3. Murnaghan

$$K = \frac{1}{\psi_{\text{Murnaghan}}} = K_0 + K'_0 p \quad (\text{C.3})$$

D. Experimental Setup



(a) Front view



(b) Isometric view

Figure D.1.: Rolling bearing test rig. CAD Visualization

E. Implementations and Source Codes

E.1. thermalEfsiFoam

```

#include "fvCFD.H"
#include "dynamicFvMesh.H"
#include "fluidSolidInterface.H"
int main(int argc, char *argv[])
{
#include "setRootCase.H"
#include "createTime.H"
#include "createDynamicFvMesh.H"
#include "createSolidMesh.H"
fluidSolidInterface fsi(mesh, solidMesh);
for (runTime++; !runTime.end(); runTime++)
{
    fsi.initializeFields();
    fsi.updateInterpolator();
    scalar residualNorm = 0;
    if (runTime.value() > fsi.couplingTime())
    {
        fsi.set("coupled", true);
    }
    if (runTime.value() > 5*fsi.couplingTime())
    {
        fsi.movespecificFluidMeshSurface
        (
            "SurfaceInnerRing", "SurfaceInnerRingZone"
        );
    }
    if (fsi.predictor())
    {
        fsi.updatepressureForce();
        fsi.stress().evolve();
        residualNorm = fsi.updateResidual();
    }
    do
    {
        fsi.outerCorr()++;
        fsi.updateDisplacement();
        fsi.moveFluidMesh();
        fsi.flow().evolve();
        fsi.updateTemperature();
        fsi.updatepressureForce();
        fsi.stress().updateTotalFields();
        fsi.stress().evolve();
        fsi.updateHeatFlux();
        residualNorm = fsi.updateResidual();
    }
    while
    (
        (residualNorm > fsi.outerCorrTolerance())
        && (fsi.outerCorr() < fsi.nOuterCorr())
    );
    fsi.charge().evolve();
    fsi.flow().updateFields();
}

```

```

    fsi.stress().updateTotalFields();
    fsi.charge().updateFields();
    runTime.write();
}
return(0);
}

```

E.2. pmdRelease

```

#include "pmdRelease.H"
#include "volFields.H"
#include "fvCFD.H"
#include "addToRunTimeSelectionTable.H"
#include "findRefCell.H"
#include "adjustPhi.H"
#include "fluidSolidInterface.H"
#include "fixedGradientFvPatchFields.H"
#include "temperatureFluidFvPatchScalarField.H"
#include "heatFluxFluidFvPatchScalarField.H"
#include "IOReferencer.H" //added
namespace Foam
{
    namespace fluidSolvers
    {
        // Static Data Members
        defineTypeNameAndDebug(pmdRelease, 0);
        addToRunTimeSelectionTable(fluidSolver, pmdRelease, dictionary);
        // Constructors
        pmdRelease::pmdRelease(const fvMesh& mesh)
        :
        fluidSolver(this->typeName, mesh),
        pThermo_(basicRhoThermo::New(mesh)),
        thermo_(pThermo_()),
        psi_(thermo_.psi()),
        p_(thermo_.p()),
        T_(thermo_.T()),
        pref_
        (
            IOobject
            (
                "pref",
                runTime().timeName(),
                mesh,
                IOobject::MUST_READ,
                IOobject::NO_WRITE
            ),
            mesh
        ),
        prel_
        (
            IOobject
            (
                "prel",
                runTime().timeName(),
                mesh,
                IOobject::MUST_READ,
                IOobject::AUTO_WRITE
            ),
            mesh
        ),
        U_
        (
            IOobject

```

```

(
    "U",
    runTime().timeName(),
    mesh,
    IOobject::MUST_READ,
    IOobject::AUTO_WRITE
),
mesh
),
h_(thermo_.h()),
rho_
(
    IOobject
    (
        "rho",
        runTime().timeName(),
        mesh,
        IOobject::NO_READ,
        IOobject::AUTO_WRITE
    ),
    thermo_.rho()
),
gradp_(fvc::grad(p_)),
gradU_(fvc::grad(U_)),
phi_
(
    IOobject
    (
        "phi",
        runTime().timeName(),
        mesh,
        IOobject::READ_IF_PRESENT,
        IOobject::AUTO_WRITE
    ),
    fvc::interpolate(rho_*U_) & mesh.Sf()
),
turbulence_
(
    compressible::turbulenceModel::New
    (
        rho_, U_, phi_, thermo_
    )
),
heatFlux_
(
    IOobject
    (
        "heatFlux",
        runTime().timeName(),
        mesh,
        IOobject::NO_READ,
        IOobject::NO_WRITE
    ),
    mesh.magSf()*fvc::interpolate(turbulence_>alphaEff()) * fvc::snGrad(h_)
),
DpDt_(fvc::DDt(surfaceScalarField("phiU", phi_/fvc::interpolate(rho_)), p_)),
//K_("K", 0.5*magSqr(U_)),
pimple_(const_cast<fvMesh&>(mesh)),
pMin_(pimple_.dict().lookup("pMin")),
hMin_(min(h_)),
CoNum_(0.0)
{}
// Member Functions
const volVectorField& pmdRelease::U() const
{
    return U_;
}

```

```

}
const volScalarField& pmdRelease::p() const
{
    return p_;
}
const volScalarField& pmdRelease::T() const
{
    return T_;
}
const scalar& pmdRelease::CoNum() const
{
    return CoNum_;
}
tmp<vectorField> pmdRelease::patchViscousForce(const label patchID) const
{
    tmp<vectorField> tvF
    (
        new vectorField(mesh().boundary()[patchID].size(), vector::zero)
    );
    tvF() =
    -(
        mesh().boundary()[patchID].nf()
        & turbulence_>devRhoReff().boundaryField()[patchID]
    );
    return tvF;
}
tmp<scalarField> pmdRelease::patchPressureForce(const label patchID) const
{
    tmp<scalarField> tpF
    (
        new scalarField(mesh().boundary()[patchID].size(), 0)
    );
    tpF() = p_.boundaryField()[patchID] - pref_.boundaryField()[patchID];
    return tpF;
}
tmp<scalarField> pmdRelease::patchheatFlux(const label patchID) const
{
    tmp<scalarField> thF
    (
        new scalarField(mesh().boundary()[patchID].size(), 0)
    );
    thF() = heatFlux_.boundaryField()[patchID];
    return thF;
}
tmp<scalarField> pmdRelease::patchTemperature(const label patchID) const
{
    tmp<scalarField> tT
    (
        new scalarField(mesh().boundary()[patchID].size(), 0)
    );
    tT() = T_.boundaryField()[patchID];
    return tT;
}
tmp<vectorField> pmdRelease::faceZoneViscousForce
(
    const label zoneID,
    const label patchID
) const
{
    vectorField pVF = patchViscousForce(patchID);
    tmp<vectorField> tvF
    (
        new vectorField(mesh().faceZones()[zoneID].size(), vector::zero)
    );
    vectorField& vF = tvF();
    const label patchStart =

```

```

mesh().boundaryMesh()[patchID].start();
forAll(pVF, i)
{
    vF[mesh().faceZones()[zoneID].whichFace(patchStart + i)] =
    pVF[i];
}
reduce(vF, sumOp<vectorField>());
return tvF;
}
tmp<scalarField> pmdRelease::faceZonePressureForce
(
    const label zoneID,
    const label patchID
) const
{
    scalarField pPF = patchPressureForce(patchID);
    tmp<scalarField> tpF
    (
        new scalarField(mesh().faceZones()[zoneID].size(), 0)
    );
    scalarField& pF = tpF();
    const label patchStart =
    mesh().boundaryMesh()[patchID].start();
    forAll(pPF, i)
    {
        pF[mesh().faceZones()[zoneID].whichFace(patchStart + i)] =
        pPF[i];
    }
    reduce(pF, sumOp<scalarField>());
    return tpF;
}
tmp<scalarField> pmdRelease::faceZoneheatFlux
(
    const label zoneID,
    const label patchID
) const
{
    scalarField phF = patchheatFlux(patchID);
    tmp<scalarField> thF
    (
        new scalarField(mesh().faceZones()[zoneID].size(), 0)
    );
    scalarField& hF = thF();
    const label patchStart =
    mesh().boundaryMesh()[patchID].start();
    forAll(phF, i)
    {
        hF[mesh().faceZones()[zoneID].whichFace(patchStart + i)] =
        phF[i];
    }
    reduce(hF, sumOp<scalarField>());
    return thF;
}
tmp<scalarField> pmdRelease::faceZoneTemperature
(
    const label zoneID,
    const label patchID
) const
{
    scalarField pT = patchTemperature(patchID);
    tmp<scalarField> tT
    (
        new scalarField(mesh().faceZones()[zoneID].size(), 0)
    );
    scalarField& sT = tT();
    const label patchStart =

```

```

mesh().boundaryMesh()[patchID].start();
forAll(pT, i)
{
    sT[mesh().faceZones()[zoneID].whichFace(patchStart + i)] =
    pT[i];
}
reduce(sT, sumOp<scalarField>());
return tT;
}
tmp<scalarField> pmdRelease::faceZoneMuEff
(
    const label zoneID,
    const label patchID
) const
{
    scalarField pMuEff =
    turbulence->mut().boundaryField()[patchID];
    tmp<scalarField> tMuEff
    (
        new scalarField(mesh().faceZones()[zoneID].size(), 0)
    );
    scalarField& muEff = tMuEff();
    const label patchStart =
    mesh().boundaryMesh()[patchID].start();
    forAll(pMuEff, i)
    {
        muEff[mesh().faceZones()[zoneID].whichFace(patchStart + i)] =
        pMuEff[i];
    }
    reduce(muEff, sumOp<scalarField>());
    return tMuEff;
}
void pmdRelease::setTemperature
(
    const label patchID,
    const scalarField& Temperature
){
    temperatureFluidFvPatchScalarField& patchU =
    refCast<temperatureFluidFvPatchScalarField>
    (
        T_.boundaryField()[patchID]
    );
    patchU.Temperature() = Temperature;
}
void pmdRelease::setTemperature
(
    const label patchID,
    const label zoneID,
    const scalarField& faceZoneTemperature
){
    scalarField patchTemperature(mesh().boundary()[patchID].size(), 0.0);
    const label patchStart =
    mesh().boundaryMesh()[patchID].start();
    forAll(patchTemperature, i)
    {
        patchTemperature[i] =
        faceZoneTemperature
        [
            mesh().faceZones()[zoneID].whichFace(patchStart + i)
        ];
    }
    setTemperature(patchID, patchTemperature);
}
void pmdRelease::setheatFlux
(
    const label patchID,

```

```

    const scalarField& heatFlux
){
    heatFluxFluidFvPatchScalarField& patchU =
    refCast<heatFluxFluidFvPatchScalarField>
    (
    T_.boundaryField()[patchID]
    );
    patchU.heatFlux() = -heatFlux;
}
void pmdRelease::setheatFlux
(
    const label patchID,
    const label zoneID,
    const scalarField& faceZoneheatFlux
){
    scalarField patchheatFlux(mesh().boundary()[patchID].size(), 0.0);
    const label patchStart =
    mesh().boundaryMesh()[patchID].start();
    forAll(patchheatFlux, i)
    {
        patchheatFlux[i] =
        faceZoneheatFlux
        [
            mesh().faceZones()[zoneID].whichFace(patchStart + i)
        ];
    }
    setheatFlux(patchID, patchheatFlux);
}
void pmdRelease::evolve()
{
    Info << "Evolving fluid solver" << endl;
    const fvMesh& mesh = fluidSolver::mesh();
    mesh.schemesDict().setFluxRequired(p_.name());
    fvc::makeRelative(phi_, rho_, U_);
    #ifndef initContinuityErrs_H
    #define initContinuityErrs_H
    scalar sumLocalContErr = 0;
    scalar globalContErr = 0;
    scalar cumulativeContErr = 0;
    #endif
    //compressibleCourantNo.H
    scalar meanCoNum_ = 0.0;
    scalar velMag_ = 0.0;
    if (mesh.nInternalFaces())
    {
        surfaceScalarField phiOverRho = mag(phi_)/fvc::interpolate(rho_);
        surfaceScalarField SfUfbyDelta =
        mesh.surfaceInterpolation::deltaCoeffs()*phiOverRho;
        CoNum_ = max(SfUfbyDelta/mesh.magSf()).value()*runTime().deltaT().value();
        meanCoNum_ = (sum(SfUfbyDelta)/
        sum(mesh.magSf())).value()*runTime().deltaT().value();
        velMag_ = max(phiOverRho/mesh.magSf()).value();
    }
    {
        solve(fvm::ddt(rho_) + fvc::div(phi_));
    }
    while (pimple_.loop())
    {
        fvVectorMatrix UEqn
        (
            fvm::ddt(rho_, U_)
            + fvm::div(phi_, U_)
            + turbulence_>divDevRhoReff()
        );
        UEqn.relax
        (
            mesh.solutionDict().equationRelaxationFactor(U_.select(pimple_.finalIter()))
        );
    }
}

```

```

);
volScalarField rUA = 1.0/UEqn.A();
if (pimple_.momentumPredictor())
{
  solve(UEqn == -
  fvc::grad(p_), mesh.solutionDict().solver((U_.select(pimple_.finalIter()))));
}
else
{
  U_ = rUA*(UEqn.H() - fvc::grad(p_));
  U_.correctBoundaryConditions();
}
{
  volScalarField D("D", turbulence_>devRhoReff() && gradU_);
  fvScalarMatrix hEqn
  ( fvm::ddt(rho_, h_)
  + fvm::div(phi_, h_)
  - fvm::laplacian(turbulence_>alphaEff(), h_)
  - D
  ==
  DpDt_
  );
  hEqn.relax(mesh.solutionDict().equationRelaxationFactor(h_.select(pimple_.finalIter())));
  hEqn.solve(mesh.solutionDict().solver((h_.select(pimple_.finalIter()))));
  bound(h_, hMin_);
  thermo_.correct();
}
while (pimple_.correct())
{
  rho_ = thermo_.rho();
  volScalarField rUA = 1.0/UEqn.A();
  U_ = rUA*UEqn.H();
  phi_ =
  fvc::interpolate(rho_)*
  ( fvc::interpolate(U_) &
  mesh.Sf()
  );
  while (pimple_.correctNonOrthogonal())
  {
    fvScalarMatrix pEqn
    (
    fvm::ddt(psi_, p_)
    + fvc::div(phi_)
    - fvm::laplacian(rho_*rUA, p_)
    );
    pEqn.solve(mesh.solutionDict().solver(p_.select(pimple_.finalInnerIter())));
    if (pimple_.finalNonOrthogonalIter())
    {
      phi_ -= pEqn.flux();
    }
  }
  solve(fvm::ddt(rho_) + fvc::div(phi_));
  dimensionedScalar totalMass = fvc::domainIntegrate(rho_);
  sumLocalContErr = (fvc::domainIntegrate(mag(rho_ -
  thermo_.rho()))/totalMass).value();
  globalContErr = (fvc::domainIntegrate(rho_ -
  thermo_.rho())/totalMass).value();
  cumulativeContErr += globalContErr;
  p_.relax();
  rho_ = thermo_.rho();
  rho_.relax();
  U_ -= rUA*fvc::grad(p_);
  U_.correctBoundaryConditions();
  heatFlux_ = mesh.magSf() * fvc::interpolate(turbulence_>
  alphaEff()) * fvc::snGrad(h_);
  DpDt_ = fvc::DDt(surfaceScalarField("phiU", phi_/

```

```

    fvc::interpolate(rho_), p_);
    bound(p_, pMin_);
}
turbulence_>correct();
}
fvc::makeAbsolute(phi_, rho_, U_);
}
}
}

```

E.3. temperatureuntotalLagrangian

```

#ifndef unsIncrTotalLagrangianSolid_H
#define unsIncrTotalLagrangianSolid_H
#include "solidSolver.H"
#include "volFields.H"
#include "surfaceFields.H"
#include "pointFields.H"
#include "constitutiveModel.H"
#include "leastSquaresVolPointInterpolation.H"
#include "ITLMaterialInterface.H"
namespace Foam
{
namespace solidSolvers
{
class unsIncrTotalLagrangianSolid
:
public solidSolver
{
// Private data
volVectorField DD_;
volVectorField D_;
volScalarField Tsolid_;
surfaceScalarField heatFlux_;
volVectorField U_;
pointMesh pMesh_;
pointVectorField pointDD_;
pointVectorField pointD_;
volSymmTensorField DSigma_;
volSymmTensorField sigma_;
volSymmTensorField DEpsilon_;
surfaceSymmTensorField DEpsilonf_;
volSymmTensorField epsilon_;
surfaceSymmTensorField epsilonf_;
surfaceSymmTensorField epsilonPf_;
surfaceSymmTensorField DSigmaf_;
surfaceSymmTensorField sigmaf_;
constitutiveModel rheology_;
leastSquaresVolPointInterpolation volToPoint_;
surfaceTensorField gradDDf_;
surfaceTensorField gradDf_;
volTensorField gradDD_;
volTensorField gradD_;
volScalarField rho_;
volScalarField mu_;
surfaceScalarField muf_;
volScalarField lambda_;
surfaceScalarField lambdaf_;
autoPtr<materialInterface> interface_;
label curTimeIndex_;
// Private Member Functions
// Disallow default bitwise copy construct
unsIncrTotalLagrangianSolid(const unsIncrTotalLagrangianSolid&);

```

```

// - Disallow default bitwise assignment
void operator=(const unsIncrTotalLagrangianSolid&);
public:
// - Runtime type information
TypeName("unsIncrTotalLagrangianSolid");
// - Constructors
// - Construct from components
unsIncrTotalLagrangianSolid(const fvMesh& mesh);
// - Destructor
virtual ~unsIncrTotalLagrangianSolid()
{}
// - Member Functions
// - Access
const pointMesh& pMesh() const
{
return pMesh_;
}
// - Return temperature field
const volScalarField& T() const
{
return Tsolid_;
}
leastSquaresVolPointInterpolation& volToPoint()
{
return volToPoint_;
}
const leastSquaresVolPointInterpolation& volToPoint() const
{
return volToPoint_;
}
pointVectorField& pointDD()
{
return pointDD_;
}
const volSymmTensorField& DSigma() const
{
return DSigma_;
}
volSymmTensorField& DSigma()
{
return DSigma_;
}
const volSymmTensorField& sigma() const
{
return sigma_;
}
volSymmTensorField& sigma()
{
return sigma_;
}
surfaceSymmTensorField& DSigmaf()
{
return DSigmaf_;
}
const surfaceSymmTensorField& DSigmaf() const
{
return DSigmaf_;
}
const volSymmTensorField& DEpsilon() const
{
return DEpsilon_;
}
volSymmTensorField& DEpsilon()
{
return DEpsilon_;
}
}

```

```
const surfaceSymmTensorField& DEpsilonf() const
{
    return DEpsilonf_;
}
surfaceSymmTensorField& DEpsilonf()
{
    return DEpsilonf_;
}
const volScalarField& rho() const
{
    return rho_;
}
const volScalarField& mu() const
{
    return mu_;
}
const surfaceScalarField& muf() const
{
    return muf_;
}
const volScalarField& lambda() const
{
    return lambda_;
}
const surfaceScalarField& lambdaf() const
{
    return lambdaf_;
}
const volVectorField& DD() const
{
    return DD_;
}
volVectorField& DD()
{
    return DD_;
}
const volVectorField& D() const
{
    return D_;
}
volVectorField& D()
{
    return D_;
}
const surfaceSymmTensorField& sigmaf() const
{
    return sigmaf_;
}
surfaceSymmTensorField& sigmaf()
{
    return sigmaf_;
}
const volSymmTensorField& epsilon() const
{
    return epsilon_;
}
volSymmTensorField& epsilon()
{
    return epsilon_;
}
const surfaceSymmTensorField& epsilonf() const
{
    return epsilonf_;
}
surfaceSymmTensorField& epsilonf()
{
```

```

    return epsilonf_;
}
virtual const constitutiveModel& rheology() const
{
    return rheology_;
}
constitutiveModel& rheology()
{
    return rheology_;
}
virtual const pointVectorField& pointDD() const
{
    return pointDD_;
}
virtual const pointVectorField& pointD() const
{
    return pointD_;
}
pointVectorField& pointD()
{
    return pointD_;
}
surfaceTensorField& gradDDf()
{
    return gradDDf_;
}
const surfaceTensorField& gradDDf() const
{
    return gradDDf_;
}
surfaceTensorField& gradDf()
{
    return gradDf_;
}
const surfaceTensorField& gradDf() const
{
    return gradDf_;
}
const volTensorField& gradDD() const
{
    return gradDD_;
}
volTensorField& gradDD()
{
    return gradDD_;
}
const volTensorField& gradD() const
{
    return gradD_;
}
volTensorField& gradD()
{
    return gradD_;
}
virtual const autoPtr<materialInterface>& interface() const
{
    return interface_;
}
autoPtr<materialInterface>& interface()
{
    return interface_;
}
}
virtual vector pointU(label pointID) const;
virtual tmp<vectorField> patchPointDisplacementIncrement
(
    const label patchID

```

```

) const;
virtual tmp<vectorField> faceZonePointDisplacementIncrement
(
    const label zoneID
) const;
virtual tmp<vectorField> patchPointDisplacement
(
    const label patchID
) const;
virtual tmp<vectorField> faceZonePointDisplacement
(
    const label zoneID
) const;
virtual tmp<tensorField> faceZoneSurfaceGradientOfVelocity
(
    const label zoneID,
    const label patchID
) const;
virtual tmp<vectorField> faceZoneNormal
(
    const label zoneID,
    const label patchID
) const;
virtual tmp<vectorField>
currentFaceZonePoints(const label zoneID) const;
virtual tmp<scalarField> patchTemperature
(
    const label patchID
) const;
virtual tmp<scalarField> patchheatFlux
(
    const label patchID
) const;
virtual tmp<scalarField> faceZoneTemperature
(
    const label zoneID,
    const label patchID
) const;
virtual tmp<scalarField> faceZoneheatFlux
(
    const label zoneID,
    const label patchID
) const;
// Edit
virtual void setTraction
(
    const label patchID,
    const vectorField& traction
);
virtual void setPressure
(
    const label patchID,
    const scalarField& pressure
);
virtual void setTemperature
(
    const label patchID,
    const scalarField& Temperature
);
virtual void setheatFlux
(
    const label patchID,
    const scalarField& heatFlux
);
virtual void setTraction
(

```

```

    const label patchID,
    const label zoneID,
    const vectorField& zoneTraction
);
virtual void setPressure
(
    const label patchID,
    const label zoneID,
    const scalarField& zonePressure
);
virtual void setTemperature
(
    const label patchID,
    const label zoneID,
    const scalarField& zoneTemperature
);
virtual void setheatFlux
(
    const label patchID,
    const label zoneID,
    const scalarField& zoneheatFlux
);
virtual tmp<vectorField> predictTraction
(
    const label patchID,
    const label zoneID
);
virtual tmp<scalarField> predictPressure
(
    const label patchID,
    const label zoneID
);
virtual bool evolve();
virtual void predict();
virtual scalar smooth
(
    const volVectorField& source,
    label nCorrectors = 0
);
virtual scalar smooth
(
    const volVectorField& source,
    const volVectorField& refSolution,
    label nCorrectors = 0
);
virtual const volVectorField& solution() const
{
    return DD_;
}
virtual volVectorField& solution()
{
    return DD_;
}
virtual void initialise
(
    const volVectorField& sol,
    bool consistentBoundaryField
);
virtual tmp<volVectorField> residual
(
    const volVectorField& source
);
virtual void updateTotalFields();
scalar residual() const;
virtual tmp<surfaceVectorField> traction() const;
virtual bool writeObject

```

```

(
  IOstream::streamFormat,
  IOstream::versionNumber,
  IOstream::compressionType
) const;
};
} // End namespace fluidSolvers
} // End namespace Foam
#endif

```

E.4. electrostaticthermophysicalCharge

```

#include "electrostaticthermophysicalCharge.H"
#include "volFields.H"
#include "fvCFD.H"
#include "addToRunTimeSelectionTable.H"
#include "findRefCell.H"
#include "adjustPhi.H"
#include "fluidSolidInterface.H"
#include "fixedGradientFvPatchFields.H"
namespace Foam
{
  namespace efieldSolvers
  {
    // Static Data Members
    defineTypeNameAndDebug(electrostaticthermophysicalCharge, 0);
    addToRunTimeSelectionTable(efieldSolver, electrostaticthermophysicalCharge, dictionary);
    // Constructors
    electrostaticthermophysicalCharge::electrostaticthermophysicalCharge(const fvMesh& mesh)
    :
    efieldSolver(this->typeName, mesh),
    pThermo_(basicRhoThermo::New(mesh)),
    thermo_(pThermo_()),
    physicalProperties_
    (
      IOobject
      (
        "physicalProperties",
        mesh.time().constant(),
        mesh,
        IOobject::MUST_READ,
        IOobject::NO_WRITE
      )
    ),
    dielectric_(thermo_.dielectric()),
    kE_
    (
      physicalProperties_.lookup("k")
    ),
    phiE_
    (
      IOobject
      (
        "phiE",
        runTime().timeName(),
        mesh,
        IOobject::MUST_READ,
        IOobject::AUTO_WRITE
      ),
      mesh
    ),
    rhoE_
    (

```

```

IOobject
(
    "rhoE",
    runTime().timeName(),
    mesh,
    IOobject::MUST_READ,
    IOobject::AUTO_WRITE
),
mesh
),
rhoEFlux_
(
    IOobject
    (
        "rhoEFlux",
        runTime().timeName(),
        mesh,
        IOobject::NO_READ,
        IOobject::NO_WRITE
    ),
    -kE_*mesh.magSf()*fvc::snGrad(phiE_)
),
E_
(
    IOobject
    (
        "E",
        runTime().timeName(),
        mesh,
        IOobject::NO_READ,
        IOobject::AUTO_WRITE
    ),
    -fvc::grad(phiE_)
),
magE_
(
    IOobject
    (
        "magE",
        runTime().timeName(),
        mesh,
        IOobject::NO_READ,
        IOobject::AUTO_WRITE
    ),
    mag(fvc::grad(phiE_))
)
{}
// Member Functions
void electrostaticthermophysicalCharge::evolve()
{
    Info << "Evolving_ufield_solver" << endl;
    const fvMesh& mesh = efieldSolver::mesh();
    dielectric_ = thermo_.dielectric();
    solve
    (
        fvm::laplacian(phiE_) + rhoE_/dielectric_
    );
    rhoEFlux_ = -kE_*mesh.magSf()*fvc::snGrad(phiE_);
    E_ = -fvc::grad(phiE_);
    magE_ = mag(fvc::grad(phiE_));
    solve
    (
        fvm::ddt(rhoE_) + fvm::div(rhoEFlux_, rhoE_)
    );
}
}

```

}

E.5. ionicChargeSolver

```

#include "ionicCharge.H"
#include "volFields.H"
#include "fvn.H"
#include "fvc.H"
#include "fvMatrices.H"
#include "addToRunTimeSelectionTable.H"
#include "findRefCell.H"
#include "adjustPhi.H"
#include "fluidSolidInterface.H"
#include "fixedGradientFvPatchFields.H"
namespace Foam
{
    namespace efieldSolvers
    {
        // Static Data Members
        defineTypeNameAndDebug(ionicCharge, 0);
        addToRunTimeSelectionTable(efieldSolver, ionicCharge, dictionary);
        // Constructors
        ionicCharge::ionicCharge(const fvMesh& mesh)
        :
        efieldSolver(this->typeName, mesh),
        physicalProperties_
        (
            IOobject
            (
                "physicalProperties",
                mesh.time().constant(),
                mesh,
                IOobject::MUST_READ,
                IOobject::NO_WRITE
            )
        ),
        epsilon0_
        (
            physicalProperties_.lookup("epsilon0")
        ),
        e_
        (
            physicalProperties_.lookup("e")
        ),
        mue_
        (
            physicalProperties_.lookup("mu")
        ),
        De_
        (
            physicalProperties_.lookup("D")
        ),
        Ze_
        (
            physicalProperties_.lookup("Z")
        ),
        kE_
        (
            physicalProperties_.lookup("k")
        ),
        U_
        (
            mesh.objectRegistry::lookupObject<volVectorField>("U")
        )
    }
}

```

```

),
phiE_
(
IOobject
(
"phiE",
runTime().timeName(),
mesh,
IOobject::MUST_READ,
IOobject::AUTO_WRITE
),
mesh
),
phiEGrad_
(
IOobject
(
"PhiEGrad",
runTime().timeName(),
mesh,
IOobject::READ_IF_PRESENT,
IOobject::AUTO_WRITE
),
fvc::grad(phiE_)
),
snphiEGrad_
(
IOobject
(
"snphiEGrad",
runTime().timeName(),
mesh,
IOobject::READ_IF_PRESENT,
IOobject::AUTO_WRITE
),
fvc::snGrad(phiE_) * mesh.magSf()
),
ion_
(
IOobject
(
"ion",
runTime().timeName(),
mesh,
IOobject::MUST_READ,
IOobject::AUTO_WRITE
),
mesh
),
mueSnphiEGrad_
(
IOobject
(
"mueSnphiEGrad",
runTime().timeName(),
mesh,
IOobject::READ_IF_PRESENT,
IOobject::AUTO_WRITE
),
snphiEGrad_*mue_
),
ionGrad_
(
IOobject
(
"ionGrad",

```

```

runTime().timeName(),
mesh,
IOobject::READ_IF_PRESENT,
IOobject::AUTO_WRITE
),
fvc::grad(ion_)
),
ionSnGrad_
(
IOobject
(
"ionSnGrad",
runTime().timeName(),
mesh,
IOobject::READ_IF_PRESENT,
IOobject::AUTO_WRITE
),
fvc::interpolate(ionGrad_) & mesh.Sf()
),
rhoE_
(
IOobject
(
"rhoE",
runTime().timeName(),
mesh,
IOobject::MUST_READ,
IOobject::AUTO_WRITE
),
mesh
),
rhoEFlux_
(
IOobject
(
"rhoEFlux",
runTime().timeName(),
mesh,
IOobject::NO_READ,
IOobject::NO_WRITE
),
-kE_*mesh.magSf()*fvc::snGrad(phiE_)
),
E_
(
IOobject
(
"E",
runTime().timeName(),
mesh,
IOobject::NO_READ,
IOobject::AUTO_WRITE
),
-fvc::grad(phiE_)
),
magE_
(
IOobject
(
"magE",
runTime().timeName(),
mesh,
IOobject::NO_READ,
IOobject::AUTO_WRITE
),
mag(fvc::grad(phiE_))

```

```

),
nOuterCorrIons_(5)
{}
// Member Functions
void ionicCharge::evolve()
{
  Info << "Evolving_eField_solver" << endl;
  const fvMesh& mesh = efieldSolver::mesh();
  surfaceScalarField phi_ = fvc::interpolate(U_) & mesh.Sf();
  for (int corr=0; corr<nOuterCorrIons_; corr++)
  {
    snPhiEGrad_ = fvc::snGrad(phiE_) * mesh.magSf();
    Info << "set_up_ion_equation" << endl;
    mueSnPhiEGrad_ = snPhiEGrad_*mue_*Ze_; //mueSnPhiEGrad_ = mue_*Ze_*
    fvc::snGrad(phiE_) * mesh.magSf() * fvc::snGrad(ion_);
    fvScalarMatrix ionEqn
    (
      fvm::ddt(ion_)
      +fvm::div(phi_,ion_)
      -fvm::laplacian(De_,ion_)
      -fvc::div(mueSnPhiEGrad_,ion_)
    );
    ionEqn.solve();
    ion_.correctBoundaryConditions();
    solve
    (
      fvm::laplacian(phiE_) + rhoE_/epsilon0_
    );
    rhoEFlux_ = -kE_*mesh.magSf()*fvc::snGrad(phiE_);
    E_ = -fvc::grad(phiE_);
    magE_ = mag(fvc::grad(phiE_));
    solve
    (
      fvm::ddt(rhoE_) + fvm::div(rhoEFlux_, rhoE_)
    );
  }
}
}
}

```

Bibliography

- [1] G. S. Kushwaha and N. K. Sharma, “Green initiatives: A step towards sustainable development and firm’s performance in the automobile industry,” *Journal of Cleaner Production*, vol. 121, no. 3, pp. 116–129, 2016, ISSN: 09596526. DOI: 10.1016/j.jclepro.2015.07.072.
- [2] A. Furtmann, *Elektrisches Verhalten von Maschinenelementen im Antriebsstrang*, 2017. DOI: 10.15488/8972.
- [3] V. Hausberg, “Elektrische lagerbeanspruchung umrichter gespeister Induktionsmaschinen,” *Fortschritt-Berichte VDI Reihe 21, Elektrotechnik*, vol. 324, 2002.
- [4] V. Hausberg and H. O. Seinsch, “Wellenspannungen und zirkulierende Lagerströme bei umrichter gespeisten Induktionsmaschinen,” *Electrical Engineering*, vol. 82, no. 6, pp. 313–326, 2000, ISSN: 0948-7921. DOI: 10.1007/s002020000045.
- [5] F. Lin, K. T. Chau, C. C. Chan, and C. Liu, “Fault diagnosis of power components in electric vehicles,” *Journal of Asian Electric Vehicles*, vol. 11, no. 2, pp. 1659–1666, 2013, ISSN: 1348-3927. DOI: 10.4130/jaev.11.1659.
- [6] S. Nandi, H. A. Toliyat, and X. Li, “Condition monitoring and fault diagnosis of electrical motors—a review,” *IEEE Transactions on Energy Conversion*, vol. 20, no. 4, pp. 719–729, 2005, ISSN: 0885-8969. DOI: 10.1109/TEC.2005.847955.
- [7] H. Prashad, *Tribology in electrical environments*, ser. Tribology and interface engineering series. Amsterdam: Elsevier, 2006, vol. 49, ISBN: 978-0-444-51880-4.
- [8] A. Mütze, “Thousands of hits: On inverter-induced bearing currents, related work, and the literature,” *e & i Elektrotechnik und Informationstechnik*, vol. 128, no. 11-12, pp. 382–388, 2011, ISSN: 0932-383X. DOI: 10.1007/s00502-011-0053-1.
- [9] D. Cornel, F. Gutiérrez Guzmán, G. Jacobs, and S. Neumann, “Condition monitoring of roller bearings using acoustic emission,” *Wind Energy Science*, vol. 6, no. 2, pp. 367–376, 2021. DOI: 10.5194/wes-6-367-2021.
- [10] T. Harriehausen and D. Schwarzenau, *Moeller Grundlagen der Elektrotechnik, 24.*, durchgesehene und korrigierte Auflage, ser. Lehrbuch. Wiesbaden and Heidelberg: Springer Vieweg, 2020, ISBN: 978-3-658-27839-7.
- [11] T. Schirra, G. Martin, S. Puchtler, and E. Kirchner, “Electric impedance of rolling bearings - consideration of unloaded rolling elements,” *Tribology International*, vol. 158, p. 106927, 2021, ISSN: 0301679X. DOI: 10.1016/j.triboint.2021.106927.

-
- [12] N. Bader, A. Furtmann, H. Tischmacher, and G. Poll, “Capacitances and lubricant film thicknesses of grease and oil lubricated bearings: Rolling element bearings ii: Rolling element bearing dynamics,” in *STLE Annual Meeting & Exhibition*.
- [13] Y. Gemeinder, M. Schuster, B. Radnai, B. Sauer, and A. Binder, “Calculation and validation of a bearing impedance model for ball bearings and the influence on edm-currents,” in *2014 International Conference on Electrical Machines (ICEM)*, IEEE, 2014, pp. 1804–1810, ISBN: 978-1-4799-4389-0. DOI: 10.1109/ICELMACH.2014.6960428.
- [14] O. Magdun and A. Binder, “Calculation of roller and ball bearing capacitances and prediction of edm currents,” in *IECON 2009 - 35th Annual Conference of IEEE Industrial Electronics*, IEEE, 2009, pp. 1051–1056, ISBN: 978-1-4244-4648-3. DOI: 10.1109/IECON.2009.5414669.
- [15] T. Schirra, “Phänomenologische Betrachtung der sensorisch nutzbaren Effekte am Wälzlager: Einfluss unbelasteter Wälzkörper auf die elektrische Impedanz,” Ph.D. dissertation, Technische Universität Darmstadt, Darmstadt, 2021. DOI: 10.26083/tuprints-00017957.
- [16] Y. Gemeinder, “Lagerimpedanz und Lagerschädigung bei Stromdurchgang in umrichter gespeisten elektrischen Maschinen,” Dissertation, 2016.
- [17] D. Dowson and G. R. Higginson, “The effect of material properties on the lubrication of elastic rollers,” *Journal of Mechanical Engineering Science*, vol. 2, no. 3, pp. 188–194, 1960, ISSN: 0022-2542. DOI: 10.1243/JMES_JOUR_1960_002_028_02.
- [18] D. Dowson, G. R. Higginson, and A. V. Whitaker, “Elasto-hydrodynamic lubrication: A survey of isothermal solutions,” *Journal of Mechanical Engineering Science*, vol. 4, no. 2, pp. 121–126, 1962, ISSN: 0022-2542. DOI: 10.1243/JMES_JOUR_1962_004_018_02.
- [19] D. Dowson and G. R. Higginson, “A numerical solution to the elasto-hydrodynamic problem,” *Journal of Mechanical Engineering Science*, vol. 1, no. 1, pp. 6–15, 1959, ISSN: 0022-2542. DOI: 10.1243/JMES_JOUR_1959_001_004_02.
- [20] A. I. Petrusevich, “Fundamental conclusions from the contact-hydrodynamic theory of lubrication,” *Izvestiya Akademii Nauk SSSR*, no. 2, pp. 209–223, 1951.
- [21] B. J. Hamrock and D. Dowson, “Isothermal elasto-hydrodynamic lubrication of point contacts: Part 1—theoretical formulation,” *Journal of Lubrication Technology*, vol. 98, no. 2, pp. 223–228, 1976, ISSN: 0022-2305. DOI: 10.1115/1.3452801.
- [22] B. J. Hamrock and D. Dowson, “Isothermal elasto-hydrodynamic lubrication of point contacts: Part ii—ellipticity parameter results,” *Journal of Lubrication Technology*, vol. 98, no. 3, pp. 375–381, 1976, ISSN: 0022-2305. DOI: 10.1115/1.3452861.

-
- [23] B. J. Hamrock and D. Dowson, “Isothermal elastohydrodynamic lubrication of point contacts: Part iii—fully flooded results,” *Journal of Lubrication Technology*, vol. 99, no. 2, pp. 264–275, 1977, ISSN: 0022-2305. DOI: 10.1115/1.3453074.
- [24] B. J. Hamrock and D. Dowson, “Isothermal elastohydrodynamic lubrication of point contacts: Part iv—starvation results,” *Journal of Lubrication Technology*, vol. 99, no. 1, pp. 15–23, 1977, ISSN: 0022-2305. DOI: 10.1115/1.3452973.
- [25] H. Moes, “Optimum similarity analysis with applications to elastohydrodynamic lubrication,” *Wear*, vol. 159, no. 1, pp. 57–66, 1992, ISSN: 00431648. DOI: 10.1016/0043-1648(92)90286-h.
- [26] A. A. Lubrecht, *The numerical Solution of the elastohydrodynamically lubricated line- and point contact problem, using multigrid techniques*. Enschede: University of Twente, 1987, ISBN: 9789090015835.
- [27] C. H. Venner, *Multilevel solution of the EHL line and point contact problems*. Enschede: University of Twente, 1991.
- [28] S. Bair, M. Khonsari, and W. O. Winer, “High-pressure rheology of lubricants and limitations of the reynolds equation,” *Tribology International*, vol. 31, no. 10, pp. 573–586, 1998, ISSN: 0301679X. DOI: 10.1016/S0301-679X(98)00078-4.
- [29] C. T. Schäfer, P. Giese, W. B. Rowe, and N. H. Woolley, “Elastohydrodynamically lubricated line contact based on the navier-stokes equations,” in *Thinning Films and Tribological Interfaces, Proceedings of the 26th Leeds-Lyon Symposium on Tribology*, ser. Tribology Series, vol. 38, Elsevier, 2000, pp. 57–69, ISBN: 9780444505316. DOI: 10.1016/S0167-8922(00)80112-1.
- [30] T. Almqvist and R. Larsson, “The navier–stokes approach for thermal ehl line contact solutions,” *Tribology International*, vol. 35, no. 3, pp. 163–170, 2002, ISSN: 0301679X. DOI: 10.1016/S0301-679X(01)00112-8.
- [31] T. Almqvist and R. Larsson, “Some remarks on the validity of reynolds equation in the modeling of lubricant film flows on the surface roughness scale,” *Journal of Tribology*, vol. 126, no. 4, pp. 703–710, 2004, ISSN: 0742-4787. DOI: 10.1115/1.1760554.
- [32] M. Hartinger, M.-L. Dumont, S. Ioannides, D. Gosman, and H. Spikes, “Cfd modeling of a thermal and shear-thinning elastohydrodynamic line contact,” *Journal of Tribology*, vol. 130, no. 4, 2008, ISSN: 0742-4787. DOI: 10.1115/1.2958077.
- [33] A. Hajishafiee, A. Kadiric, S. Ioannides, and D. Dini, “A coupled finite-volume cfd solver for two-dimensional elasto-hydrodynamic lubrication problems with particular application to rolling element bearings,” *Tribology International*, vol. 109, no. 4905, pp. 258–273, 2017, ISSN: 0301679X. DOI: 10.1016/j.triboint.2016.12.046.
- [34] M. Hartinger and T. Reddyhoff, “Cfd modeling compared to temperature and friction measurements of an ehl line contact,” *Tribology International*, vol. 126, pp. 144–152, 2018, ISSN: 0301679X. DOI: 10.1016/j.triboint.2018.05.012.

-
- [35] M. Tošić, R. Larsson, J. Jovanović, T. Lohner, M. Björling, and K. Stahl, “A computational fluid dynamics study on shearing mechanisms in thermal elastohydrodynamic line contacts,” *Lubricants*, vol. 7, no. 8, p. 69, 2019. DOI: 10.3390/lubricants7080069.
- [36] C. H. Venner and J. Bos, “Effects of lubricant compressibility on the film thickness in ehl line and circular contacts,” *Wear*, vol. 173, no. 1-2, pp. 151–165, 1994, ISSN: 00431648. DOI: 10.1016/0043-1648(94)90268-2.
- [37] W. Habchi and S. Bair, “Quantitative compressibility effects in thermal elastohydrodynamic circular contacts,” *Journal of Tribology*, vol. 135, no. 1, 2013, ISSN: 0742-4787. DOI: 10.1115/1.4023082.
- [38] M. Marian, M. Bartz, S. Wartzack, and A. Rosenkranz, “Non-dimensional groups, film thickness equations and correction factors for elastohydrodynamic lubrication: A review,” *Lubricants*, vol. 8, no. 10, p. 95, 2020. DOI: 10.3390/lubricants8100095.
- [39] B. J. Hamrock and D. Dowson, *Ball bearing lubrication: The elastohydrodynamics of elliptical contacts*. New York: Wiley, 1981, ISBN: 978-0471035534.
- [40] L. E. Murch and W. R. D. Wilson, “A thermal elastohydrodynamic inlet zone analysis,” *Journal of Lubrication Technology*, vol. 97, no. 2, pp. 212–216, 1975, ISSN: 0022-2305. DOI: 10.1115/1.3452559.
- [41] G. Hou, J. Wang, and A. Layton, “Numerical methods for fluid-structure interaction — a review,” *Communications in Computational Physics*, vol. 12, no. 2, pp. 337–377, 2012, ISSN: 1815-2406. DOI: 10.4208/cicp.291210.290411s.
- [42] Ž. Tuković, A. Karač, P. Cardiff, H. Jasak, and A. Ivanković, “Openfoam finite volume solver for fluid-solid interaction,” *Transactions of FAMENA*, vol. 42, no. 3, pp. 1–31, 2018, ISSN: 13331124. DOI: 10.21278/T0F.42301.
- [43] K. Jablonka, R. Glovnea, and J. Bongaerts, “Quantitative measurements of film thickness in a radially loaded deep-groove ball bearing,” *Tribology International*, vol. 119, pp. 239–249, 2018, ISSN: 0301679X. DOI: 10.1016/j.triboint.2017.11.001.
- [44] D. Dowson, *History of tribology*, 2. ed. London: Professional Engineering Publ, 1998, ISBN: 978-1-860-58070-3.
- [45] T. A. Harris and M. N. Kotzalas, *Rolling Bearing Analysis, 4th Edition // Rolling bearing analysis*. Boca Raton: CRC - Taylor & Francis, 2007, ISBN: 9780849381676.
- [46] R. Stribeck, *Die wesentlichen Eigenschaften der Gleit- und Rollenlager*, ser. Mitteilungen über Forschungsarbeiten auf dem Gebiete des Ingenieurwesens, insbesondere aus den Laboratorien der technischen Hochschulen. Julius Springer, 1903.

-
- [47] G. Niemann, H. Winter, B.-R. Höhn, and K. Stahl, *Maschinenelemente 1: Konstruktion und Berechnung von Verbindungen, Lagern, Wellen*, 5., vollständig überarbeitete Auflage, ser. Springer eBook Collection. Berlin and Heidelberg: Springer Vieweg, 2019, ISBN: 978-3-662-55481-4. DOI: 10.1007/978-3-662-55482-1.
- [48] B. J. Hamrock, S. R. Schmid, and B. O. Jacobson, *Fundamentals of fluid film lubrication*, 2nd ed., ser. Mechanical engineering. New York: Dekker, 2004, vol. 169, ISBN: 9780824753719.
- [49] H. Czichos and K.-H. Habig, Eds., *Tribologie-Handbuch: Tribometrie, Tribomaterialien, Tribotechnik*, 4., vollst. überarb. und erw. Aufl. Wiesbaden: Springer Vieweg, 2015, ISBN: 978-3-8348-2236-9.
- [50] H. A. Spikes, “Mixed lubrication — an overview,” *Lubrication Science*, vol. 9, no. 3, pp. 221–253, 1997, ISSN: 0954-0075. DOI: 10.1002/lis.3010090302.
- [51] D. Zhu and Q. Jane Wang, “Elastohydrodynamic lubrication: A gateway to interfacial mechanics—review and prospect,” *Journal of Tribology*, vol. 133, no. 4, p. 156, 2011, ISSN: 0742-4787. DOI: 10.1115/1.4004457.
- [52] T. Almqvist and R. Larsson, “Thermal transient rough ehl line contact simulations by aid of computational fluid dynamics,” *Tribology International*, vol. 41, no. 8, pp. 683–693, 2008, ISSN: 0301679X. DOI: 10.1016/j.triboint.2007.11.004.
- [53] H.-D. Tietz, Ed., *Technische Keramik: Aufbau, Eigenschaften, Herstellung, Bearbeitung, Prüfung*, ser. Springer eBook Collection Computer Science and Engineering. Berlin, Heidelberg and s.l.: Springer Berlin Heidelberg, 1994, ISBN: 9783642579028. DOI: 10.1007/978-3-642-57902-8.
- [54] D. Bartel, *Simulation von Tribosystemen: Grundlagen und Anwendungen: Zugl.: Magdeburg, Univ., Fak. für Maschinenbau, Habil.-Schr., 2009*, 1. Aufl., ser. Vieweg + Teubner Research. Wiesbaden: Vieweg + Teubner, 2010, ISBN: 978-3-8348-1241-4.
- [55] D. E. Keyes, L. C. McInnes, C. Woodward, W. Gropp, E. Myra, M. Pernice, J. Bell, J. Brown, A. Clo, J. Connors, E. Constantinescu, D. Estep, K. Evans, C. Farhat, A. Hakim, G. Hammond, G. Hansen, J. Hill, T. Isaac, X. Jiao, K. Jordan, D. Kaushik, E. Kaxiras, A. Koniges, K. Lee, A. Lott, Q. Lu, J. Magerlein, R. Maxwell, M. McCourt, M. Mehl, R. Pawlowski, A. P. Randles, D. Reynolds, B. Rivière, U. Rüde, T. Scheibe, J. Shadid, B. Sheehan, M. Shephard, A. Siegel, B. Smith, X. Tang, C. Wilson, and B. Wohlmuth, “Multiphysics simulations,” *The International Journal of High Performance Computing Applications*, vol. 27, no. 1, pp. 4–83, 2013, ISSN: 1094-3420. DOI: 10.1177/1094342012468181.
- [56] R. B. Bird, W. E. Stewart, and E. N. Lightfoot, *Transport phenomena*, Rev. 2. ed. New York: Wiley, 2007, ISBN: 0470115394.
- [57] T. Richter, *Fluid-structure Interactions: Models, analysis and finite elements*, ser. Lecture notes in computational science and engineering. Cham: Springer, 2017, vol. 118, ISBN: 978-3-319-63970-3.

-
- [58] E. H. van Brummelen, “Added mass effects of compressible and incompressible flows in fluid-structure interaction,” *Journal of Applied Mechanics*, vol. 76, no. 2, p. 3, 2009, ISSN: 1064-8275. DOI: 10.1115/1.3059565.
- [59] K. L. Johnson, “Regimes of elastohydrodynamic lubrication,” *Journal of Mechanical Engineering Science*, vol. 12, no. 1, pp. 9–16, 1970, ISSN: 0022-2542. DOI: 10.1243/JMES_JOUR_1970_012_004_02.
- [60] T. G. Myers, Hall R.W., Savage M.D., and Gaskell P.H., “The transition region of elastohydrodynamic lubrication,” *Proceedings of the Royal Society of London. Series A: Mathematical and Physical Sciences*, vol. 432, no. 1886, pp. 467–479, 1991, ISSN: 0962-8444. DOI: 10.1098/rspa.1991.0026.
- [61] F. Moukalled, L. Mangani, and M. Darwish, *The finite volume method in computational fluid dynamics: An advanced introduction with OpenFOAM and Matlab*, ser. Fluid mechanics and its applications. Cham et al.: Springer, 2016, vol. volume 113, ISBN: 3319168738.
- [62] H. Spikes and Z. Jie, “History, origins and prediction of elastohydrodynamic friction,” *Tribology Letters*, vol. 56, no. 1, pp. 1–25, 2014, ISSN: 1023-8883. DOI: 10.1007/s11249-014-0396-y.
- [63] S. Bair, P. Vergne, P. Kumar, G. Poll, I. Krupka, M. Hartl, W. Habchi, and R. Larsson, “Comment on “history, origins and prediction of elastohydrodynamic friction” by spikes and jie,” *Tribology Letters*, vol. 58, no. 1, 2015, ISSN: 1023-8883. DOI: 10.1007/s11249-015-0481-x.
- [64] P. W. McDonald, “The computation of transonic flow through two-dimensional gas turbine cascades,” in *ASME 1971 International Gas Turbine Conference and Products Show*, American Society of Mechanical Engineers, 1971, ISBN: 978-0-7918-7982-5. DOI: 10.1115/71-GT-89.
- [65] H. K. Versteeg and W. Malalasekera, *An introduction to computational fluid dynamics: The finite volume method*, 2. ed., [Nachdr.] Harlow: Pearson/Prentice Hall, 2007, ISBN: 978-0-13-127498-3.
- [66] M. Kaneta and P. Yang, “Effects of thermal conductivity of contacting surfaces on point ehl contacts,” *Journal of Tribology*, vol. 125, no. 4, pp. 731–738, 2003, ISSN: 0742-4787. DOI: 10.1115/1.1540121.
- [67] J. H. Ferziger, M. Peric, and R. L. Street, *Numerische Strömungsmechanik*, 2., aktualisierte Auflage. Berlin: Springer Vieweg, 2020, ISBN: 978-3-662-46543-1.
- [68] R. Larsson, P. O. Larsson, E. Eriksson, M. Sjöberg, and E. Höglund, “Lubricant properties for input to hydrodynamic and elastohydrodynamic lubrication analyses,” *Proceedings of the Institution of Mechanical Engineers, Part J: Journal of Engineering Tribology*, vol. 214, no. 1, pp. 17–27, 2000, ISSN: 1350-6501. DOI: 10.1243/1350650001542981.

-
- [69] E. Höglund and R. Larsson, “Modelling non-steady ehl with focus on lubricant density,” in *Elastohydrodynamics '96*, ser. Tribology Series, D. Dowson, Ed., vol. 32, Amsterdam and New York: Elsevier for the Institute of Tribology the University of Leeds and Institut national des Sciences appliquées de Lyon, 2010, pp. 511–521, ISBN: 9780444828095. DOI: 10.1016/S0167-8922(08)70478-4.
- [70] H. D. Baehr and S. Kabelac, *Thermodynamik: Grundlagen und technische Anwendungen*, 16. Aufl. 2016. Berlin, Heidelberg: Springer Berlin Heidelberg, 2016, ISBN: 9783662495681.
- [71] D. Dowson and G. R. Higginson, *Elasto-hydrodynamic lubrication*, SI ed., 2. ed., ser. International series on materials science and technology. Oxford: Pergamon Press, 1977, vol. 23, ISBN: 0-08-021303-0.
- [72] P. E. Scott Bair, *High-pressure rheology for quantitative elastohydrodynamics*, 1st ed., ser. Tribology and interface engineering series. Amsterdam: Elsevier, 2007, vol. 54, ISBN: 9780080475301.
- [73] Y. A. Fakhreddine and P. Zoller, “The equation of state of a polydimethylsiloxane fluid,” *Journal of Applied Polymer Science*, vol. 41, no. 56, pp. 1087–1093, 1990, ISSN: 00218995. DOI: 10.1002/app.1990.070410518.
- [74] J. O. Hirschfelder, C. F. Curtiss, and R. B. Bird, *Molecular theory of gases and liquids*, Corr. print. with notes added., ser. Structure of matter series. New York, NY: Wiley, 1964, ISBN: 9780471400653.
- [75] F. D. Murnaghan, “Finite deformations of an elastic solid,” *American Journal of Mathematics*, vol. 59, no. 2, p. 235, 1937, ISSN: 00029327. DOI: 10.2307/2371405.
- [76] C. A. N. d. Castro, J. Millat, and J. H. Dymond, Eds., *Transport properties of fluids: Their correlation, prediction and estimation*. Cambridge: Cambridge University Press, 1996, ISBN: 978-0-521-46178-8. DOI: 10.1017/CB09780511529603.
- [77] J. R. MACDONALD, “Some simple isothermal equations of state,” *Reviews of Modern Physics*, vol. 38, no. 4, pp. 669–679, 1966, ISSN: 0034-6861. DOI: 10.1103/RevModPhys.38.669.
- [78] C. Barus, “Isothermals, isopiestic and isometrics relative to viscosity,” *American Journal of Science*, vol. s3-45, no. 266, pp. 87–96, 1893, ISSN: 0002-9599. DOI: 10.2475/ajs.s3-45.266.87.
- [79] W. R. D. Wilson, “An isoviscous model for the hydrodynamic lubrication of plane strain forging processes with flat dies,” *Journal of Lubrication Technology*, vol. 96, no. 4, pp. 539–546, 1974, ISSN: 0022-2305. DOI: 10.1115/1.3452478.
- [80] C. J. A. Roelands, J. C. Vlugter, and H. I. Waterman, “The viscosity-temperature-pressure relationship of lubricating oils and its correlation with chemical constitution,” *Journal of Basic Engineering*, vol. 85, no. 4, pp. 601–607, 1963, ISSN: 0021-9223. DOI: 10.1115/1.3656919.

-
- [81] C. J. A. Roelands, W. O. Winer, and W. A. Wright, “Correlational aspects of the viscosity-temperature-pressure relationship of lubricating oils (dr in dissertation at technical university of delft, 1966),” *Journal of Lubrication Technology*, vol. 93, no. 1, pp. 209–210, 1971, ISSN: 0022-2305. DOI: 10.1115/1.3451519.
- [82] A. K. Doolittle, “Studies in newtonian flow. i. the dependence of the viscosity of liquids on temperature,” *Journal of Applied Physics*, vol. 22, no. 8, pp. 1031–1035, 1951, ISSN: 0037-9646. DOI: 10.1063/1.1700096.
- [83] A. K. Doolittle, “Studies in newtonian flow. ii. the dependence of the viscosity of liquids on free-space,” *Journal of Applied Physics*, vol. 22, no. 12, pp. 1471–1475, 1951, ISSN: 0037-9646. DOI: 10.1063/1.1699894.
- [84] A. K. Doolittle, “Studies in newtonian flow. iii. the dependence of the viscosity of liquids on molecular weight and free space (in homologous series),” *Journal of Applied Physics*, vol. 23, no. 2, pp. 236–239, 1952, ISSN: 0037-9646. DOI: 10.1063/1.1702182.
- [85] C. A. Angell, “Formation of glasses from liquids and biopolymers,” *Science (New York, N.Y.)*, vol. 267, no. 5206, pp. 1924–1935, 1995, ISSN: 0036-8075. DOI: 10.1126/science.267.5206.1924.
- [86] J.-P. Hansen and I. R. McDonald, *Theory of simple liquids: With applications to soft matter*, Fourth edition. Amsterdam: Elsevier, 2013, ISBN: 978-0-12-387032-2.
- [87] L. Berthier and G. Biroli, “Theoretical perspective on the glass transition and amorphous materials,” *Reviews of Modern Physics*, vol. 83, no. 2, pp. 587–645, 2011, ISSN: 0034-6861. DOI: 10.1103/RevModPhys.83.587.
- [88] S. Karmakar, C. Dasgupta, and S. Sastry, “Length scales in glass-forming liquids and related systems: A review,” *Reports on progress in physics. Physical Society (Great Britain)*, vol. 79, no. 1, p. 016601, 2016. DOI: 10.1088/0034-4885/79/1/016601.
- [89] S. S. Bair, O. Andersson, F. S. Qureshi, and M. M. Schirru, “New ehl modeling data for the reference liquids squalane and squalane plus polyisoprene,” *Tribology Transactions*, vol. 61, no. 2, pp. 247–255, 2018, ISSN: 1040-2004. DOI: 10.1080/10402004.2017.1310339.
- [90] D. Turnbull and M. H. Cohen, “Concerning reconstructive transformation and formation of glass,” *The Journal of Chemical Physics*, vol. 29, no. 5, pp. 1049–1054, 1958, ISSN: 0021-9606. DOI: 10.1063/1.1744654.
- [91] D. Turnbull and M. H. Cohen, “Free-volume model of the amorphous phase: Glass transition,” *The Journal of Chemical Physics*, vol. 34, no. 1, pp. 120–125, 1961, ISSN: 0021-9606. DOI: 10.1063/1.1731549.
- [92] M. L. Williams, R. F. Landel, and J. D. Ferry, “The temperature dependence of relaxation mechanisms in amorphous polymers and other glass-forming liquids,” *Journal of the American Chemical Society*, vol. 77, no. 14, pp. 3701–3707, 1955, ISSN: 0002-7863. DOI: 10.1021/ja01619a008.

-
- [93] I. Demirdžić and S. Muzaferija, “Finite volume method for stress analysis in complex domains,” *International Journal for Numerical Methods in Engineering*, vol. 37, no. 21, pp. 3751–3766, 1994, ISSN: 0029-5981. DOI: 10.1002/nme.1620372110.
- [94] I. Demirdžić and S. Muzaferija, “Numerical method for coupled fluid flow, heat transfer and stress analysis using unstructured moving meshes with cells of arbitrary topology,” *Computer Methods in Applied Mechanics and Engineering*, vol. 125, no. 1-4, pp. 235–255, 1995, ISSN: 00457825. DOI: 10.1016/0045-7825(95)00800-G.
- [95] H. Jasak and H. G. Weller, “Application of the finite volume method and unstructured meshes to linear elasticity,” *International Journal for Numerical Methods in Engineering*, vol. 48, no. 2, pp. 267–287, 2000, ISSN: 0029-5981. DOI: 10.1002/(SICI)1097-0207(20000520)48:2<267::AID-NME884>3.0.CO;2-Q.
- [96] D. Dowson, “A central film thickness formula for elastohydrodynamic line contacts, elastohydrodynamics and related topics,” *Proceedings 5th Leeds-Lyon Symposium*, no. 60, pp. 60–65, 1978.
- [97] K. Singh, F. Sadeghi, T. Russell, S. J. Lorenz, W. Peterson, J. Villarreal, and T. Jinmon, “Fluid–structure interaction modeling of elastohydrodynamically lubricated line contacts,” *Journal of Tribology*, vol. 143, no. 9, p. 1, 2021, ISSN: 0742-4787. DOI: 10.1115/1.4049260.
- [98] J. Spurk and N. Aksel, *Strömungslehre: Einführung in die Theorie der Strömungen*, 8. Aufl. 2010, ser. Springer-Lehrbuch. Berlin, Heidelberg: Springer Berlin Heidelberg, 2010, ISBN: 9783642131431.
- [99] D. Dowson, E. S. Song, and C. M. Taylor, “Non-dimensional groups in elastohydrodynamic lubrication,” in *Thin films in tribology*, ser. Tribology Series, vol. 25, Amsterdam and New York: Elsevier for the Institute of Tribology Leeds University and the Institut national des Sciences appliquées de Lyon, 2010, pp. 237–242, ISBN: 9780444897893. DOI: 10.1016/S0167-8922(08)70379-1.
- [100] A. Küchler, *High Voltage Engineering: Fundamentals - Technology - Applications*, ser. VDI-Buch. Berlin, Heidelberg: Springer Berlin Heidelberg, 2017, ISBN: 978-3-642-11992-7.
- [101] J. R. Melcher, *Continuum electromechanics*. Cambridge, Mass.: MIT Press, 1981, ISBN: 026213165X.
- [102] S. Puchtler, T. Schirra, E. Kirchner, Y. Späck-Leigsnering, and H. D. Gersem, “Comparison of analytic and numeric methods to calculate ball bearing capacitance,” 2021.
- [103] J. H. Masliyah and S. Bhattacharjee, *Electrokinetic and colloid transport phenomena*. Hoboken, N.J: Wiley-Interscience, 2011, ISBN: 9780471799733. DOI: 10.1002/0471799742.

-
- [104] A. Einstein, “Über die von der molekularkinetischen Theorie der Wärme geforderte Bewegung von in ruhenden Flüssigkeiten suspendierten Teilchen,” *Annalen der Physik*, vol. 322, no. 8, pp. 549–560, 1905, ISSN: 00033804. DOI: 10.1002/andp.19053220806.
- [105] W. Sutherland, “Lxxv. a dynamical theory of diffusion for non-electrolytes and the molecular mass of albumin,” *The London, Edinburgh, and Dublin Philosophical Magazine and Journal of Science*, vol. 9, no. 54, pp. 781–785, 1905, ISSN: 1941-5982. DOI: 10.1080/14786440509463331.
- [106] R. Schrader, “Zur Schmierfilmbildung von Schmierölen und Schmierfetten in elasto-hydrodynamischen Wälzkontakten,” Dissertation, Universität Hannover, Hannover, 1988.
- [107] K. Roth, *Konstruieren mit Konstruktionskatalogen: Band 1: Konstruktionslehre*, 3. Auflage, erweitert und neu gestaltet, ser. Springer eBook Collection. Berlin, Heidelberg and s.l.: Springer Berlin Heidelberg, 2000, ISBN: 978-3-642-17466-7. DOI: 10.1007/978-3-642-17466-7.
- [108] J. Feldhusen and K.-H. Grote, Eds., *Pahl/Beitz Konstruktionslehre: Methoden und Anwendung erfolgreicher Produktentwicklung*, 8. Aufl. 2013. Berlin, Heidelberg: Springer Berlin Heidelberg, 2013, ISBN: 9783642295683.
- [109] S. Gramlich, *Vom fertigungsgerechten Konstruieren zum produktionsintegrierenden Entwickeln: Durchgängige Modelle und Methoden im Produktlebenszyklus: Zugl.: Darmstadt, Techn. Univ., Diss., 2013*, Als Ms. gedr, ser. Berichte aus dem Fachgebiet Produktentwicklung und Maschinenelemente der TU Darmstadt. Düsseldorf: VDI-Verl., 2013, vol. 423, ISBN: 978-3-18-342301-9.
- [110] H. Stachowiak, *Allgemeine Modelltheorie*, Softcover reprint of the hardcover 1. ed. 1973. Wien: Springer, 2013, ISBN: 978-3-7091-8328-1.
- [111] D. C. Ince, L. Hatton, and J. Graham-Cumming, “The case for open computer programs,” *Nature*, vol. 482, no. 7386, pp. 485–488, 2012, ISSN: 0028-0836. DOI: 10.1038/nature10836.
- [112] J. Degroote, K.-J. Bathe, and J. Vierendeels, “Performance of a new partitioned procedure versus a monolithic procedure in fluid–structure interaction,” *Computers & Structures*, vol. 87, no. 11-12, pp. 793–801, 2009, ISSN: 00457949. DOI: 10.1016/j.compstruc.2008.11.013.
- [113] S. B. Lippman, *C++ primer*, 5th ed. Upper Saddle River, N.J.: Addison-Wesley, 2013, ISBN: 9780321714114.
- [114] S. Khodaei, A. Henstock, R. Sadeghi, S. Sellers, P. Blanke, J. Leipsic, A. Emadi, and Z. Keshavarz-Motamed, “Personalized intervention cardiology with transcatheter aortic valve replacement made possible with a non-invasive monitoring and diagnostic framework,” *Scientific reports*, vol. 11, no. 1, p. 10 888, 2021. DOI: 10.1038/s41598-021-85500-2.

-
- [115] K. Beck, *Test-driven development: By example*, 20. printing, ser. A Kent Beck signature book. Boston: Addison-Wesley, 2015, ISBN: 9780321146533.
- [116] German Institute for Standardization, *Din66001:information processing: Graphical symbols and their application*, Berlin, 1983.
- [117] M. Beaudoin and H. Jasak, *Development of a generalized grid interface for turbomachinery simulations with openfoam*, 2008.
- [118] R. Issa, “Solution of the implicitly discretised fluid flow equations by operator-splitting,” *Journal of Computational Physics*, vol. 62, no. 1, pp. 40–65, 1986, ISSN: 00219991. DOI: 10.1016/0021-9991(86)90099-9.
- [119] H. A. Schwarz, *Gesammelte Mathematische Abhandlungen: Erster Band*. Berlin, Heidelberg: Springer Berlin / Heidelberg, 1890, ISBN: 978-3-642-50665-9.
- [120] S. V. PATANKAR and D. B. SPALDING, “A calculation procedure for heat, mass and momentum transfer in three-dimensional parabolic flows,” in *Numerical Prediction of Flow, Heat Transfer, Turbulence and Combustion*, vol. 6, Elsevier, 1983, pp. 54–73, ISBN: 9780080309378. DOI: 10.1016/B978-0-08-030937-8.50013-1.
- [121] C. Habchi, S. Russeil, D. Bougeard, J.-L. Harion, T. Lemenand, A. Ghanem, D. Della Valle, and H. Peerhossaini, “Partitioned solver for strongly coupled fluid–structure interaction,” *Computers & Fluids*, vol. 71, pp. 306–319, 2013, ISSN: 00457930. DOI: 10.1016/j.compfluid.2012.11.004.
- [122] P. Cardiff, Ž. Tuković, H. Jasak, and A. Ivanković, “A block-coupled finite volume methodology for linear elasticity and unstructured meshes,” *Computers & Structures*, vol. 175, pp. 100–122, 2016, ISSN: 00457949. DOI: 10.1016/j.compstruc.2016.07.004.
- [123] A. Harder, L. Piske, M. Neu, and E. Kirchner, “Initiierungs- und Abklingeffekte von elektrischen Schädigungsmechanismen im Wälzlager,” in *Gleit- und Wälzlagerungen 2021*, VDI Verlag, 2021, pp. 65–74, ISBN: 9783181023785. DOI: 10.51202/9783181023785-65.
- [124] G. Martin, “Die Wälzlagerimpedanz als werkzeug zur Untersuchung von Oberflächenabweichungen in Wälzlagern,” Ph.D. dissertation, Technische Universität Darmstadt, Darmstadt, 2021.
- [125] P. Schuler, *Einfluss von Grenzflächeneffekten auf den Dichtmechanismus der Radial-Wellendichtung: Zugl.: Stuttgart, Univ., Diss., 2014*, ser. Berichte aus dem Institut für Maschinenelemente. Stuttgart: IMA, 2014, vol. 153, ISBN: 978-3-936100-54-9.
- [126] G. Martin, F. M. Becker, and E. Kirchner, “A novel method for diagnosing rolling bearing surface damage by electric impedance analysis,” *Tribology International*, vol. 170, 2022. DOI: 10.31224/osf.io/dgb8s.

-
- [127] A. Feldermann, S. Neumann, and G. Jacobs, “Cfd simulation of elasto-hydrodynamic lubrication problems with reduced order models for fluid–structure interaction,” *Tribology - Materials, Surfaces & Interfaces*, vol. 11, no. 1, pp. 30–38, 2017, ISSN: 1751-5831. DOI: 10.1080/17515831.2017.1279846.
- [128] A. Hajishafiee, *Finite-volume cfd modelling of fluid-solid interaction in ehl contacts*, 2013. DOI: 10.25560/32100.
- [129] I. Demirdžić, Ž. Lilek, and M. Perić, “Fluid flow and heat transfer test problems for non-orthogonal grids: Bench-mark solutions,” *International Journal for Numerical Methods in Fluids*, vol. 15, no. 3, pp. 329–354, 1992, ISSN: 0271-2091. DOI: 10.1002/flid.1650150306.
- [130] D. Gross, W. Hauger, J. Schröder, and W. A. Wall, *Technische Mechanik 2: Elastostatik*, 12. Aufl. 2014, ser. Springer-Lehrbuch. Berlin, Heidelberg: Springer Berlin Heidelberg, 2014, ISBN: 978-3-642-40965-3.
- [131] J. Taler, *Solving Direct and Inverse Heat Conduction Problems*. Berlin, Heidelberg: Springer Berlin / Heidelberg, 2006, ISBN: 978-3-540-33470-5.
- [132] S. Turek and J. Hron, “Proposal for numerical benchmarking of fluid-structure interaction between an elastic object and laminar incompressible flow,” in *Fluid-Structure Interaction*, ser. Lecture notes in computational science and engineering, H.-J. Bungartz and M. Schäfer, Eds., vol. 53, Berlin, Heidelberg: Springer Berlin Heidelberg, 2006, pp. 371–385, ISBN: 978-3-540-34595-4. DOI: 10.1007/3-540-34596-5_15.
- [133] H. Mulrav, “Experimentelle Untersuchung elektrischer Felder in Wälzlagerkontakten mithilfe keramischer Lager,” Bachelorthesis, Technische Universität Darmstadt, Darmstadt, 2021.
- [134] A. Zaiat, “Numerische Simulation der elektrischen Eigenschaften eines Wälzkontaktes mit gemessenen Oberflächen,” Masterthesis, Technische Universität Darmstadt, Darmstadt, 2021.
- [135] J.-P. Franc and J.-M. Michel, *Fundamentals of cavitation*, ser. Fluid mechanics and its applications. Dordrecht: Kluwer Acad. Publ, 2004, vol. 76, ISBN: 978-1-4020-2233-3.
- [136] K. Sommer, R. Heinz, and J. Schöfer, *Verschleiß metallischer Werkstoffe: Erscheinungsformen sicher beurteilen ; mit zahlreichen Tabellen*, 1. Aufl., ser. Praxis Werkzeugtechnik. Wiesbaden: Vieweg + Teubner, 2010, ISBN: 978-3-8351-0126-5.

Acronyms

AC	Alternating Current
ALE	Arbitrary Lagrangian-Eulerian
API	Application Programming Interface
CAD	Computer Aided Design
CFD	Computational Fluid Dynamics
CFL	Courant-Friedrichs-Lewy
char	Character
DC	Direct Current
EDM	Electric Discharge Machining
EHL	Elastohydrodynamic Lubrication
EoS	Equation of State
EQS	Electro-Quasi-Static
EV	Electric Vehicle
FEM	Finite Element Method
float	Floating Point Number
foamExtend	Field Operation and Manipulation Extend
FSI	Fluid-Structure Interaction
FVA	Forschungsvereinigung Antriebstechnik e.V.
FVM	Finite Volume Method
GGI	General Grid Interface
GUI	Graphical User Interface
HDD	Hard Disk Drive

I/O	Input and Output
IIBC	Inverter-Induced Bearing Currents
int	Integer
KCM	Kinetically Constraint Models
LVI	Low Viscosity Index
MB	MegaByte
MQS	Magneto-Quasi-Static
NSE	Navier-Stokes Equation
OOP	Object-Oriented Programming
OpenFOAM	Open Source Field Operation and Manipulation
PDE	Partial Differential Equations
PISO	Pressure Implicit with Splitting of Operators
pmd	Institute for Product Development and Machine Elements
PNP	Poisson-Nernst-Planck
PTFE	Polytetrafluoroethylene
PWM	Pulse Width Modulation
RAM	Random Access Memory
RPM	Rotations per Minute
SDD	Schwartz Domain Decomposition
SIMPLE	Semi-Implicit Method for Pressure-Linked Equations
SOFA	Simulation Open Framework Architecture
SRR	Slide-to-Roll Ratio
STL	Stereolithography
TDD	Test-Driven Development
TEHL	Thermal Elastohydrodynamic Lubrication

Symbols

Symbol	Name	Description	Unit
a	Semi Axis		m
a^*	Dimensionless Semi Axis	tabulated values	-
$a_{\mathcal{F}}$	Thermal Diffusivity	$\kappa_{\mathcal{F}}/(\rho_{\mathcal{F}}c_{\mathcal{F}})$	$\text{m}^2 \text{s}^{-1}$
$a_{\mathcal{S}}$	Thermal Diffusivity	$\kappa_{\mathcal{S}}/(\rho_{\mathcal{S}}c_{\mathcal{S}})$	$\text{m}^2 \text{s}^{-1}$
A_{Hz}	Hertzian Contact Area		m^2
b	Semi Axis		m
b^*	Dimensionless Semi Axis	tabulated values	-
Bi	Biot Number		-
$c_{\mathcal{S}}$	Specific Heat Capacity		$\text{J s}^{-2} \text{K}^{-1}(\text{m}^2 \text{s}^{-2} \text{K}^{-1})$
$c_{\mathcal{F}}$	Specific Heat Capacity		$\text{J s}^{-2} \text{K}^{-1}(\text{m}^2 \text{s}^{-2} \text{K}^{-1})$
$C_{\mathcal{E}}$	Electrical Capacity		$\text{F}(\text{s}^4 \text{A}^2/\text{kg}/\text{m}^2)$
C	Dynamic Load Parameter		$\text{N}(\text{kg m s}^{-2})$
d_{i}	Diametre	inner ring	m
d_{iR}	Diametre	inner raceway	m
d_{C}	Diametre	cage	m

Symbol	Name	Description	Unit
d_{oR}	Diametre	outer ring raceway	m
d_{oO}	Diametre	outer ring surface	m
D	Displacement	$\mathbf{D}(x_1, x_2, x_3, t)$	m
$D_{\mathcal{E}}$	Electric Diffusivity	$\mu_{\mathcal{E}} k_B T / q_E$	$\text{J m}^2 \text{V}^{-1} \text{s}^{-1}$
e	Specific Thermal Energy		$\text{J kg}^{-1} (\text{m}^2 \text{s}^{-2})$
\mathcal{E}	Domain	electrostatics	-
E	Young's Modulus		$\text{Pa} (\text{kg s}^{-2} \text{m}^{-1})$
E'	Young's Modulus	reduced	$\text{Pa} (\text{kg s}^{-2} \text{m}^{-1})$
E	Electric field	$\mathbf{E}(x_1, x_2, x_3, t)$	$\text{V m}^{-1} (\text{kg m A}^{-1} \text{s}^{-3})$
f	Frequency		s^{-1}
F_R	Radial Load		$\text{N} (\text{kg m s}^{-2})$
\mathcal{F}	Domain	fluid	-
Fo	Fourier Number		—
F_{Ax}	Axial Load		$\text{N} (\text{kg m s}^{-2})$
$F(\rho)$	Curvature Difference		-
F_N	Normal Force		$\text{N} (\text{kg m s}^{-2})$
F_{fr}	Friction Force		$\text{N} (\text{kg m s}^{-2})$
F	Force		$\text{N} (\text{kg m s}^{-2})$
g_v	Viscosity Parameter	dimensionless	-

Symbol	Name	Description	Unit
g_E	Elasticity Parameter	dimensionless	-
g	Gravitational Acceleration	9.81	m s^{-2}
\bar{G}	Material Parameter	dimensionless	-
h_c	Lubrication Film Thickness	central	m
h_0	Lubrication Film Thickness	mean	m
h	Lubrication Film Thickness		m
h_e	Specific Enthalpy		$\text{J kg}^{-1}(\text{m}^2 \text{s}^{-2})$
\bar{H}	Lubrication Film Thickness	dimensionless	-
k_B	Boltzmann Constant	$1,380649 \cdot 10^{-23}$	$\text{J K}^{-1}(\text{kg m}^2 \text{s}^{-2} \text{K}^{-1})$
K	Bulk Modulus		$\text{Pa}(\text{kg m}^{-1} \text{s}^{-2})$
K_0	Bulk Modulus	at p_0, T_0	$\text{Pa}(\text{kg m}^{-1} \text{s}^{-2})$
K'_0	Bulk Modulus Rate of Change	$\partial K / \partial p$ at p_0, T_0	-
K'	Bulk Modulus Rate of Change	$\partial K / \partial p$	-
$L_{\mathcal{E}}$	Electrical Inductivity		$\text{H}(\text{kg m}^2 \text{s}^{-2} \text{A}^{-2})$
L_{10}	Bearing Lifetime		h
L	Characteristic Length		m
m	Mass		kg
\dot{m}	Mass Flux		kg s^{-1}
M	Molar Mass	m / n	kg mol^{-1}

Symbol	Name	Description	Unit
n_o	Rotational Speed	RPM	s^{-1}
n_i	Rotational Speed	RPM	s^{-1}
n_R	Rotational Speed	RPM	s^{-1}
n_m	Rotational Speed	RPM	s^{-1}
n	Amount of Substance		mol
N_A	Avogadro Constant	$6,02214076 \cdot 10^{23}$	mol^{-1}
p_{ref}	Pressure	reference	$\text{Pa}(\text{kg m}^{-1} \text{s}^{-2})$
p	Pressure	$p(x_1, x_2, x_3, t)$	$\text{Pa}(\text{kg m}^{-1} \text{s}^{-2})$
p_0	Pressure	ambient	$\text{Pa}(\text{kg m}^{-1} \text{s}^{-2})$
P	Equivalent Bearing Load		$\text{kN}(\text{kg m s}^{-2})$
q_E	Electric Charge	$1.602 \cdot 10^{-19}$	$\text{C}(\text{A s})$
q	Heat Flux		$\text{W m}^{-2}(\text{kg s}^{-3})$
Q	Point Contact Load		$\text{N}(\text{kg m s}^{-2})$
Q_{aim}	Target Point Contact Load		$\text{N}(\text{kg m s}^{-2})$
r_R	Radius	rolling element	m
r_i	Radius	inner raceway	m
r_o	Radius	outer ring raceway	m
$R_{\mathcal{E}}$	Electrical Resistance		$\Omega(\text{kg m}^2 \text{A}^{-2} \text{s}^{-3})$
R_s	Specific Gasconstant	R/M	$\text{J kg}^{-1} \text{K}^{-1}$

Symbol	Name	Description	Unit
Re	Reynolds Number		-
R	Gasconstant	8.31446261815324	J mol ⁻¹ K ⁻¹
\mathcal{S}	Domain	solid	-
t	Time		s
t_{cd}	Characteristic Deformation Time		s
\mathcal{J}	Domain	thermodynamics	-
T	Temperature	$T(x_1, x_2, x_3, t)$	K
T_{ref}	Temperature	reference	K
T_G	Glass Transition Temperature		K
u_e	Velocity	$0.5(u_1 + u_2)$	m s ⁻¹
u_{oR}	Velocity	$2\pi/60n_o \cdot 0.5d_{oR}$	m s ⁻¹
u_C	Velocity	cage	m s ⁻¹
u_{iR}	Velocity	$2\pi/60n_i \cdot 0.5d_{iR}$	m s ⁻¹
u_B	Velocity	base body	m s ⁻¹
u_C	Velocity	counter body	m s ⁻¹
\mathbf{u}	Velocity	$\mathbf{u}(x_1, x_2, x_3, t)$	m s ⁻¹
$u_{\mathcal{E}}$	Phase Velocity		m s ⁻¹
u_s	Sonic Solid	Velocity $\sqrt{\frac{\lambda_s + 2\mu_s}{\rho_s}}$	m s ⁻¹

Symbol	Name	Description	Unit
U_{CM}	Voltage	common mode	$\text{V}(\text{kg m}^2 \text{s}^{-3} \text{A}^{-1})$
\bar{U}	Dimensionless Velocity		-
U	Voltage		$\text{V}(\text{kg m}^2 \text{s}^{-3} \text{A}^{-1})$
v	Specific Volume	$1/\rho$	$\text{m}^3 \text{kg}^{-1}$
V	Volume		m^3
V_0	Volume	at p_0, T_0	m^3
V_∞	occupied Volume		m^3
V_{ref}	Volume	at $p_{\text{ref}}, T_{\text{ref}}$	m^3
$V_{\infty\text{ref}}$	occupied Volume	at $p_{\text{ref}}, T_{\text{ref}}$	m^3
V_g	Volume	at T_g, p_0	m^3
\bar{W}	Dimensionless Load Parameter		-
Y	Characteristic Height		m
z	Charge Number	integer	-
Z	Impedance		$\Omega(\text{kg m}^2 \text{s}^{-3} \text{A}^{-2})$
Z	Number of Rolling elements	7 (6205-C3)	-
α	Contact Angle		-
α	thermal expansion	$1/V \cdot (\partial V / \partial T)_p$	K^{-1}
$\alpha_{\mathcal{F}}$	Pressure Viscosity Coefficient		Pa^{-1}
α_{G}	thermal expansion		K^{-1}

Symbol	Name	Description	Unit
$\beta_{\mathcal{F}}$	Temperature Viscosity Coefficient		K^{-1}
$\dot{\gamma}$	Strain Rate	$\nabla \mathbf{u} + \nabla \mathbf{u}^{\top}$	s^{-1}
Γ	Domain Boundary		-
Γ_{FSI}	FSI Interface Boundary		-
Γ_{Raceway}	Raceway Interface Boundary		-
Γ_{Inlet}	Inlet Boundary		-
Γ_{Outlet}	Outlet Boundary		-
Γ_{RE}	Rolling Element Boundary		-
Γ_{IR}	Inner Ring Boundary		-
δ	Hertzian Deformation		m
δ^*	Hertzian Deformation	dimensionless	-
ε_r	Relative Permittivity		-
ε	Permittivity		$\text{F m}^{-1} (\text{s A}^2 \text{ kg}^{-1} \text{ m}^{-3})$
ε_0	Vacuum Permittivity		$\text{F m}^{-1} (\text{s A}^2 \text{ kg}^{-1} \text{ m}^{-3})$
$\boldsymbol{\varepsilon}$	Strain Tensor	$0.5(\nabla \mathbf{D} + \nabla \mathbf{D}^{\top})$	m m^{-1}
η	Dynamic Viscosity		$\text{Pa s} (\text{kg m}^{-1} \text{ s}^{-1})$
η_{ref}	Dynamic Viscosity	at $p_{\text{ref}}, T_{\text{ref}}$	$\text{Pa s} (\text{kg m}^{-1} \text{ s}^{-1})$
η_0	Dynamic Viscosity	at p_0, T_0	$\text{Pa s} (\text{kg m}^{-1} \text{ s}^{-1})$

Symbol	Name	Description	Unit
κ_S	thermal Conductivity	solid	$\text{W m}^{-1} \text{K}^{-1} (\text{kg m s}^{-3} \text{K}^{-1})$
$\kappa_{\mathcal{F}}$	thermal Conductivity	fluid	$\text{W m}^{-1} \text{K}^{-1} (\text{kg m s}^{-3} \text{K}^{-1})$
$\kappa_{\mathcal{E}}$	electrical Conductivity		$\text{S m}^{-1} (\text{s}^3 \text{A}^2 \text{kg}^{-1} \text{m}^{-3})$
λ	Specific Film Thickness	h / ς	-
λ_S	Second Lamé Coefficient		$\text{Pa} (\text{kg s}^{-2} \text{m}^{-1})$
μ	Friction Coefficient	F_N / F_{fr}	-
μ_S	First Lamé Co- efficient		$\text{Pa} (\text{kg s}^{-2} \text{m}^{-1})$
$\mu_{\mathcal{E}}$	Ion Mobility	u_{drift}/E	$\text{m}^2 \text{V}^{-1} \text{s}^{-1} (\text{A s}^2 \text{kg}^{-1})$
ν	Poisson Ratio		-
ξ	Polarizability		-
ρ_S	Density	solid	kg m^{-3}
ρ	Density		kg m^{-3}
ρ_{ref}	Density	at $p_{\text{ref}}, T_{\text{ref}}$	kg m^{-3}
$\rho_{\mathcal{F}}$	Density	fluid	kg m^{-3}
ρ_0	Density	at p_0, T_0	kg m^{-3}
$\rho_{\mathcal{E}}$	Electric Charge Density		$\text{C m}^{-3} (\text{A s m}^{-3})$
ς	Surface Rough- ness	$\sqrt{R_1^2 + R_2^2}$	m
σ	Stress Tensor		$\text{Pa} (\text{kg m}^{-1} \text{s}^{-2})$
$\Sigma\rho$	Curvature Sum		m^{-1}

Symbol	Name	Description	Unit
τ	Stress Tensor	dyad $\tau(x_1, x_2, x_3, t)$	Pa(kg m ⁻¹ s ⁻²)
τ_{em}	Electromagnetic Timeconstant		s
φ	Load Zone Angle		-
ϕ	Osculation	$(r_R/r_o)/(r_R/r_i)$	-
Φ	Electric Poten- tial Difference		V(kg m ² A ⁻¹ s ⁻³)
Ω	Domain		-

Supervised Theses

The author supervised the following theses as a research associate at the institute pmd of the Technical University Darmstadt. This dissertation would not have been possible without the help of the listed students. The theses are available on request via the institute pmd of the Technical University Darmstadt.

- **Experimentelle Untersuchung elektrischer Felder in Wälzlagerkontakten mithilfe keramischer Lager**
Experimental investigation of electric fields in rolling bearing contacts with ceramic bearings
Mulrav, Harsh (2021);
[Bachelor Thesis]
- **Numerische Simulation der elektrischen Eigenschaften eines Wälzkontaktes mit gemessenen Oberflächen**
Numerical simulation of the electrical properties of a rolling contact with measured surfaces
Zaiat, Anatoly (2021);
[Master Thesis]
- **Konstruktion einer Versuchseinrichtung zur Vermessung elektrischer Eigenschaften von tribologischen Systemen**
Design of an experimental testing rig for measurement of electrical properties in tribological systems
Lee, Niklas (2019);
[Bachelor Thesis]
- **Konstruktion einer tribologischen Versuchseinrichtung zur Untersuchung elektrischer Eigenschaften und Schadensmechanismen in Wälzkontakten**
Design of a tribological test facility for the research of electrical properties and damage mechanisms of rolling contacts
Bauch, Viviane; Bender, Fabian; Fehn, Patrick Paul; Ramachandran, Shabetha; Thein, Johannes (2018);
[Advanced Design Project]

- **Weiterentwicklung und Evaluation von Algorithmen zur CFD Simulation des elasto-hydrodynamischen (EHD) Wälzkontakts**
Improvement and evaluation of algorithms for CFD simulations of elasto-hydrodynamic roller bearing contacts
Möller, Christoph Michael (2018);
[Bachelor Thesis]
- **Konstruktion einer Gleitlagerversuchsanordnung zur Messung der Impedanz bei einstellbarer Wellenposition**
Construction of an experimental plain bearing setup for impedance measuring with adjustable shaft position
Jung, Justin (2018);
[Bachelor Thesis]

Publications

- **Sensorische Eigenschaften von Wälz- und Gleitlagerungen: Beherrschen von Unsicherheiten von und durch die Zusatzfunktion.**
Neu, Marcel; Harder, André; Kirchner, Eckhard (2019);
In: VDI Berichte, 2348, S. 183-192, Düsseldorf, VDI Verlag GmbH, 13. VDI Fachtagung Gleit- und Wälzlagerungen, Schweinfurt, 05.-06.06.2019, ISSN 00838860, ISBN 9873180923482;
[Conference publication]
- **Feasibility Study of Impedance Analysis for Measuring Rolling Bearing Loads.**
Schirra, Tobias; Martin, Georg; Neu, Marcel; Kirchner, Eckhard (2019);
Nashville, Tennessee, USA, STLE Annual Meeting, Nashville, Tennessee, USA, 19.-23.05.2019;
[Conference publication]
- **Simulation elektrostatischer Felder in thermischen elastohydrodynamischen Wälzkontakten.**
Neu, Marcel; Wenzel, Jan; Kirchner, Eckhard (2019);
In: Reibung, Schmierung und Verschleiß : 60. Tribologie-Fachtagung, S. 452-461, Aachen, Gesellschaft für Tribologie, Tribologie-Fachtagung, Göttingen, 23.-25.9.2019, ISBN 978-3-9817451-4-6
[Conference publication]
- **Erweiterung der Auslegung von Festlager-Laufrollenführungen bei trockenem Kontakt.**
Wenzel, Jan; Neu, Marcel ; Kirchner, Eckhard (2019);
In: 60. Tribologie-Fachtagung 2019; Reibung, Schmierung und Verschleiß, S. 111, Göttingen, 23.-25.09.2019, ISBN 978-3-9817451-4-6
[Conference publication]
- **Erweiterung der Auslegung von Festlager-Laufrollenführungen bei trockenem Kontakt.**
Wenzel, Jan; Neu, Marcel; Kirchner, Eckhard (2019);
In: Tribologie und Schmierungstechnik, 66 (6), S. 40-47. expert Verlag, ISSN 0724-3472,
[Article]

- **Auslegung und Zustandsüberwachung ungeschmierter, angetriebener Laufrollen.**
Wenzel, Jan; Neu, Marcel; Kirchner, Eckhard (2020);
In: 61. Tribologie-Fachtagung 2020: Reibung, Schmierung und Verschleiß, S. 24/1-24/10, Online-Konferenz, 28.-30.09.2020;
[Conference publication]
- **Sensing machine elements as enablers of comprehensive digitization – A review.**
Kraus, Benjamin; Neu, Marcel; Kirchner, Eckhard (2020);
In: 2020 10th International Electric Drives Production Conference (EDPC), S. 1-8, Ludwigsburg, IEEE, 10th International Electric Drives Production Conference (EDPC), Ludwigsburg, Germany, 8-9 Dec. 2020, ISBN 978-1-7281-8458-6, DOI: 10.1109/EDPC51184.2020.9388181
[Conference publication]
- **Initiierungs- und Abklingeffekte von elektrischen Schädigungsmechanismen im Wälzlager.**
Harder, André; Piske, Lukas; Neu, Marcel; Kirchner, Eckhard (2021);
In: VDI Berichte, 2378, In: 14. Fachtagung VDI Gleit- und Wälzlagerungen, 03.-04.05.2021, S. 65-74, Düsseldorf, VDI Verlag, ISSN 0083-5560, ISBN 987-3-18-09237-8;
[Conference publication]
- **An approach for the quantitative description of uncertainty to support robust design in sensing technology.**
Welzbacher, Peter; Schulte, Fiona; Neu, Marcel; Koch, Yanik; Kirchner, Eckhard (2021);
In: Design Science, 7, S. 1-18. Cambridge University Press, ISSN 2053-4701, DOI: 10.1017/dsj.2021.19;
[Article]